Application of Cucurbit[n]urils Immobilization in Chemosensor Microarray and Molecular Electronics

Zur Erlangung des akademischen Grades eines

DOKTORS DER NATURWISSENSCHAFTEN

(Dr. rer. nat.)

von der KIT-Fakultät für Chemie und Biowissenschaften

des Karlsruher Instituts für Technologie (KIT)

genehmigte

DISSERTATION

von

M. Sc. Chunting Zhong

Dekan:	Prof. Dr. Hans Achim Wagenknecht
Referent:	PD Dr. Dr. Michael Hirtz
Korreferentin:	Prof. Dr. Annie K. Powell
Tag der mündlichen Prüfung:	19.07.2022

This thesis was prepared from 15st of September 2018 to 20th of May 2022 at the Institute of Nanotechnology, Faculty of Chemistry and Biosciences of the Karlsruhe Institute of Technology (KIT) under the supervision of PD Dr. Dr. Michael Hirtz, Dr. Frank Biedermann and Prof. Dr. Annie K. Powell.

Eidesstattliche Erklärung

Bei der vorliegenden Dissertation zu dem Thema

Application of Cucurbit[n]urils Immobilization in Chemosensor Microarray and Molecular Electronics

handelt es sich um meine eigenständig erbrachte Leistung.

Ich habe nur die angegebenen Quellen und Hilfsmittel benutzt und mich keiner unzulässigen Hilfe Dritter bedient. Insbesondere habe ich wörtlich oder sinngemäß aus anderen Werken übernommene Inhalte als solche kenntlich gemacht.

Die Arbeit oder Teile davon habe ich bislang nicht an einer Hochschule des In- oder Auslands als Bestandteil einer Prüfungs- oder Qualifikationsleistung vorgelegt.

Die Richtigkeit der vorstehenden Erklärungen bestätige ich.

Die Bedeutung der eidesstattlichen Versicherung und die strafrechtlichen Folgen einer unrichtigen oder unvollständigen eidesstattlichen Versicherung sind mir bekannt.

Ich versichere an Eides statt, dass ich nach bestem Wissen die reine Wahrheit erklärt und nichts verschwiegen habe.

Karlsruhe, 25.05.2022

Ort und Datum

Kurzzusammenfassung / Abstract in German

Host-Gast-Interaktionen wurden erfolgreich für die Entwicklung von Materialien und Bauteilen verwendet. Die Entdeckung, Modifizierung und Immobilisierung von Hosts („Wirten“) oder Guests („Gästen“) zieht Wissenschaftler aus Gebieten wie der Chemie, Elektrochemie und Biologie an. Die Synthese von Cucurbit[n]urilen (CBn), einer Klasse von neuen Wirten, eröffnet aufgrund der hohen Bindungsaffinität zu ihren Gästen eine neue Ära. Die isolierten CBn zeigen mehr neue Möglichkeiten für Chemosensoren, Elektronik, Bausteine einschließlich Netzwerke und Nanostrukturen. Außerdem können sie auf Oberflächen immobilisiert werden, entweder direkt durch kovalente Bindung nach Modifikation, indirekt durch Gastvermittlung oder Adsorption an Gold durch Carbonyl, das insbesondere Möglichkeiten zur Grenzflächenfunktionalisierung bereitstellt. Die homogene CBn-Immobilisierung und Mikro-/Nanostrukturierung verleihen der modifizierten Oberfläche neue Eigenschaften. Um biomimetische Sensoren mit zell-ähnlicher Umgebung zu konstruieren, erscheint die Kombination von CBn mit biomimetischen Lipidmembranen möglich.

Molekulares Drucken, einschließlich soft („weicher“) Lithographie und der Rastersondenlithographie, kann Materialien in kontrollierte Formen auf spezifische Bereiche der Oberfläche übertragen. Die Entwicklung dieser Ansätze verspricht niedrige Kosten, Oberflächen-Bemusterung in großem Maßstab in kurzer Zeit, Flexibilität für Multiplexing und gezieltem Druck auf Vorstrukturen. Ihre Anwendungen umfassen die Verarbeitung von Materialien in Chemie, Biologie und Ingenieurwissenschaften. Aufliegende Lipiddoppelschichten (SLBs) sind ein effizienter Weg, um biomimetische Zellumgebungen sowie Grenzflächenfunktionen zwischen Zellen und der äußeren Umgebung nachzuahmen. Grundsätzlich sind alle molekularen Drucktechniken in der Lage, Lipide auf Oberflächen zu übertragen und Muster zu bilden. Jedoch können homogene SLBs, die durch Lösungsmittelaustausch und Bicelle-Fusion hergestellt wurden, insbesondere zur großflächigen Bedeckung mit einer einzigen Lipid-Zusammensetzung verwendet werden und weisen dabei eine relativ geringe Defektdichte auf.

Die Wirt-Gast-Chemie wurde zur Verbesserung der Leitfähigkeit in elektronischen Bauteilen verwendet, indem die Mikroumgebung der Redoxreaktion auf einer

selbstorganisierten Monolage (SAM) geändert und intermolekulare Umlagerungen vermieden wurden. Für CBn nimmt die Auswirkung auf den Leitwert ab, wenn n zunimmt. Ein gängiger CB8-Gast, Methylviologen (MV), kann nach Anlegen einer negativen Spannung reduziert werden und bildet ein $MV^{\bullet+}$-Radikal. Das Redox-Dimer $[MV^{\bullet+}]_2$ bildet sich, wenn die $MV^{\bullet+}$-Moleküle nahe genug beieinander liegen. CB8 stabilisiert $[MV^{\bullet+}]_2$-Dimere, dies wurde in Lösung durch elektrochemische Verfahren, zum Beispiel Cyclovoltammetrie (CV), nachgewiesen. $[MV^{\bullet+}]_2$ weist bei negativer Vorspannung eine große Hysterese auf, welche mit verschiedenen Gegenionen im Schaltkreis variiert. MVSAMs haben ein Potenzial als Materialien für resistiven Direktzugriffsspeicher (RRAMs). Allerdings muss die Stabilität der Hysterese weiter verbessert werden, um reale Anwendungen zu ermöglichen.

In dieser Arbeit wurden CBn/Indikator-Chemosensoren zunächst mit modifizierten CBn mittels Mikrokanal-Cantilever-Spotting (µCS) auf der Oberfläche immobilisiert. Die Sensoreigenschaften von Mono/Multi-Mikroarrays wurden im trockenen und nassen Zustand bewertet. Diese CBn-basierten Chemosensoren wurden dann mittels Gast-Vermittlung durch oberflächengebundene Gäste auf Alkin-Substraten immobilisiert, gefolgt von der Detektion von Analyten. Um das Problem des Mangels an waschbaren Indikatoren und des schwachen Signal der CBn-Monolage zu lösen, wurde ein CB8/DAP-Rotaxan mit zwei β-Cyclodextrin (CD) als Stopper auf zwei Seiten, um CB8/DAP vor der Demontage zu schützen, auf einer Isocyanatoberfläche strukturiert immobilisiert. Das hydrophile β-CD kann die unspezifische Adsorption des DAP-Indikators vermeiden und damit das Auslesesignal erhöhen. SLBs wurden durch Dip-Pen-Nanolithographie (DPN), Polymer-Pen-Lithographie (PPL) und µCS über die bereits etablierten Chemosensor-Mikroarrays mikrostrukturiert, um ein Sensorsystem in einer zellulären Umgebung zu imitieren.

Zusammenfassend lässt sich sagen, dass CBn/Indikator-Chemosensor-Mikroarrays eine hohe Empfindlichkeit für den Nachweis von nicht-chromophoren Analyten durch emissive Indicator Displacement Assays (IDA) zeigen mit Nachweisgrenzen (LOD) bis in den Nanomol-Bereich hinunter. Die Immobilisierung von CBn löst das Problem der Signalmaskierung durch den verdrängten Farbstoff, wobei der verdrängte Indikator im Vergleich zu nicht immobilisierten Gast-vermittelten Chemosensoren einfach

weggewaschen werden kann. Darüber hinaus bietet die Integration dieser CBn/Indikator-Chemosensor-Mikroarrays in mikrofluidische Chips eine effiziente Möglichkeit, den gesamten Prozess der Analytdetektion an der Flüssig-Feststoff-Grenzfläche in Echtzeit zu überwachen, die Handhabung zu vereinfachen und die Menge des benötigten Analyten zu reduzieren. Das Multiplexing von Mikroarrays zeigt den generellen Vorteil, verschiedene Komponenten durch Multi-CBn und/oder Multiindikator nachweisen zu können, da diese unterschiedlich auf verschiedene Analyten ansprechen. Das CB8/DAP-Rotaxan-Mikroarray mit einem festen Indikator innerhalb von CB8 zeigt eine bemerkenswerte Empfindlichkeit für den Nachweis von L-Tryptamin (L-Trp), mit einem LOD bis zu submikromolaren Konzentrationen. Nach dem Bedecken mit SLBs war das Rotaxansystem in der Lage, die Membrandurchlässigkeit in einer biomimetischen zellähnlichen Umgebung anzuzeigen. Mit DOPS SALB bedeckte Mikroarrays zeigten eine langsamere Abnahme der Fluoreszenz, was den langsameren Transport von L-Trp durch die Membran aufgrund von Ladungseffekten demonstrierte. Die CBn-Immobilisierung für Chemosensorsysteme eröffnet ihr Potenzial für die Integration von Sensoren in vollwertige Lab-on-a-Chip-Geräte.

Für die angestrebten elektronischen Anwendungen war das isolierte MV-vermittelte CB8 in der Lage, ein zweites Viologen aus der Lösung zu rekrutieren, die absoluten Oberflächenbelegungen von CB8, $MV^{\bullet+}$ und $[MV^{\bullet+}]_2$ wurden durch CV-Messung nachgewiesen. Die Oberflächendichte von CB8 (sowie $[MV^{\bullet+}]_2$) auf 5% MV SAMs beträgt $2{,}32 \times 10^{-11}$ mol/cm^2. Sie sinkt auf 0,13 x 10-11 mol/cm^2 bei 50 % MV SAMs wo aufgrund sterischer Effekte fast kein CB8 für eine weitere $[MV^{\bullet+}]_2$-Bildung immobilisiert werden. Die eutektischen Gallium-Indium (EGaIn)-Kontaktübergänge auf 5% MV SAMs zeigten eine große unipolare Hysterese bei negativer angelegten Vorspannung mit einem hohen Stromgleichrichtungsverhältnis von $1{,}10 \times 10^3$ und einem Ein/Aus-Zustandsverhältnis von $3{,}16 \times 10^4$. Die Stabilität der Hysterese wurde aufgrund der idealen Mikroumgebung durch CB8 erhöht, die im Vergleich zu 100 % MV SAMs die intramolekulare Umlagerung von MV und Störungen durch umgebende Moleküle vermeidet. Darüber hinaus verstärkt CB8 den Ladungstransport von $MV^{\bullet+}$, der aus einer großen intermolekularen LUMO-LUMO-Kopplung resultiert. Dies erhöht die Leitfähigkeit der Übergänge selbst bei niedrigen $[MV^{\bullet+}]_2$-Dichten. Die molekulare Verbindung von CB8/MV_2 hat ein hohes Potenzial als

Bauelement in resistiven Direktzugriffsspeichern (RRAMs). Das Konzept der Wirt-Gast-Chemie kann zukünftig für die Entwicklung neuartiger Halbleiterchips wie CMOS (Complementary Metal-Oxide Semiconductor) angewendet werden.

Abstract

Host-guest interaction has been used for developing materials and devices. The discovery, modification and immobilization of hosts or guests attract scientists, varying from chemistry, electrochemistry to biology. The synthesis of cucurbit[n]urils (CBn), one series of the new hosts, opens a new era due to the high binding affinity to their guests. The isolated CBn show more capabilities for chemosensors, electronics, building blocks including networks and nanostructures. In addition, they can be immobilized on the surface either directly by covalent binding after modification, indirectly through guest mediation or adsorption on Au through carbonyl, which provides in particular more interfacial functionality. The homogeneous CBn immobilization and micro/nanopatterning endow the modified surface with new properties. In order to construct biomimetic sensors with a cell-like environment, combination of CBn with lipid membranes seems feasible.

Molecular printing including soft lithography and scanning probe lithography can transfer materials onto the specific area of the surface with controlled features. The development of these approaches meets the requirements of low cost, large-scale patterning in a short time, flexibility for multiplexing and reprinting. Their applications cover materials processing in chemistry, biology and engineering. Supported lipid bilayers (SLBs) are an efficient way to construct biomimetic cell membranes as well as to mimic interfacial functions between cells and the outside environment. In principle, all the molecular printing techniques are able to transfer lipids onto surfaces and form patterns. However, also homogeneous SLBs prepared by solvent exchange and bicelle fusion can be used for large area covering in single composition and have a relatively low defect.

Host-guest chemistry has been used for conductance enhancement in electronics devices through changing the microenvironment of redox reactions on self-assembled monolayers (SAMs) and avoiding molecular rearrangement. For CBn, the effect on the conductance decreases when n increases. One common guest of CB8, methyl viologen (MV), can be reduced after loading a negative voltage and forms $MV^{\bullet+}$ radical. Redox dimer $[MV^{\bullet+}]_2$ forms when the $MV^{\bullet+}$ molecules are close enough to each other. Coincidentally, CB8 stabilizes $[MV^{\bullet+}]_2$ dimers, and has be detected in solution by electrochemical method, for example, cyclic voltammetry (CV). $[MV^{\bullet+}]_2$ were proved having big hysteresis in negative bias, varying with different counterions in a circuit. MV SAMs with CBn functionalization

have a potential as computing materials for resistive random access memories (RRAMs). However, the stability of the hysteresis needs to be improved to achieve real applications.

In this work, CBn/indicator chemosensors have been immobilized on surface first by modified CBn through microchannel cantilever spotting (μCS). The sensing properties of mono/multi-microarrays have been evaluated in dry and wet states. These CBn-based chemosensors were then immobilized by guest-mediation through surface-bound guests on alkyne substrates, followed by the detection of analytes. In order to solve the shortcoming of washable indicators and the weak readout of CBn assembly, a CB8/DAP rotaxane, with two β-cyclodextrin (CD) as stoppers on two sides to lock CB8/DAP from disassembly, was patterned on an isocyanate surface. The hydrophilic β-CD can avoid unspecific adsorption of DAP indicator, therefore increasing the readout signal. SLB were micropatterned by dip-pen nanolithography (DPN), polymer pen lithography (PPL) and μCS over the established chemosensor microarrays to imitate a sensing system in a cellular environment.

In conclusion, CBn/indicator chemosensor microarrays show high sensitivity for detection of non-chromophoric analytes through emissive indicator displacement assays (IDA) and the limit of detection (LOD) is down to nanomole. Immobilization of CBn solves the problem of signal interference by the displaced dye, where the displaced indicator can be simply washed away, compared with non-immobilized guest-mediated chemosensors. In addition, the integration of these CBn/indicator chemosensor microarrays into microfluidic chips provides an efficient way to enable real-timely monitoring the whole process of analyte detection at the liquid-solid interface, simplifies handling and reduces the amount of needed analyte. The multiplexing of microarrays shows the general advantage to detect multi-components through multi-CBn and/or multi-indicator use that respond differentially to different analytes. The CB8/DAP rotaxane microarray, with a fixed indicator inside CB8, shows remarkable sensitivity for L-tryptamine (L-Trp) detection and the LOD can be down to submicromolar concentrations. After covered with SLBs, the rotaxane system was able to evaluate the membrane permeability in a biomimetic cell-like setup. DOPS SALB covered microarrays showed slower fluorescence quenching, which demonstrated the slower transport of L-Trp through the membrane due to charge effects. CBn immobilization

for chemosensors systems opens up its potential for integration of sensors into full-fledged lab-on-a-chip devices.

Towards the envisioned electronic applications, the isolated MV mediated CB8 was able to bring a second viologen from the solution and the absolute surface coverages of CB8, $MV^{\bullet+}$ and $[MV^{\bullet+}]_2$ were detected through CV measurement. The surface density of CB8 (as well as $[MV^{\bullet+}]_2$) on 5% MV SAM is 2.32×10^{-11} mole / cm^2. It decreases to 0.13×10^{-11} mole / cm^2 at 50% MV SAM and almost no CB8 can be immobilized for further $[MV^{\bullet+}]_2$ formation due to steric effects. The eutectic Gallium-Indium (EGaIn) based junctions of 5% MV SAM showed a large unipolar hysteresis in the negative applied bias with a high current rectification ratio of 1.10×10^3 and an on/off state ratio of 3.16×10^4. The stability of the hysteresis has been increased because of the ideal microenvironment provided by CB8, which avoids the rearrangement of MV and interference from surrounding molecules, compared with 100% MV SAMs. Furthermore, CB8 enhances the charge transport of $MV^{\bullet+}$ resulting from large intermolecular LUMO-LUMO coupling and this increases the conductance of the junctions even with low $[MV^{\bullet+}]_2$ densities. CB8/MV_2 molecular junctions have high potential as a constituent of resistive random access memories (RRAMs). The concept of host-guest chemistry is possible to be applied for development of novel semiconductor chips such as CMOS (complementary metal-oxide semiconductor) in the future.

Table of contents

1. Introduction and theory

In the past decades, host-guest supramolecular interaction has been discovered to play a key role in chemistry, electrochemistry and biology. The development of host-guest chemistry diversified with the discovery and design of new hosts e.g., cyclodextrin and guests e.g., adamantane. The synthesis of cucurbit[*n*]urils (CBn) with high binding affinity to their guests opens a new era. Their isolation enables CBn more capabilities in applications to form chemosensors, electronics, and building blocks, including networks and nanostructures. The direct or indirect immobilization of CBn, either homogeneous or patterned, is another hot topic, which provides more interfacial functionality with high potential. In order to create biomimetic sensors in a cell-like environment, combination with lipid membranes seems feasible, which also attracts researchers' attention.

This chapter discusses CBn, including their modification, applications and immobilization on the surface. Then the molecular printing approaches for materials transport are covered. Finally, the conventional approaches for supported lipid membranes (SLM) are summarized.

1.1. Cucurbit[n]urils (CBn)

Cucurbit[*n*]urils are glycoluril (=$C_4H_2N_4O_2$=) made macrocyclic molecules linked by methylene (-CH_2-). The inwards tilted oxygen atoms located along the band's edges form a partly enclosed cavity. The name came from the resemblance structure to a pumpkin family, Cucurbitaceae[1]. Cucurbit[n]urils are abbreviated as CB[n] or CBn, where *n* is the number of glycoluril units. The most prominent CBn homologs are CB5, CB6, CB7 and CB8 (Figure 1- 1).[2]

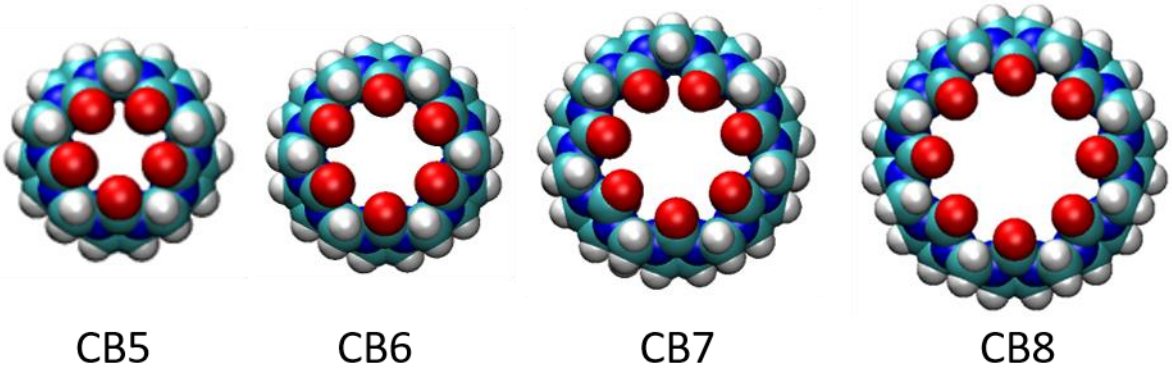

Figure 1- 1 Most prominent CBn homologues, CB5, CB6, CB7 and CB8.[2]

The dimensions of the CBn are generally on the ~ 10 Å size scale, the most prominent CBn shown in Figure 1- 2. For instance, the cavity of CB6 has a height of ~ 9.1 Å, an outer diameter of ~ 5.8 Å, and an inner diameter of ~ 3.9 Å.[3]

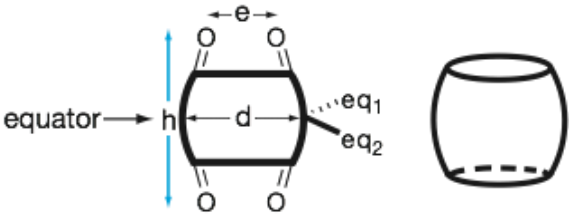

CB[n]	5	6	7	8
cavity, d (Å)	4.4	5.8	7.3	8.8
entry, e (Å)	2.4	3.9	5.4	6.9
height, h (Å)	9.1	9.1	9.1	9.1

Figure 1- 2 The dimensions of CB5, CB6, CB7 and CB8.[3]

1.1.1. Synthesis

Robert Behrend first synthesized CBn in 1905 through condensing glycoluril with formaldehyde[4] and the structures were clarified in 1981 by W. A. Freeman et al.[1] Recently, the synthesis steps including the preparation of glycoluril via a nucleophilic addition (Figure 1- 3)[5] and condensation into CBn above 110 °C (Figure 1- 4)[6], have been improved using more efficient oxidize agents. The temperature between 75 and 90 °C accesses other sizes of CBn including CB5, CB7, CB8, and CB10, while CB6 is still the major product. The isolation of sizes other than CB6 requires fractional crystallization and dissolution, which is complicated and time-consuming. CB5, CB7, and CB8 were first discovered and isolated by Kim Kimoon in 2000.[7] Nowadays CB5, CB6, CB7, CB8, CB10 and CB14 have all been separated.[8] Cyclodextrins, calixarenes, and pillararenes share a similar molecular shape with CBn.

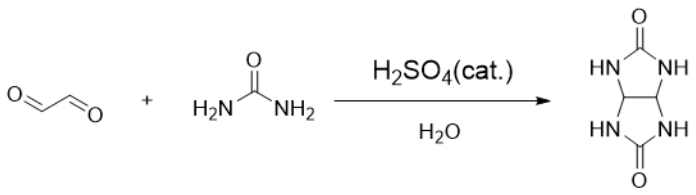

Figure 1- 3 Synthesis of glycoluril.[5]

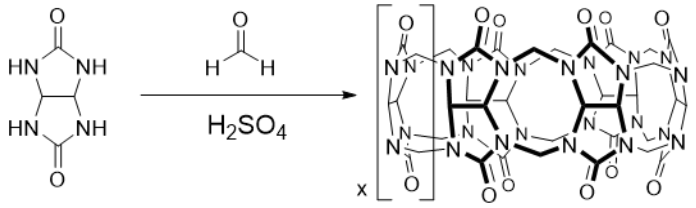

Figure 1- 4 Synthesis of CBn through condensing glycoluril with formaldehyde.[6]

1.1.2. Modification

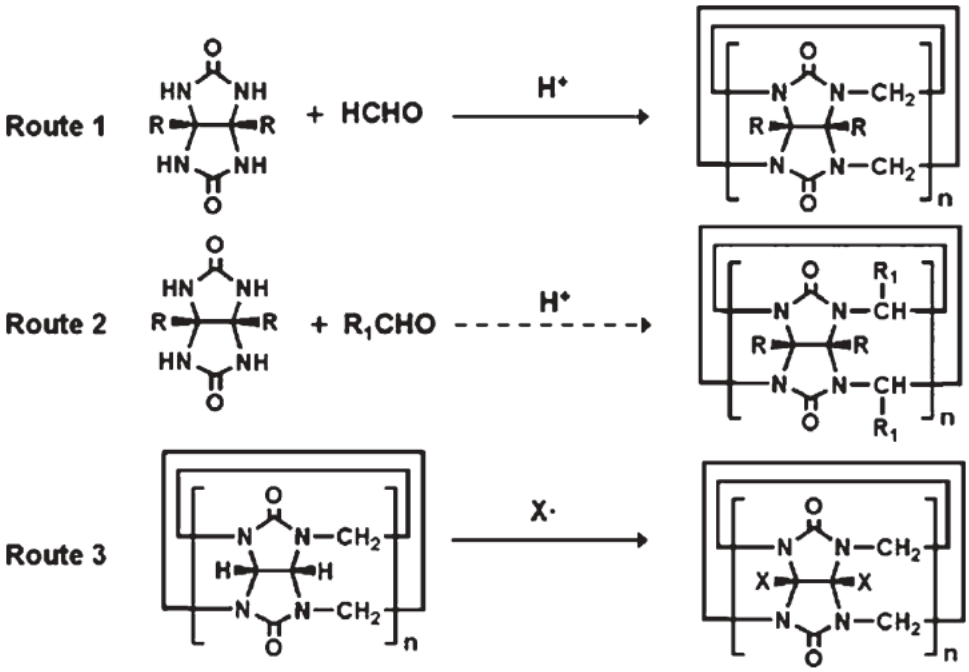

Figure 1- 5 Strategies of CBn modification.[9]

The discovery of CBn homologues firstly broadened the scope of CB chemistry. However, the application of CBn was still limited because they dissolved poorly in common solvents. Compared to other host families, including crown ethers, cyclodextrins and calixarenes, it

was also challenging to modify CBn with functional groups. The introduction of functional groups in the peripheral part was particularly a long-standing problem. There are principally three ways to accomplish the modification of CBn (Figure 1- 5)[9]: i) condensation of glycoluril having substituents at the 'bridging' carbon atom with formaldehyde gives CBn derivatives carrying the functional groups at the ''equator'' positions (Figure 1- 6)[10]; ii) condensation of glycoluril with varying aldehydes that have substituents would introduce the corresponding functional groups at the methylene bridges of CBn; iii) direct introduction of functional groups at the tertiary carbon atom of the CBn. This part mainly introduces the direct functionalization of CBn. Firstly, the tertiary carbons of CBn were oxidized and linked with, e.g., a hydroxyl group (Figure 1- 7)[11] that was further modified with functional groups such as alkenyl (Figure 1- 8),[12] or alkyne (Figure 1- 9).[13]

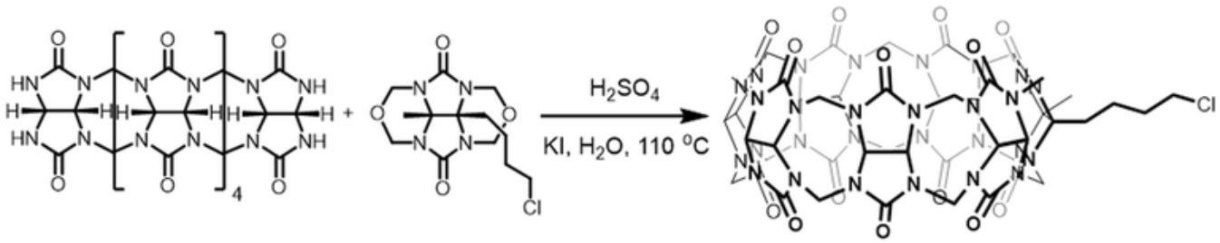

Figure 1- 6 Modified CB7 through condensation of glycoluril having substituents.[10]

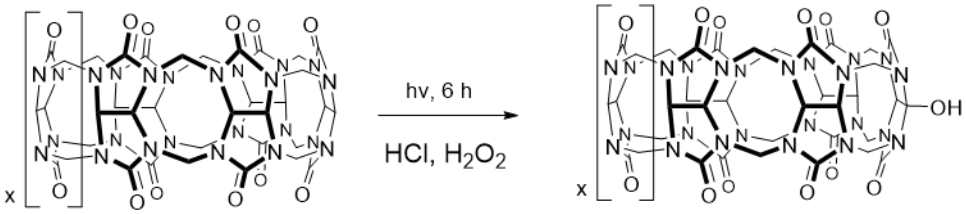

Figure 1- 7 Modification of CBn with hydroxyl.[11]

Figure 1- 8 Modification of CBn with alkenyl.[12]

Figure 1- 9 Modification of CBn with alkyne.[13]

1.1.3. Application

CBn has been used by chemists for various applications[14-20], including drug delivery[14], asymmetric synthesis[15], click reaction catalyst[16], networks[19], nanostructures[20], chemosensors[17] and molecular electronics[18]. Here, applications in chemosensors, electronics, networks and nanostructures are mainly introduced below.

1.1.3.1. Chemosensors

There are three main sensing strategies adopted for CBn-based sensing studies (Figure 1- 10):[21] i) Direct-binding assay (DBA) where CBn directly bind analyte or CBn-derivatives containing a dye component yield a spectroscopic response upon binding of an analyte. ii) Indicator-displacement assay (IDA) where an emissive or chromophoric indicator sensitive to the environment is assembled with CBn. The indicator will be displaced by a CBn-binding analyte present in the solution, which generates a readily measurable and quantifiable signal change. iii) Associative-binding assay (ABA) where the binding cavity is formed by the host and a non-covalently incorporated reporter dye, mainly for detecting aromatic analytes.

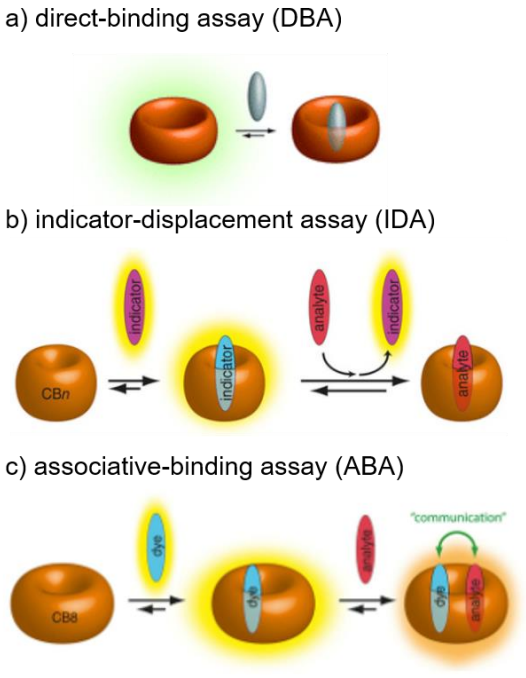

Figure 1- 10 Scheme of the direct-binding assay (DBA), indicator-displacement assay (IDA) and associative-binding assay (ABA).[21]

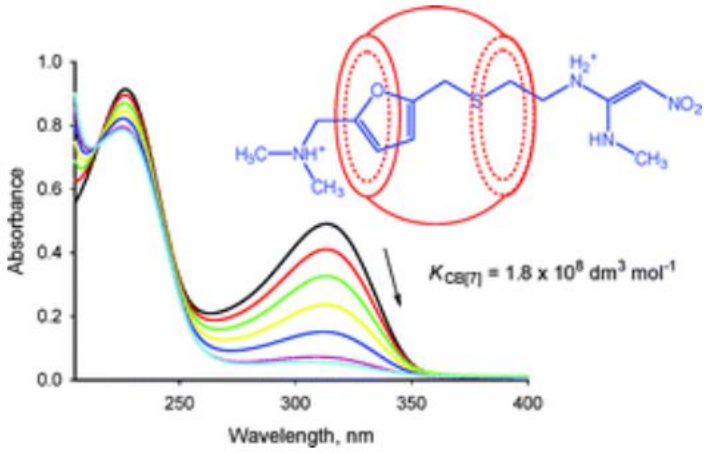

Figure 1- 11 Direct-binding assay (DBA) of CB7 for histamine H_2-receptor antagonist ranitidine.[22]

The macrocyclic host CB7 forms very stable complexes with the diprotonated (K_{CB7}^1 = 1.8 × 10^8 dm^3 mol^{-1}), monoprotonated (K_{CB7}^2 = 1.0 × 10^7 dm^3 mol^{-1}), and neutral (K_{CB7}^3 = 1.2 × 10^3 dm^3 mol^{-1}) histamine H_2-receptor antagonist ranitidine in aqueous system investigated through ^{1}H NMR and UV–visible spectroscopy (Figure 1- 11).[22] The pK_a values of the ranitidine were observed to increase (ΔpK_{a1} = 1.5 and ΔpK_{a2} = 1.6) upon host-guest interaction. The host-guest complexes with minimized energy provide

agreement with the NMR results that indicate CB7 over the central portion of the guest. The inclusion of the monoprotonated ranitidine changes the normally (*E*)–(*Z*) exchange process from rapid to slow, which generates a preference for the (*Z*) isomer. The formation of the CB7-ranitidine complex dramatically enhances the thermal stability of ranitidine in an acidic system at 50 °C without affecting its photochemical reactivity.

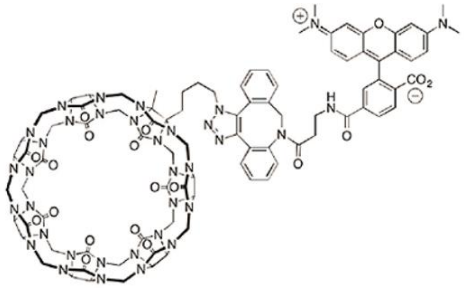

Figure 1- 12 CB7-TMR conjugate.[23]

To be conjugated with a fluorescent dye, CB7 was linked with tetramethylrhodamine (TMR) in two steps from monofunctionalized azidobutyl-CB7 and NHS-activated TMR (Figure 1-12).[23] CB7-TMR behaviors in different fluorescence, guest-binding properties and cellular uptake. The fluorescence of CB7-TMR is quenched after binding with the guest, which was able to determine equilibrium dissociation constant (Kd) values that are essentially identical to unmodified CB7 but across 3 orders of magnitude and at concentrations as low as 0.7 nM. Revealed the cellular uptake of CB7-TMR and its punctate localization in the cytoplasm. CB7-TMR did not alter HT22 neurons cells growth at concentrations up to 2.2 μM over four days.

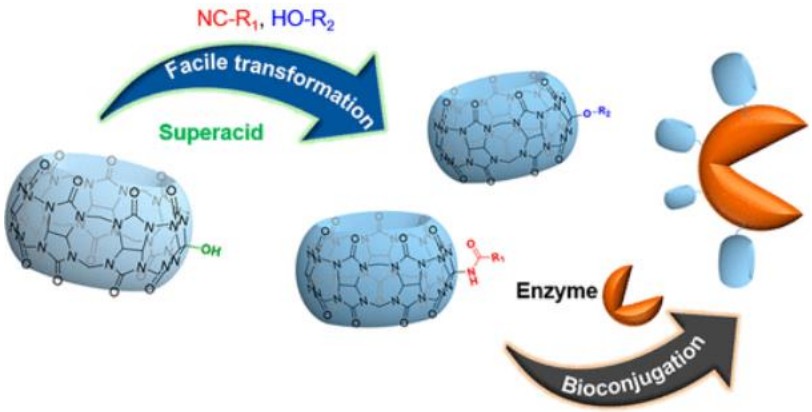

Figure 1- 13 CB7-HRP conjugate for protein detection.[24]

S. K. Ghosh and coworkers reported a facile transformation of hydroxylated CB6 and CB7 through nucleophilic substitution with a wide range of nitriles and alcohols (Figure 1- 13).[24] It resulted in monocarboxylated CB7 that is efficiently conjugated to horseradish peroxidase (HRP) by amide coupling. The conjugated CB7-HRP can selectively detect proteins that were labeled with a guest, adamantylammonium. The study overcame the limitations in preparing reactive functional CBn derivatives that enable the broadening of novel bioapplications of CBn-based supramolecular chemistry. CB7-indicator conjugate e.g. CB7-BE (berberine, one CB7 guest) as a chemosensor can be buffer and saline-stable, which allows for selective detection of amantadine in urine and saliva from Parkinson patients (Figure 1- 15).[25]

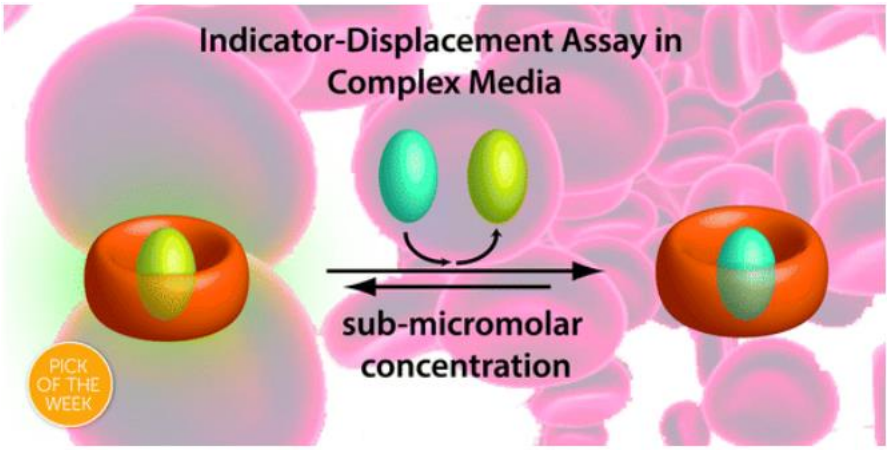

Figure 1- 14 Indicator-displacement assay (IDA) in complex media.[26]

Mathematical simulations of rational design principles for host-guest chemosensing in competitively binding media show that currently known CBn-based chemosensing ensembles are not suited for use in highly competitive matrices such as blood serum. Conversely, S. Sinn et al reported the first CBn-based IDA operational in blood serum (Figure 1- 14).[26] A novel series of [2.2]paracyclophane-derived indicators for CB8 was developed and it possesses one of the highest host-guest binding affinities (Ka > 10^{12} M^{-1} in water) known in supramolecular host-guest chemistry and a large Stokes shift (up to 200 nm). The detection of Alzheimer's drug memantine evaluated the novel IDA in blood serum, which corresponds to the initial simulations that a combination of CB8 and an ultra-

high affinity indicator would be a promising IDA reporter pair for the detection of memantine in blood serum. C. Hu et al show two buffer- and saline-stable CB7-BE conjugates (Figure 1- 15) and allow for selective sensing of Parkinson's drug amantadine in human urine and saliva.[25] The in-depth analysis of the CB7-BE conjugates in the gas-phase, and deionized versus saline aqueous media revealed the structural, thermodynamic and kinetic effects different from free CBn chemosensors.

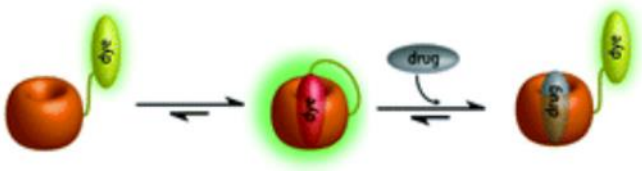

Figure 1- 15 CB7-BE conjugate for selective detection.[25]

1.1.3.2. Supramolecular electronics

The environment of local molecules is a critical factor that should be considered when measuring single-molecule electronics in condensed media or the design of future molecular electronic devices. Supramolecular interactions can be used to adjust the local environment through molecular assemblies and have been used to change microenvironments for chemical reactions[27-28]. The design and construction of supramolecular electronic devices require to probe binding interaction and the electron transport of supramolecular bridging electrodes (Figure 1- 16).[28]

Figure 1- 16 Scheme of supramolecular junctions.[28]

Scanning tunneling microscopy break junction (STM-BJ) technique has been employed to measure the conductance of CBn-based single molecular junctions (Figure 1- 17).[29] The electrostatic interactions from the carbonyl portals to the gold surface (Au) form the molecular junctions. The molecule conductance linearly decreases as CB5 > CB6 > CB7 conversely as the increase of the terminal carbonyl groups, which arises from the different interfacial coupling. CB8 was used to create microenvironments to host the viologen (bipyridinium) forming a 1:1 complex, which influences the electrical conductance of single-molecule wires (Figure 1- 18).[30] The significant increase in the CB8/viologen wire single-molecule conductance is observed due to large changes of the molecular microenvironment around viologen (Figure 1- 19).[28]

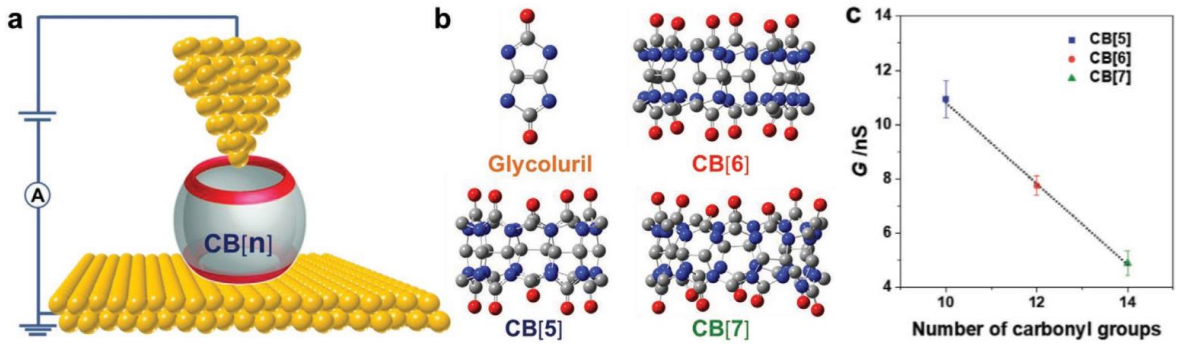

Figure 1- 17 a) Scheme of STM-BJ method for the fabrication of CBn molecular junction. b) The optimized molecular structures of glycoluril, CB5, CB6, and CB7. The plot of single-molecule conductance against the number of the terminal carbonyl groups of CB5, CB6, and CB7.[29]

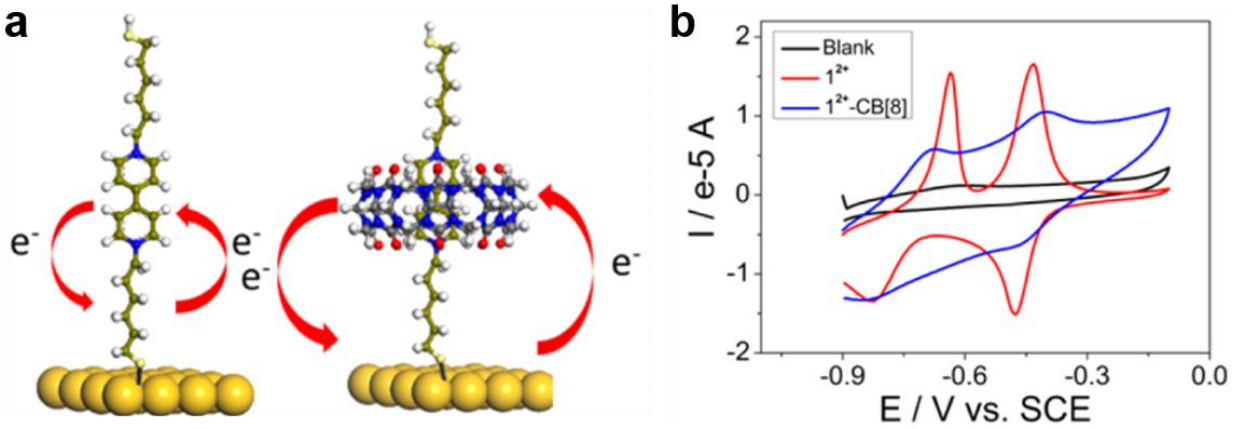

Figure 1- 18 a) Scheme of electron transport on viologen (1^{2+}) and CB8/viologen (1^{2+}-CB8) monolayer on Au. b) CVs of 1^{2+} and 1^{2+}-CB8 monolayer modified Au in 0.1 M phosphate buffer at a scan rate of 400 mV/s; redox reaction for 1^{2+} and 1^{2+}-CB8.[30]

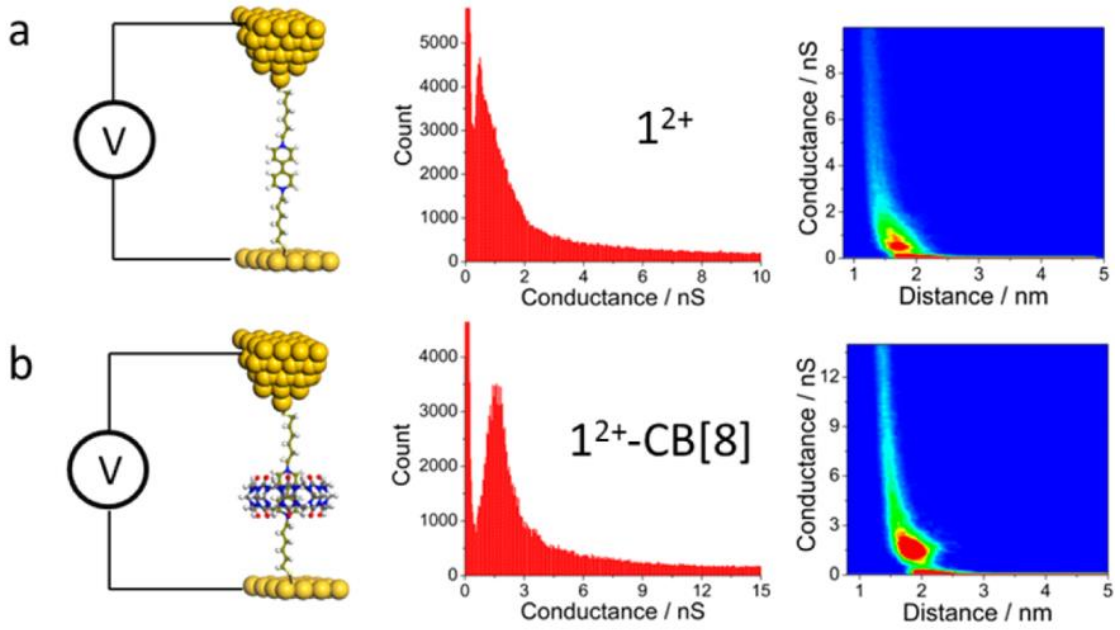

Figure 1- 19 Molecular junction schematic (left), 1-D conductance histograms (center) and 2-D (conductance-junction distance) histograms (right) of (a) 1^{2+} and (b) 1^{2+}-CB8 junctions.[28]

The conductance of single-molecule junctions may be governed by the structure, the way it bonds with the leads, or the rotation of the molecule. In order to know the reason of enhanced conductance, a STM-AFM (AFM: atomic force microscope) system has been used to measure viologen junction (Figure 1- 20),[31] where a rearrangement occurs during each conductance step. STM-TERS (TERS: tip-enhanced Raman spectroscopy) allows mutually verifiable single-molecule conductance and Raman signals with single-molecule contributions to be acquired simultaneously at room temperature, which has been used to characterize the molecule-to-surface bonding of CB8/viologen junction during electron transport (Figure 1- 21).[32] The mismatching between current and Raman shift demonstrates that a stronger bonding interaction between the molecule and the drain may account for the nonlinear dependence of conductance on the bias voltage. These studies reveal that rearrangement of viologen in the CB8 host is suppresed, therefore CB8 stabilizes viologen and enhances the conductance.

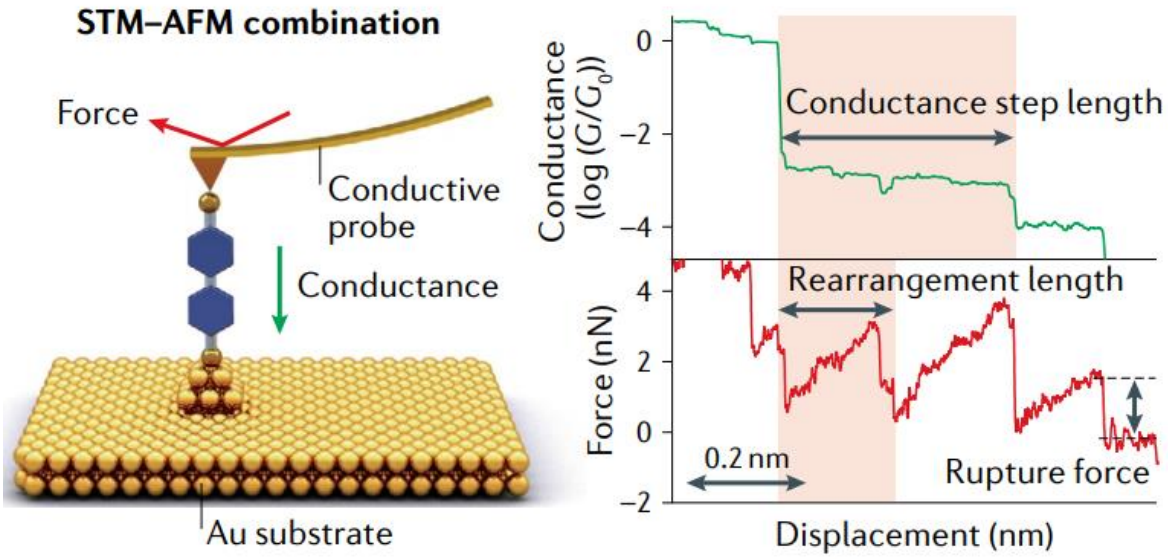

Figure 1- 20 Scheme of a STM-AFM (left) for simultaneous single-molecule measurements (right) of current (green) and force (red).[31]

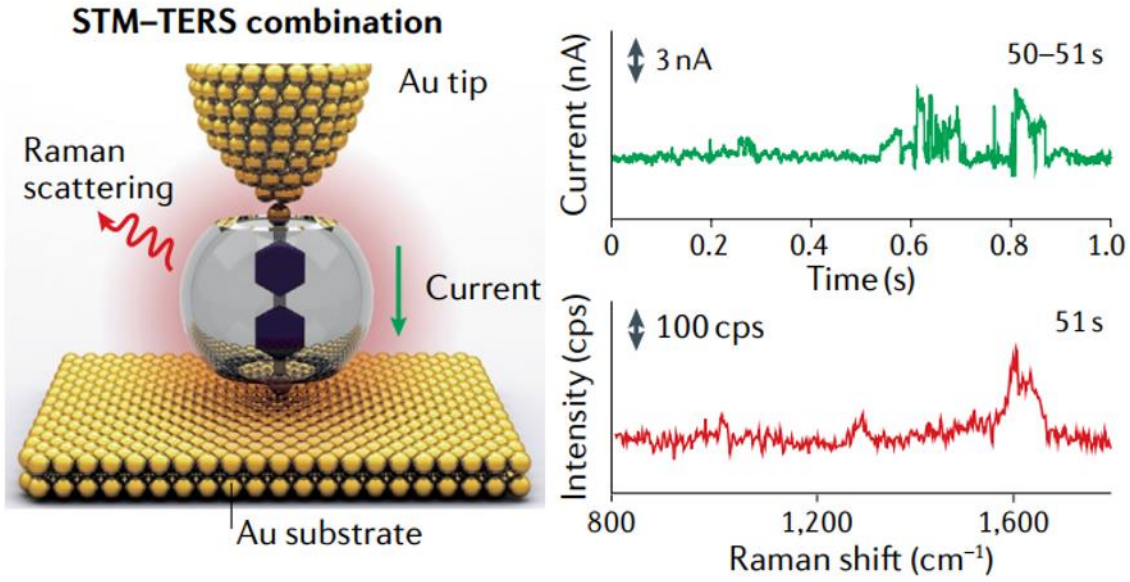

Figure 1- 21 Scheme of (left) a STM-TERS for simultaneous measurements (right) of the current (green) and corresponding TERS spectra (red) for a duration of 1s. cps, counts per second.[32]

Intermolecular charge transport through π-conjugated molecules plays an essential role in biochemical redox processes and energy storage applications.[18] The highly efficient intermolecular charge transport was observed upon dimerization of pyridinium molecules

in the cavity of CB8 host (Figure 1- 22). The results show that π-stacked pyridinium dimers behave comparable molecular conductance to isolated pyridinium molecules although there are a longer transport pathway and a switch from intra- to intermolecular charge transport. Molecular modeling using density functional theory (DFT) reveals that pyridinium molecules are planarized due to dimerization inside the CB8 cavity, which is beneficial to charge transport. Additionally, large intermolecular LUMO−LUMO couplings that lead to enhanced intermolecular charge transport exist in the π-stacked pyridinium dimers.

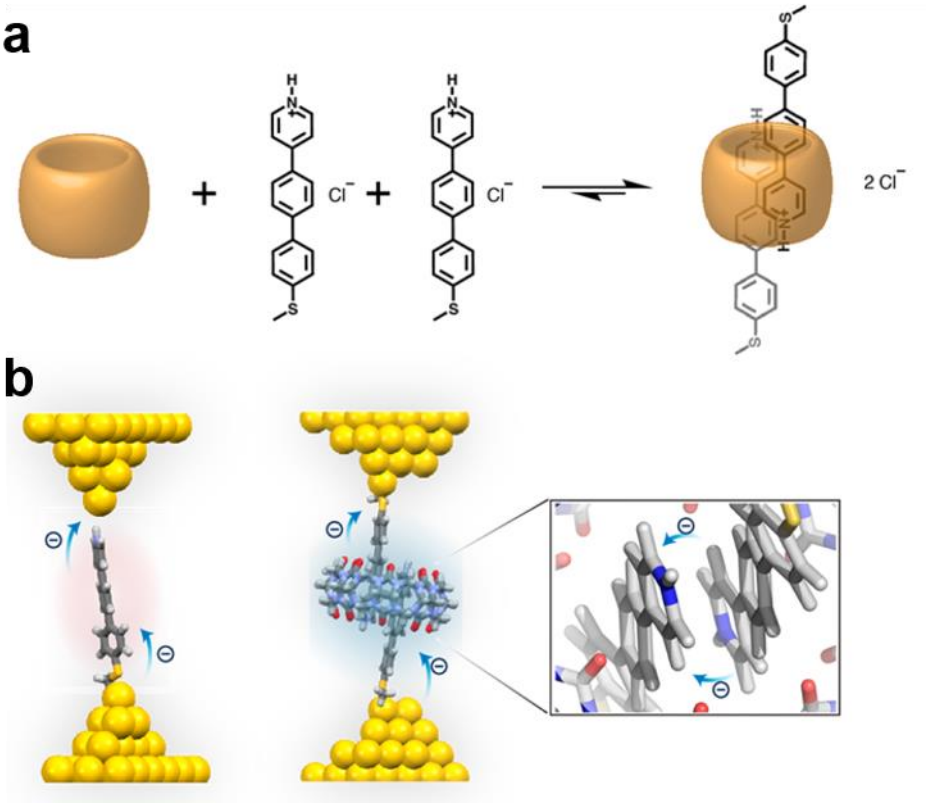

Figure 1- 22 Macrocycle-Mediated Dimerization of Pyridinium Molecule in CB8; (b) Schematic of Molecular Junction.[18]

1.1.3.3. Supramolecular network

The formation of a CBn-based supramolecular network is to obtain e.g., injectable and printable hydrogels with control of gelation kinetics. Supramolecular organic frameworks (SOFs) has been attracted many chemists. Either direct-binding of two polymers, one with

host and one with corresponding guest, or associative-binding of two guests linked on two polymers in additional CB8 is feasible.

The gelation kinetics of CB7-AD (adamantane) cross-linked supramolecular hydrogels can be controlled from seconds to hours by using competing guest molecules as shown in Figure 1- 23.[19] The good mechanical properties and stability are because of the strong interaction of the CB7-AD pair. Additionally, the binding of functionalized guests offers a facile approach for tailoring the hydrogels' scaffold.

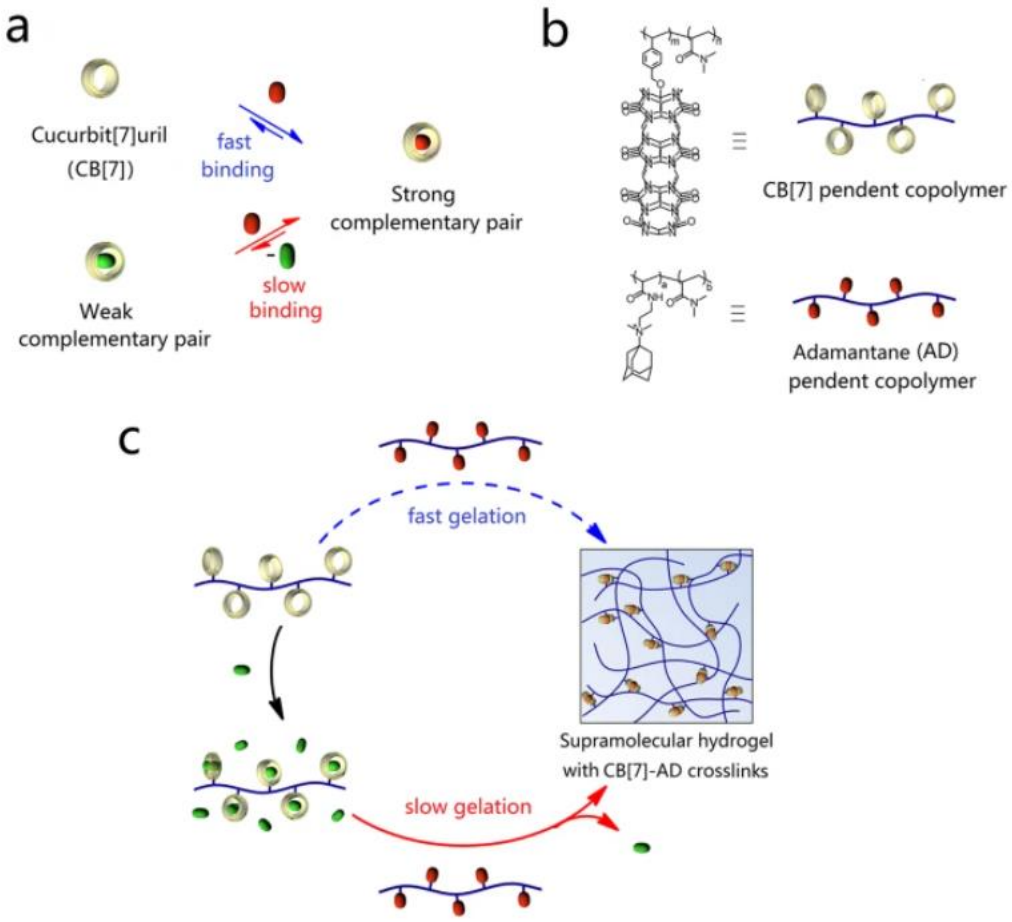

Figure 1- 23 Scheme of control gelation kinetics of the CB7-AD cross-linked hydrogels with competing guest molecules.[19]

A two-dimensional SOF has been constructed in water from a rigid water-soluble triangular building block (Figure 1- 24),[33] which is driven by the dimerization of three appended viologen radical cation units. In addition, CB8 stabilizes the single-layer network through encapsulation of the stacking viologen radical dimers.[34] After being characterized

through UV-vis absorption, electron paramagnetic resonance, dynamic light scattering, solution and solid phase small-angle X-ray diffraction, and AFM experiments, the aggregation behavior of the new SOFs is shown in sharp contrast in the absence or presence of CB8.

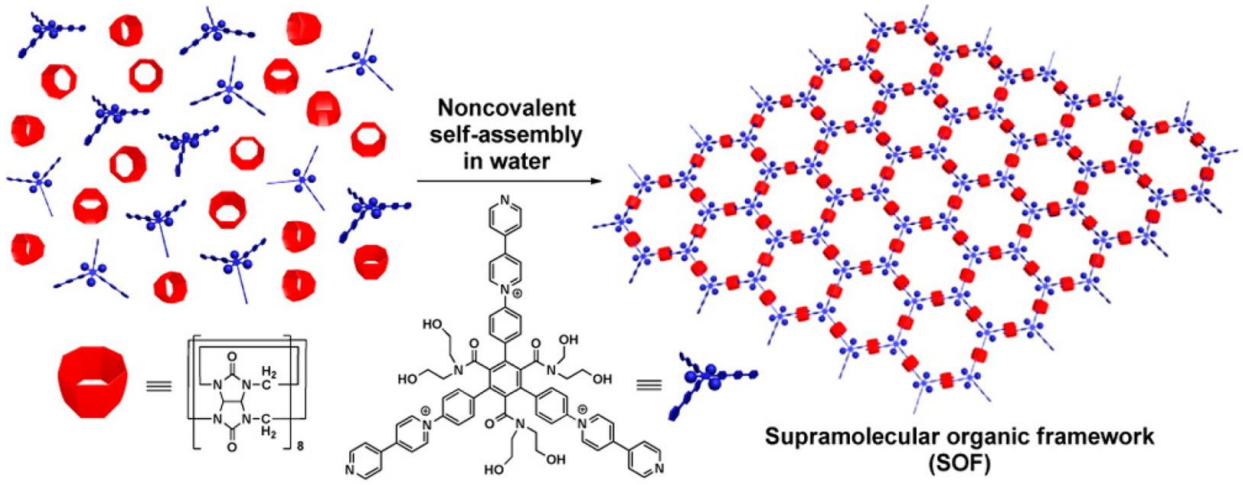

Figure 1- 24 Scheme of the self-assembly CB8-based SOF.[33]

1.1.3.4. Nanostructures

Some CBn-based host-guest complexes modified with hydrophilic/hydrophobic chains act as molecular amphiphiles (MAs), which hierarchically self-assemble into various nanostructures e.g., vesicles, micelles, nanorods, and nanosheets (Figure 1- 25).[35] Given the advantage of CBn cavities and the strong guest recognition, the surface of the self-assembled nanomaterials can be easily decorated with various functional tags in a non-covalent manner (Figure 1- 26).[20]

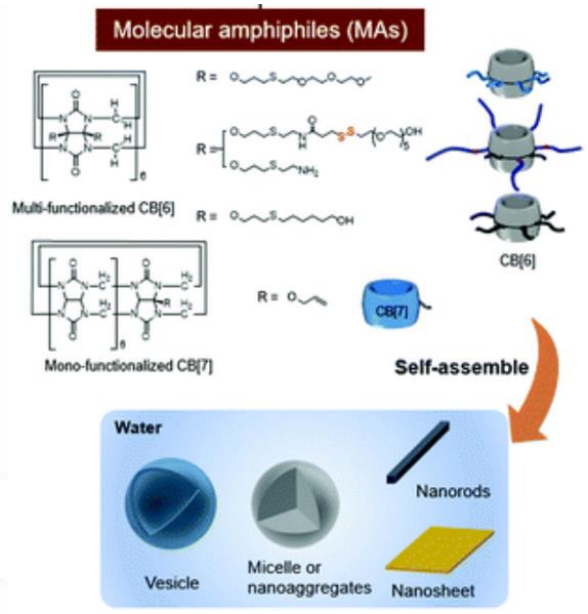

Figure 1- 25 Molecular amphiphiles.[35]

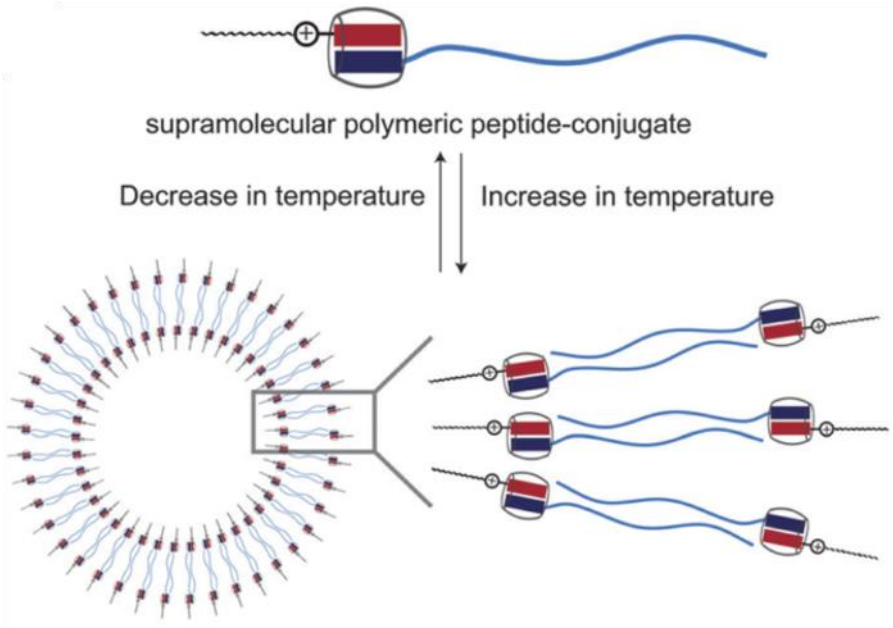

Figure 1- 26 Aqueous self-sorting of supramolecular polymers allows for vesicle formation.[20]

1.2. Immobilization of CBn

In the systems involving CBn and surfaces, the binding properties of the CBn are usually studied in solution and it is assumed that CBn retains its molecular recognition behavior on surfaces. The ability to transfer CBn onto surface-based systems offers new

opportunities to fabricate dynamic surfaces by exploiting stimulus-responsive CBn systems. Dynamic surfaces play an important role in many processes in living systems and such CBn-mediated dynamic surfaces could be important in achieving a mimic of dynamic aspects of living systems and subsequently could be utilized in biomaterials, tissue engineering, biosensors and cell biology. In general, immobilization of CBn to surfaces has been achieved through mainly three ways, i) covalent linking by modified CBn, ii) electrostatic adsorption on gold and iii) guest-mediated immobilization, shown in Figure 1- 27.[36]

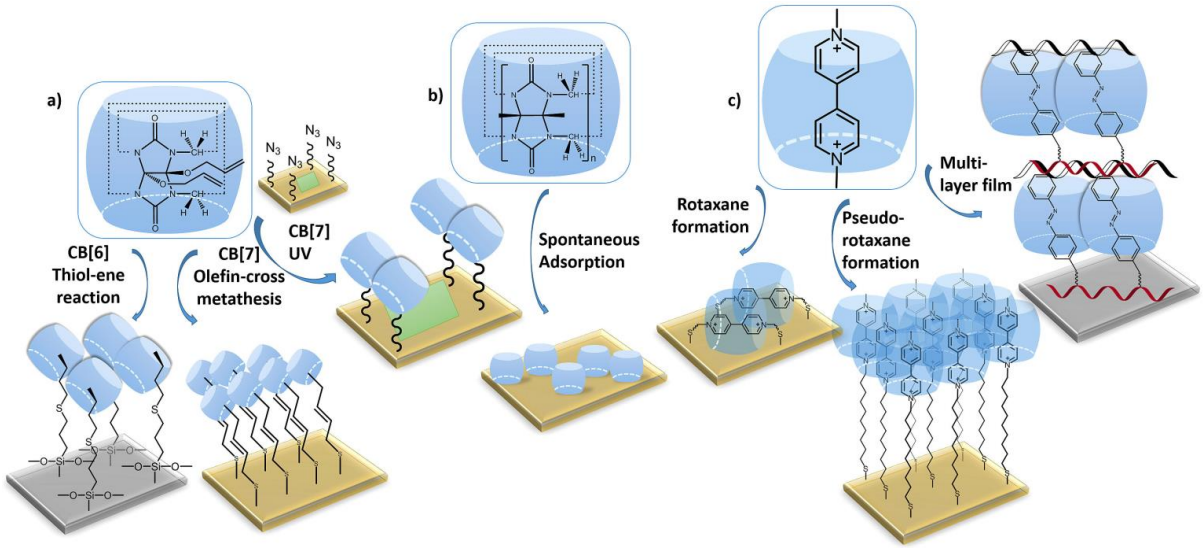

Figure 1- 27 Scheme of different ways to immobilize CBn. a) Covalent lingking with functionalized CBn derivatives. b) Electrostatic adsorption on gold. c) Guest-mediated linking of CBn.[36]

1.2.1. Electrostatic adsorption on gold

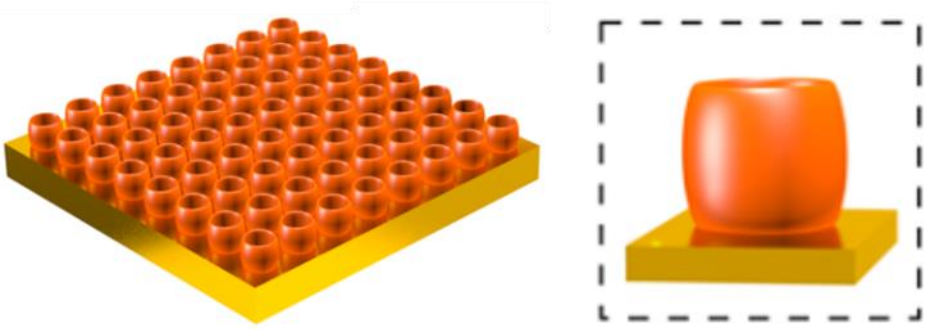

Figure 1- 28 carbonyl portal-mediated binding electrostatic interactions.[2]

With the availability of sophisticated tools such as AFM, the host-guest interaction can be quantified down to the single-molecule level even on surfaces.[2] For example, the interactions between a CB7 monolayer and neutral adamantyl guests (Ad) have been resolved at the single-molecule level using dynamic force spectroscopy (Figure 1- 29).[37] It is noted from such studies that the proximity of a surface does not appear to significantly alter CB[n] molecular recognition properties.

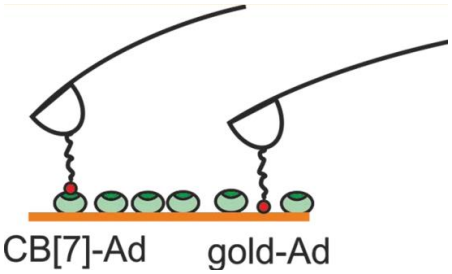

Figure 1- 29 Measurement of CB7 surface on gold by AFM tip modified with Ad.[37]

1.2.2. Guest-mediated immobilization of CBn via noncovalent host-guest chemistry

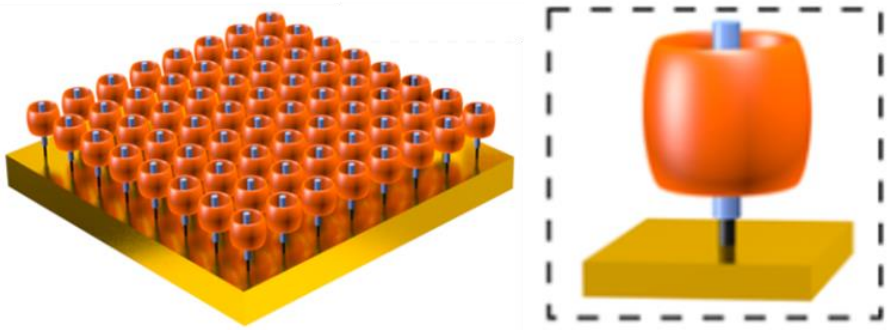

Figure 1- 30 Guest-mediated CBn immobilization.[2]

In guest-mediated immobilization, a mixed self-assembled monolayer (SAM) consisting of e.g., a guest and a guest-free, shorter thiol on gold is necessary to retain space for CBn assembly (Figure 1- 30).[2] The host−guest recognition at the nanoscale has been proved by electrochemical analysis, which is a sensitive probe for structural heterogeneity in organized molecular assemblies on surfaces.[38] Cyclic voltammetric (CV) studies have been used to evaluate the binding of CB7 on gold surfaces modified with mixed ferrocenylundecanethiolate/n-alkanethiolate SAMs (FcC11S-/CmS-Au) (Figure 1- 31).

The FcC11S-/C8S-Au prepared by coadsorption in a binary solution with a low mole fraction of FcC11SH (5%) has the “ideal” structure with isolated and uniformly distributed Fc groups on the surface. Besides, the single-molecule force spectroscopy (SMFS) modified with a guest can detect a single CBn on the surface (Figure 1- 32).[39]

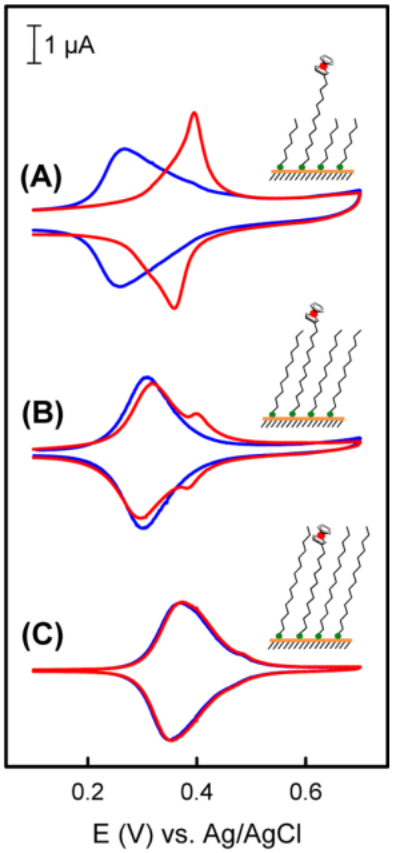

Figure 1- 31 CVs of binary FcC11S-/CmS-Au SAMs prepared by coadsorption of FcC11SH with different n-alkanethiols: (A) C6SH (χFc soln = 3%), (B) C11SH (χFc soln = 10%), and (C) C14SH (χFc soln = 20%). The blue and red curves are the CV responses before and after incubation with 1.0 mM CB7 for 3 h. The supporting electrolyte was 0.1 M $NaClO_4$, and the scan rate was kept as 50 mV/s.[38]

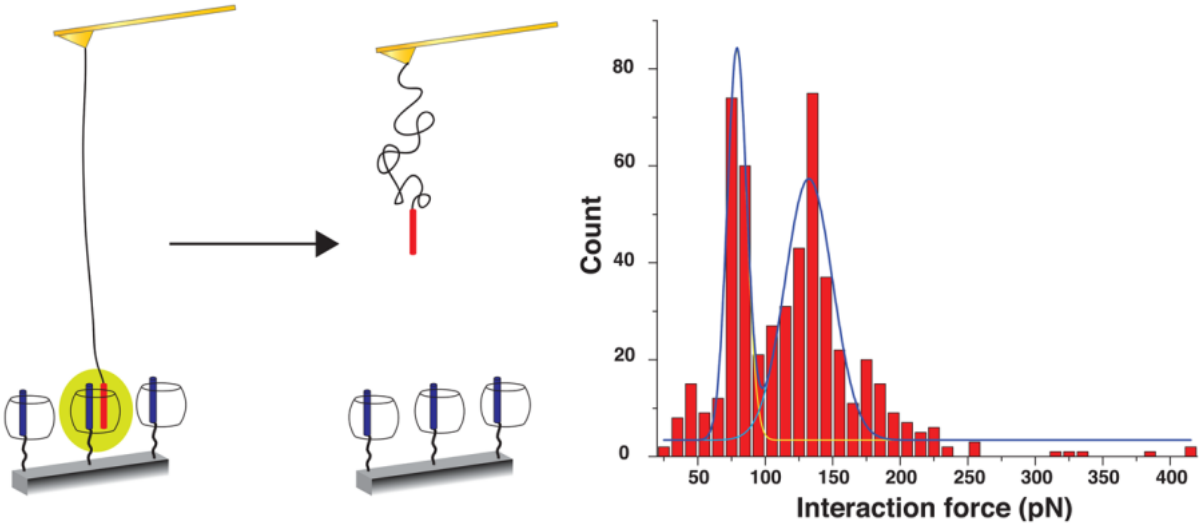

Figure 1- 32 Measurement of MV-mediated CB8 SAM by single-molecule force spectroscopy (SMFS).[39]

Additionally, CBn can be locked through two sides-bound guests on the surface. The advantage of this approach is the tuneable surface density through varying the concentration of present guests.[40] The disadvantage is, for small CBn e.g. CB6 and CB7, the cavities are not able to bind another guests. For the bigger CB8 pseudorotaxanes formed by MV, can further functionalize the surface by a second guest (Figure 1- 33).[41]

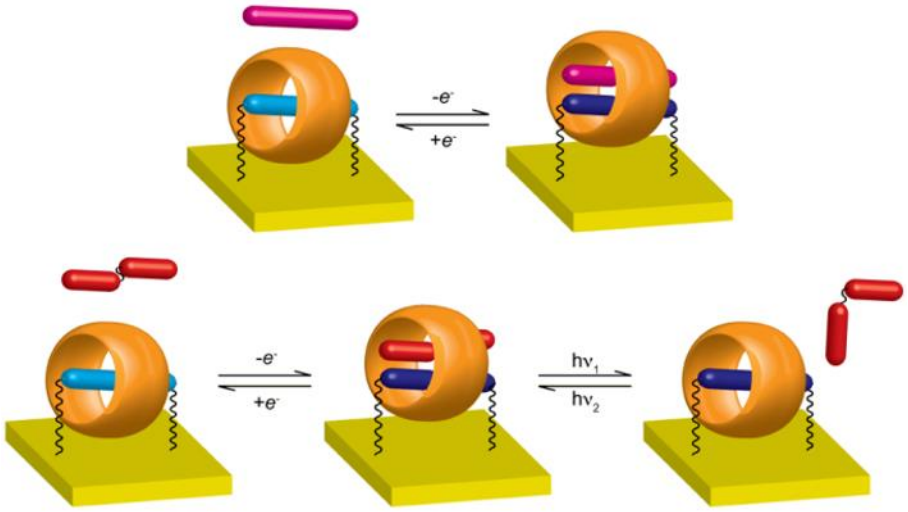

Figure 1- 33 CB8-based rotaxane on Au surface threaded onto a viologen (MV^{2+}) axle.[41]

1.2.3. Direct and covalent attachment with functionalized CBn derivative

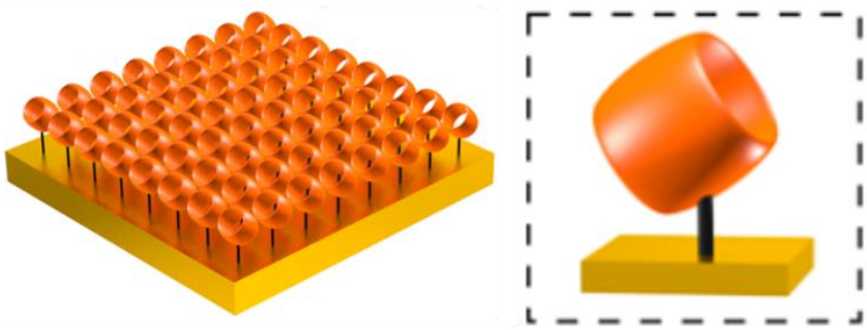

Figure 1- 34 Covalent immobilization by modified CBn.[2]

Based on CBn modification, it is possible to covalently immobilize CBn on a surface (Figure 1- 34).[2] CBn modified surface can be characterized through AFM same as the approaches described above. A spermine-functionalized AFM tip has been used to measure the rupture force with CB6 partially allyloxylated on Au substrates by olefin cross-metathesis reaction with vinyl terminated SAMs (Figure 1- 35).[42] Another feasible way to characterize CBn modified surfaces is imaging by additional indicators dyes. A FITC-spermine conjugate was used to indicate the surface-bound CB6 through the thiol-ene reaction with thiol-functionalized glass slides (Figure 1- 36).[12] However, the binding affinities in both cases were not verified.

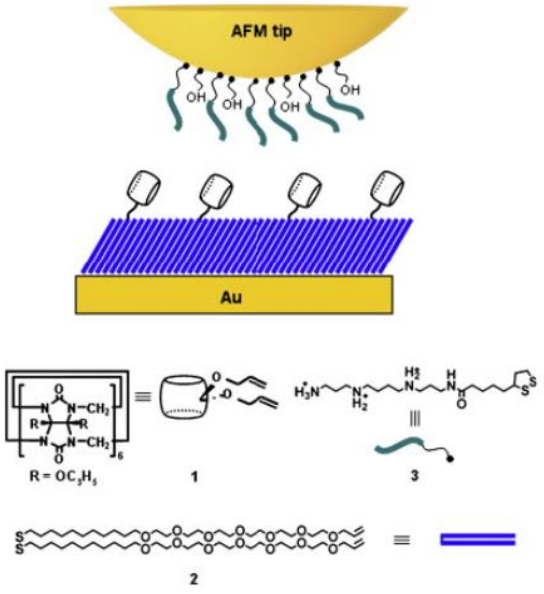

Figure 1- 35 A spermine-functionalized AFM tip for measurement of the rupture force with CB6 covalently tethered on Au.[42]

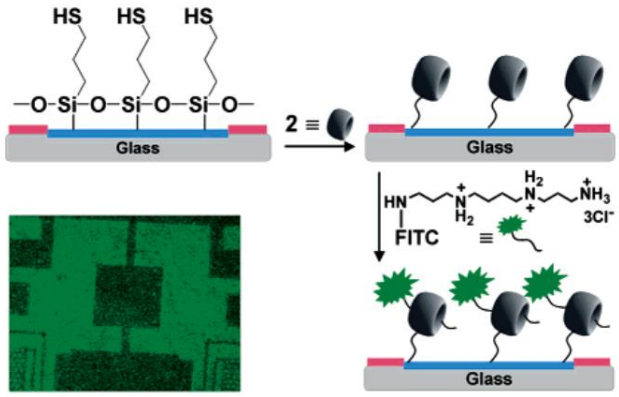

Figure 1- 36 CB6 immobilization through thiol-ene reaction and assembled with FITC-spermine conjugate.[12]

1.2.4. Comparison of homogeneous and micropatterned CBn immobilization

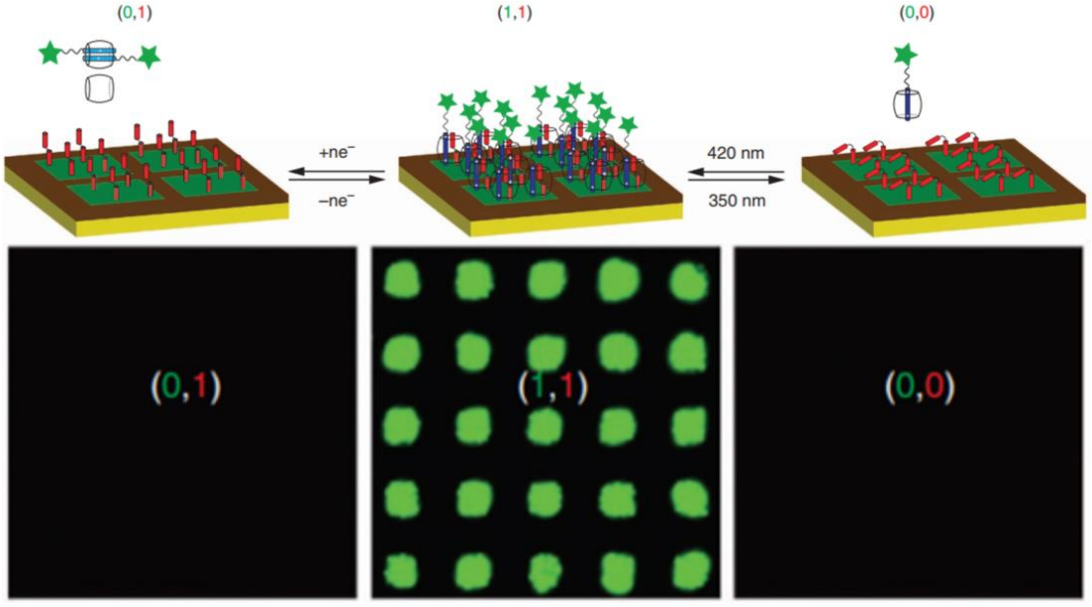

Figure 1- 37 Schematic illustration and corresponding fluorescence microscopy images of isomerization-driven photoswitching (1,1)↔(0,0) and dimerization-driven electrochemical switching (1,1)↔(0,1). Micro-patterned fluorescent arrays prepared by the addition of CB8/MV-FITC to the (phenyldiazenyl)phenol-terminated Au substrate.[43]

With the increasing biological applications of CBn-modified surfaces e.g. in biosensing, peptide separation, and cells identification, the micropatterning of CBn attracts chemists' attention. Compared with homogeneous modification, CBn microarrays exhibit mainly four advantages: i) in intrinsic reference, as the sensing features can be easily compared to

the blank area around as negative control (Figure 1- 37);[43] ii) higher sensitivity down to nanomole; iii) smaller need of liquid from the human body (less analyte volume); iii) multiplexing of CBn and indicators is more feasible for different analytes (Figure 1- 38).

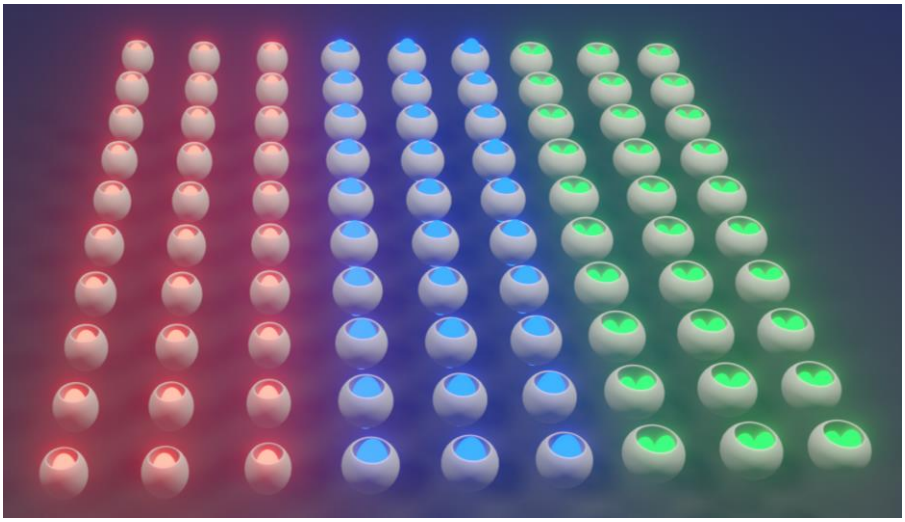

Figure 1- 38 Multi-CBn/multi-indicator microarrays.

1.3. Molecular printing

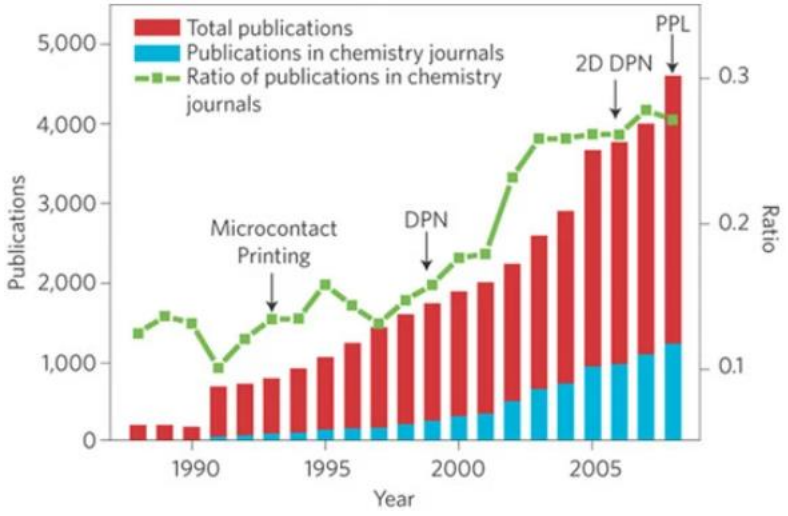

Figure 1- 39 Nanoscale printing.[44]

Molecular printing enables the direct transfer of molecules onto a substrate with a submicrometre resolution and has been extensively developed over the past decade, achieving many applications[45-47]. Generated microarrays have been used to direct

molecular assembly[45], modify nanoelectronics[46], and synthesize peptides[47]. The past ten years have witnessed two molecular printing technologies synergistically by soft lithography e.g. microcontact printing (μCP) and scanning probe lithography (SPL) including dip-pen nanolithography (DPN), polymer-pen lithography (PPL) and microchannel cantilever spotting (μCS) (Figure 1- 39).[44]

1.3.1. Microcontact printing (μCP)

As a form of soft lithography, μCP uses a polydimethylsiloxane (PDMS) stamp or Urethane rubber micro stamp to directly transfer materials to a surface (Figure 1- 40).[48] Due to the ease of use, low cost, and high throughput, the μCP approach has become a research-grade molecular printing approach. For printing, elastomeric stamps are made putting an elastomer in a mold prepared by conventional photolithographic approaches. These stamps can then be used to pattern molecules including proteins, DNA, cells, alkanethiols, silanes, colloids and salts on a variety of flat as well as curved surfaces.[49] Several limitations can not be ignored: i) The μCP can only deposit a single pattern as designed and a new mold is needed each time for a new pattern. ii) Stamp swelling and shrinking, during curing and stamp inking affects the feature size. iii) The mechanical properties of the stamps also limit the flexibility of array design.[50]

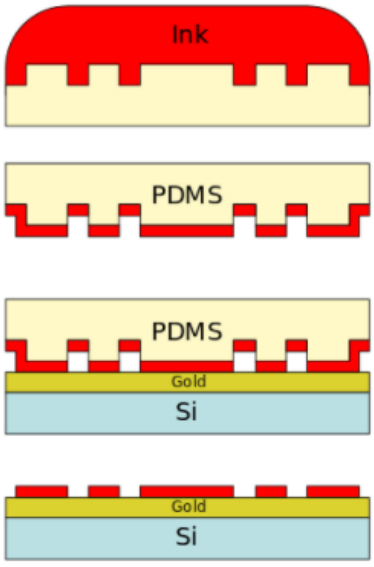

Figure 1- 40 Scheme of μCP.[48]

1.3.2. Microchannel Cantilever Spotting (µCS)

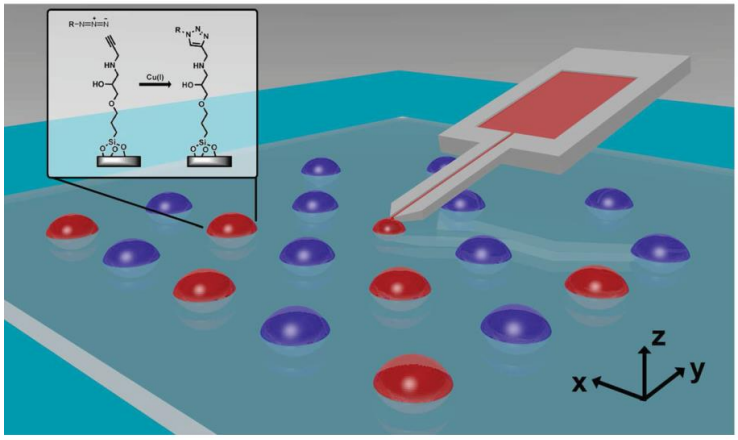

Figure 1- 41 a) Scheme of the µCS spotting process. The pattering tip applies microdroplets of ink onto a previously written pattern. The inset shows the CuAAC reaction taking place in the microdroplets, immobilizing the azide contained in the ink to the surface.[51]

Microchannel Cantilever spotting (µCS) is able to print several inks on one and has high flexibility to print ink with good control of dot size. Multi-component spot microarrays have been developed by blotting different ink solutions via arrays of quill-like pens (Figure 1-41).[51] Three fluorescent azides are immobilized on an alkyne surface by copper(I)-catalyzed azide-alkyne cycloaddition (CuAAC) and are stable to washing and soaking in aqueous solutions. The average spot radius distributes from 10 to 20 µm, and is easily controlled by the dwell time (i.e. the pen-surface contact time) (Figure 1- 42). The use of µCS-created microarrays as a binding assay is demonstrated through streptavidin capture and bioactive sandwich structures from neutravidin and biotin-labeled fibronectin (Figure 1- 43).

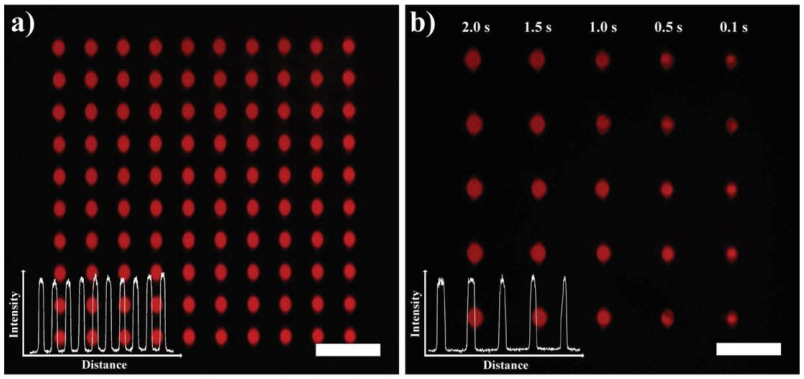

Figure 1- 42 a) Fluorescence image of TAMRA microarray written with a dwell time of 0.5 s after washing. b) TAMRA microarray with varying dwell time. The insets show the intensity profile lines through one row of spots. Exposure time was 3 s and the scale bars equal 100 µm.[51]

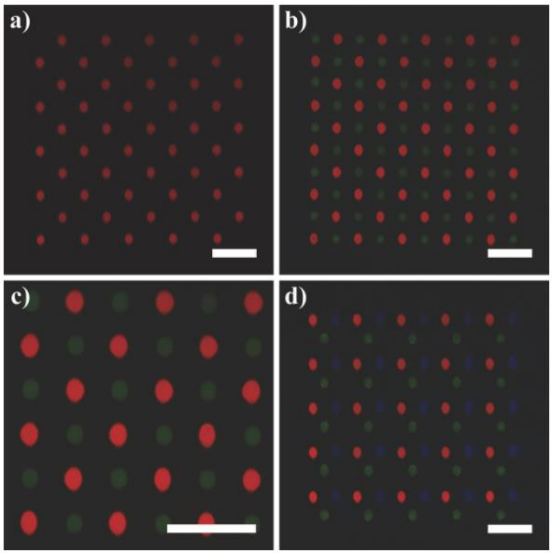

Figure 1- 43 Multi-printing of TAMRA-azide, Cascade Blue azide, and biotin-azide. a) Fluorescent image of an alternate TAMRA-azide/biotin-azide spot microarray. b) Same microarray after incubation with green fluorescently-labeled streptavidin. c) Close up of the spot microarray in b). d) Fluorescence image of a three azides microarray after incubation with green fluorescently-labeled streptavidin. All scale bars equal 100 µm.[51]

Besides, µCS is able to reprint on previously printed patterns and is feasible for biomedical applications. For example, the combinatorial in-situ synthesis of peptides by µCS is presented in microarray format (Figure 1- 44).[47] A multiplexed array with synthesized functional protein tags is selective to bind the respective epitope-recognizing antibodies (Figure 1- 45). This approach with µCS needs only small amounts of base chemicals and

can be further parallelized, therefore, opening up a new route to flexible, highly dense, and cost-effective microarrays.

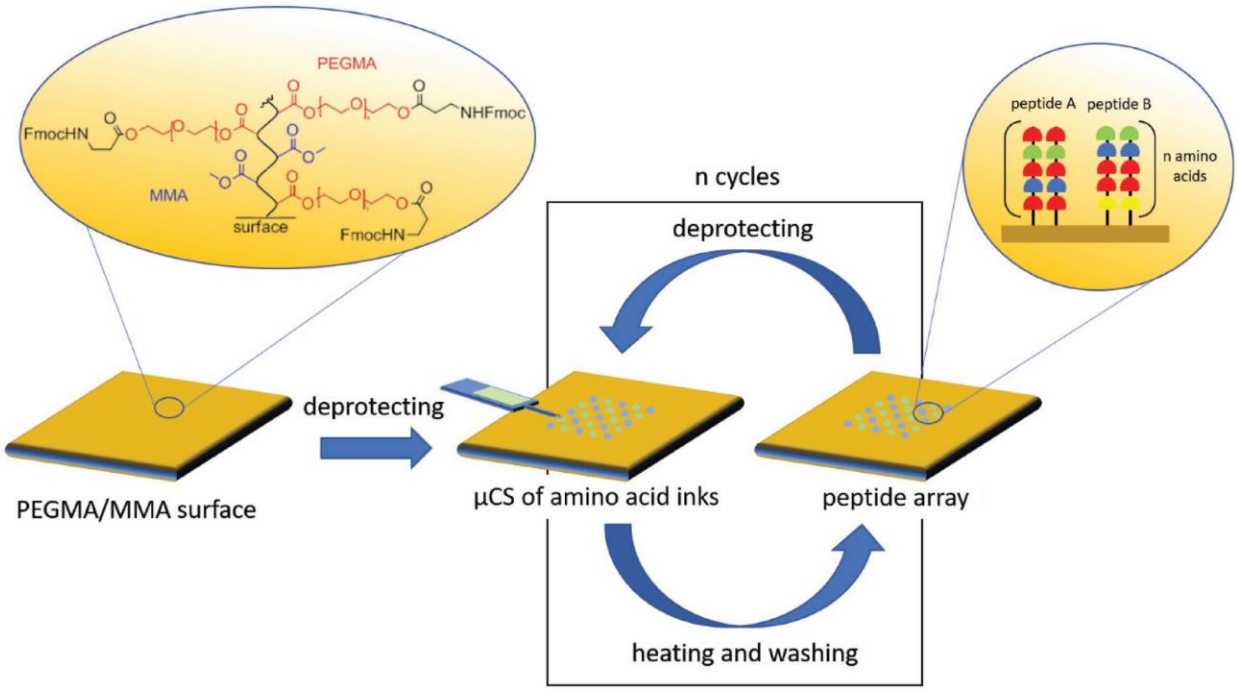

Figure 1- 44 Scheme of peptides synthesis process.[47]

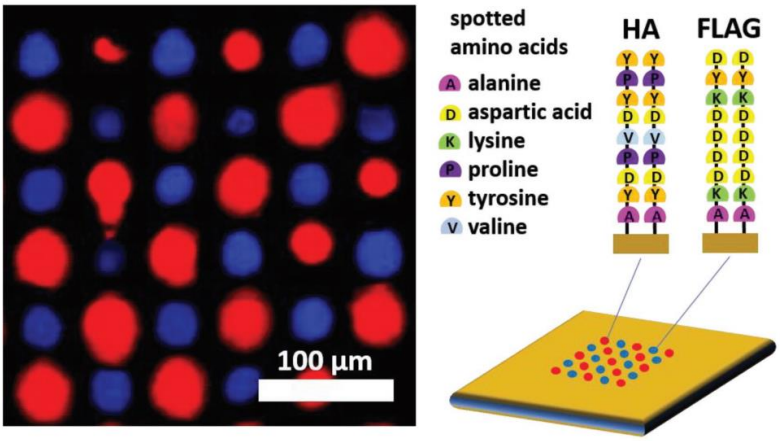

Figure 1- 45 Multiplexed peptide microarray. Fluorescence image of a synthesized multiplexed peptide microarray (left) and scheme of the synthesized peptides and spotted amino acids (right).[47]

1.3.3. Dip-Pen Nanolithography (DPN)

The ability to tailor the chemicals and structures on a surface in the nanoscale is important for many fields, from electronic conduction, catalysis, to biological recognition in nanosystems. DPN has become a new SPL technique on the base of direct-writing to generate surface-patterned chemical functionality on the nanoscale, and it is accessible to any researcher who can use AFM (Figure 1- 46).[52] An AFM tip is used to write e.g. alkanethiols with nanometer resolution on a gold thin film in a manner analogous to that of a dip pen.[53] For example, a water meniscus forms between the AFM tip coated with 1-octadecanethiol and the Au substrate (Figure 1- 47). The humidity-controlled size of the meniscus affects the transport of 1-octadecanethiol, the effective contact area, and resolution. 1-octadecanethiol molecules are delivered from the AFM tip to a solid substrate via capillary transport, which enables DPN to create and functionalize nanoscale devices. Nowadays, the application of DPN covers biomolecular micro- and nanoarrays,[54] controlling biorecognition processes from the molecular to the cellular level,[55] building nanostructured materials[56], and patterned etch resists[57] (Figure 1- 48).

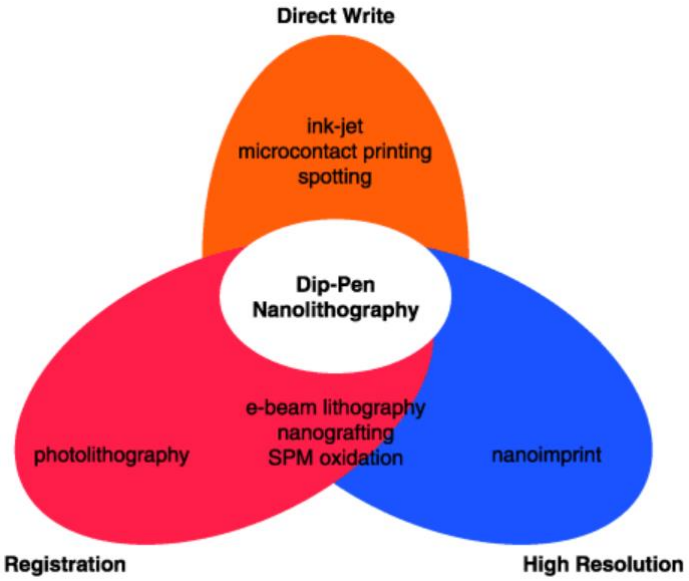

Figure 1- 46 Comparison of DPN with various other lithographic tools. SPM=scanning probe microscopy.[52]

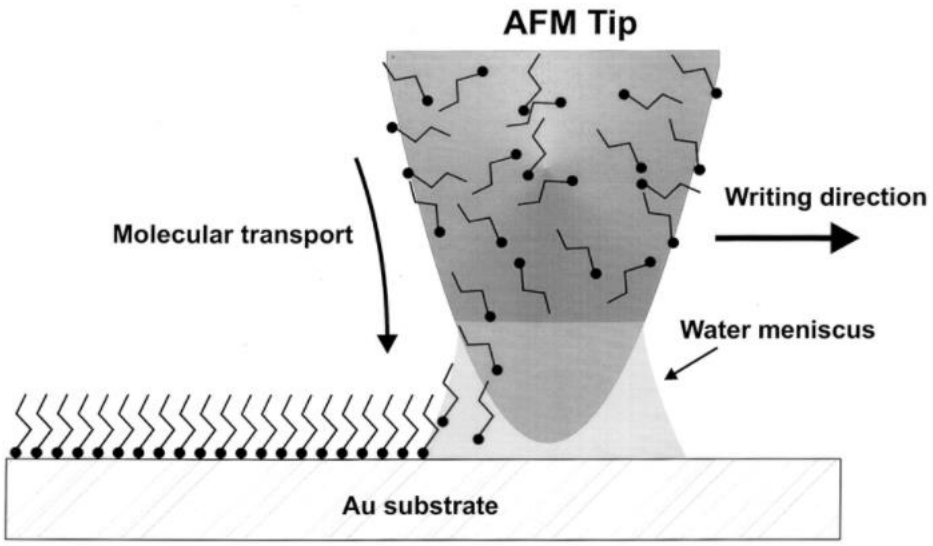

Figure 1- 47 Scheme of DPN.[52]

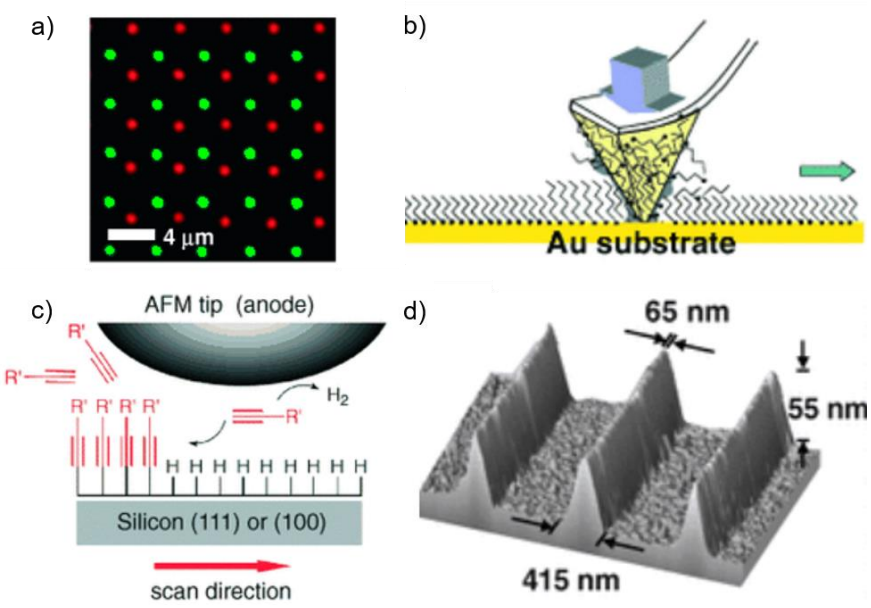

Figure 1- 48 Applications of DPN. a) Direct-patterning of multiple-DNA inks.[54] Overlay fluorescence image of two different fluorophore-labeled sequences simultaneously hybridized to a two-sequence array. b) Direct-write of thiol.[55] By applying a high contact force on the tip shaves away some of the passivating molecules, which allows the ink from the tip to generate patterns. c) Nanopatterning alkynes to a hydrogen-passivated surface while applying an electrical bias.[56] d) 3D Si(100) nanostructures.[57]

1.3.4. Polymer Pen Lithography (PPL)

The challenge of constructing surfaces with nanostructured chemical functionality is broadening to large areas of biology and biotechnology. Rather than individual cantilevers, PPL uses a soft elastomeric tip array (e.g., made of PDMS) to deliver inks onto a surface in a “direct write” manner, which shows the advantages of a low-cost and high-throughput (Figure 1- 49).[46] PPL is also able to control the feature with the large-area capability. The nano features and macroscopic length scales are formed with the tip array due to the ink delivery dependent on time and force. Uniform patterns are developed by arrays with around 11 million pyramid-shaped pens in contact with substrates (Figure 1- 50).[58] PPL enables researchers to easily create combinatorial arrays of nanostructures, a powerful approach for high-throughput screening. A typical protocol for fabricating PPL arrays and printing with the arrays takes 48–72 h to complete, including two overnight waiting steps.[58] As an example, a protein-repellent polymer brush is functionalized by localized molecular binding sites using PPL.[59] PPL can print square centimeter areas due to the massive parallelization of the tip array (Figure 1- 51). These surface sites selectively bind to streptavidin while the remaining surface is resisted to nonspecific adsorption. This can be the solution for the immobilization of single proteins in complex biological fluids and shows the potential to enhance the multiplexing capabilities for patterning of proteins.

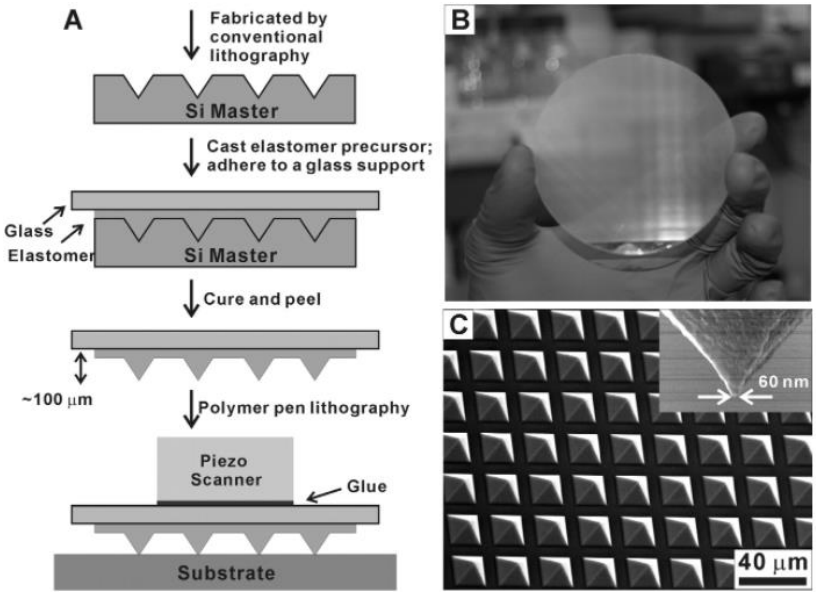

Figure 1- 49 A) Scheme of the PPL setup. B) Image of an 11-million-pen array. C) Scanning electron microscope (SEM) image of the tip array.[46]

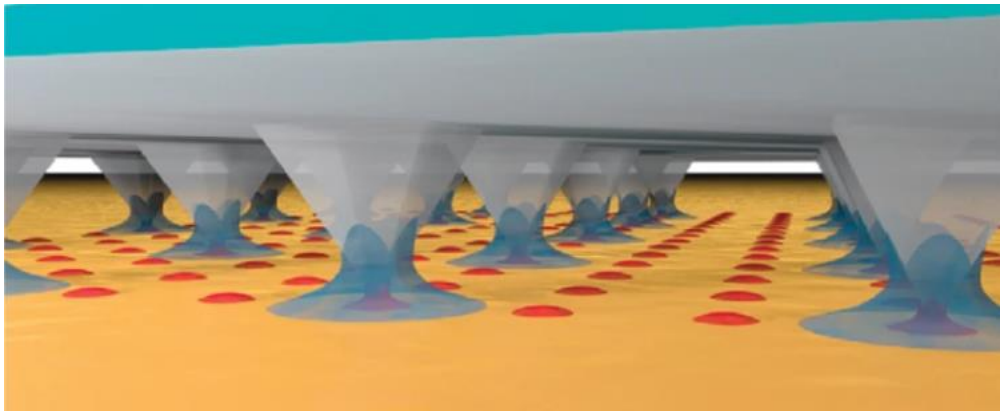

Figure 1- 50 Lithography by polymer pen array.[58]

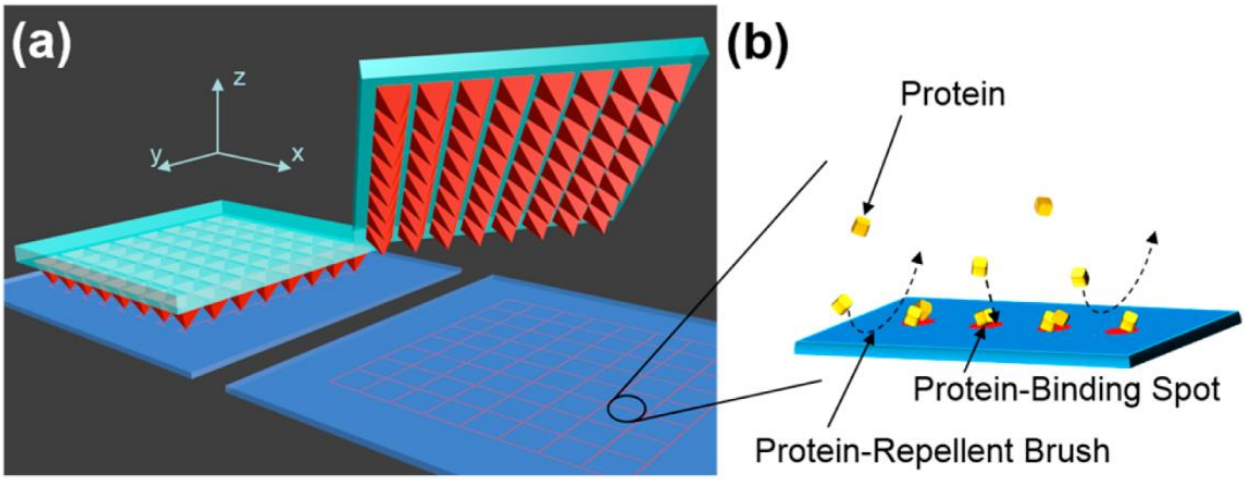

Figure 1- 51 PPL of protein-repellent polymer brush for protein immobilization.[59]

1.4. Supported Lipid Bilayers (SLBs)

Lipid membranes have immense importance for life because they are ubiquitous in eukaryotic cells to compartmentalize volumes, which enables different milieus for biological tasks. The cell membrane is made of lipids as the carrier for a plethora of proteins and other functional molecules, defines borders to the environment. Countless functions are provided in cellular metabolism, communication and interaction with the outside world. Thus, the construction of SLBs on varying substrates with low defects attracts many researchers. The approaches vary from solution-based to patterning including vesicle fusion, bicelle adsorption, solvent-assisted lipid bilayer fabrication, DPN

or PPL-printed arrays, where SLB of different quality forms for the desired applications. In this subchapter, a few examples of patterned and homogenous SLB fabrication are summarized.

1.4.1. DPN-printed supported lipid bilayers (SLB)

For micro/nanopatterning of SLB, previously mentioned molecular printing techniques (μCP, DPN, PPL and μCS) can be all used to generate SLB arrays. Here, a few examples of DPN and PPL for SLB patterning are introduced. The lipid patches generated by DPN bind on substrates well and are stable even after several steps of buffer incubation and washing (Figure 1- 52). For example, a novel extracellular vesicle (EV)-capture strategy of cancer-associated EVs has been developed on DPN-printed SLB arrays that carry specific antibodies recognizing EV- and cancer-specific surface biomarkers (Figure 1- 53).[60-61] The nucleic acid cargo of captured EVs retains on the lipid array, which enables downstream analysis. The generated platform enables rapid EV capture using a small volume of analyte before any purification steps with high specificity and sensitivity.

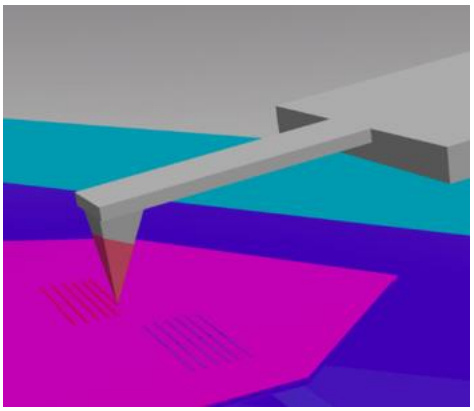

Figure 1- 52 DPN for lipid printing.[61]

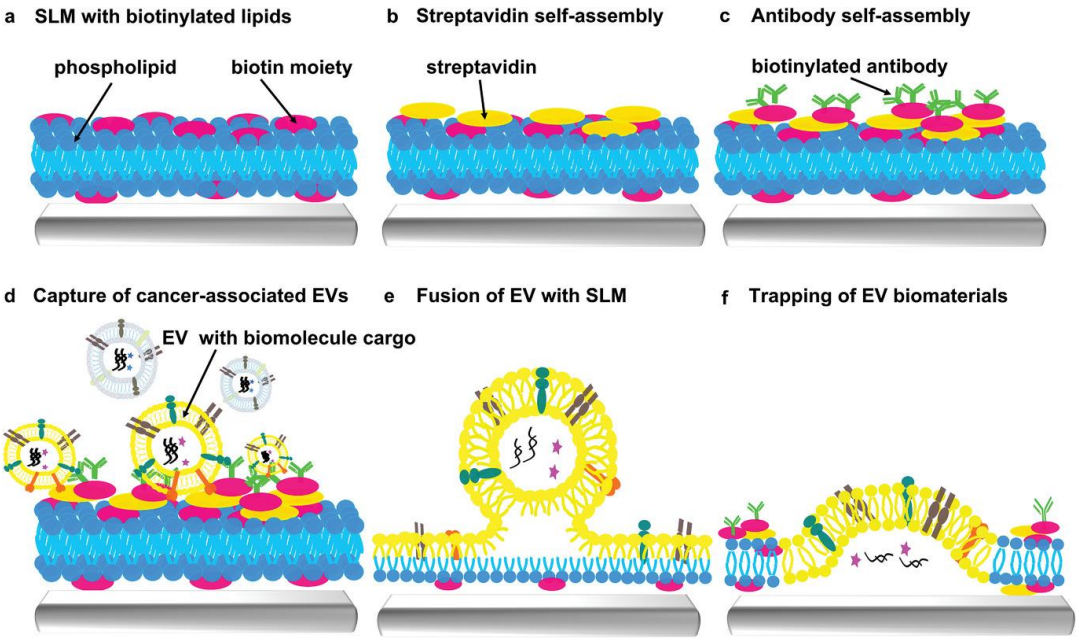

Figure 1- 53 Scheme of extracellular vesicle capture by SLM (supported lipid membrane) printed through DPN.[60]

1.4.2. PPL-printed supported lipid bilayers (SLB)

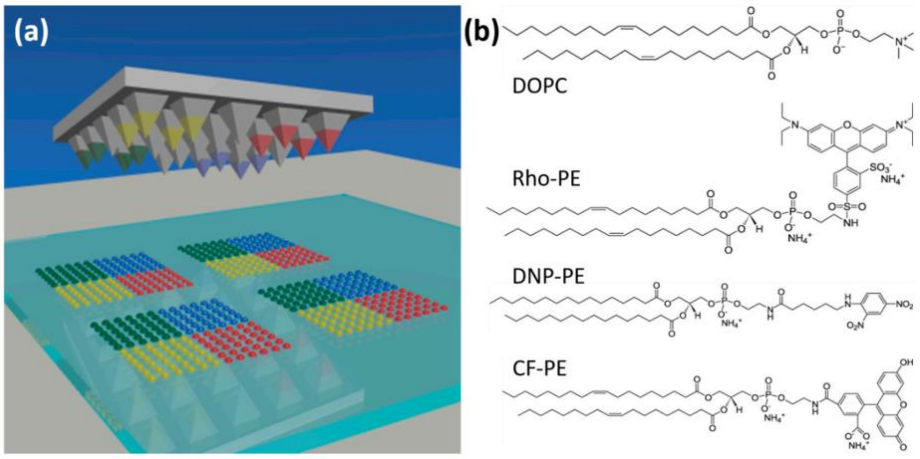

Figure 1- 54 a) A polymer stamp with pyramidal pen array inked with different phospholipids for multiplexed lipid printing. b) The chemical structure of the different phospholipids.[62]

PPL has been used for the creation of lipid micropatterns over large areas on glass substrates. The bioactivity of SLB with two compositions was demonstrated in the first systematic study in PPL-printed SLB (Figure 1- 54).[62] The influence of dwell time, humidity, and printing pressure was evaluated to better understand and control lipid

transfer. The established arrays are suitable for cell activation experiments, as demonstrated on mast cells in this case.

1.4.3. Solvent-assisted lipid bilayers (SALBs)

While the micro/nanopatterning approaches require specialized fabrication equipment and domain-specific knowledge, homogeneous SLBs seem more accessible for applications. Solvent-assisted lipid bilayers (SALBs), a simple and versatile SLB protocol has become one of the most popular approaches.[63-64] The detailed protocol is shown in Figure 1- 55. It requires only basic microfluidics, which makes it technically feasible for researchers across different scientific topics. It is compatible with diverse lipid compositions including sterols and signaling lipids on a wide range of substrates. The main procedure is the exchange of organic solvent containing lipid, with the aqueous buffer. The quality of SALB has been characterized to be homogeneous with low number of defects (Figure 1- 56),[63] which is useful in various applications e.g., biosensing.[65]

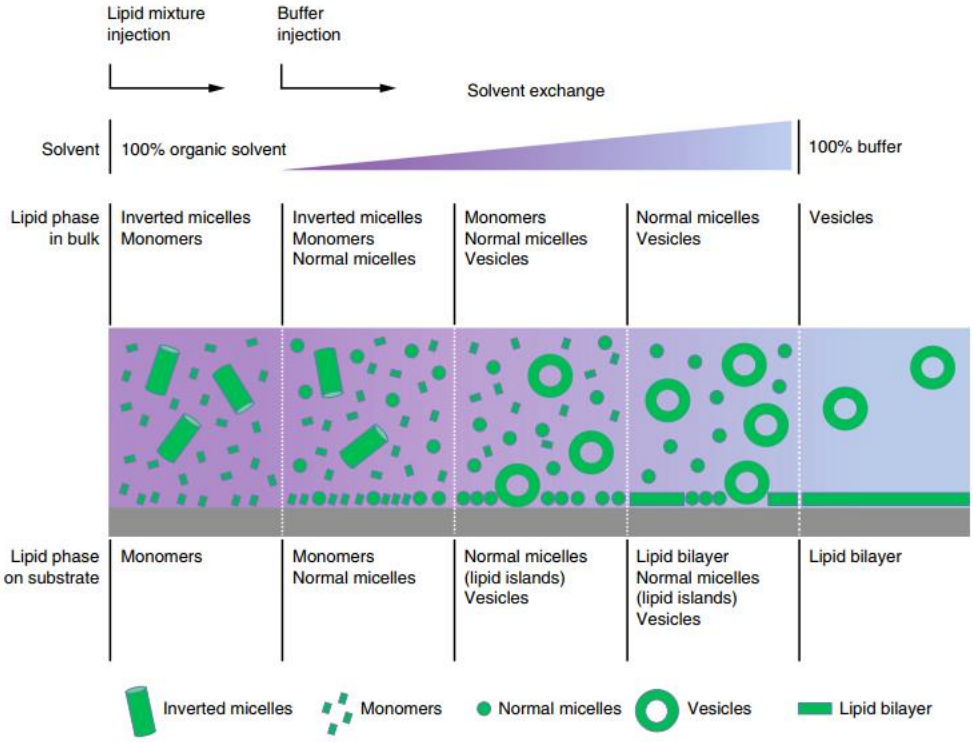

Figure 1- 55 Scheme of SALB formation during solvents exchange.[63-64]

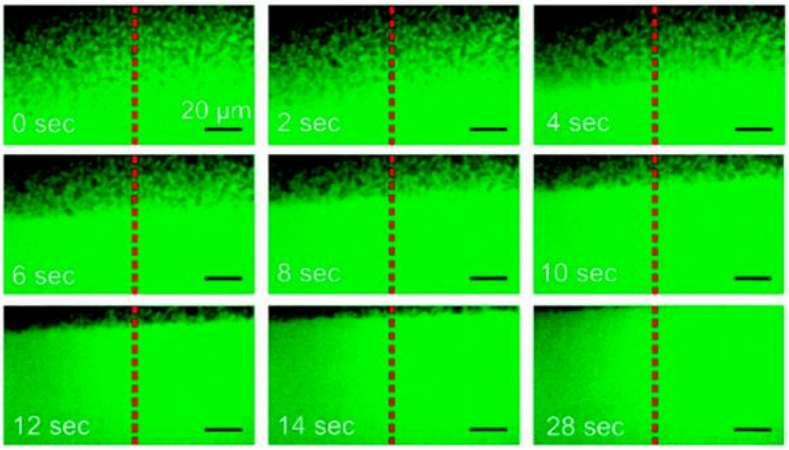

Figure 1- 56 SALB forms in the center of a microfluidic channel.[63]

1.4.4. Bicelle formation

An approach based on bicellar disks composed of a mixture of long-chain and short-chain phospholipids emerges. This quasi-two-dimensional lamellar deposition takes advantage of the thermodynamic preference of long-chain lipids to form planar SLBs, whereas short-chain lipids have brief residence times (Figure 1- 57).[66] The characterization of comprehensive quartz crystal microbalance-dissipation, fluorescence microscopy, and fluorescence recovery after photobleaching experiments show that a two-step mechanism involves a critical coverage of bicellar disks to vesicle fusion. The study indicates that the cycle of freeze-thaw-vortexing is useful during the sample preparation to produce SLBs, and identifies an optimal route for SLBs fabrication from bicellar mixtures.

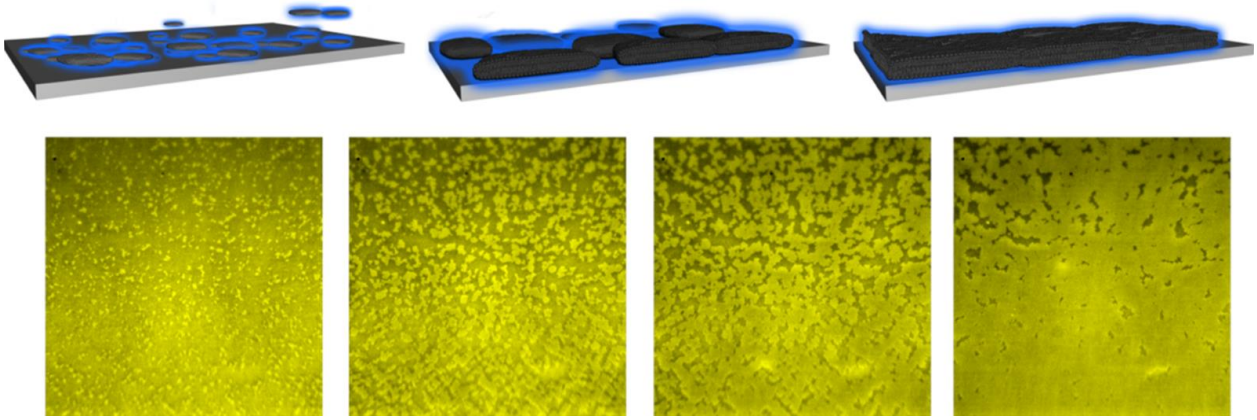

Figure 1- 57 Scheme of bicelle formed SLB.[66]

1.5. Conclusion

CBn are pumpkin-like macrocyclic molecules made of glycoluril (=$C_4H_2N_4O_2$=) linked by methylene (-CH_2-). Thanks to the relatively hydrophilic nanocavities, CBn hosts have become popular components to establish chemosensors, electronics, networks as well as nanostructures. In addition, they are able to be immobilized on the surface either directly by covalent binding because of the modifiable outer side, indirectly through guest mediation, or adsorption on Au through a carbonyl. The functionality of homogeneous CBn immobilization and micro/nanopatterning endow the modified surface with different properties, which attracts more and more researchers for desired applications.

Molecular printing including soft lithography (μCP) and scanning probe lithography (DPN, PPL and μCS) can transfer materials onto the specific area of the surface with controlled features. The development of these approaches meets the requirements of low cost (μCP, PPL), large scale patterning in a short time (PPL), flexibility for multiplex (DPN, μCS) and reprinting (μCS). Their applications cover materials transport in chemistry, biology and engineering.

SLB is an efficient way to create biomimetic cell-like environments as well as interfacial functions between cells and the outside environment. In principle, all the molecular printing techniques are able to transfer lipids onto the surface and form patterns. DPN-printed SLBs are stable for buffer incubation and washable, and PPL enables SLB patterning on large scales (i.e. several squre centimeters). The homogeneous SLB prepared by solvent exchange and bicelle fusion can only pattern indirectly and lack multiplexing but are capable of very large area covering with low number of defects.

2. Motivation & Strategies

2.1. Immobilization of CBn/indicator chemosensor by covalent-bound CBn for analyte detection

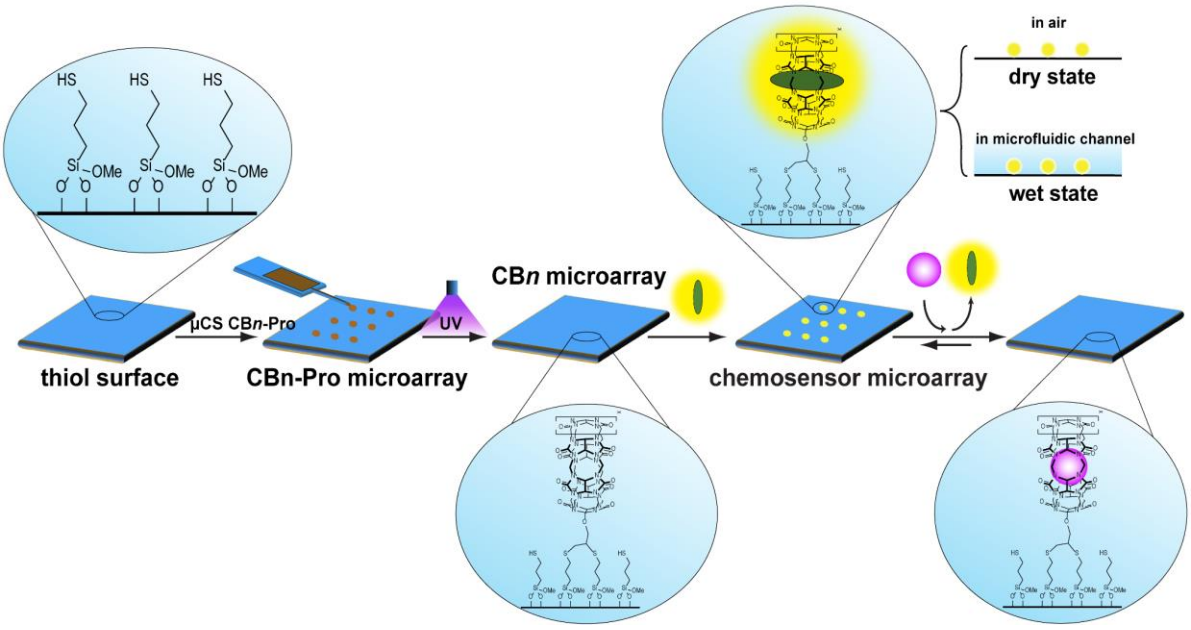

Figure 2- 1 Scheme of CBn immobilization by CBn-Pro and IDA assay.[17]

The immobilization of nano-/microscaled chemosensors has often been applied in diagnostics and environmental sensing. Up to recent years, patterning of supramolecular chemosensors, especially host-guest chemosensors, has been not yet widely adopted. However having surface-immobilized recognition elements is becoming a standard practice for biosensors, e.g., in form of immobilized proteins, in particular antibodies, or DNA. Therefore, a flexible and multiplexed micropatterning approach implemented by scanning probe lithography (SPL) to immobilize CBn/indicator chemosensors on surface through functionalized CBn was envisioned. Firstly propargyl curcubit[*n*]urils (CBn-Pro) were printed on thiol surfaces (SiO_2-SH) via μCS through thiol-yne photoreaction under UV irradiation to obtain CBn microarrays and then assembled with corresponding indicators. Their IDA sensing assays are evaluated with spermine (Spm, one of the key biomarkers for early-stage cancer diagnosis that plays an important role in cell growth and differentiation,[67] [68]), cadaverine (Cad, one of food freshness indicators[69]) and amantadine (Ama, a medication used to treat dyskinesia associated with parkinsonism).[70]

2.2. Multiplex CBn/indicator chemosensor microarrays for analyte detection

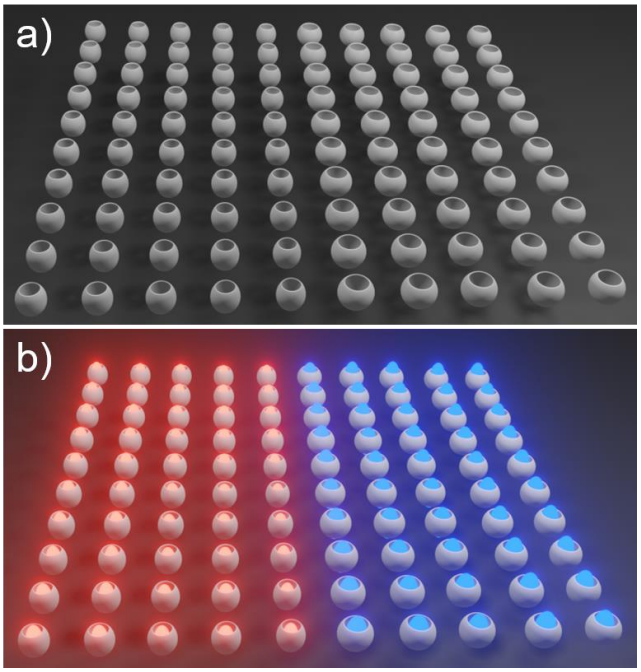

Figure 2- 2 Scheme of a) di-CBn microarray, with CB6 on the left and CB7 on the right, and b) di-CBn/di-indicator chemosensor microarray.

Mono-CBn/indicator microarrays can rapidly detect analytes with high affinity and have high sensitivity. However, the discrimination of different analytes requires specific CBn/indicator pairs for each. Therefore multiplexed chemosensor microarrays would be much more favorable to break such limitation. One possible approach is immobilizing different CBn homologs on one array to get diplex or even multiplex microarrays with different CBn/indicator pairs (Figure 2- 2). Under these circumstances, indicators would be successively replaced by corresponding analytes, which allows the detection of different analytes on one microarray.

2.3. Immobilization of CBn/indicator chemosensor by guest mediation

Besides immobilization by surface-bound CBn, CBn/indicator chemosensor can be immobilized by surface-bound guests. Basically, a few indicator guests functionalized with azide or thiol groups were micropatterned on an alkyne or DBCO surface through µCS. The chemosensor microarrays after being assembled with CBn were incubated with analytes solution to evaluate their IDA property (Figure 2- 3).

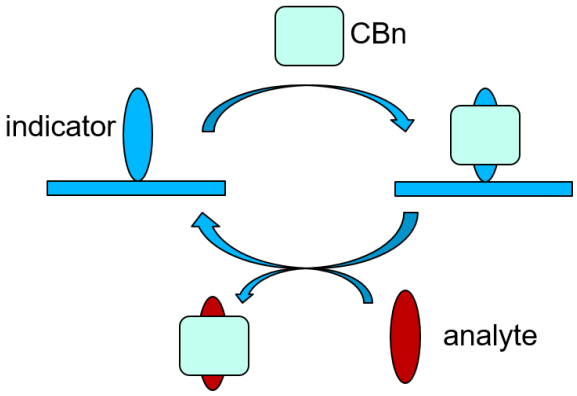

Figure 2- 3 Scheme of guest-mediated CBnimmobilization and analyte sensing.

2.4. Solvent-resisted rotaxane microarray

In order to solve the shortcoming of washable indicators and the weak readout of CBn assembly, a CB8/DAP rotaxane, with two β-cyclodextrin (CD) as stoppers on two sides to lock CB8/DAP from disassembly, was patterned on an isocyanate surface (SiO_2-NCO). The hydrophilic β-CD can avoid the unspecific adsorption of DAP indicator then increase the readout signal. The generated rotaxane microarray was evaluated through the detection of L-tryptophan (L-Trp), indole, memantine (Mem), penicillin (Pen), indole acetic acid (IAA), hydroxyl indole acetic acid (H-IAA) and insulin (Figure 2- 4).

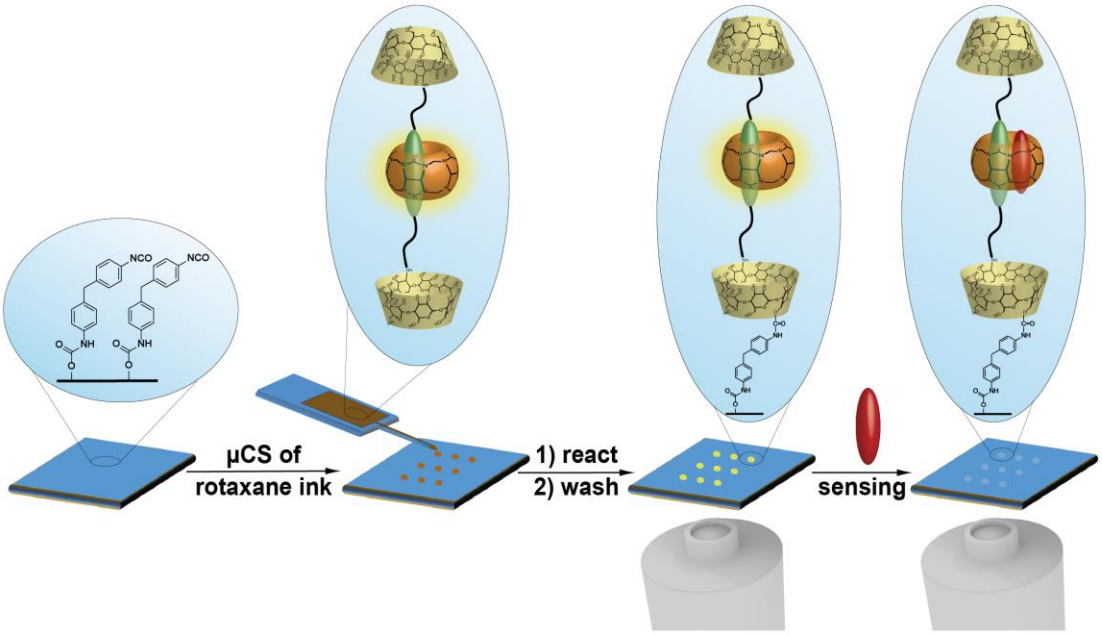

Figure 2- 4 Scheme of rotaxane micropatterning and analyte detection.

2.5. Analyte sensing in a biomimetic cell environment

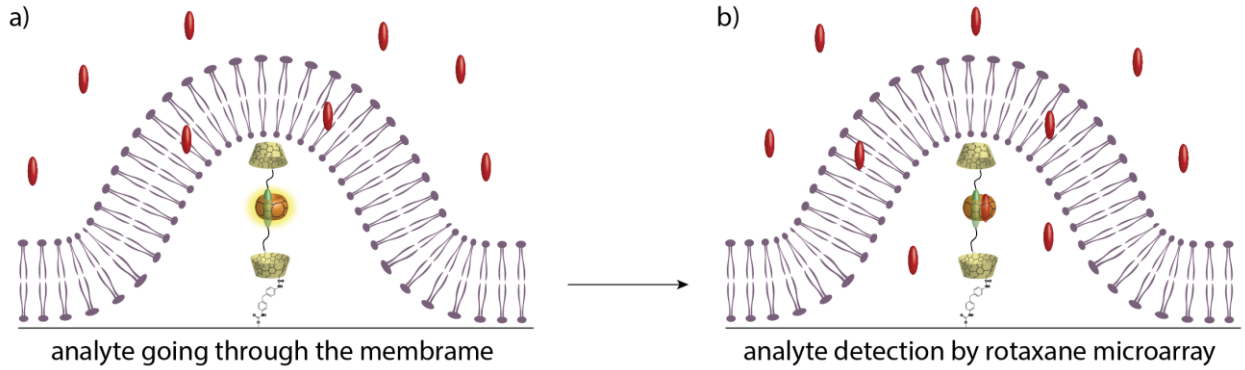

Figure 2- 5 Scheme of lipid membrane-covered rotaxane chemosensor.

Lipid bilayers are the fundamental of cells to have an independent environment from outside. In order to imitate a sensing system in a cellular environment, biomimetic supported lipid bilayers (SLB) were micropatterned by DPN, PPL and μCS. Then the sensing system was evaluated through CBn-bound, guest-mediated and rotaxane chemosensor microarrays.

2.6. Application of CBn in molecular electronics

Host-guest chemistry has been used in the electronics area to increase the conductance of the junctions through changing the microenvironment of redox to save the reorganization energy. Either an additional host or guest generates the enhancement and it differs from the size of the host. For CBn, the effect on the conductance decreases when *n* increases. One common guest of CB8, methyl viologen (MV), can be reduced after loading a negative voltage and forms $MV^{\bullet+}$ radical. When the $MV^{\bullet+}$ radical is close enough to each other, redox dimer $[MV^{\bullet+}]_2$ forms. Han Y. et al reported a low defect MV self-assembled monolayer (SAM) on Au and Ag surfaces and demonstrated the hysteresis of $[MV^{\bullet+}]_2$ in negative bias through Eutectic Gallium-Indium (EGaIn) measurement.[71] It shows the promising potential of MV SAM in resistive random access memories (RRAMs). However, the stability of hysteresis of $[MV^{\bullet+}]_2$ needs to be increased to achieve real application. Coincidentally, CB8 stabilizes $[MV^{\bullet+}]_2$ dimers in solution by perfect matching size and hydrophilicity, and the redox reaction could be detected by electrochemical method, for example, cyclic voltammetry (CV), proved since 2002. Therefore, CB8 was

planned to be immobilized on a MV modified electrode to stabilize the SAM and the hysteresis of $[MV^{\bullet+}]_2$. The dimerization of MV was aimed to be measured by CV and the hysteresis by EGaIn (Figure 2- 6).

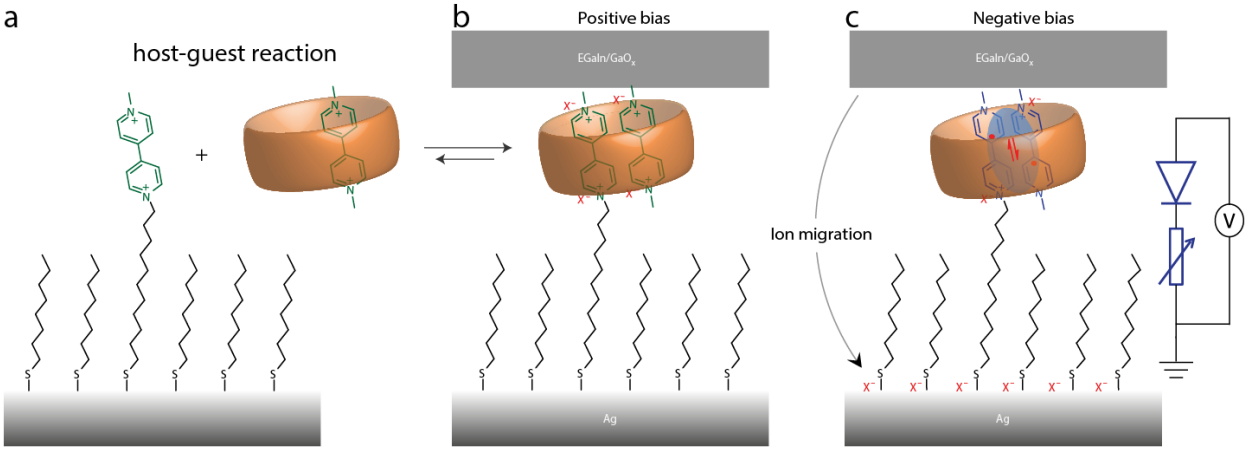

Figure 2- 6 Scheme of formation of MV_2@CB8 complex and EGaIn measurement.

3. Results and discussion

3.1. Modified CBn for immobilization

The results presented in this chapter were a basis of a published paper “Cucurbit[n]uril-Immobilized Sensor Arrays for Indicator-Displacement Assays of Small Bioactive Metabolites”[17].

Firstly thiol surfaces (SiO_2-SH) were prepared by (3-mercaptopropyl) trimethoxysilane (MPTMS) and characterized by contact angle and XPS measurements. Then propargyl curcubit[*n*]urils (CBn-Pro) were printed on SiO_2-SH via μCS through thiol-yne photoreaction under UV irradiation. The generated CBn microarrays were then assembled with corresponding indicators to obtain CBn/indicator chemosensor microarrays. Their IDA sensing assays are evaluated with Spm, Cad and Ama in a dry state or wet state in microfluidic channels.

3.1.1. Surface modification

Before micropatterning, the immobilization of CBn was proven on homogeneous surfaces as shown in Figure 3- 1. A clean glass was activated by plasma and then modified with thiol (SiO_2-SH) groups using (3-mercaptopropyl)trimethoxysilane (MPTMS). SiO_2-SH linked with CBn through thiol-yne photoreaction.

The results presented in this chapter are the basis of a published paper[17].

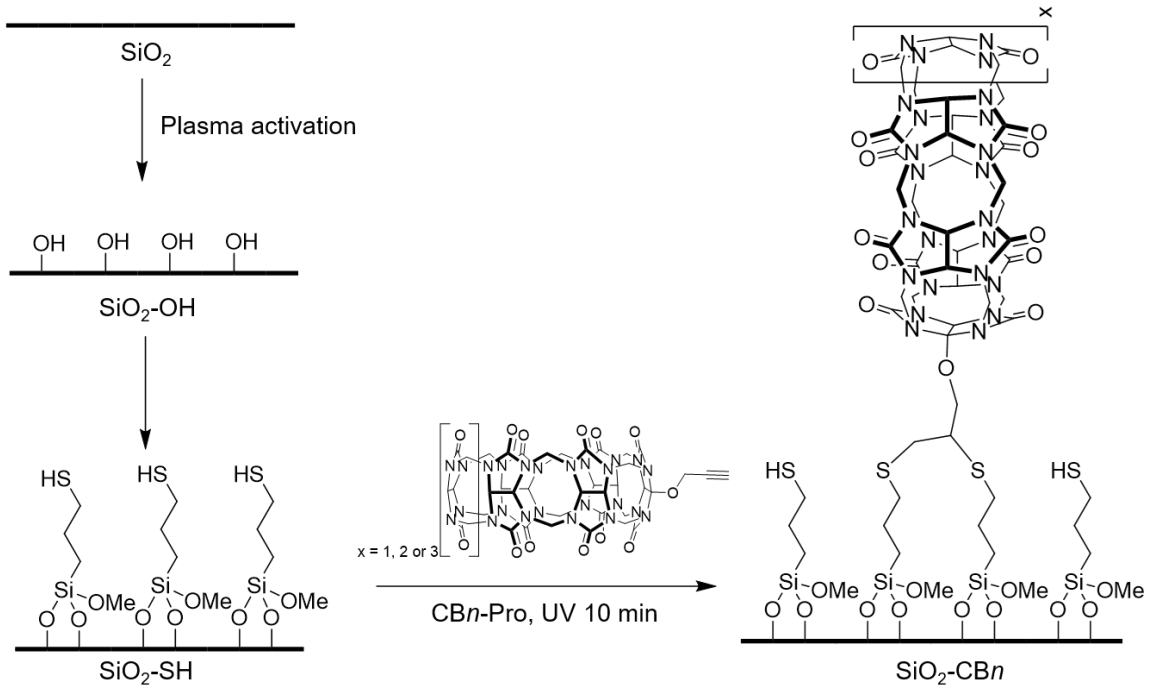

Figure 3- 1 Scheme of CBn immobilization through thiol-yne photoreaction.[17]

The homogeneous modified surfaces were measured firstly by contact angle (CA) and results are shown in Figure 3- 2, Figure 3- 3 and Table 3- 1. The freshly cleaned glass had a contact angle of 27.91 ± 1.16 ° and became highly hydrophilic with an angle near to 0 after plasma activation. After modification of thiol, SiO_2-SH had a higher one of 40.59 ± 1.86 °. The decreased contact angles for SiO_2-CBn surfaces compared to SiO_2-SH surfaces is indicative of CBn immobilization, which differs to CB, 28.94 ± 5.33 ° for CB6, 20.64 ± 3.58 ° for CB7 and 23.51 ± 2. 30 ° for CB8.[3]

The results presented in this chapter are the basis of a published paper[17].

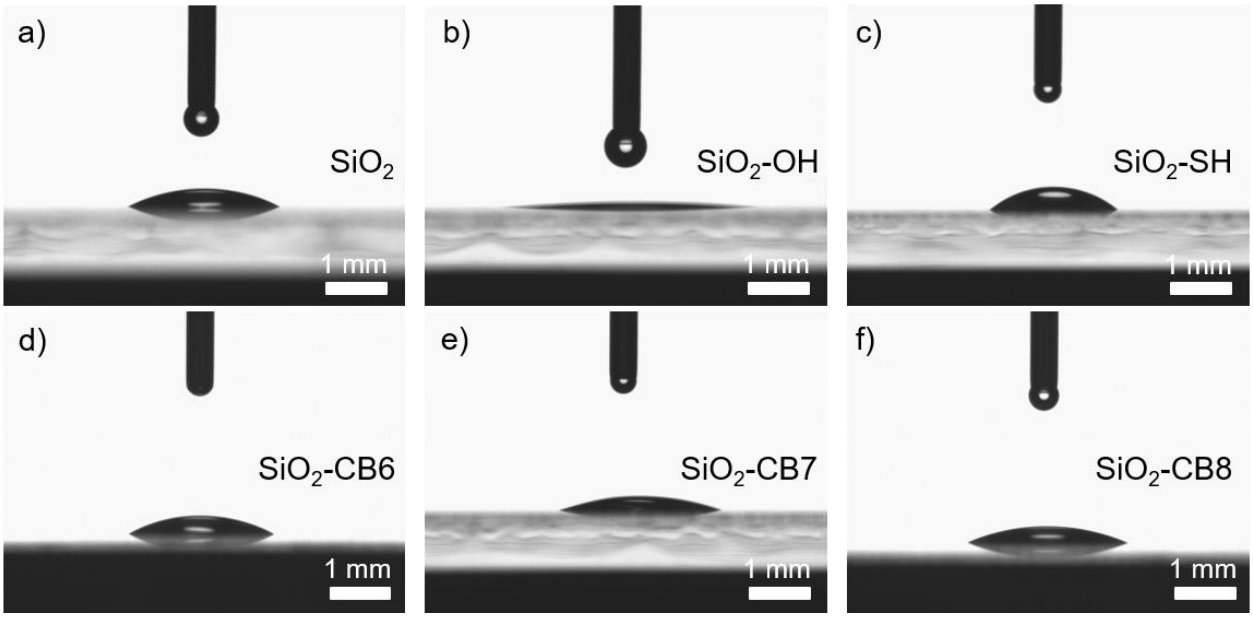

Figure 3- 2 Contact angles of modified surfaces, a) SiO_2, b) SiO_2-OH, c) SiO_2-SH, d) SiO_2-CB6, e) SiO_2-CB7 and f) SiO_2-CB8.[17]

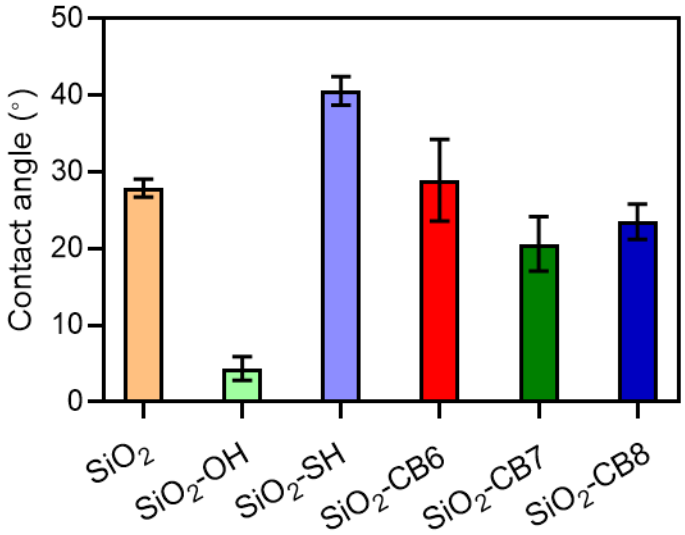

Figure 3- 3 Graph of contact angles.[17]

Table 3- 1 Static contact angles of water droplets on the bare and functionalized glass surfaces.[17]

sample	SiO_2	SiO_2-OH	SiO_2-SH	SiO_2-CB6	SiO_2-CB7	SiO_2-CB8
angle	27.91 ± 1.16	4.36 ± 1.54	40.59 ± 1.86	28.94 ± 5.33	20.64 ± 3.58	23.51 ± 2. 30

A further measurement is X-ray Photoelectron Spectroscopy (XPS). The successful thiol-modification of SiO_2-SH is proved by the appearance of an S 2p doublet with S $2p_{3/2}$ at 163.5 eV (Figure 3- 4, left), which is attributed to S-H bonds. A further doublet of weak

The results presented in this chapter are the basis of a published paper[17].

intensity at 168.0 eV proves the oxidation of the thiol functionalities. In order to obtain SiO_2-CBn surfaces, SiO_2-SH surfaces were homogenously functionalized with CB6, CB7 and CB8 respectively through thiol-yne photoreaction[72]). Two additional components, namely N-C-N at 287.6 eV and N-CO-N at 289.2 eV, with an expected ratio of the intensity of 2:1 (Figure 3- 4, right), give a more direct evidence for the successful attachment of the various CBn.

Furthermore, the ratios of N 1s in different components confirms the integrity of the CBn through corresponding N 1s peak of carbamide at 400.3 eV having a ratio of ~1.0 to the corresponding carbon components at 287.6 eV, and ~1.5 to that at 289.2 eV (Table 3- 2). Compared with SiO_2-SH, the relative densities of CBn to thiol group were calculated to be 0.2, 0.5 and 0.7 for CB6, CB7 and CB8, respectively, which indicate a similar grafting density for CB7 and CB8 shown in Table 3- 3. The purities of CBn-Pro used for surface modification in this project were around 22.5 % (CB6-Pro), 79.3 % (CB7-Pro) and 22.4 % (CB8-Pro).[17] The lower modifying density of the CB6 surface in XPS data might be caused by impurities in the CB6-Pro product, but compared to CB7-Pro with high purity, the CB8 modification is not affected even CB8-Pro has similar low purity. Another detailed discussion is given in the subchapter “Influence of Impurities in CBn-Pro” below. Overall, results above prove the successful modification of the thiol surface and the subsequent immobilization of CBn on it by thiol-yne photoreaction.

The results presented in this chapter are a basis of a published paper[17].

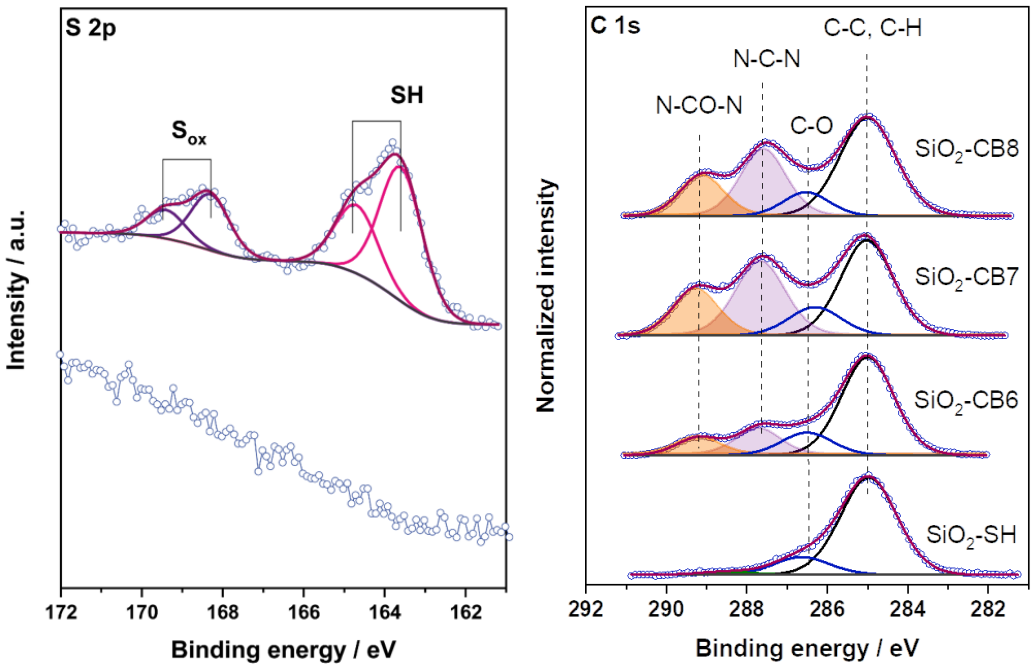

Figure 3- 4 Left, S 2p XP spectra of the plasma-activated surface SiO_2-OH (bottom) and the thiol functionalized one, SiO_2-SH (top). Right, C 1s XP spectra of SiO_2-SH, SiO_2-CB6, SiO_2-CB7 and SiO_2-CB8. Spectra are normalized to the maximum intensity. The two peaks at 287.6 eV and 289.2 eV indicate the presence of CBn on the surface.[17]

Table 3- 2 The concentration of the relevant elements determined by XPS. The table entries in bold are indicative for CBn.[17]

	Assignment	Binding energy (eV)	Concentration (at%)				
			SiO_2-OH	SiO_2-SH	SiO_2-CB6	SiO_2-CB7	SiO_2-CB8
S $2p_{3/2}$	C-S-C, C-S-H	163.5	-	1.1	0.8	0.7	0.6
C 1s	C-C, C-H	285.0	4.2	10.4	14.8	12.1	16.0
	C-O, C-N	286.4	2.1	1.6	3.4	3.2	2.8
	N-C-N	287.6	-	-	**3.4**	**9.8**	**9.0**
	N-CO-N	289.2	-	-	**2.2**	**4.9**	**4.5**
N 1s	O=C-N, C-N	400.3	0.4	0.4	**3.7**	**9.6**	**8.7**
	N+	402.2	0.4	0.3	**0.4**	**0.6**	**0.4**
O 1s	O=C	531.0	6.0	5.1	4.9	1.8	3.1
	O-Si, O-C	532.5	58.6	53.5	43.6	39.7	37.2
Si $2p_{3/2}$	SiO2	102.9	24.5	23.3	19.3	15.4	15.2

The results presented in this chapter are the basis of a published paper[17].

Table 3- 3 Relative densities of CBn to thiol from XPS peaks.[17]

	SiO_2-CB6	SiO_2-CB7	SiO_2-CB8
S $2p_{3/2}$	0.8	0.7	0.6
C 1s (N-CO-N)	2.2	4.9	4.5
Number of N-CO-N	12	14	16
Relative densities	**0.2**	**0.5**	**0.5**

3.1.2. Microchannel Cantilever Spotting

After confirmation of the successful immobilization of CB6, CB7 abd CB8 in homogenous coatings, micropatterning of the CBn is the next step. CBn-Pro or a reference-dye (RD, BDP-630/650-alkyne was used as RD to mark the microarray position) ink was loaded on a microchannel cantilever, and the cantilever was then installed in the SPL system. After contacting the desired positions on the surface for 0.5 s, the cantilever is allowed to release ink by capillary forces and let ink flowing from the reservoir to the surface and form the microscaled spots. The process is automatically controlled by SPL system to print desired microarrays. Figure 3- 5 shows the optical micrographs of typical microarrays in the bright field and in fluorescence after spotting. Before washing, the spotted CBn-Pro microarray and two flanking RD columns are both visible in a bright field (Figure 3- 5a). Having the average feature dot radius being (8.43 ± 0.49) µm, the dot size is within a narrow distribution automatically controlled by µCS process. Afterward, the micropatterned arrays were irradiated under UV light for 10 min to accelerate the thiol-yne photoreaction of the CBn-Pro and the RD onto the surface. Finally, no observable feature remains in the bright field after washing away the excess ink (Figure 3- 5b). In GFP filter, only RD spots (first and last column) are visible while CBn-Pro microarray is non-fluorescent (Figure 3- 5c and d).

The results presented in this chapter are the basis of a published paper[17].

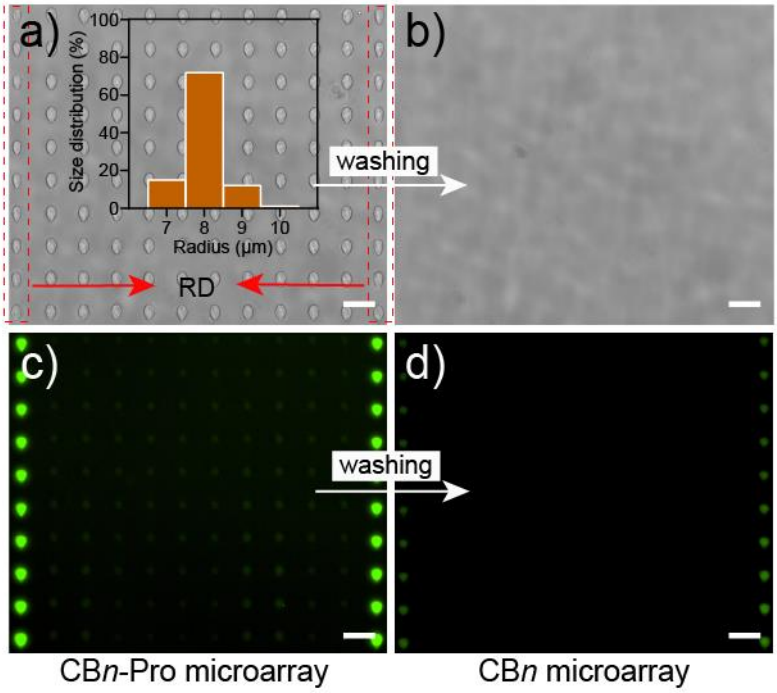

Figure 3- 5 CBn microarray patterning. a) Freshly printed CBn-Pro microarray in bright field (BF), BDP-630/650-alkyne as a reference dye (abbreviated as RD) was marked out in a red box. The inset graph shows the average feature dot radius. b) Immobilized CBn microarray in BF. c) CBn-Pro microarray in GFP and d) CBn microarray after UV irradiation, washing with water and ethanol and drying. Scale bars equal 50 µm in all images.[17]

3.1.3. Indicators assembly

Before indicator assembly, the rest of the thiol groups on the microarray substrates were blocked by N-Ethylmaleinimid (NEM) to reduce the unspecific adsorption of indicators. The CBn microarray becomes only fluorescently observable after being assembled with indicator dye. For different CBn, suitable indicator dyes were chosen depending on their affinity and photophysical parameters. The structures of indicator dyes used in this subchapter are shown in Figure 3- 6.

The results presented in this chapter are the basis of a published paper[17].

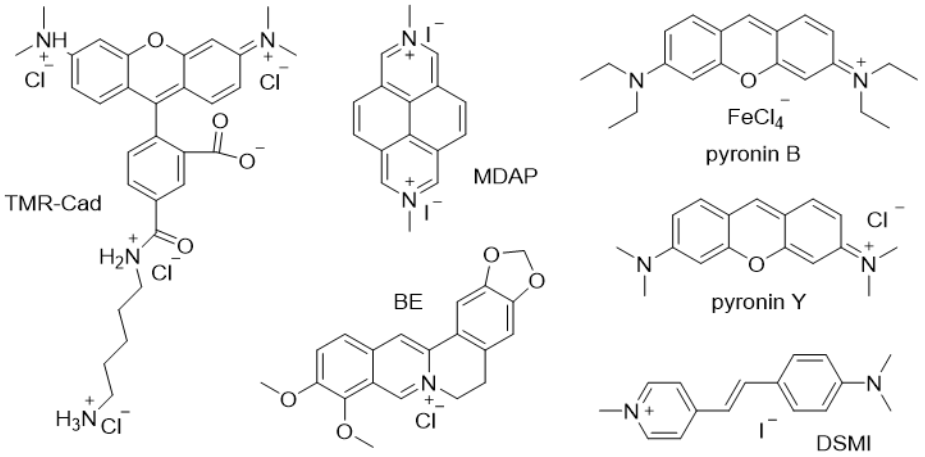

Figure 3- 6 Structures of indicator dyes.

3.1.3.1. CB6/TMR-Cad

For CB6 microarray, tetramethylrhodamine cadaverine (TMR-Cad) has high-affinity as the indicator dye with the tetramethylrhodamine side as a chromophore and the cadaverine part as a binding group to assembly with CB6).[73] From Figure 3- 7, TMR-Cad is visible in both Cy3 and GFP filters because of its broad emission and high intensity. Single filter channels are given in a) to h) and overlayed channels shown in i) to l). The inset pictures show the homogeneous CB6/TMR-Cad chemosensor microarray dots. A normalized intensity (Cy3, GFP and overlay) line plots along twelve dots show the quality of CB6/TMR-Cad chemosensor microarray.

The results presented in this chapter are the basis of a published paper[17].

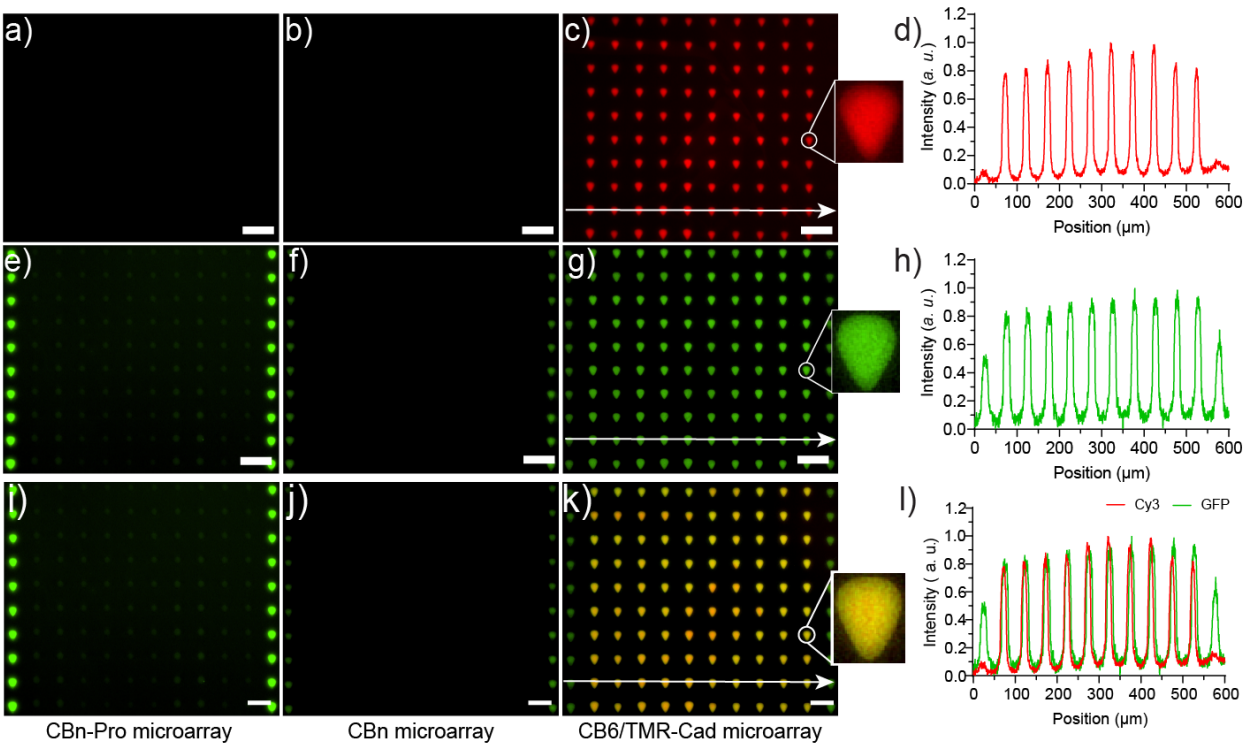

Figure 3- 7 CB6-microarray a) after printing, b) washing and c) incubation with TMR-Cad in Cy3 channel, 40 ms of exposure time. d) Fluorescence intensity plot along the line indicated by the white arrow in c). CB6-microarray e) after printing, f) washing and g) incubation with TMR-Cad in GFP channel, 10 s of exposure time. h) Fluorescence intensity plot along the line indicated by the white arrow in g). Overlay two channels shown in i), j) and k). The inset picture shows the homogeneous property of chemosensor microarray dots. l) The overlay of fluorescence intensity plot along the line indicated by the white arrow in k). Scale bars equal 50 μm in all images.[17]

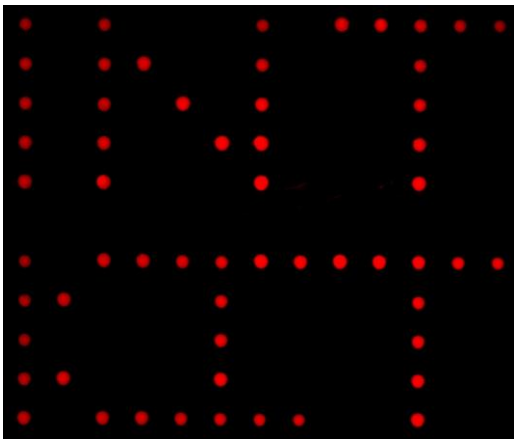

Figure 3- 8 “INT” and “KIT” logo made of CB6/TMA-Cad microarray.

3.1.3.2. CB6/pyronin B

The results presented in this chapter are the basis of a published paper[17].

Pyronin B can also assemble with CB6 and indicate the microarray (Figure 3- 9). However, the strong background resulting from the unspecific adsorption makes the array appear inhomogeneous as shown in Figure 3- 9b and thus unstable for analyte detection.

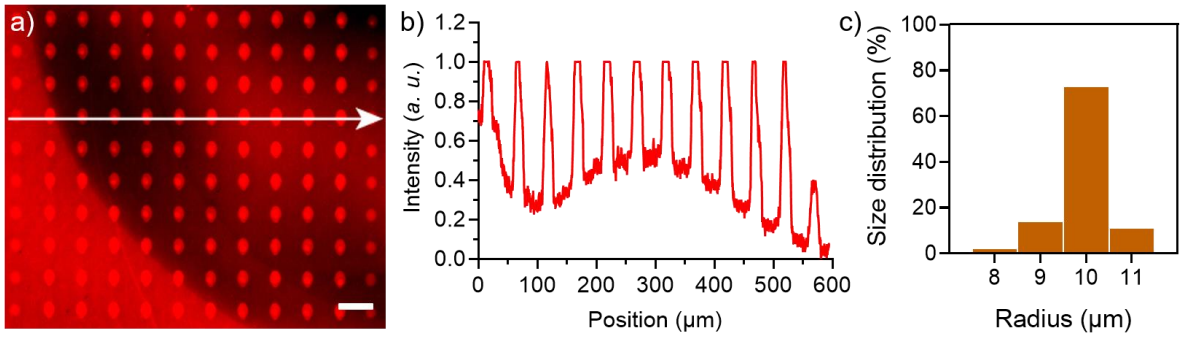

Figure 3- 9 a) CB6/pyronin B microarray, b) fluorescence intensity plot along the line indicated by the white arrow in a) and c) bar chart of the dot radius. Scale bars equal 50 µm in all images.

3.1.3.3. CB6/pyronin Y

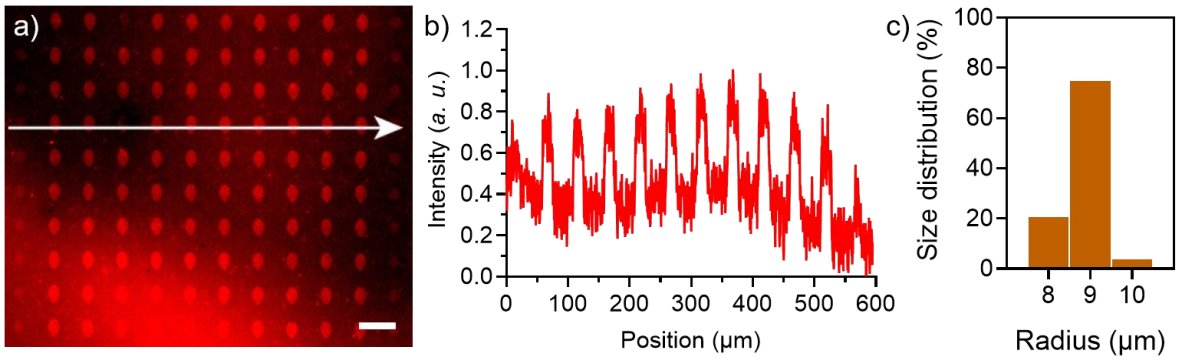

Figure 3- 10 a) CB6/pyronin Y microarray, b) fluorescence intensity plot along the line indicated by the white arrow in a) and c) bar chart of the dot radius.

Another similar indicator is pyronin Y which assembles with CB6 as well (Figure 3- 10). The background resulting from the unspecific adsorption is less, which seems more suitable for analyte detection.

3.1.3.4. CB7/BE

Berberine (BE) is a good indicator for CB7[74-75] and observable in GFP channel (Figure 3- 11). The inset picture in Figure 3- 11c shows the homogeneous CB7/BE chemosensor microarray dots and the inset graph shows the fluorescence intensity plot indicated by the

The results presented in this chapter are the basis of a published paper[17].

white arrow. The average feature dot radius of CB7/BE microarray is 9.77 ± 0.34 µm (Figure 3- 11d).

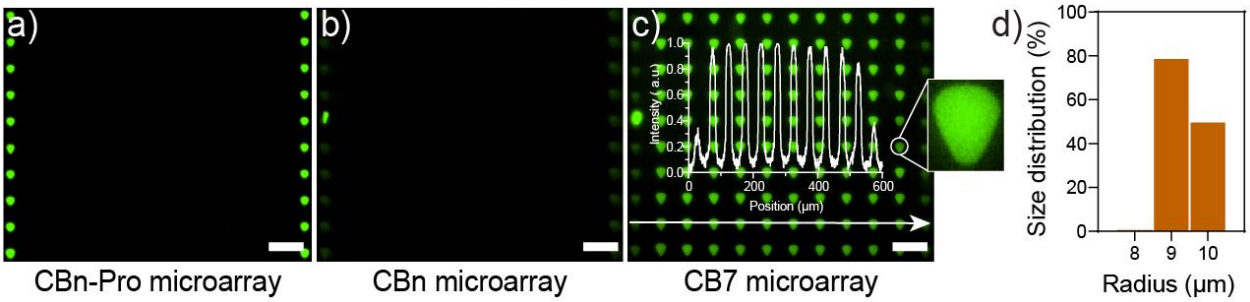

Figure 3- 11 CB7-microarray a) after printing, b) washing and c) incubation with BC in GFP channel, 8 s of exposure time. The inset picture shows the homogeneous property of chemosensor microarray dots. The inset graph shows the fluorescence intensity plot along the line indicated by the white arrow. (d) The average feature dot radius of CB7/BC-microarray is 9.77 ± 0.34 µm. Scale bars equal 50 µm in all images.[17]

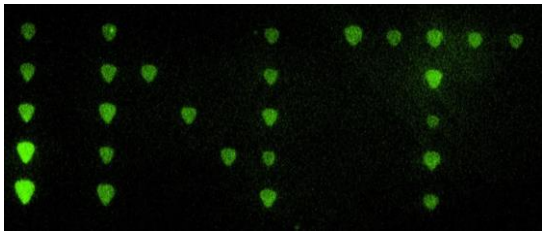

Figure 3- 12 “INT” logo made of CB7/BE microarray.

3.1.3.5. CB7/MDAP

N,*N*’-dimethyl-2,7,diazapyrenium (MDAP) is another good indicator for CB7[74-75] due to its higher binding affinity and observable in DAPI channel (Figure 3- 13). The inset picture in Figure 3- 13c shows the homogeneous CB7/MDAP chemosensor microarray dots and the inset graph shows the fluorescence intensity plot indicated by the white arrow. The average feature dot radius of CB7/MDAP microarray is 7.62 ± 0.35 µm (Figure 3- 13d).

The results presented in this chapter are the basis of a published paper[17].

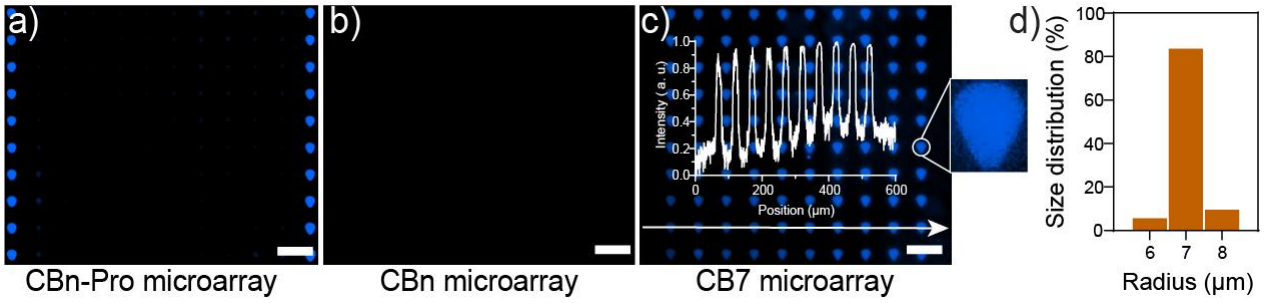

Figure 3- 13 CB7-microarray a) after printing, b) washing and c) incubation with MDAP in DAPI channel, 10 s of exposure time. The inset picture shows the homogeneous property of chemosensor microarray dots. The inset graph shows the fluorescence intensity plot along the line indicated by the white arrow. d)The average feature dot radius of CB7/MDAP-microarray is 7.62 ± 0.35 µm. Scale bars equal 50 µm in all images.[17]

Figure 3- 14 “INT” logo made of CB7/MDAP microarray.

The above results demonstrate the establishment of surface-bound CBn chemosensor microarrays visible in fluorescence, validating the proposed immobilization strategy.

3.1.3.6. Influence of impurities in CBn-Pro

As mentioned above when discussing the XPS data on homogeneous CBn immobilization, the CBn-Pro used in this subchapter are crude products containing some CBn and their hydroxylated derivatives (CBn-OH) from reactions in each step. Through repeated chromatographic separations it is possible to purify these products. [17],[12] Still it is interesting if the crude materials at such lower percentage and effort can be as effective as the purified CBn-Pro. Therefore, the influence of impurities, CBn and CBn-OH, on the thiol-yne photoreaction between CBn-Pro and thiol groups on the surface was evaluated by printing pure CB7, CB7-OH and CB7-Pro (with only minor remains of CB7) and BE assembly. After 10 min of UV irradiation and washing with ethanol and water, three microarrays were incubated with BE solution. From the images in Figure 3- 15,

The results presented in this chapter are the basis of a published paper[17].

fluorescence chemosensor microarray was only found in CB7-Pro printed sample but no signal was detected on CB7 and CB7-OH samples. Thus, the remaining impurities (CBn and CBn-OH) in CBn-Pro crude products will not affect the CBn immobilization. The CBn-Pro printing and the subsequent washing of the chemosensor microarrays can be treated as a purification process because only the CBn-Pro can bind onto the surface desired, which allows bypassing cumbersome and time-consuming chromatographic purification.

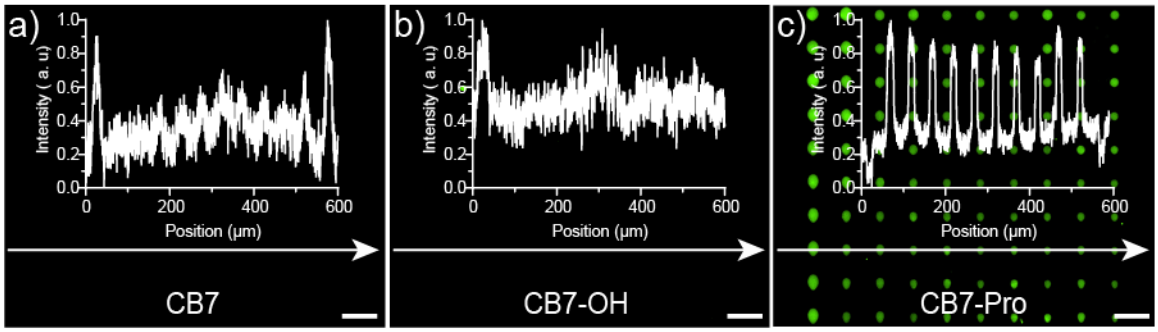

Figure 3- 15 Printing controls. Images after BC loading on (a) CB7, (b) CB7-OH and (c) CB7-Pro microarrays. The insets show the fluorescence intensity plot along the line indicated by white arrows.[17]

3.1.4. Inidicator-Displacement Assay (IDA)

In order to demonstrate the possibility and functionality of these generated microarrays as IDA chemical sensors shown in Figure 3- 16, different CBn/indicator chemosensor microarrays including mono-CBn/indicator, di-CBn/mono-indicator, multiplexed-CBn/mono-indicator, di-CBn/di-indicator and multi-CBn/indicator were incubated with non-chromophoric analytes (Figure 3- 17).

The results presented in this chapter are the basis of a published paper[17].

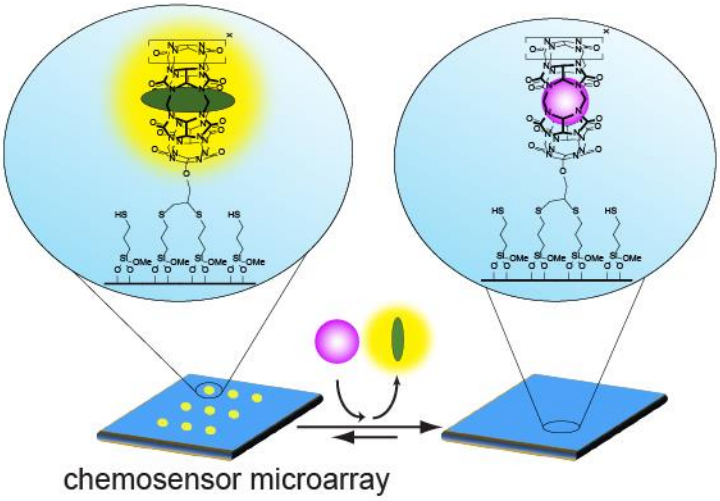

Figure 3- 16 Scheme of IDA.[17]

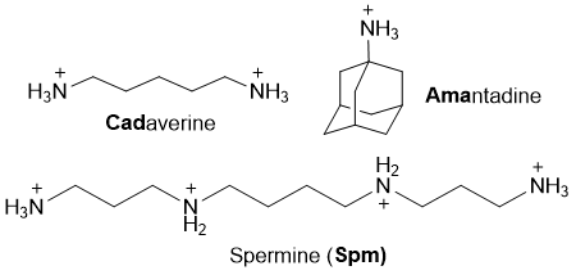

Figure 3- 17 Structures of analytes.

3.1.4.1. Mono-CBn/indicator microarray

3.1.4.1.1. CB6/TMR-Cad

Firstly, the detection of Spm on a CB6/TMR-Cad microarray was evaluated (Figure 3- 18, for better visual comparison in following images, all RD columns are cut out). After incubation of Spm solution in PBS for 10 min, washing and drying (images were taken in a dry state, same below if not particularly mentioned as obtained in microfluidic channels), the fluorescence signal on the chemosensor microarray disappears (Figure 3- 18a and b) resulted from the replacement of the indicator dye TMR-Cad by Spm due to the higher binding affinity between CB6 and Spm (log K_a = 9.52 in 50 mM sodium chloride buffer) compared to that between CB6 and Cad (log K_a = 8.18).[73] However in the negative control, after incubation with only PBS, the fluorescence of the chemosensor microarray keeps almost constant (Figure 3- 18d and e). The quantification of the fluorescence intensity in

The results presented in this chapter are the basis of a published paper[17].

Figure 3- 18g and Table 3- 4 show an obvious decrease on exposure to Spm and only a small loss in the control microarray.

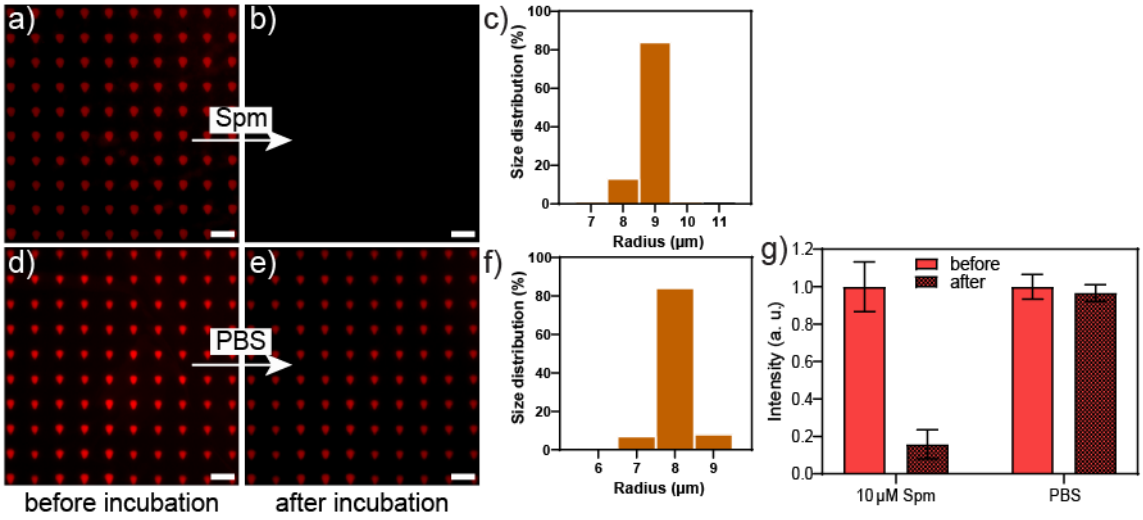

Figure 3- 18 CB6/TMR-Cad for Spm detection.[17]

Table 3- 4 Fluorescent intensities of CB6/TMR-Cad microarray for Spm detection.[17]

Intensity (*a. u.*)	control	Spm
before	1.00 ± 0.07	1.00 ± 0.13
after	0.97 ± 0.04	0.16 ± 0.08

3.1.4.1.2. CB7/BE

The performance of CB7/BE microarray was trialed for Ama detection (Figure 3- 19 and Table 3- 5). The Ama sensing happened almost instantly and finished in less than 1 min. The fluorescence signal is absent after Ama incubation (Figure 3- 19a and b), while the control microarray keeps bright fluorescence after PBS incubation(Figure 3- 19d and e). Figure 3- 19g shows an obvious decrease in fluorescence intensity after Ama incubation and a small decrease after PBS incubation.

The results presented in this chapter are the basis of a published paper[17].

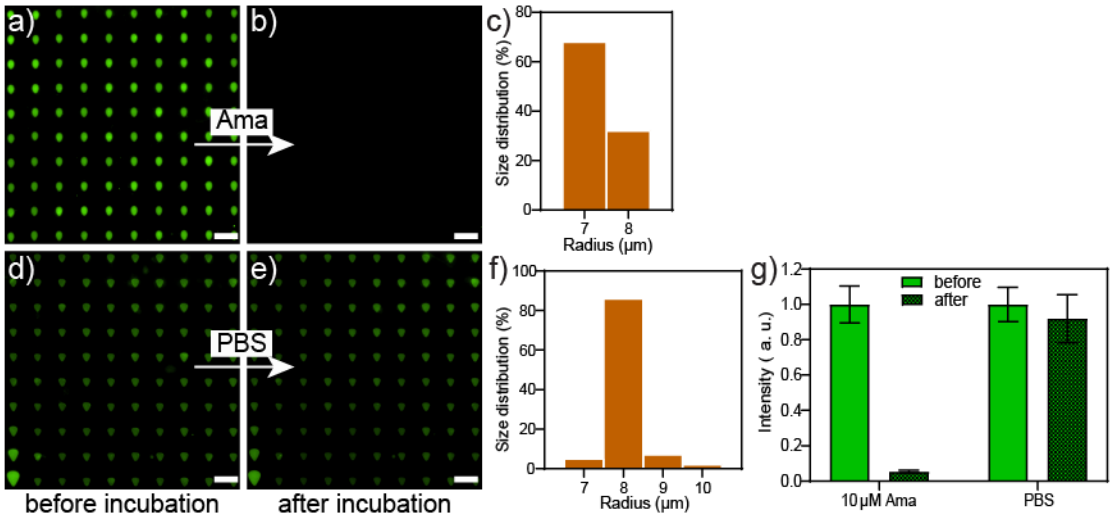

Figure 3- 19 CB7/BE for Ama detection.[17]

Table 3- 5 Fluorescent intensities of mono-ink CB7/BE chemosensor for Ama detection.[17]

Intensity (*a. u.*)	PBS	10 μM Ama
before	1.00 ± 0.10	1.00 ± 0.10
after	0.92 ± 0.14	0.05 ± 0.01

Cad can be sensed on CB7/BE microarray in nanomolar level shown in Figure 3- 20 and Table 3- 6. The fluorescence intensity slightly decreases in the control while that decreases more and more in the incubation of Cad in varying concentrations (Figure 3- 20a). The fluorescence in the control microarray remains (Figure 3- 20b and c) and that in Cad incubation in increasing concentrations disappears faster (Figure 3- 20d-o). It achieves an incomplete replacement near from 1 to 2 nM. However, the sensitivity is much higher compared to the solution-based IDA assay, where more than three orders of magnitude higher analyte concentrations (micromolar) are required, even when only low-salt "minimal" buffers are used.[76] The higher sensitivity of CB7/BE for Cad detection may be due to the high ratio of analyte molecule to the micropatterned CB7 (log K_a = 8.37 in water).[77]

The results presented in this chapter are the basis of a published paper[17].

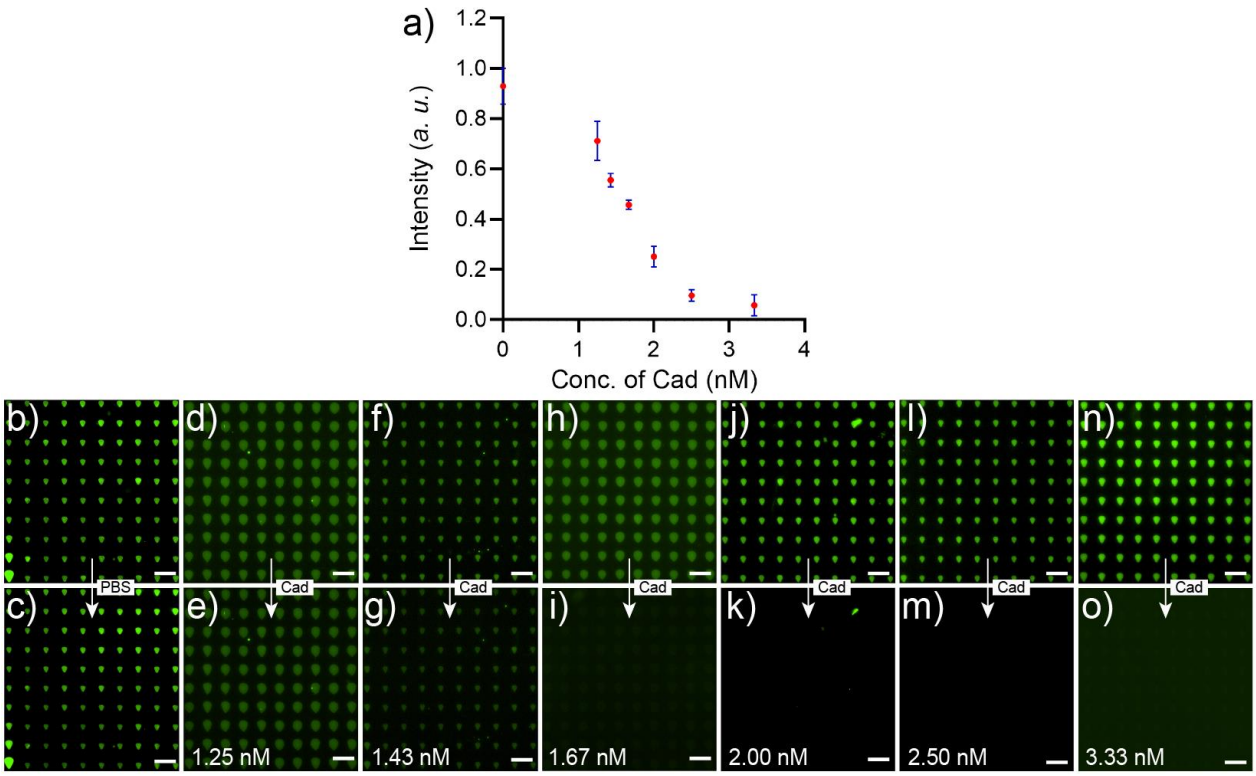

Figure 3- 20 CB7/BE chemosensor microarray for Cad detection in nanomolar concentration. (a) The intensity changes in different concentrations. Images of microarray for PBS control (b) and (c). Images of microarrays for Cad detection from 1.25 – 3.33 nM (d) – (o). At 1 to 2 nM, no full replacement is achieved.[17]

Table 3- 6 Fluorescent intensities of CB7/BE microarray for Cad detection.[17]

Intensity (*a. u.*)	control	Cad					
concentration (M)	PBS	1.25×10^{-9}	1.43×10^{-9}	1.67×10^{-9}	2.00×10^{-9}	2.50×10^{-9}	3.33×10^{-9}
before	1.00 ± 0.10	1.00 ± 0.05	1.00 ± 0.05	1.00 ± 0.03	1.00 ± 0.15	1.00 ± 0.08	1.00 ± 0.03
after	0.93 ± 0.07	0.72 ± 0.08	0.56 ± 0.03	0.46 ± 0.02	0.25 ± 0.04	0.10 ± 0.02	0.06 ± 0.04

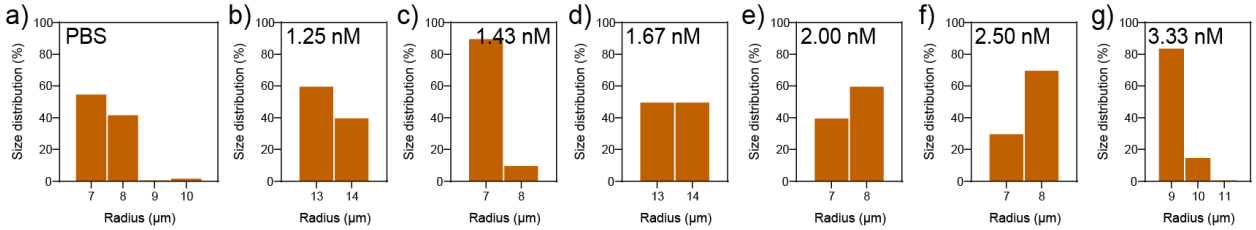

Figure 3- 21 Bar chart of CB7/BE microarray in Figure 3- 20. [17]

The results presented in this chapter are the basis of a published paper[17].

There are about 2.4 $\times 10^{10}$ molecules in a 10 × 10 array assuming an area per spot of 240 µm² and one CBn molecule per nm² (size estimates for CBn from literature).[3] Same, there are already 2.4 $\times 10^{17}$ analyte molecules in only 20 µL of analyte solution with a concentration of 2.0 nM. Therefore, it gives a ratio of analyte to surface-bond sensor molecules of 1.0 $\times 10^{7}$. As above, the molecule ratio of BE to Cad bound on CB7 microarray is 5.0 $\times 10^{11}$. Thus, the indicator dyes in the surface-bound chemosensor microarray can be easily and quickly replaced by the vast excess of analyte molecules in the. Another effect of the enhanced detection is that the indicator dyes will diffuse away from the surface even they are still fluorescent after being replaced and leaving the CBn hosts. This is also the focal plane for the fluorescence detection, hence they at the same time do not increase significantly the overall background as they usually do in in-solution IDA assay. However, it may reveal the limitation of the mass transport in liquid-solid interfaces by the incomplete replacement of BE (discussion below in section “Equilibrium of CBn/indicator Microarray”).

3.1.4.1.3. CB7/MDAP

Due to the stronger binding affinity with CB7, (log K_a = 9.43),[77] MDAP is another indicator for CB7 based chemosensor microarray. However, the replacement takes longer than that for CB7/BE, normally 5 min of analyte incubation. As shown in Figure 3- 22 and Table 3-7, after Ama incubation, the fluorescence diminishes while it remains in the control.

The results presented in this chapter are the basis of a published paper[17].

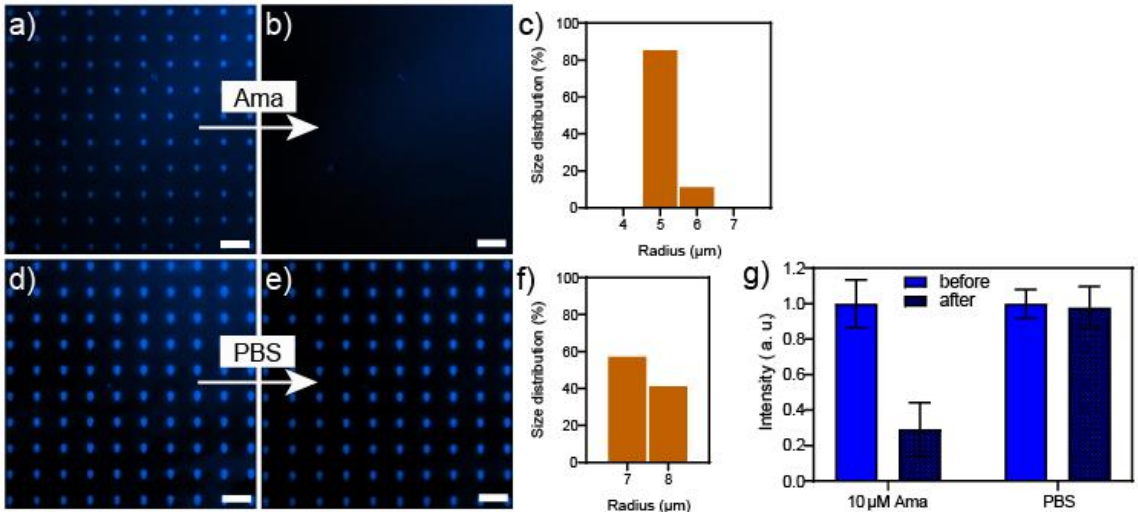

Figure 3- 22 CB7/MDAP microarray for Ama detection. CB7/MDAP microarray (a) before and (b) after incubation with 10 μM Ama for 5 min. (c) Bar chart in (a). (d) Before and (e) after incubation with PBS buffer for 5 min. (f) Radius distribution in (d). Images were taken in DAPI channel, 20 s of exposure time. Scale bars equal to 50 μm. (g) Quantification of fluorescence intensity.[17]

Table 3- 7 Fluorescent intensities of CB7/MDAP microarray for Ama detection.[17]

Intensity (*a. u.*)	control	Ama
before	1.00 ± 0.08	1.00 ± 0.13
after	0.98 ± 0.12	0.29 ± 0.15

The above-discussed results demonstrate that the mono-CBn/indicator microarrays are feasible for analyte detection through IDA, exemplified with CB6/TMR-Cad for Spm detection, and CB7/BE or CB7/MDAP for Ama and Cad detection.

3.1.4.1.4. Regeneration

As the chemosensor microarrays are based on the non-covalent host-guest molecular interaction, it should be feasible to recycle CBn/indicator microarrays. Even though the reuse of chemosensors is often not desired to avoid cross-contamination for instance in medical applications, it is still an option for the IDA detection in the above microarrays. As a demonstration, a CB7/BE microarray was incubated with Cad which resulted in an obvious fluorescence decrease (Figure 3- 23 and Table 3- 8). In the second round, the same microarray sample was assembled with BE indicator by incubation with 100 μM BE solution. The regenerated CB7/BE chemosensor microarray was still bright enough for

The results presented in this chapter are the basis of a published paper[17].

the second feasible Cad sensing even with a reduced fluorescence signal. This result demonstrates the mechanism of indicator replacement from another perspective due to the high ratio of BE to Cad molecules on such a CB7 microarray (5.0 $\times 10^{11}$, calculation mentioned above).

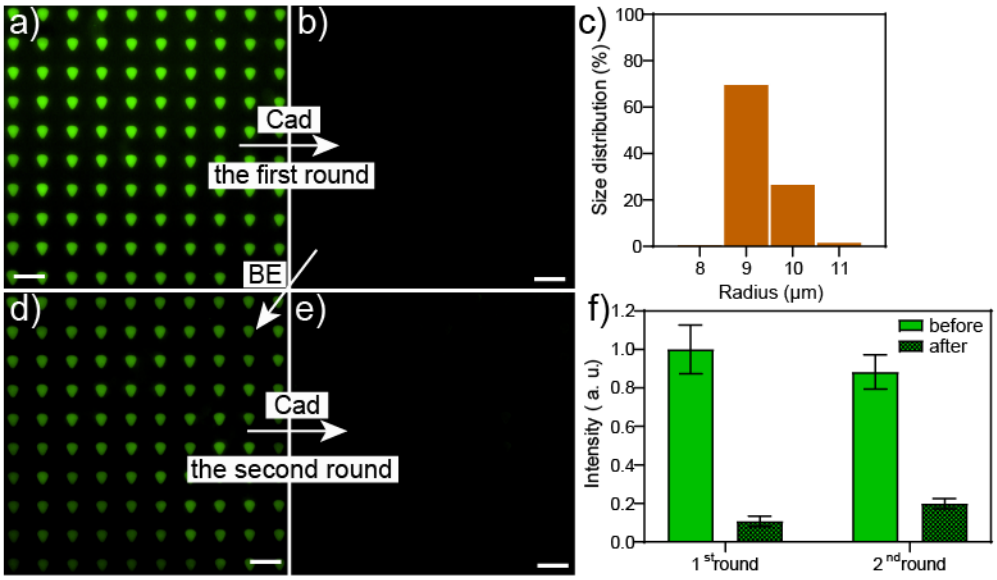

Figure 3- 23 Regeneration of CB7/BE microarray for 10 μM Cad detection. The first round (a) before and (b) after Cad incubation for 1 min. (c) Bar chart of microarray. The second round (d) before and (e) after Cad incubation for 1 min. (f) Quantification of fluorescence intensity.[17]

Table 3- 8 Fluorescent intensities of the regeneration of CB7/BE chemosensor microarray for Cad detection.[17]

Intensity (*a. u.*)	1st round	2nd round
before	1.00 ± 0.13	0.88 ± 0.9
after	0.11 ± 0.03	0.20 ± 0.03

3.1.4.1.5. Real-time sensing in a microfluidic channel

In order to further dynamically monitor the process and demonstrate the feasibility of the combination of such CBn/indicator microarrays into a microfluidic system for analyte detection, a microfluidic channel chip was mounted onto a matching microscopic cover slide that has been printed with CBn microarrays (Figure 3- 35). The Cad detection was real-time monitored and shows the progressive replacement.

The results presented in this chapter are the basis of a published paper[17].

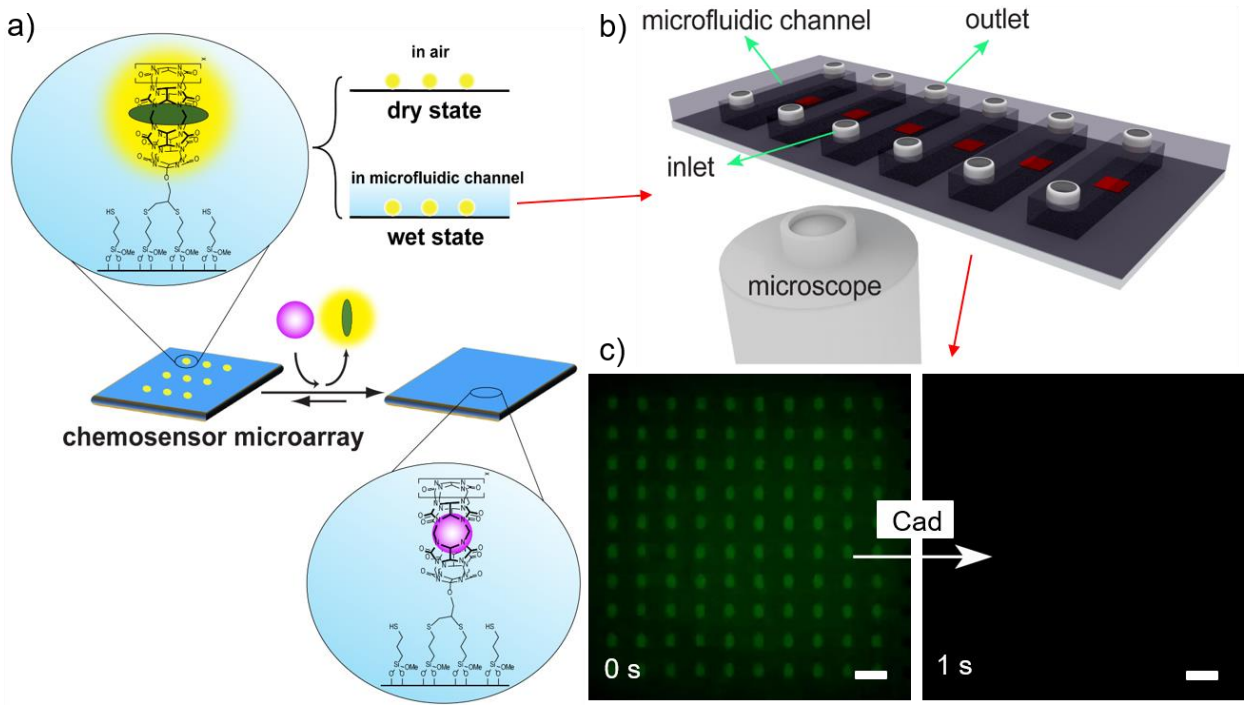

Figure 3- 24 CB7/BE microarray for real-time monitoring. a) Scheme of sensing, b) microfluidic channel and c) pictures of transient sensing.[17]

3.1.4.2. Di-CBn/mono-indicator microarray

As demonstrated above, mono-CBn/indicator microarrays can rapidly detect analytes with high affinity and have high sensitivity. However, the discrimination of different analytes requires specific CBn/indicator pairs for each. Therefore multiplexed chemosensor microarrays would be much more favorable to overcome such limitations. One possible approach is immobilizing different CBn homologs on one array to get diplex or even multiplex microarrays with different CBn/indicator pairs. Under these circumstances, indicators would be successively replaced by corresponding analytes, which allows the detection of different analytes on one microarray. In order to realize this concept, CB6-CB7 microarrays were printed and then assembled with respective matching indicators.

3.1.4.2.1. CB6-CB7/BE

After single indicator BE incubation, as BE is too large to get into the CB6 host, it can only assemble with CB7 thus only the CB7 part of the microarray is bright (Figure 3- 25 and Table 3- 9). Therefore, it is an effective way to control the host-guest assembly. After

The results presented in this chapter were a basis of a published paper[17].

incubating with 0.1 μM Cad, the fluorescence disappears compared with the control microarray.

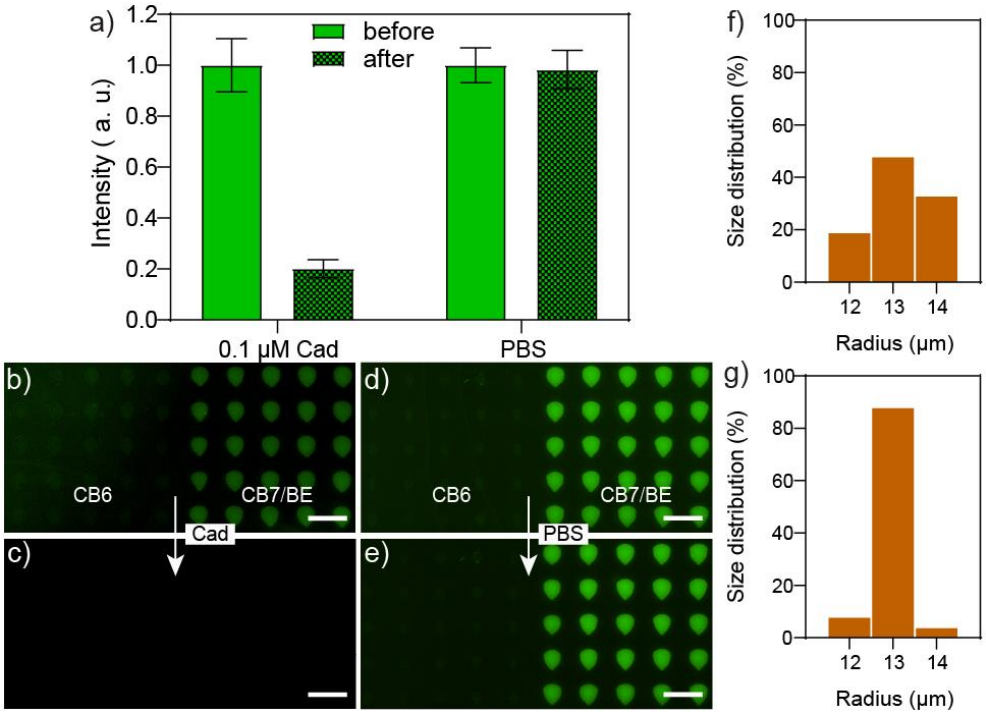

Figure 3- 25 CB6-CB7/BE microarray for Cad detection. (a) Quantification of fluorescence intensity. (b) Before and (c) after incubation with 0.1 μM Cad solution, and (d) before and (e) after incubation with PBS for 1 min in GFP channel. 10 s of exposure time. Scale bars equal to 50 μm. Bar charts of these two microarrays are shown in (f) and (g), respectively.[17]

Table 3- 9 Fluorescent intensities of CB6-CB7/BE microarray for Cad detection.[17]

Intensity (*a. u.*)	control	Cad
before	1.00 ± 0.07	1.00 ± 0.10
after	0.98 ± 0.08	0.20 ± 0.04

3.1.4.2.2. CB6-CB7/MDAP

MDAP indicator has the same behavior, which also only assembles into the CB7 host as BE above (Figure 3- 26 and Table 3- 10). The duplex chemosensor microarray was then used for Ama detection. After 0.1 μM Ama incubation for 5 min, the fluorescence intensity disappears again compared with the control microarray.

The results presented in this chapter were a basis of a published paper[17].

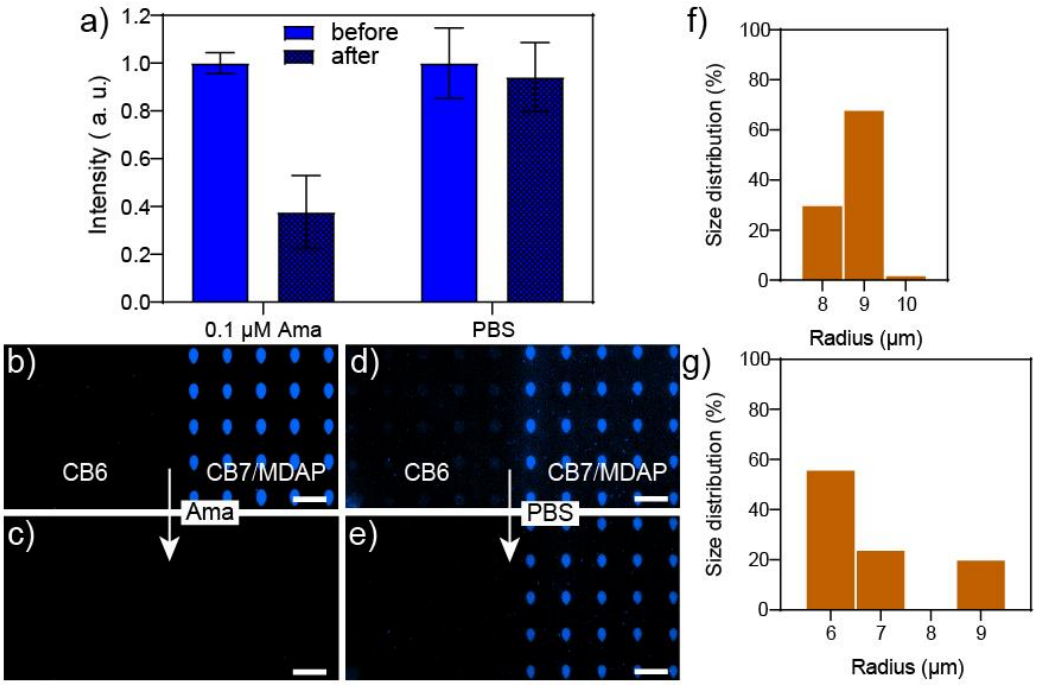

Figure 3- 26 CB6-CB7/MDAP microarray for Ama detection. a) Quantification of fluorescence intensity. b) Before and c) after incubation with 0.1 μM Ama solution, and d) before and e) after incubation with PBS for 5 min in GFP channel. 8 s of exposure time. Scale bars equal to 50 μm. Bar charts of these two microarrays are shown in f) and g), respectively.[17]

Table 3- 10 Fluorescent intensities of CB6-CB7/MDAP microarray for Ama detection.[17]

Intensity (*a. u.*)	control	Ama
before	1.00 ± 0.15	1.00 ± 0.04
after	0.94 ± 0.14	0.38 ± 0.15

3.1.4.2.3. CB6-CB7/DSMI

When a smaller indicator can be assembled with both CB6 and CB7, both sub-microarrays can be imaged. As an example, a CB6-CB7 microarray was incubated with trans-4-[4-(dimethylamino)styryl]-1-methylpyridinium iodide (DSMI) for 1 min. CB6 and CB7 patterns are visible both in Cy3 and GFP channels after loading with DSMI. The fluorescence of CB6/DSMI is weaker than that of CB7/DSMI, overlay shown in Figure 3- 27a and images in single-channel in Figure 3- 28. However, DSMI can be easily taken away from the surface by PBS incubation due to the lower binding affinity, thus not suitable for establishing chemosensor microarrays.

The results presented in this chapter were a basis of a published paper[17].

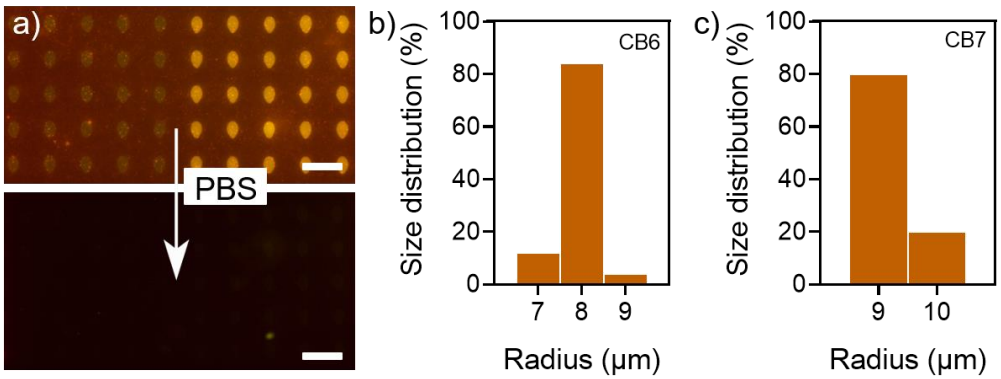

Figure 3- 27 CB6-CB7/DSMI microarray. a) Overlay images before and after PBS incubation. Bar charts of b) CB6 and c) CB7 sub-microarray. Scale bars equal to 50 μm. Cy3 8 s, GFP 10 s.

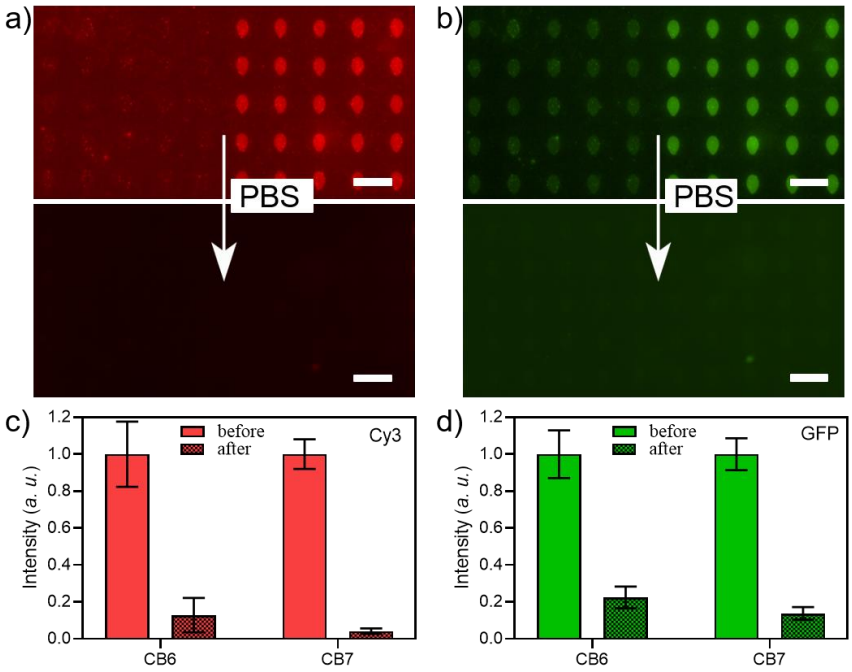

Figure 3- 28 Images of CB6-CB7/DSMI microarray for PBS incubation in a) Cy3 and b) GFP channels. Quantification of fluorescence intensity in c) Cy3 and d) GFP channels. Scale bars equal to 50 μm. Cy3 8 s, GFP 10 s.

Table 3- 11 Fluorescent intensities of CB6-CB7/DSMI microarray for PBS detection.

	Cy3		GFP	
Intensity (*a. u.*)	CB6	CB7	CB6	CB7
before	1.00 ± 0.18	1.00 ± 0.08	1.00 ± 0.13	1.00 ± 0.09
after	0.13 ± 0.09	0.04 ± 0.01	0.22 ± 0.06	0.14 ± 0.03

The results presented in this chapter were a basis of a published paper[17].

3.1.4.3. Multiplexed-CBn/mono-indicator microarray: CB6-CB7-CB8/TMR-Cad

In order to create a more complex multiplexed chemosensor microarray and real-time monitor analyte detection, CB8-Pro was printed beside the CB6 and CB7 pattern (Figure 3- 29). After photoreaction and washing, the generated CB6-CB7-CB8 microarray was combined with a microfluidic channel (Figure 3- 30a). After TMR-Cad injection and continuously washing with PBS, it is visible that to TMR-Cad assembles into all CB cavities in different quantities, distinguished with varying brightness, where the fluorescence intensity is CB6 > CB8 > CB7 (Figure 3- 30b and Table 3- 12). The CB6-CB7-CB8 chemosensor microarrays were either incubated with PBS as a negative control or 10 µM Spm solution in PBS. The whole process of analyte detection was real-timely recorded after indicator assembly. The overall fluorescence intensity in both cases decreases over time, which demonstrates the TMR-Cad molecules are statistically disassembled from the CB hosts and diffusing away from the microarray surface, even in the case of PBS (Figure 3- 30d). In the control microarray, the loss of fluorescence is 20%. decrease. However, it is near-complete and the fluorescence intensity decrease is faster for the Spm-incubated chemosensor microarray. The overall decrease is significantly higher visible that generates a clear and highly significant difference. In detail, the fluorescence intensity of the CB6/TMR-Cad sub-microarray decreases fastest, slower for the CB8/TMR-Cad and slowest for the CB7/TMR-Cad. Furthermore, CB7/TMR-Cad chemosensor sub-microarray losses visual inspection of the micrographs firstly (after 3 min), then CB8/TMR-Cad part (after 6 min) and finally the CB6/TMR-Cad part (after 10 min) due to the different start intensities. After 10 min of incubation, the intensity is almost stable for all sub-microarrays.

The results presented in this chapter were a basis of a published paper[17].

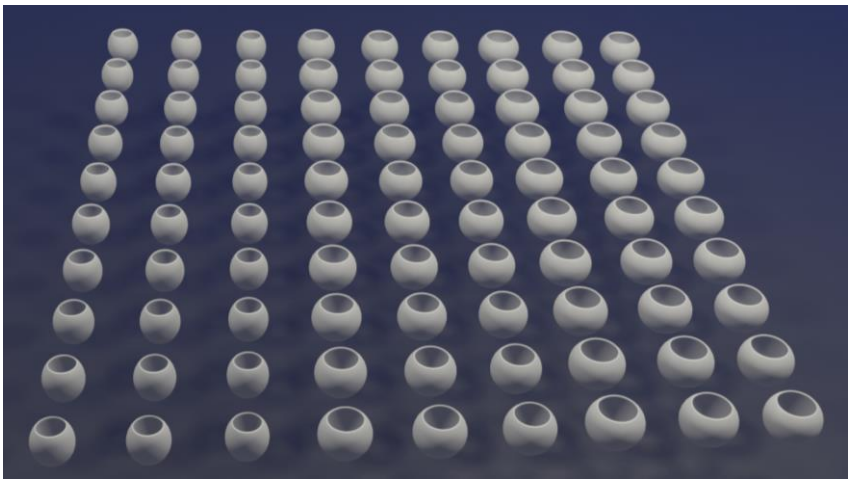

Figure 3- 29 Scheme of CB6-CB7-CB8 microarray.

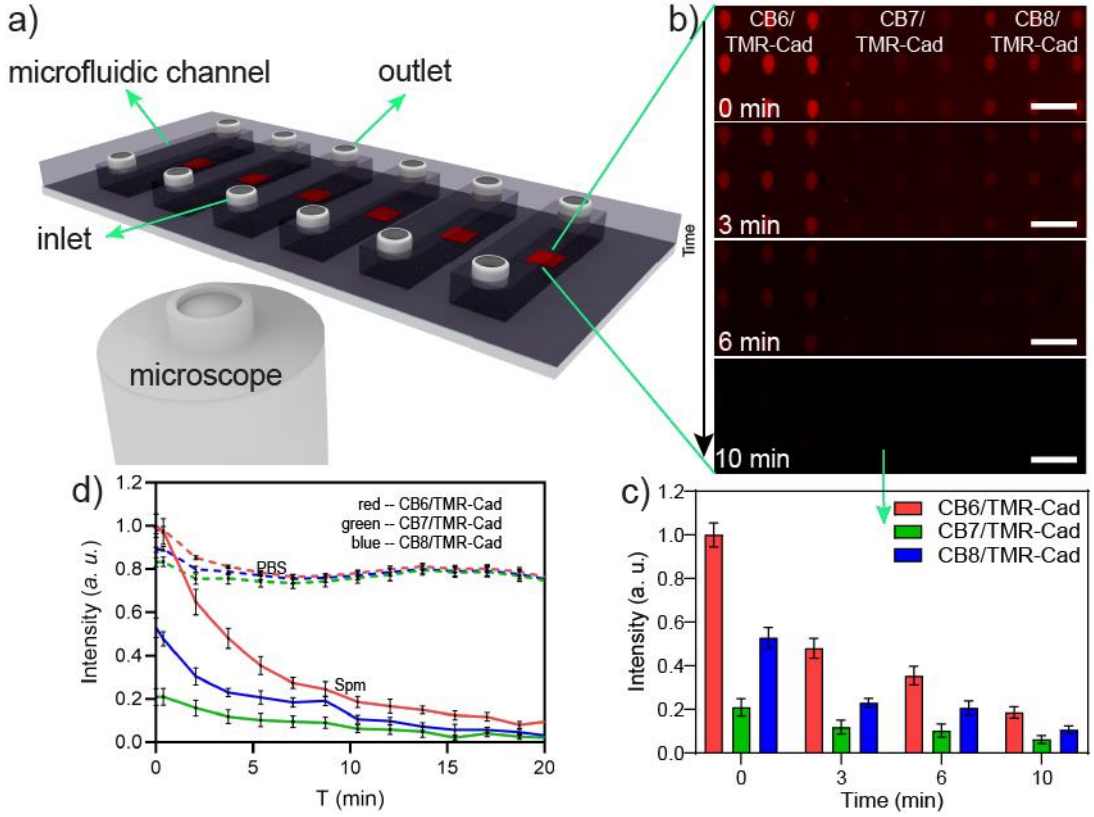

Figure 3- 30 CB6-CB7-CB8/TMR-Cad microarray for Spm detection in microfluidic channels. (a) Scheme of the microfluidic channel chip. (b) Images of chemosensor microarray containing 9 × 10 spot subpatterns of CB6, CB7 and CB8, all loaded with TMR-Cad in fluorescence, at time points of 0, 3, 6 and 10 min on incubation with 10 µM Spm. Scale bars equal to 50 µm. (c) Intensities of CB6-CB7-CB8/TMR-Cad microarray at 0, 3, 6 and 10 min incubated with 10 µM Spm in PBS screenshotted from live videos. (d) Graph of the fluorescence intensity time evolution of an array in PBS (negative control) and 10 µM Spm.[17]

The results presented in this chapter were a basis of a published paper[17].

Table 3- 12 Fluorescent intensities of CB6-CB7-CB8/TMR-Cad microarray for Spm detection at 0, 3, 6 and 10 min.[17]

Intensity (*a. u.*)	CB6	CB7	CB8
0	1.00 ± 0.05	0.21 ± 0.04	0.53 ± 0.09
3 min	0.48 ± 0.05	0.12 ± 0.03	0.23 ± 0.02
6 min	0.35 ± 0.04	0.10 ± 0.03	0.21 ± 0.03
10 min	0.18 ± 0.03	0.06 ± 0.02	0.11 ± 0.02

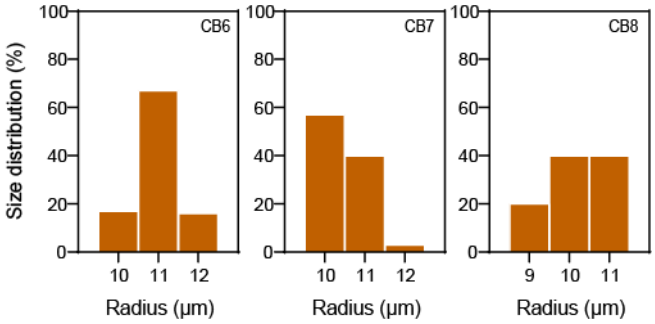

Figure 3- 31 Bar charts of CB6, CB7 and CB8 parts in CB6-CB7-CB8/TMR-Cad microarray.[17]

3.1.4.4. Di-CBn/di-indicator microarray: CB6/TMR-Cad and CB7/MDAP

After knowing different indicators affinities to different CBn hosts and these indicators visible in different fluorescence channels, it can design the multiplexed microarray with multi-fluorescent indicators for even more complex analyte detection. In order to realize this concept, a CB6/CB7 microarray was incubated with a TMR-Cad and MDAP mixing solution. These two indicators assembled into the respective surface-bound CBn (Figure 3- 33), where the TMR-Cad assembles into the CB6 while CB7 catches MDAP due to the higher affinity. They can be distinguished in different fluorescence channels, Cy3 channel with red for CB6/TMR-Cad and DAPI channel with blue for CB7/MDAP (overlays in Figure 3- 33, images in single channels in Figure 3- 34, Figure 3- 35 and Figure 3- 37).

When the generated CB6/TMR-Cad CB7/MDAP multiplexed microarray is incubated with a solution of 1 μM Spm, both sections of the chemosensor microarray lose fluorescence intensity due to the high binding affinity of Spm with both CB6 and CB7. In comparison, after incubation with 1 μM Cad that is supposed to assembly with the CB6 host firstly due

The results presented in this chapter were a basis of a published paper[17].

to the higher affinity, a large loss of the fluorescence signal is only observed in the CB6/TMR-Cad sub-microarray, while that of the CB7/MDAP sub-microarray loses less. The above results demonstrate that Cad could efficiently replace the TMR-Cad indicator in CB6 host, while CB7 could keep MDAP less disturbed (Figure 3- 35 and Figure 3- 36). For a negative control incubated with PBS, both parts of the microarray have only a small fluorescence decrease. This duplex analytes detection shows the potential for the distinguishment of different analytes by varying replacement in sub-microarray sections and it works even for analytes where CBn are not fully selective, for example, Cad and Spm.

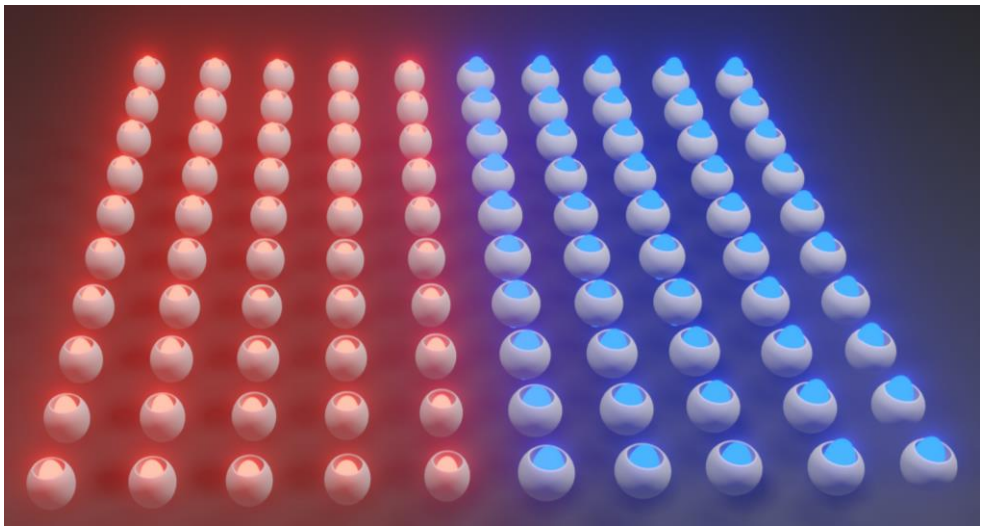

Figure 3- 32 Scheme of di-CBn/di-indicator chemosensor microarray.

The results presented in this chapter were a basis of a published paper[17].

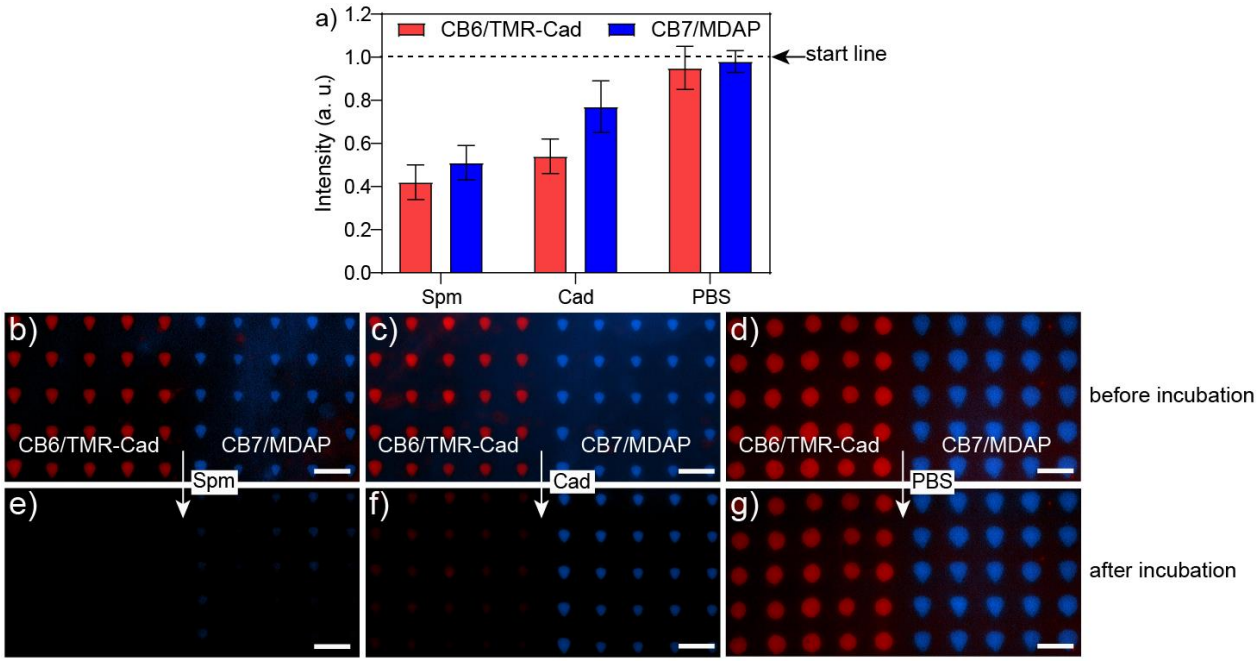

Figure 3- 33 CB6/TMR-Cad and CB7/MDAP multiplexed microarray for Cad and Spm detection. a) Fluorescence intensity graph of Spm, Cad, and PBS control after 5 min incubation. Overlay images of three CB6/TMR-Cad and CB7/MDAP multiplex microarrays b), c), and d) of Cy3 (red) and DAPI channel (blue). Overlay images of these microarrays after e) 1 μM Spm, f) Cad, or g) PBS incubation. Scale bars equal 50 μm.[17]

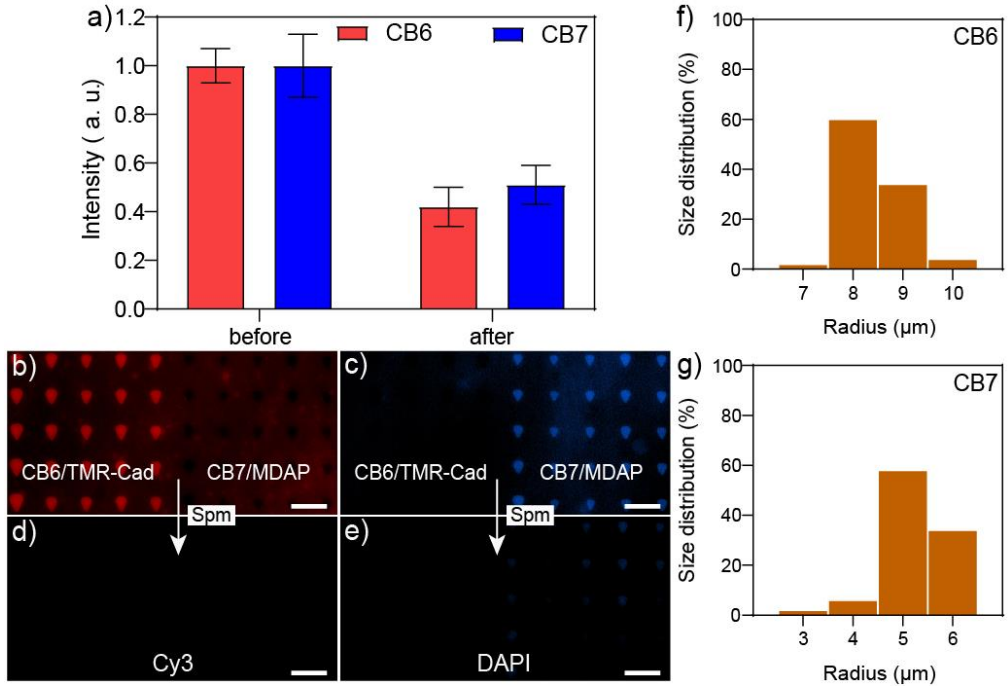

Figure 3- 34 Multiplexed CB6/TMR-Cad and CB7/MDAP microarray for Spm detection in single channels. a) Quantification of fluorescence intensity. Images of this microarray before incubation in b) Cy3 and c) DAPI channels. Images after incubation with 0.1 μM Spm solution in d) Cy3 and

The results presented in this chapter were a basis of a published paper[17].

e) DAPI channels. 60 ms of exposure time for Cy3 and 10 s for DAPI. Scale bars equal to 50 µm. Bar charts of f) CB6/TMR-Cad and g) CB7/MDAP sections.[17]

Table 3- 13 Fluorescent intensities of multiplexed CB6/TMR-Cad and CB7/MDAP microarray for Spm detection.[17]

Intensity (*a. u.*)	CB6 sensor	CB7 sensor
before	1.00 ± 0.07	1.00 ± 0.13
after	0.42 ± 0.08	0.51 ± 0.08

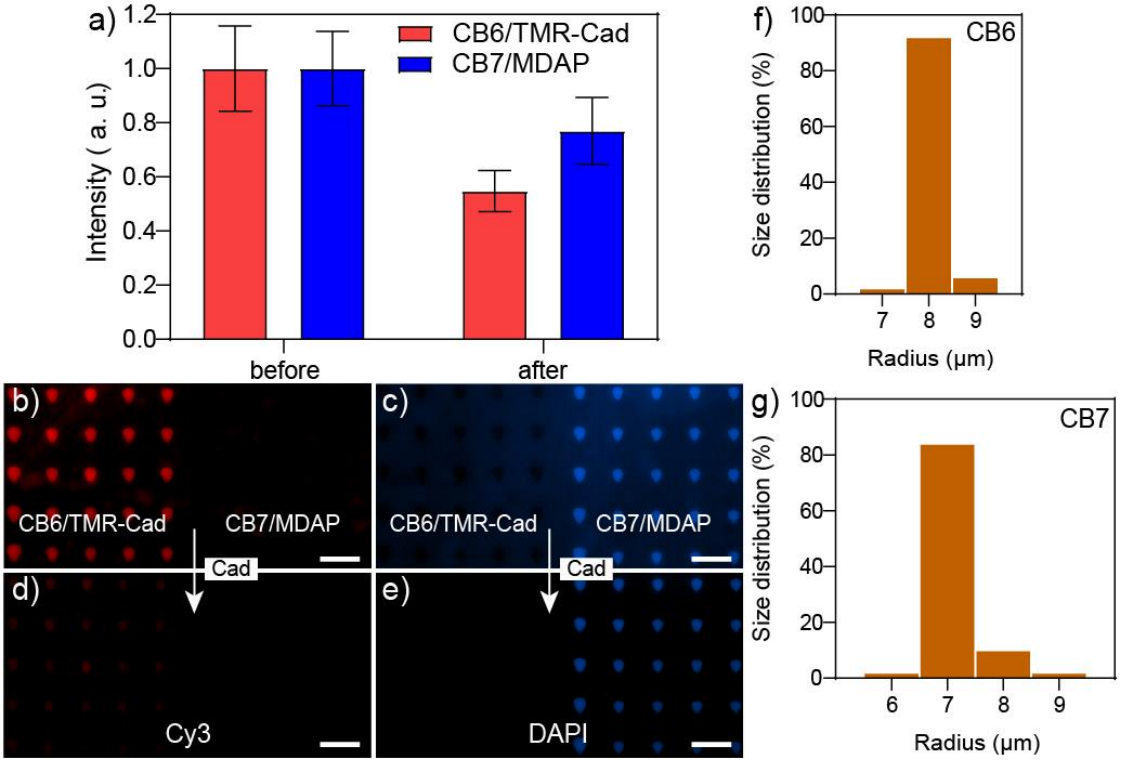

Figure 3- 35 Multiplexed CB6/TMR-Cad and CB7/MDAP microarray for Cad detection in single channels. a) Quantification of fluorescence intensity. Images of this microarray before incubation in b) Cy3 and c) DAPI channels. Images after incubation with 0.1 µM Cad solution in d) Cy3 and e) DAPI channels. 60 ms of exposure time for Cy3 and 10 s for DAPI. Scale bars equal to 50 µm. Bar charts of f) CB6/TMR-Cad and g) CB7/MDAP sections.[17]

The results presented in this chapter were a basis of a published paper[17].

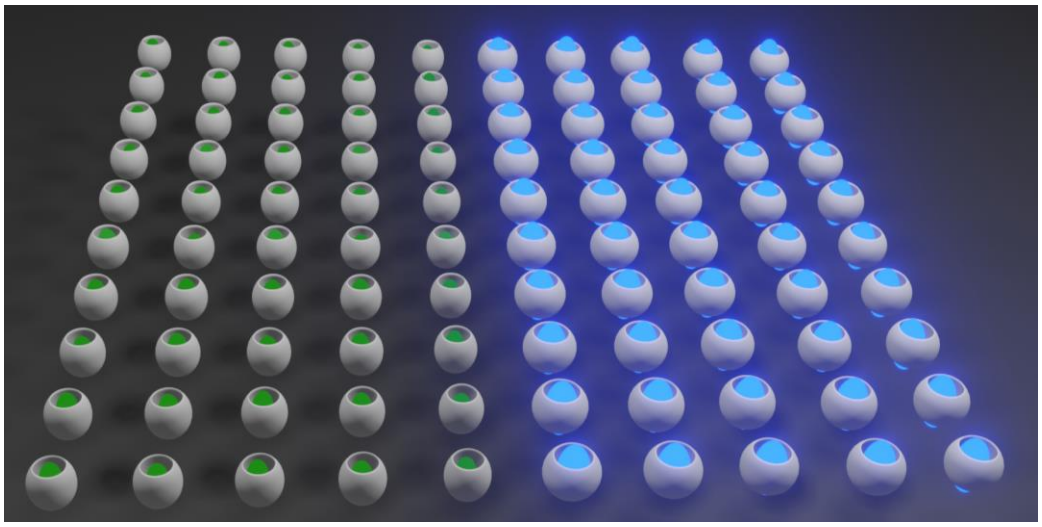

Figure 3- 36 Scheme of CB6/TMR-Cad and CB7/MDAP microarray, where TMR-Cad has be replaced by Cad and CB7 part remains bright.

Table 3- 14 Fluorescent intensities of multiplexed CB6/TMR-Cad and CB7/MDAP microarray for Cad detection.[17]

Intensity (*a. u.*)	CB6 sensor	CB7 sensor
before	1.00 ± 0.16	1.00 ± 0.14
after	0.54 ± 0.08	0.77 ± 0.12

The results presented in this chapter were a basis of a published paper[17].

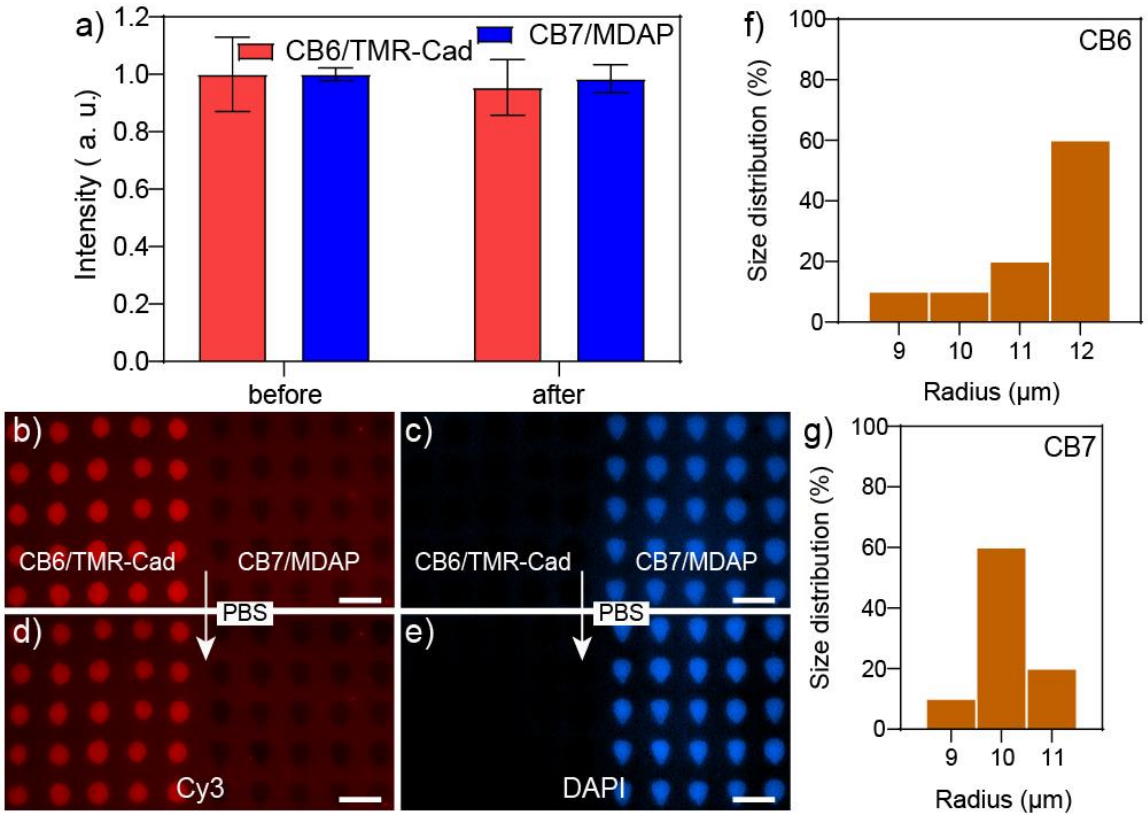

Figure 3- 37 Multiplexed CB6/TMR-Cad and CB7/MDAP microarray for PBS control in single channels. a) Quantification of fluorescence intensity. Images of this microarray before incubation in b) Cy3 and c) DAPI channels. Images after incubation with PBS in d) Cy3 and e) DAPI channels. 60 ms of exposure time for Cy3 and 10 s for DAPI. Scale bars equal to 50 μm. Bar charts of f) CB6/TMR-Cad and g) CB7/MDAP sections.[17]

Table 3- 15 Fluorescent intensities of multiplexed CB6/TMR-Cad and CB7/MDAP microarray in PBS.[17]

Intensity (*a. u.*)	CB6 sensor	CB7 sensor
before	1.00 ± 0.13	1.00 ± 0.02
after	0.95 ± 0.10	0.98 ± 0.05

3.1.4.5. Multi-CBn/di-indicator microarray: CB6/TMR-Cad, CB7/MDAP and CB8/TMR-Cad

It can be further broadened through additional CBn homologs, which in the end enables analyte distinguishment by an unequal response on the different sub-microarray resulting from the binding affinity and fluorescence color. A multiplexed CB6/CB7/CB8 microarray

The results presented in this chapter were a basis of a published paper[17].

mentioned above was incubated with a mixed solution containing TMR-Cad and MDAP. As before, the CB6 and CB7 sub-microarray show mainly the signal of TMR-Cad and the MDAP, respectively. However, the addition of the GFP channel enables the distinguishment CB6 and CB8 indicated by TMR-Cad due to the different shifts in the spectrum of TMR-Cad in the different hosts (Figure 3- 38).

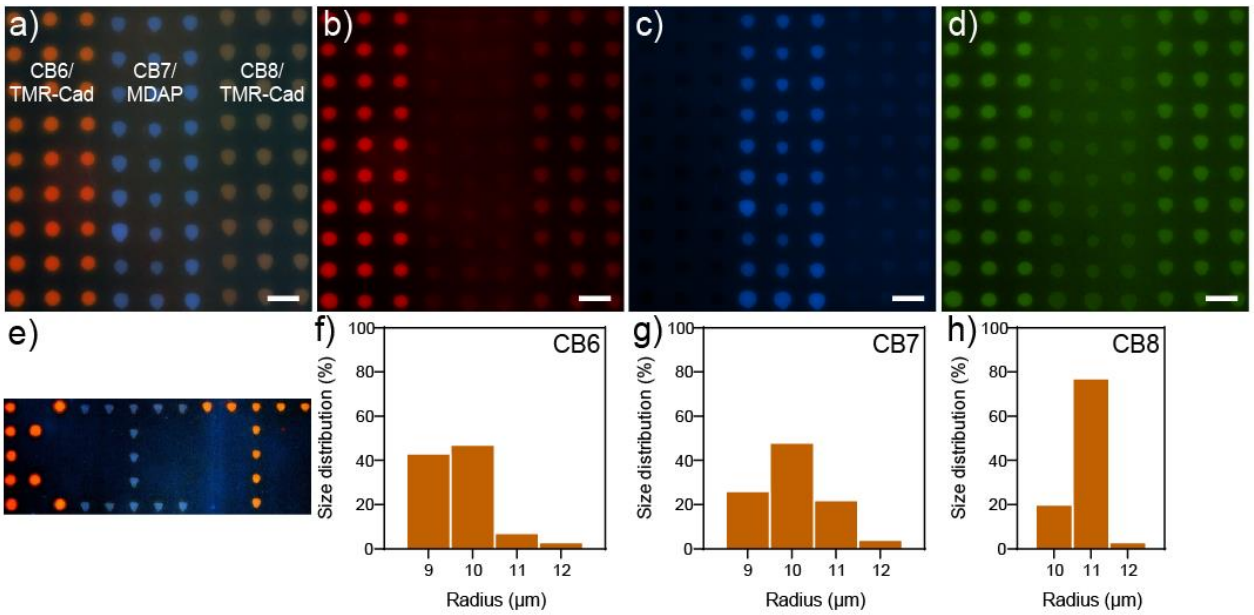

Figure 3- 38 Multiplexed CB6/TMR-Cad, CB7/MDAP and CB8/TMR-Cad microarray. a) Overlay image of b) in Cy3, c) DAPI and d) GFP channels. e) a "KIT" logo made of CB6/TMR-Cad, CB7/MDAP and CB8/TMR-Cad microarray. Dot radius distribution of f) CB6/TMR-Cad, g) CB7/MDAP and h) CB8/TMR-Cad sections. 200 ms of exposure time for Cy3, 15 s for GFP and 15 s for DAPI. Scale bars equal to 50 μm.[17]

3.1.4.6. Discussion of equilibrium of the CBn/indicator microarray

Normally upon dilution, host-guest self-assembled interactions disassembly and the kinetics of disassembly between host and guest is on the order of ~1 s. Thus the system should quickly get the disassembled equilibration,[75, 78] especially when there is only a patterned monolayer of CBn host incubated with 20 μl of buffer.[79] However, the remaining fluorescence in the microarrays after PBS incubation demonstrates the indicator guests did not disassembly that fast from the immobilized CBn microarray. The reason of this unusual phenomenon may be the enhanced binding affinity or equilibrium constant between immobilized CBn hosts and the indicators. The dielectric strength of water can be decreased in the interfaces therefore the electrostatic interactions and hydrogen

The results presented in this chapter were a basis of a published paper[17].

bonding in the guest/host system can be increased, which was firstly mentioned in the research of molecular recognition of guanidinium/phosphate pairs.[80-81] Even though this phenomenon is at the beginning presented at air/water interfaces, it is also highly significant in water/solid systems that was proved through theoretical quantum calculations in the same research group.[82-83] As summarized in recent reviews,[84] this should be applied to not only amino acids, peptides, sugars, nucleic acid bases and nucleotides but also more molecular recognition pairs. This increased stability demonstrates that surface-immobilization chemosensor systems provide potential advantages over homogenous solution-based sensing systems.

3.1.4.7. Discussion of mass transport processes

In order to better understand the differences in surface-immobilized CBn IDA systems compared with homogenous solution-based systems, a deeper comprehension into the mass transport processes is essential: The first mass transport starts from the indicator in the solution to the empty CBn microarrays, upon a reversible host-guest self-assembly[85] where the indicator molecule goes into CBn host mostly driven by uptake kinetics because of the high molecular ratio of indicator to CBn,[86] as shown in surface-immobilized CBn/indicator systems.[12] The increased mass transport coefficient is due to the higher equilibrium constant as mentioned above, which again explains the stability of the CBn/indicator chemosensor microarrays exposed to PBS buffer, which corresponds to the reported homogeneous surface-modification of CBn/indicator chemosensors.[87] The second mass transport process is between the analyte from solution and the CBn/indicator microarrays on the surface, which is namely the reversible indicator replacement process. On one hand, analyte goes into the CBn host due to favorable kinetics and higher binding affinity. On the other hand, the replaced indicator, not being tied anymore in the CBn cavity diffuses away from the monolayer just above the surface and movies to the bulk solution with increased entropy.[85, 88] During a given time, it depends on the amount of analyte for it to transport to the surface and release indicators. Principally, a low amount of analyte can therefore make it necessary for chemosensors to collect all available analytes dropped on the sample, therefore, it is mainly limited by the mass transport to the surface.[89] In the case of CBn/indicator chemosensor microarray, it can be seen that total replacement of indicators in surface-bound CBn in equilibrium conditions is obtained in

The results presented in this chapter were a basis of a published paper[17].

most cases, thus the mass transport works effectively in the sensing step. However, analyte diffusion to the CBn on the surface was too slow to reach full replacement in the low concentrations for example 1 nM of Cad in Figure 3- 20a, and only an unfull fluorescence decrease appears. This demonstrates that it reaches a mass transport limit in these cases when convection and diffusion deliver analytes so slowly to the liquid-solid interface, during when the time for the replacement interaction is comparably negligible.[90] However, the limitation could be decreased through stirring the system or additional fresh analyte solution to the system.

3.1.5. Summary of modified CBn systems

Overall, a series of micropatterned of CBn/indicator chemosensors, covalently immobilized by CBn, into microarrays was established to show the advantages for multiplexed and highly sensitive analyte detection. For this, CB6-Pro, CB7-Pro and CB8-Pro were used as covalent linkages between SiO_2-SH surface and mono/multiplex CBn microarrays. The micropatterning was automatically controlled by μCS. The generated CBn microarrays were assembled with indicator dyes and thus obtained CBn/indicator chemosensor microarrays. These CBn/indicator microarrays were evaluated for detection of non-chromophoric analytes through emissive IDA. The CBn/indicator microarrays behave increased sensitivity in the nanomolar concentration and solve the problem of signal interference by the displaced dye to interfere because the remaining indicator can be simply washed away. Moreover, the integration of these CBn/indicator chemosensor microarrays into microfluidic chips build up microfluidic systems and that provides an efficient way to real-timely monitor the whole process of analyte detection at the liquid-solid interface, which simplifies handling and reduces the amount of analyte. Finally, the multiplex microarrays show the general advantage of surface-immobilized IDA for detection of multi-component through multi-CBn and/or multi-indicator responding differentially to different analytes. The demonstrated approaches provide significant value for the development of the IDA detecting strategies in the future for multiplex detection of analytes in more complex fluids. In addition, it can build up host-guest sensing libraries by the multiplexing of CBn and indicators (Figure 3- 39), which opens up routes for industrialization in biological or environmental applications.

The results presented in this chapter were a basis of a published paper[17].

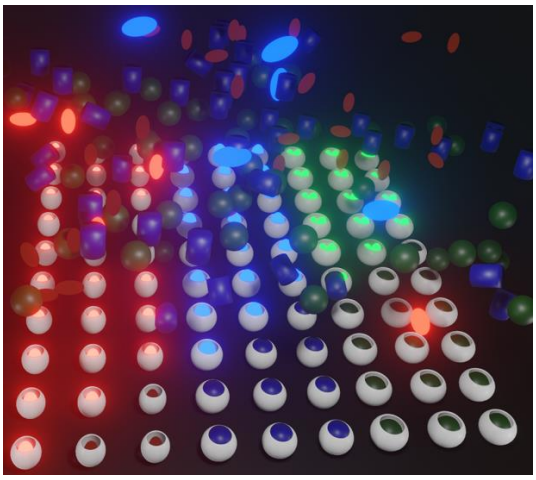

Figure 3- 39 Scheme of a multiplexed cucurbit[*n*]uril-based chemosensor microarray.[17]

3.2. Guest-mediated CBn immobilization

In this subchapter, CBn immobilization on the surface is demonstrated through guest mediation. Basically, a selection of azides or thiol functionalized guests (Figure 3- 40) were micropatterned on an alkyne or DBCO functionalized surface through µCS and then the bound guest was assembled with CBn to form chemosensor microarrays. The generated microarrays were incubated with analytes solution to evaluate their IDA property.

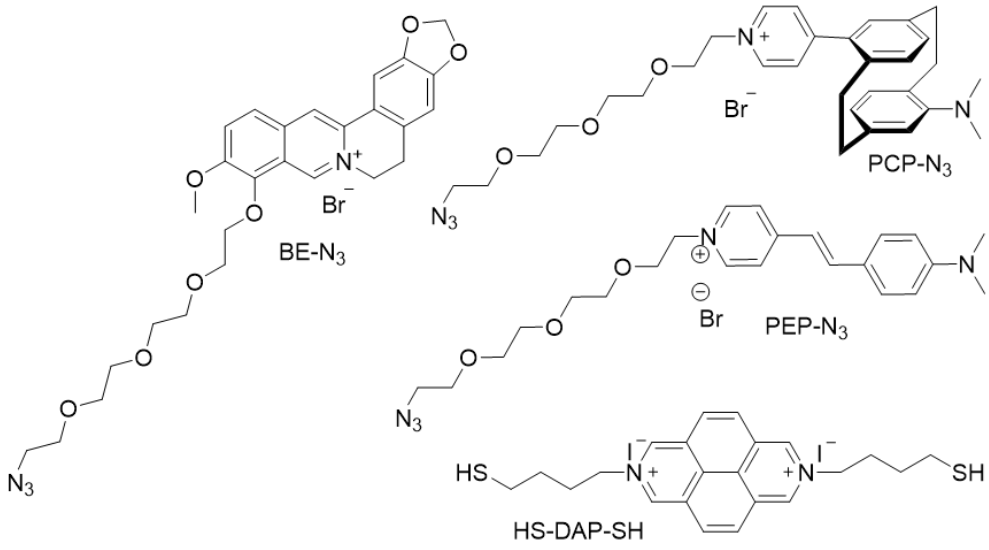

Figure 3- 40 Structures of azide and thiol functionalized guests.

The results presented in this chapter were a basis of a published paper[17].

3.2.1. Surface modification

3.2.1.1. Alkyne surface

Alkyne surface (SiO_2-Alk) for azide immobilization through CuAAC reaction was prepared according to former literature in the group[91] and the is scheme shown in Figure 3- 41.

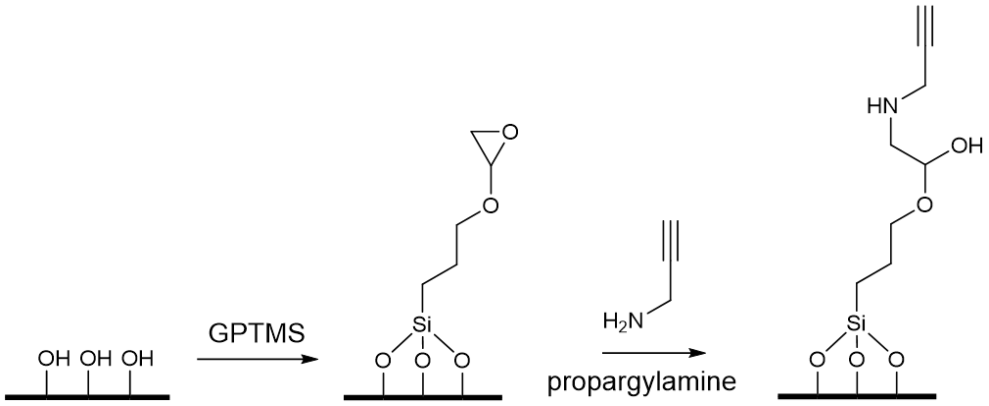

Figure 3- 41 Scheme of SiO_2-Alk surface modification.[91]

3.2.1.2. Maleimide surface

DBCO surface (SiO_2-DBCO) was prepared following the scheme in Figure 3- 42 according to the former literature in the group.[92]

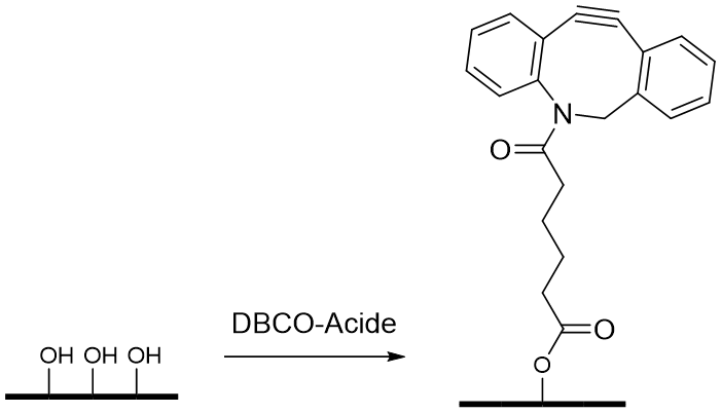

Figure 3- 42 Scheme of SiO_2-DBCO surface modification.[92]

3.2.2. Strategy of CBn immobilization

3.2.2.1. CB7/BE-N_3

BE-N_3 can be easily linked on SiO_2-Alk surface through Copper-Catalyzed Azide-Alkyne Cycloaddition (CuAAC) reaction. Firstly CB7/BE-N_3 complex mixed with a copper catalyst (Cu^+) was printed on the SiO_2-Alk surface, at the same time another ink only contains CB7/BE-N_3 as a negative control (Figure 3- 43). Just after printing, the spots of CB7/BE-N_3 (Cu^+) are less bright compared to CB7/BE-N_3 due to the lower fluorophore concentration by adding the Cu^+-solution to the ink. Same after getting dry, the spots of CB7/BE-N_3 (Cu^+) are much smaller and hard to distinguish after washing. The reason may be a strong unspecific adsorption of BE-N_3 complicating to compare if the immobilization works as intended.

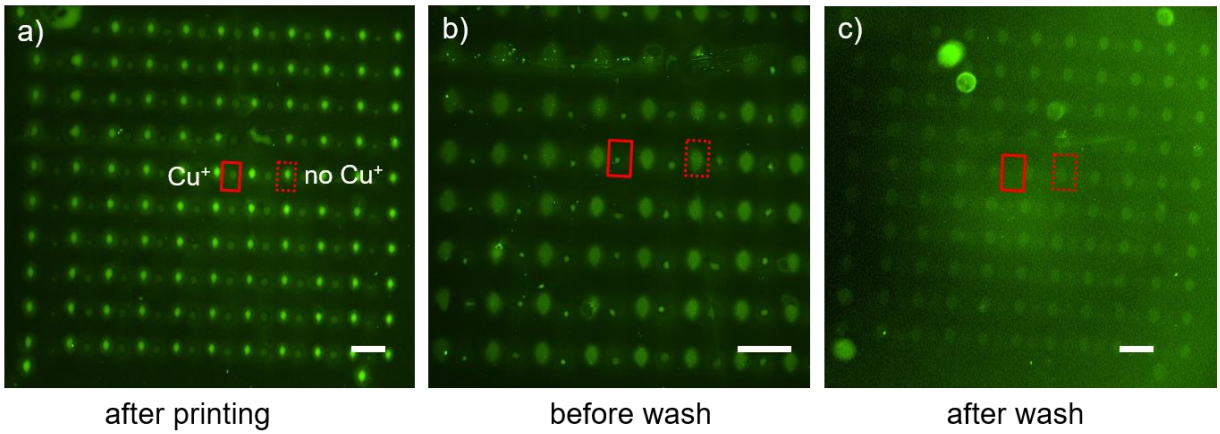

Figure 3- 43 Micropatterning of CB7/BE-N_3 chemosensor on SiO_2-Alk surface. a) After printing of CB7/BE-N_3 ink with Cu^+ as a catalyst, coming from a mixture of copper sulfate ($CuSO_4$) and Sodium Ascorbate, and ink without Cu^+. b) After drying. c) After washing. Scale bars equel to 100 µm. 3s in FITC.

In order to avoid the above reason, the control ink CB7/BE-N_3 was diluted with the same amount of water as the additional catalyst mixture and printed on the SiO_2-Alk surface (Figure 3- 44). After printing, these two inks are visibly different in fluorescent brightness under fluorescence. After drying, the shape of CB7/BE-N_3 (Cu^+) spots shrink and but that of CB7/BE-N_3 keeps the original size. The failed immobilization seems to be caused by the shrinking of spots on the surface.

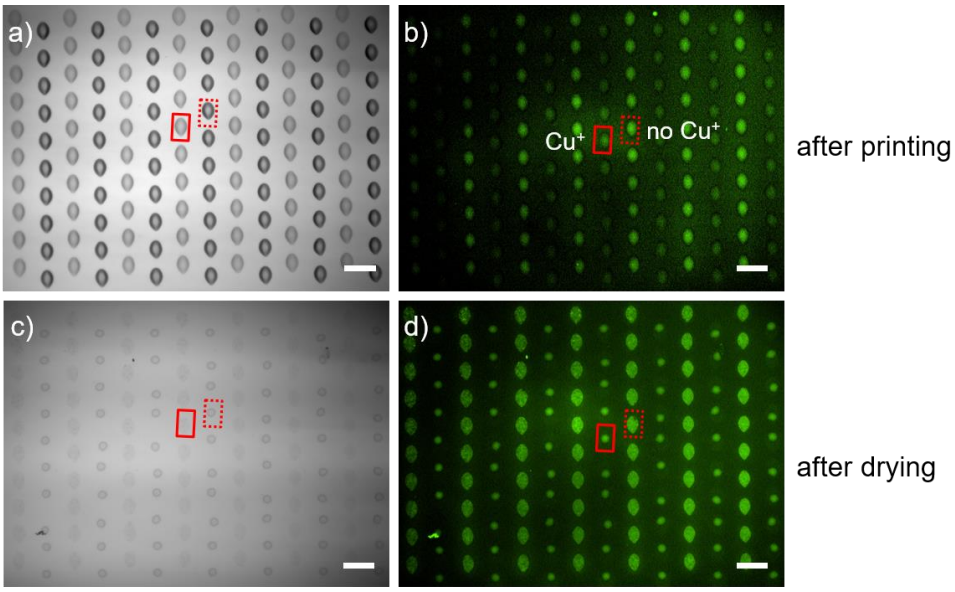

Figure 3- 44 Micropatterning of CB7/BE-N_3 chemosensor on SiO_2-Alk surface with inks in the same concentration. Figures after the printing of CB7/BE-N_3 ink with Cu^+ as a catalyst, coming from a mixture of copper sulfate ($CuSO_4$) and Sodium Ascorbate, and ink without Cu^+ but the same amount of water to keep same concentration exposure in a) BF and b) FITC. Figures after drying c) in BF and d) in FITC. Scale bars equel to 50 µm. BF 4ms, FITC 1s.

3.2.2.2. BE-N_3

To prove the CuAAC happens well between BE-N_3 and SiO_2-Alk surface, a reference dye with azide group TAMRA-N_3 was printed beside BE-N_3 (Cu^+) spots after mixing with Cu^+ (in Figure 3- 45) or beside BE-N_3 (Cu^+) and BE-N_3 spots (Figure 3- 46). BE-N_3 can be visible in FITC channel and TAMRA-N_3 visible in FITC but more in TexasRed channel. An overlay in Figure 3- 45c shows the multiplex microarray. However, BE is invisible after washing compared with much bright TAMRA. This proves the CuAAC reaction works well and the key is to find a suitable reference with near brightness in the same field (FITC) that enables BE visible. Further confirmation of CuAAC reaction by TAMRA-N_3 (Cu^+) and TAMRA-N_3 inks are given in Figure 3- 47.

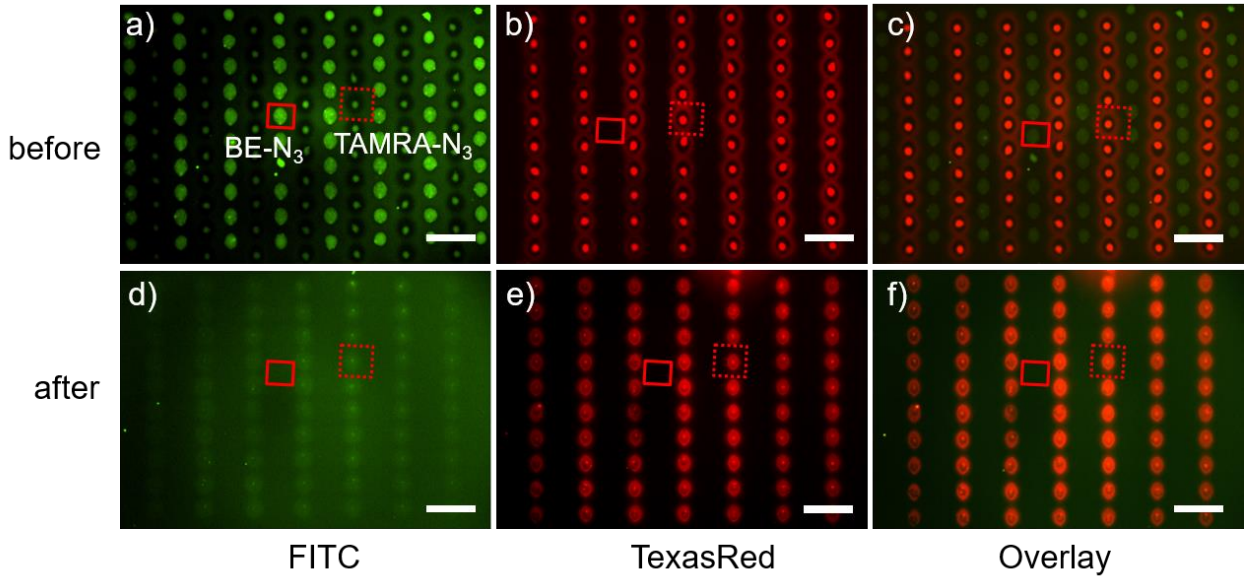

Figure 3- 45 Micropatterning of guest BE-N_3 on SiO_2-Alk surface, TAMRA-N_3 as a reference, mixed with Cu^+ catalyst. Figures before washing a) in FITC, b) in TexasRed and c) overlay. Figures after washing d) in FITC, e) TexasRed and f) overlay. Scale bars equal to 100 µm. 3 s exposure in FITC, 80 ms exposure in TexasRed.

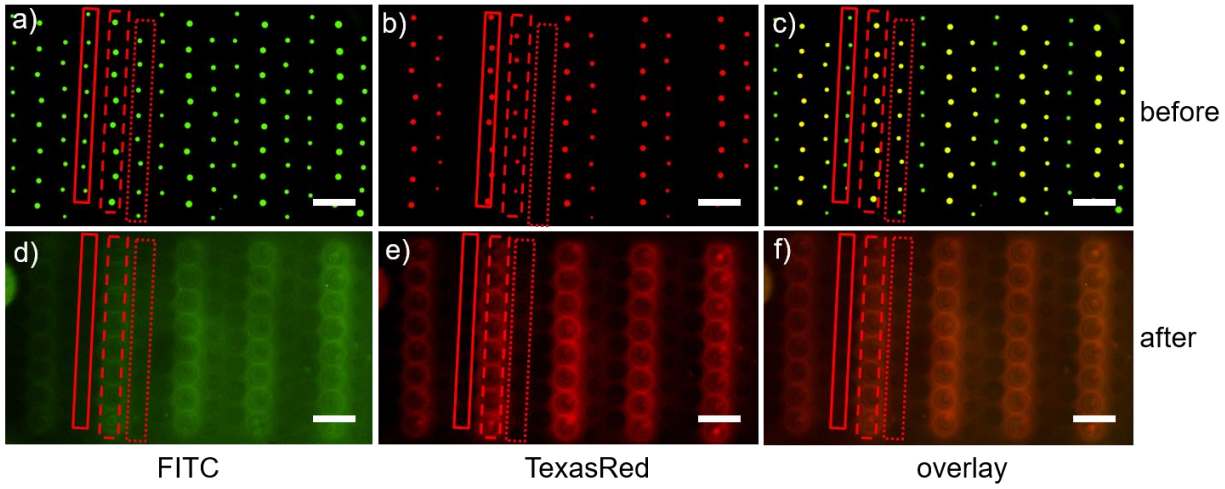

Figure 3- 46 Micropatterning of BE-N_3 (Cu^+) and TAMRA-N_3 (Cu^+) and BE-N_3 on SiO_2-Alk surface. Figures before washing in a) FITC b) TexasRed and c) overlay. Figures after washing d) FITC e) TexasRed and f) overlay. Scale bars equal to 100 µm. FITC 3 s, TexasRed 200 ms.

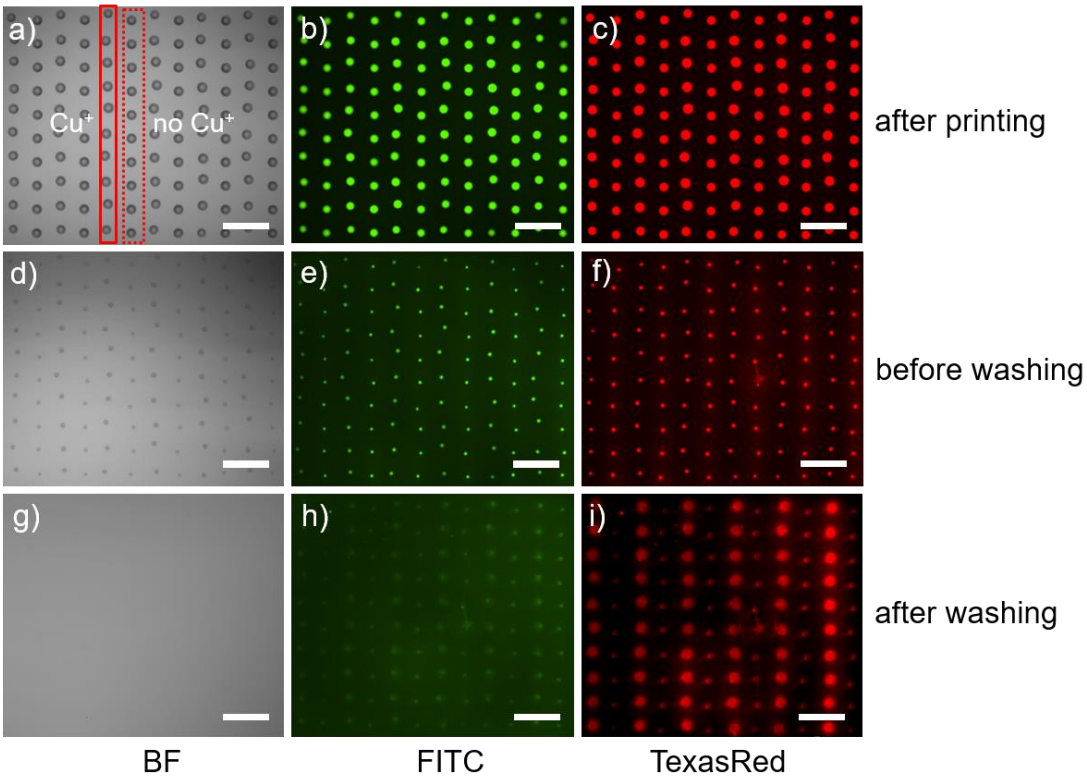

Figure 3- 47 Confirmation of azide-alkyne cycloaddition by micropatterning of TAMRA-N_3(Cu^+) and TAMRA-N_3 on SiO_2-Alk surface. Figures after printing in a) BF, b) FITC and c) TexasRed. Figures before washing in d) BF, e) FITC and f) TexasRed. Figures after washing in g) BF, h) FITC and i) TexasRed. Scale bars equal to 100 µm. BF 4 ms, FITC 3 s, TexasRed 200 ms.

In order to realize the concept, BE-N_3 was printed beside BE-N_3 (Cu^+) columns as a control (Figure 3- 48). After washing, the unspecific adsorption of BE-N_3 on the surface could be a reference as it has the same fluorescence brightness (Figure 3- 48b). The generated microarray was then incubated in a CB7 solution for 2 h to obtain CB7/BE chemosensor, proven by the increased brightness in Figure 3- 48c. After further incubation with an analyte Ama solution, the fluorescence decreases bringing an intensity loss shown in the graph.

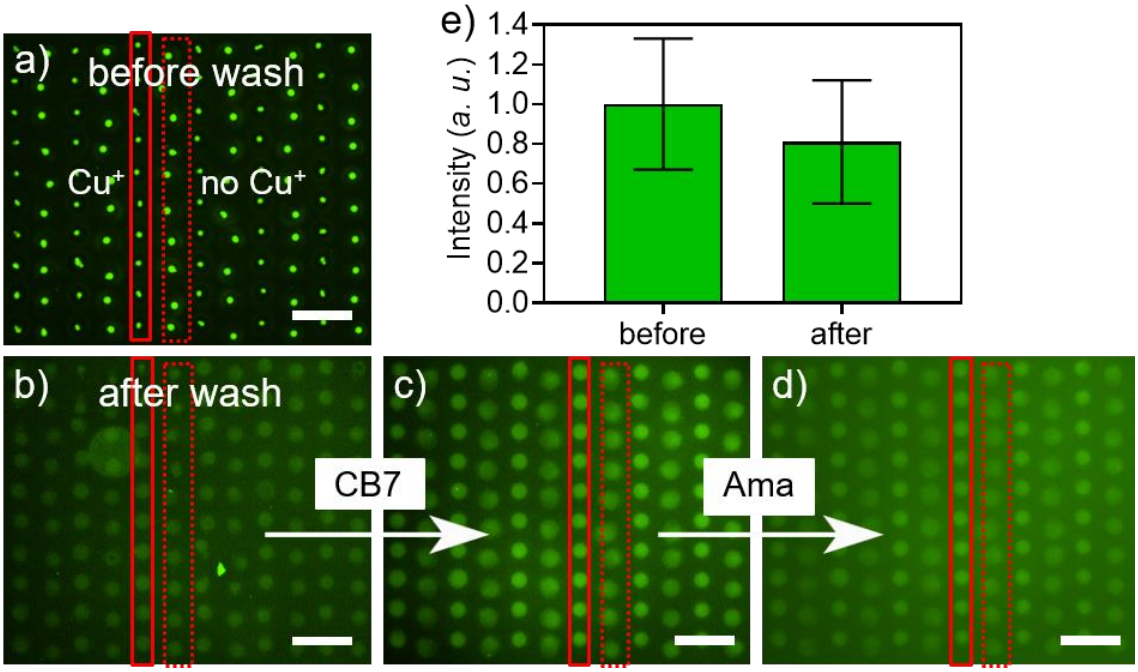

Figure 3- 48 Micropatterning of BE-N_3 (Cu^+) and BE-N_3 on SiO_2-Alk surface. a) Before washing b) after washing, c) after 10 mM CB7 incubation for 2 h and d) after 10 mM Ama incubation for 2 h. Scale bars equal to 100 µm. FITC 2 s.

3.2.2.3. CB7/PEP-N_3

CB7/PEP-N_3 was firstly printed on the SiO_2-Alk surface with a reference of AlexaFluor488-N_3 to have both dyes visible in the same filter channel (FITC) and washed by water and ethanol (Figure 3- 49). Then the substrate was incubated with CB7 as the previous CB7 might have been washed away. However, the columns printed with CB7/PEP-N_3 do not show an obvious change in brightness compared to the AlexaFluor488-N_3 after CB7 incubation. Same as previously, the reason may be the too strong AlexaFluor488 brightness that makes the slight change invisible. Therefore, to reduce brightness of the reference columns AlexaFluor488-N_3 ink was 20 times diluted by PEG8-N_3 and printed again (Figure 3- 50) but its brightness is still too high.

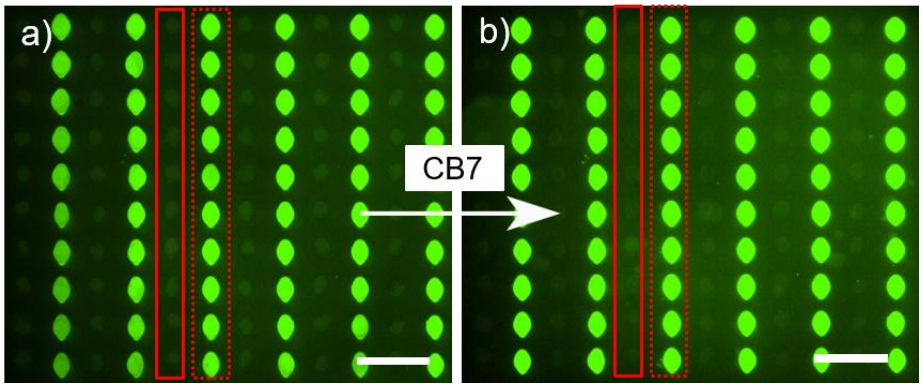

Figure 3- 49 Micropatterning of CB7/PEP-N_3 (Cu^+) and AlexaFluor-N_3 (Cu^+) on SiO_2-Alk surface. a) After washing, and b) after 10 mM CB7 incubation for 2 h. Scale bars equel to 100 µm. FITC 2s.

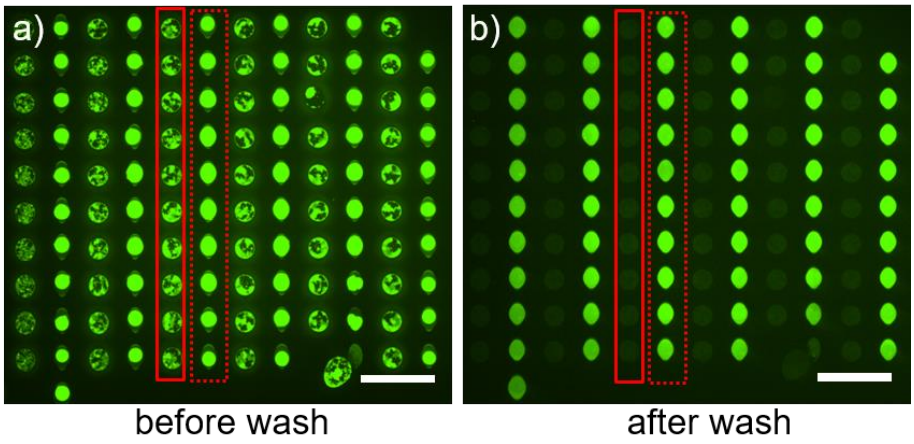

Figure 3- 50 Micropatterning of CB7/PEP-N_3 (Cu^+) and AlexaFluor-N_3 (diluted with 20 times PEG8-N_3, Cu^+) on SiO_2-Alk surface. a) Before washing and b) after washing. Scale bars equel to 100 µm. FITC 1s.

3.2.2.4. PEP-N_3

PEP-N_3 was then printed on the SiO_2-Alk surface with and without catalyst Cu^+ (two samples given in Figure 3- 51). After washing, the microarray columns with covalently bound PEP in the solid frame are brighter than that through unspecific adsorption in the dotted box. A further enhanced brightness after incubation of CB7 is due to the assembly between PEP and CB7, and then the formation of CB7/PEP chemosensor microarray. The decreased fluorescence signal after Ama incubation thanks to the replacement of PEP in CB7 by Ama and taking away CB7 from the surface. However, the unspecifically adsorbed PEP in the negative control could be washed away step by step and this should be avoided in sensing systems.

PEP-N_3 was also printed on the SiO_2-DBCO surface (Figure 3- 52). However, after washing, additional “comet tails” features appeared at the spots, which indicates a rapid click reaction during washing (enabled by the sensitivity of DBCO for click reaction), in the moment before the excess ink is diluted in the washing process.

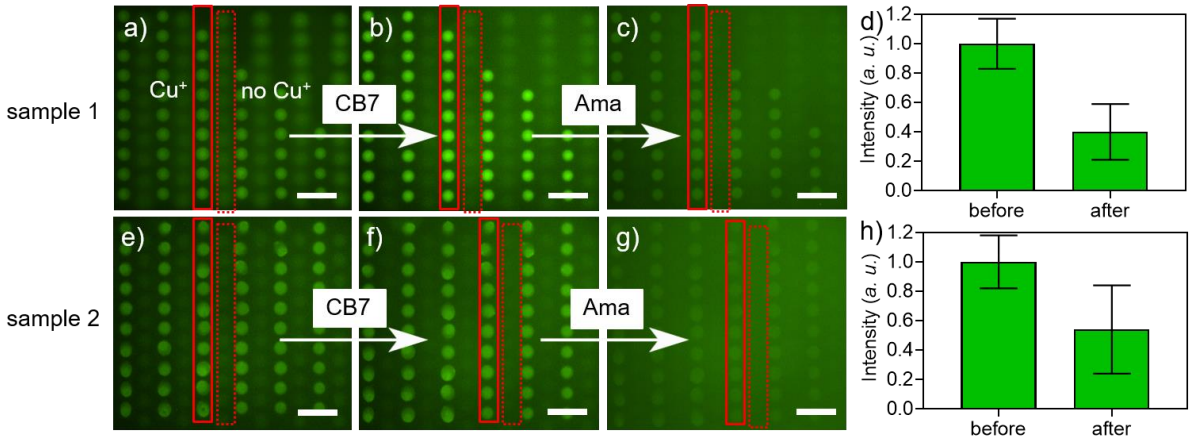

Figure 3- 51 Micropatterning of PEP-N_3 (Cu^+) and PEP-N_3 on SiO_2-Alk surface. a) Before CB7 incubation, b) after 10 mM CB7 incubation for 2 h and c) after 10 mM Ama incubation for 2 h. Scale bars equal to 100 µm. FITC 2 s.

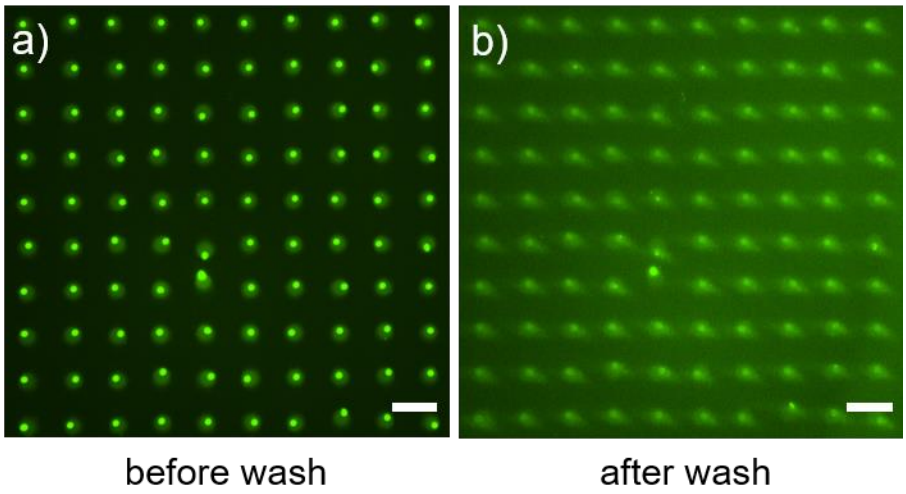

Figure 3- 52 Micropatterning of PEP-N_3 on SiO_2-DBCO surface. a) Before washing and b) after washing. Scale bars equel to 50 µm. FITC 2 s.

3.2.2.5. PCP-N_3

PCP-N_3 was printed on the SiO_2-Alk surface with and without catalyst Cu^+ (Figure 3- 53). Before washing, spots of PCP-N_3 (Cu^+) are weaker than PCP-N_3. After washing, the area

printed PCP-N_3 (Cu^+) is invisible but PCP-N_3 spots area is visible due to the dark shadow in FITC and DAPI channels. After CB8 incubation, both areas become slightly blue because of the assembly between CB8 and PCP. However, the unspecific adsorption is strong with a brighter fluorescence in the spots of PCP-N_3.

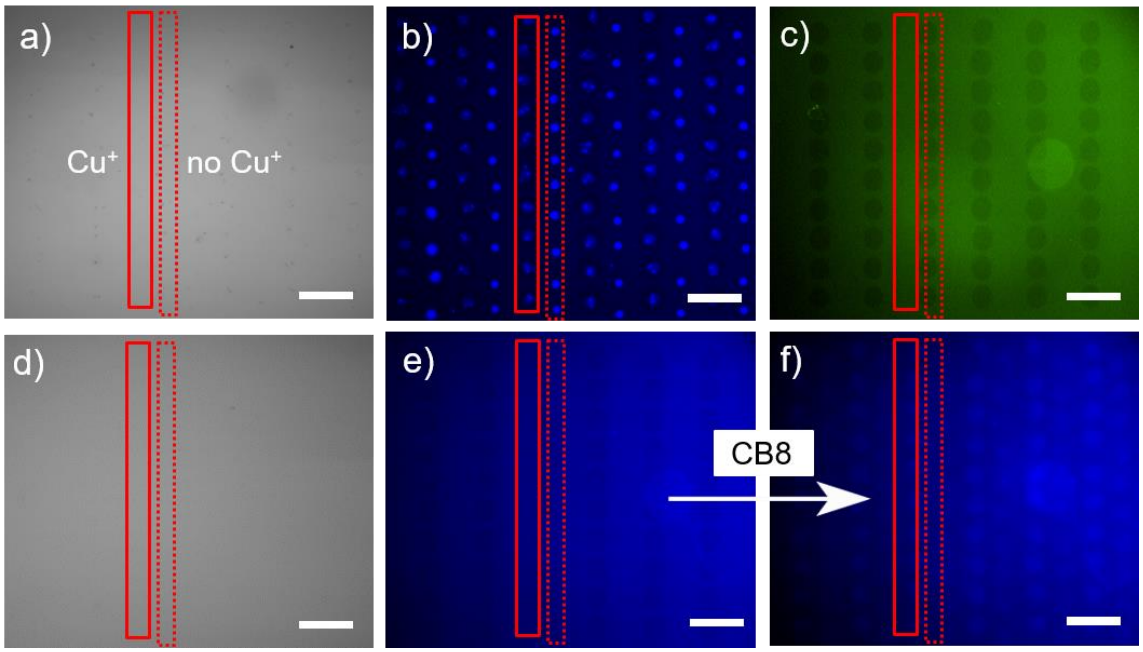

Figure 3- 53 Micropatterning of PCP-N_3 (Cu^+) and PCP-N_3 on SiO_2-Alk surface. Figures before washing in a) BF and b) DAPI. Figures after washing in c) FITC, d) BF and e) DAPI. f) Figure after 100 µm CB8 incubatioin in DAPI. Scale bars equel to 100 µm. BF 4 ms, FITC 3 s, DAPI 4 s.

3.2.2.6. HS-DAP-SH

The micropatterning of HS-DAP-SH on SiO_2-DBCO surface is shown in Figure 3- 54. HS-DAP-SH pattern is visible in DAPI, FITC and TexasRed channels. However, the microarray has vague shadows after harsh washing, which means the unspecific adsorption of HS-DAP-SH and should be avoided in the establishment of any sensing systems.

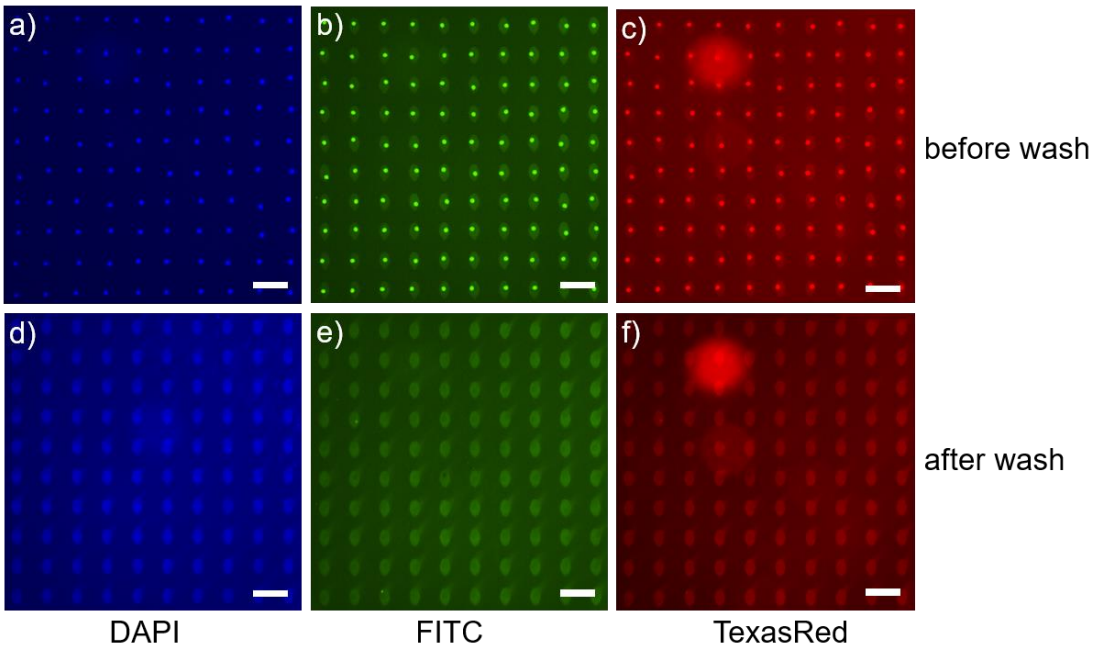

Figure 3- 54 Micropatterning of HS-DAP-SH on SiO_2-DBCO surface. Figures before washing in a) DAPI, b) FITC and c) TexasRed. Figures after washing in d) DAPI, e) FITC and f) TexasRed. Scale bars equel to 50 µm. 2 s of exposure time.

3.2.3. Summary of guest-mediated CBn systems

In this subchapter, SiO_2-Alk and SiO_2-DBCO have been prepared for CBn immobilization through alkyne-azide or thiol-DBCO reaction. The micropatterning of functionalized guest azides, BE-N_3, PEP-N_3 and PCP-N_3 on SiO_2-Alk with a negative printing control makes the microarrays visible and comparable after incubation of CBn and analyte. However, the unspecific adsorption of controls could be washed away step by step and this should be avoided in sensing systems. The printing of guest thiols on SiO_2-DBCO did not work well in terms of array fidelity due to the too sensitive click reaction that causes trailing around spots.

3.3. Rotaxane microarray

The results presented in this chapter has been submitted to *Nature Communication*.

In the above subchapters, either the indicator can be more or less washed away during incubation of solutions on CBn immobilized chemosensor microarrays, or it is difficult to obtain the signal readout from on/off CBn loading and there is always inevitable unspecific

The results presented in this chapter are a basis for a submitted paper.

adsorption in guest-mediated CBn microarray. Thus, neither the covalent nor guest-mediated CBn immobilization is ideal for CBn/indicator microarrays. To solve this shortcoming, an isocyanate surface (SiO_2-NCO) was prepared for micropatterning of CB8/DAP rotaxane, with two β-cyclodextrin (CD) as stoppers on two sides to lock CB8/DAP from disassembly. The hydrophilic β-CD can avoid the unspecific adsorption of DAP indicator and increase the readout signal. The generated rotaxane microarray was evaluated through the detection of L-Trp, indole, Mem, Pen, IAA, H-IAA and insulin.

3.3.1. Surface modification

A clean plasma-activated surface was modified with isocyanate after incubation of 4,4′-diisocyanato-methylenedibenzene (MDI) catalysed by dibutyltin dilaurate (TDL), the unreacted isocyanate group exposed on the surface is for rotaxane immobilization by reacting with the hydroxyl of β-CD mixed with TDL too (Figure 3- 55). The structure of rotaxane is shown in Figure 3- 56.

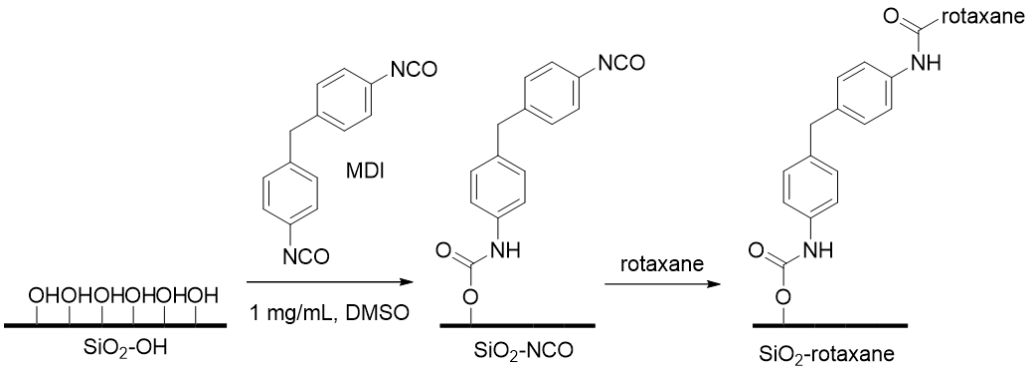

Figure 3- 55 Scheme of surface modification with isocyanate group and rotaxane.

The results presented in this chapter are a basis for a submitted paper.

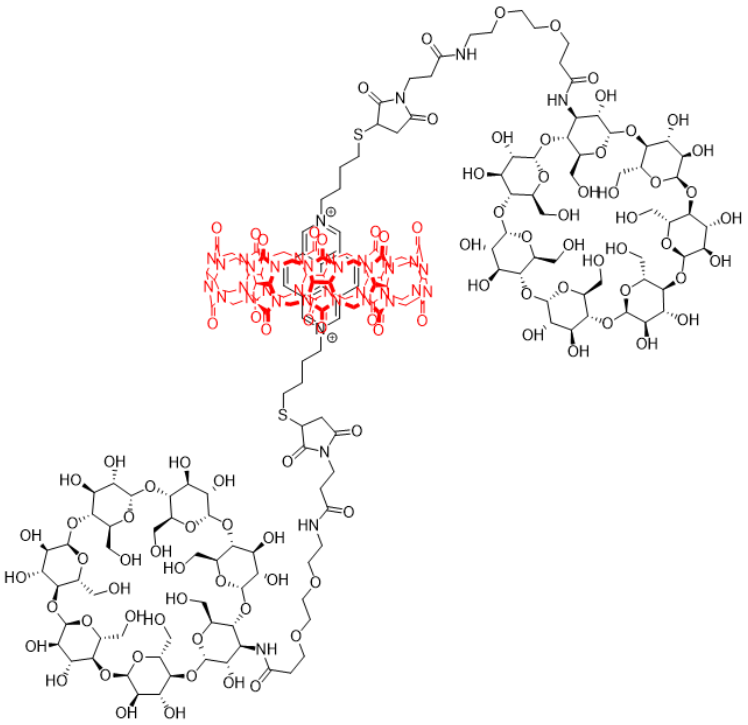

Figure 3- 56 Structure of rotaxane, CB8 marked in red.

The homogenous surface modification was proved by contact angle measurement shown in Figure 3- 57, Figure 3- 58, and Table 3- 16. The contact angle of water droplets on a clean glass (SiO_2) is 32.40 ± 2.17° and it decreases to 3.85 ± 0.61° after plasma activation due to the hydrophilicity from the hydroxyls. SiO_2-NCO has a higher angle of 76.87 ± 6.72° because of the more hydrophobic methylenedibenzene structure. Due to the hydroxyls of β-CD in the rotaxane, the contact angle of SiO_2-rotaxane surface decreases back 30.16 ± 1.71°. The above results demonstrate the successful modification of isocyanate and rotaxane.

The results presented in this chapter are a basis for a submitted paper.

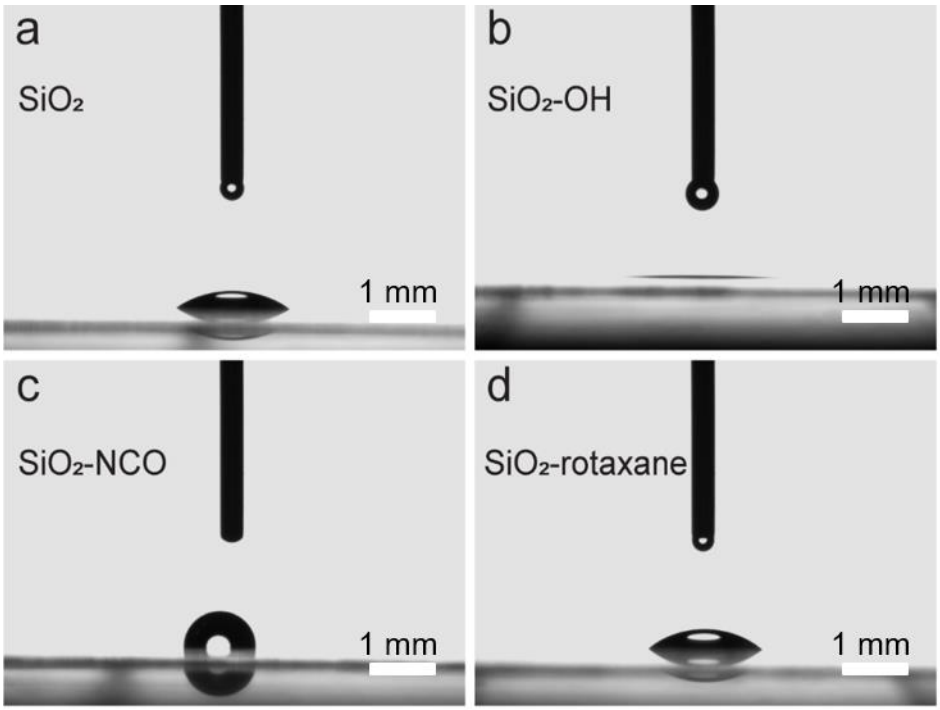

Figure 3- 57 Images of contact angles a) SiO_2, b) SiO_2-OH, c) SiO_2-NCO and d) SiO_2-rotaxane.

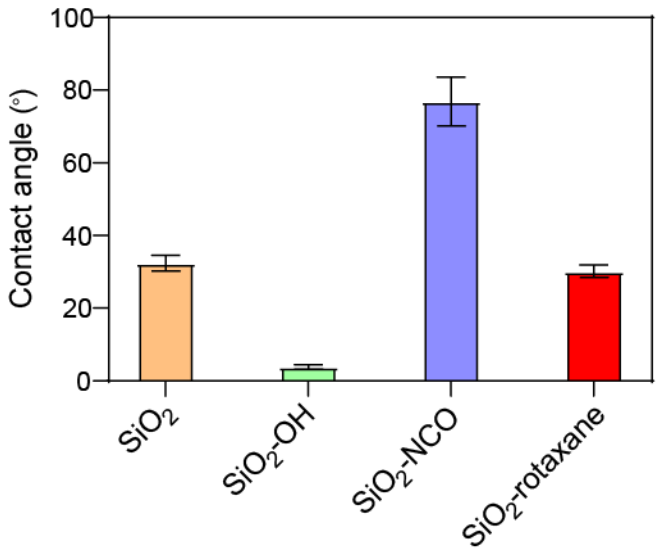

Figure 3- 58 Bargraph of contact angles of SiO_2, SiO_2-OH, SiO_2-NCO and SiO_2-rotaxane.

Table 3- 16 Static contact angles of water droplets on the bare and functionalized glass surfaces.

sample	SiO_2	SiO_2-OH	SiO_2-NCO	SiO_2-rotaxane
Angle (°)	32.40 ± 2.17	3.85 ± 0.61	76.87 ± 6.72	30.16 ± 1.71

The results presented in this chapter are a basis for a submitted paper.

3.3.2. Rotaxane micropatterning

In order to establish a both CBn and indicator immobilized chemosensor microarray, the rotaxane was further micropatterned on the SiO_2-NCO surface through µCS, images are shown in Figure 3- 59. The rotaxane spots are visible in bright field and in DAPI filter before washing with water and ethanol. After washing, only in the fluorescence the rotaxane microarray can been seen, coated homogenously within the patterned spots (see the inset enlarged image). The comparison of rotaxane patterning with and without TDL catalysts in Figure 3- 60 shows only low unspecific adsorption of rotaxane.

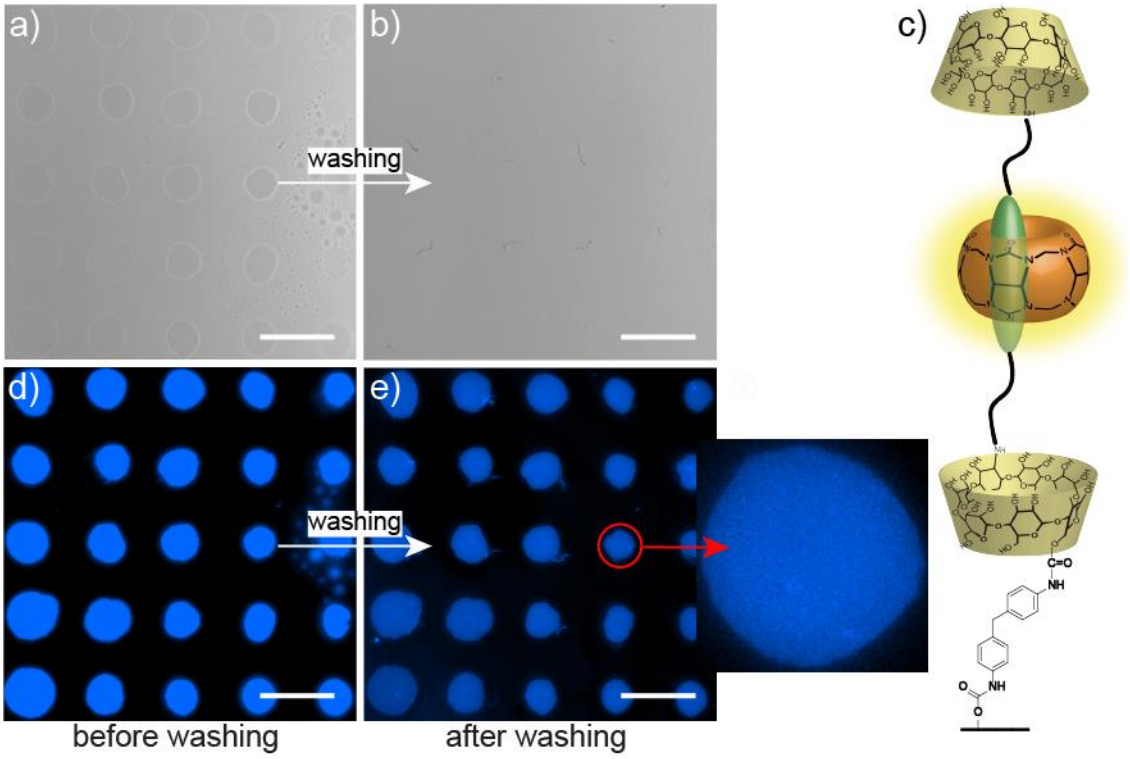

Figure 3- 59 Micropatterning of rotaxane on SiO_2-NCO surface. Figures of a) before washing with water and ethanol, b) after washing in bright field. c) Scheme of rotaxane microarray. Figures of d) before washing with water and ethanol, e) after washing in dark field, DAPI channel, 10 s of exposure. The inset shows the homogenous immobilization of rotaxane by µCS.

The results presented in this chapter are a basis for a submitted paper.

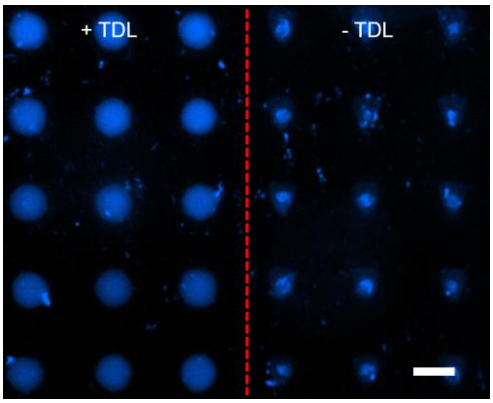

Figure 3- 60 Comparison of rotaxane immobilization with TDL catalyst (left) and without TDL (right).

3.3.3. Analyte detection

The analytes used for sensing evaluation of rotaxane microarray are listed in Figure 3- 61. Not only small non-chromophoric analytes, L-tryptophan (L-Trp), indole, memantine (Mem), penicillin (Pen), indole acetic acid (IAA) and hydroxyl indole acetic acid (H-IAA) but also macromolecule e.g. insulin are detected by rotaxane microarray.

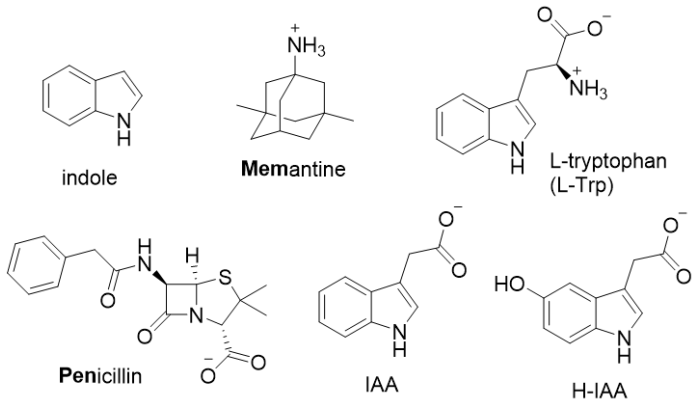

Figure 3- 61 Analyte structures.

3.3.3.1. Sensitivity evaluation of rotaxane microarray

The sensitivity of the rotaxane microarrays for sensing analyte was examined through the L-Trp incubation at varying concentrations. fluorescence images and the fluorescence intensity of the microarrays before and after the incubation with the corresponding L-Trp are shown in Figure 3- 62. It is possible to detect L-Trp concentrations down to 10^{-8} M which is indicated by the significant fluorescence loss of the rotaxane microarray after the

The results presented in this chapter are a basis for a submitted paper.

incubation with 10^{-8} M compared to the control with PBS. However, a concentration of 10^{-9} M of L-tryptophan seems to be no longer discernible from pure PBS with both exhibiting minor decrease of fluorescence.

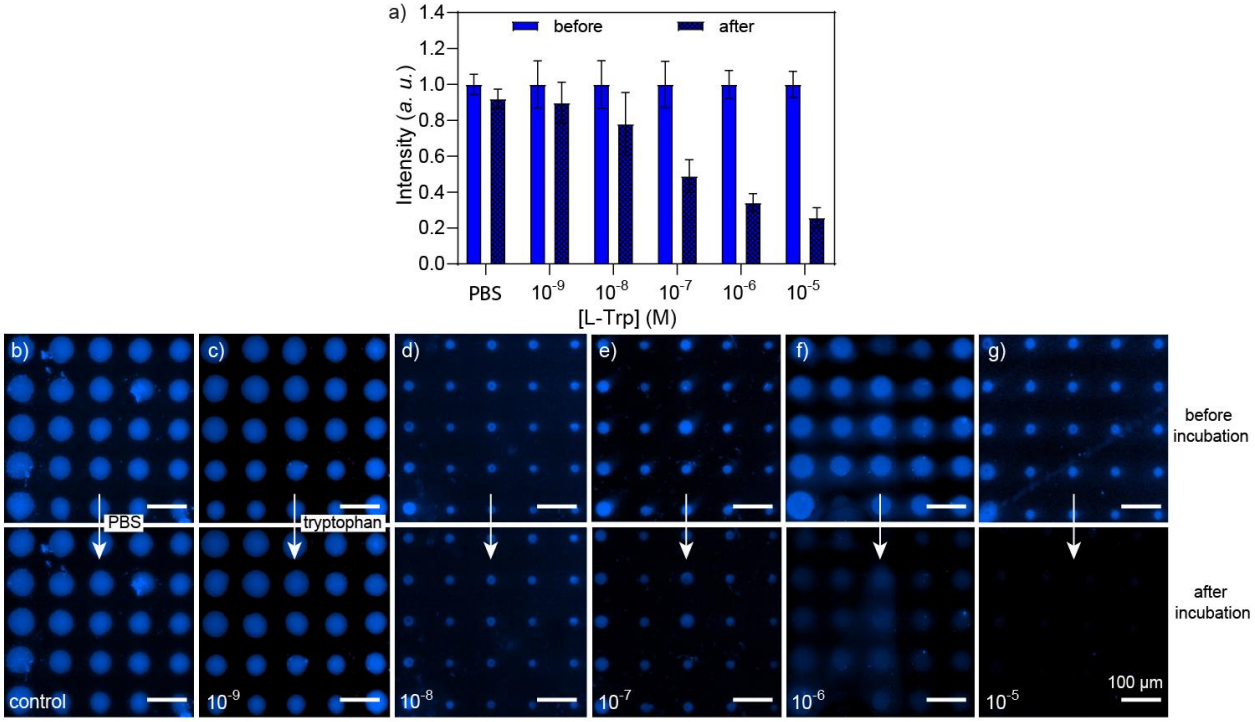

Figure 3- 62 L-Trp detection at different concentrations on rotaxane microarrays. a) Quantification of the fluorescence intensities of the rotaxane microarray spots before and after the incubation with L-Trp solutions of different concentrations and with PBS as control. b)-g) Fluorescence images of the rotaxane microarrays before and after the incubation with L-Trp solutions of various concentrations. Images were taken with 10 s exposure time and a DAPI filter. Scale bars equal to 100 µm.

Table 3- 17 Fluorescent intensities of rotaxane microarray for L-Trp detection at varying concentrations.

Intensity (*a. u.*)	control	L-Trp				
concentration (M)	PBS	10^{-9}	10^{-8}	10^{-7}	10^{-6}	10^{-5}
before	1.00 ± 0.06	1.00 ± 0.13	1.00 ± 0.13	1.00 ± 0.13	1.00 ± 0.08	1.00 ± 0.07
after	0.92 ± 0.05	0.90 ± 0.11	0.78 ± 0.18	0.49 ± 0.09	0.34 ± 0.05	0.26 ± 0.06

3.3.3.2. Comparison of rotaxane and CB8/MDAP microarrays

The results presented in this chapter are a basis for a submitted paper.

Since the DAP indicator of the rotaxane can not be replaced by any analyte as it is locked by β-CD, it is essential to compare it with the CB8/MDAP microarray, in which the indicator can be replaced, mentioned in subchapter 3.1. Therefore, a CB8/MDAP chemosensor microarray is used as a control [17] for Mem detection. The response of the rotaxane and the CB8/MDAP microarrays towards the presence of indole and Mem is shown in Figure 3- 64. The incubation of the rotaxane array with pure HEPES buffer as a negative control shows no significant decrease in fluorescence. As expected, the decreased fluorescence intensity of rotaxane from the incubation with indole demonstrates that indole binds to the immobilized rotaxane and thereby quenches the emission of the DAP indicator. In contrast, the incubation of the rotaxane microarray with Mem, an analyte that has a higher binding affinity towards CB8 than DAP, shows only an insignificant emission change, which indicates that the analyte is not bound due to the lack of space for Mem in the CB8 cavity. In contrast, the CB8/MDAP microarray shows an almost 100% emission quenching upon incubation with Mem, which indicates that the MDAP dye is displaced by the bigger and stronger binding analyte Mem.[17]

The results presented in this chapter are a basis for a submitted paper.

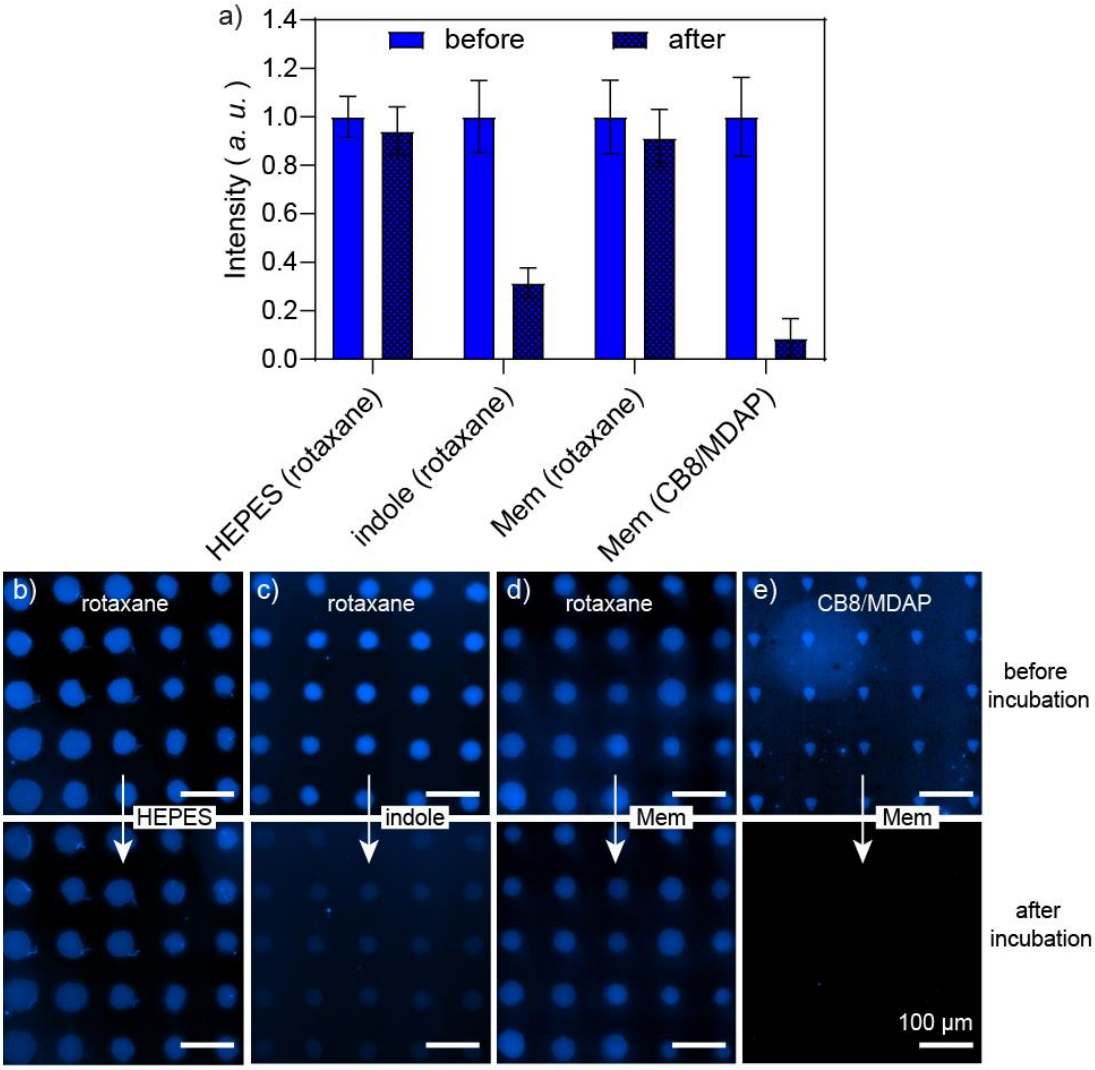

Figure 3- 63 Detection of indole and Mem with rotaxane and CB8/MDAP microarrays. a) Quantification of the fluorescence intensities of the microarray spots before and after the indole and Mem incubation. b)-e) Fluorescence images of the microarrays before and after incubation with an analyte (10 µM) or pure HEPES as control. Images were taken with 10 s exposure time and DAPI filter. Scale bars equal 100 µm.

Table 3- 18 Fluorescence intensities of rotaxane or CB8/MDAP microarrays in the absence and presence of indole and Mem.

Intensity (*a. u.*)	control	indole	Mem (CB8-MDAP chemosenaor)	Mem
before	1.00 ± 0.08	1.00 ± 0.15	1.00 ± 0.16	1.00 ± 0.15
after	0.94 ± 0.10	0.31 ± 0.06	0.09 ± 0.08	0.91 ± 0.12

The results presented in this chapter are a basis for a submitted paper.

3.3.3.3. Small analyte and protein detection

In order to expand the sensing application of rotaxane microarray, more analytes including Pen, IAA, H-IAA and a protein (insulin) are detected shown in Figure 3- 64 and Table 3-19. Incubation of Pen, IAA and H-IAA generates a large fluorescence loss compared to the HEPES control. However, the incubation of insulin causes smaller fluorescence loss, which may be due to the large size of protein having a space effect that makes the detective part in insulin as a guest harder to assembly with rotaxane.

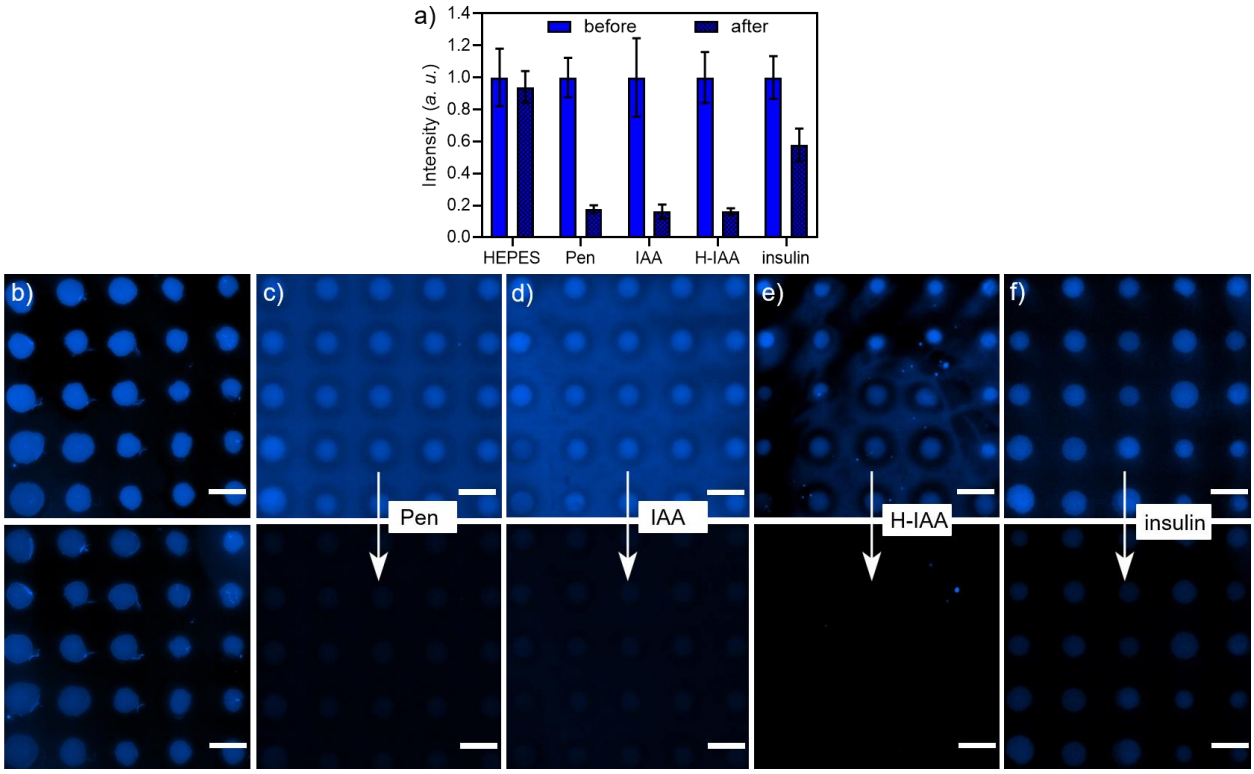

Figure 3- 64 Detection of Pen, IAA, H-IAA and insulin by rotaxane microarray. a) Quantification of the fluorescence intensities of the microarray spots before and after analyte incubation. Fluorescence images of the rotaxane microarray before and after incubation of b) HEPES buffer, 10 μM c) Pen, d) IAA, e) H-IAA and f) insulin in 10 mM HEPES. Images were taken with 10 s exposure time, DAPI filter. Scale bars equal 100 μm.

Table 3- 19 Fluorescence intensities of rotaxane microarrays in the detection of Pen, IAA, H-IAA and insulin.

Intensity (*a. u.*)	control	Pen	IAA	H-IAA	insulin
before	1.00 ± 0.08	1.00 ± 0.12	1.00 ± 0.24	1.00 ± 0.16	1.00 ± 0.13
after	0.94 ± 0.10	0.18 ± 0.02	0.16 ± 0.04	0.16 ± 0.02	0.58 ± 0.10

The results presented in this chapter are a basis for a submitted paper.

3.3.3.4. Ratiometric microarray

In a ratiometric rotaxane microarray, DAP-thiol (without CB8) was printed beside as a reference column and the L-Trp detection on this ratiometric microarray is shown in Figure 3- 65 and Table 3- 20. After L-Trp incubation, the fluorescence intensity of the rotaxane sub-microarray quenches compared to the DAP column, according to the expected binding of L-Trp to the rotaxane, and thereby excluding the hypothetical dynamic quenching of the DAP fluorophore by L-Trp.

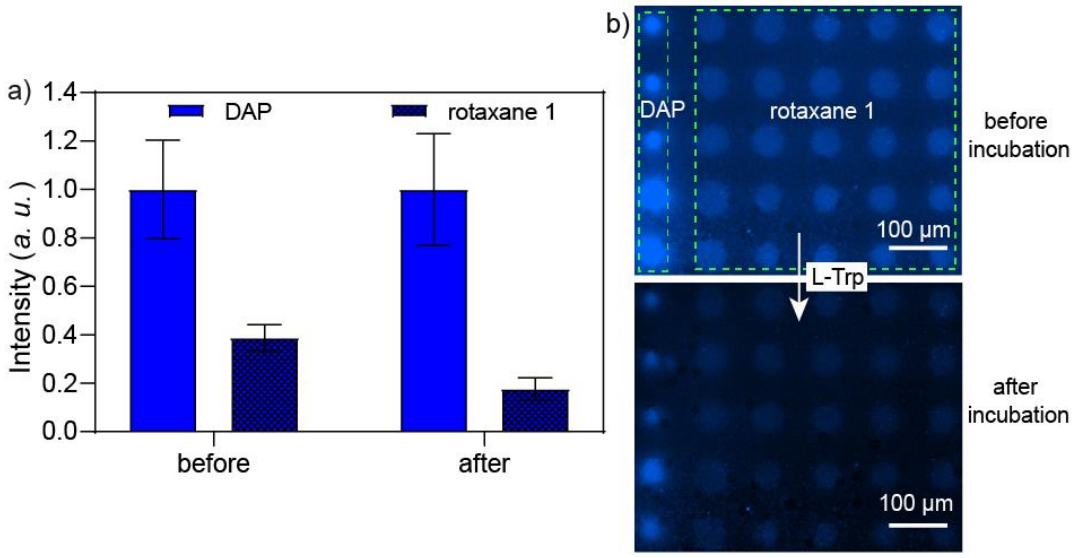

Figure 3- 65 L-Trp detection by ratiometric rotaxane microarrays with surface-bound DAP dye as reference. a) Quantification of the fluorescence intensities of the microarray spots before and after incubation with L-Trp solution (10 µM in 10 mM HEPES buffer). b) Fluorescence images of the ratiometric rotaxane microarray before and after incubation. Images were taken with 10 s exposure time, DAPI filter. Scale bars equal 100 µm.

Table 3- 20 Mean fluorescent intensities of the ratiometric rotaxane microarray and reference DAP spots for the L-Trp detection.

Intensity (*a. u.*)	DAP reference	rotaxane
before	1.00 ± 0.20	0.38 ± 0.05
after	1.00 ± 0.23	0.18 ± 0.05

3.3.4. Summary of rotaxane immobilization

The results presented in this chapter are a basis for a submitted paper.

The inherent functional groups of rotaxane provide a synthetic handle for immobilization on functionalized glass surfaces and the establishment of rotaxane microarray. Therefore, an isocyanate-functionalized (SiO_2-NCO) glass substrate was prepared and the rotaxane was μCS micropatterned on SiO_2-NCO through the reaction between the HO-groups of the β-CD stopper and isocyanate. The fabricated rotaxane microarray allows for Trp detection down to submicromolar concentrations which shows the remarkable sensitivity enhancement. Importantly, the rotaxane-functionalized microarrays are more selective than printed microarrays with the binary CB8/MDAP chemosensor complex, proved by the detection of a hydrophobic and strongly CB8-binding guest Mem. Mem is not an electron-rich aromatic compound and thus cannot bind next to the rotaxane-protected reporter dye DAP. Furthermore, the μCS immobilization also allows for printing reference dyes next to the chemosensor array to normalize the emission signal. The immobilization of CB8/indicator complex through the form of rotaxane on surfaces opens up its potential for the future integration into lab-on-a-chip designs with plasmonic biosensors.

The results presented in this chapter are a basis for a submitted paper.

3.4. Biomimetic lipid membrane

In the above chapters, CBn/indicator-based chemosensors have been immobilized on the surface and the IDA/AGA analyte detection of the generated chemosensor microarrays were evaluated in a dry/wet state through small molecules from bioliquids. Rea-time monitoring in the microfluidic channel is much closed to the cell environment. Supported lipid bilayers (SLB) micropatterned by Dip-Pen Nanolithography (DPN), Polymer-Pen Lithography (PPL) and microchannel cantilever spotting (μCS) or a homogenously solvent-assisted (SALB) in the microfluidic channel are introduced to cover CBn/indicator chemosensor microarray and build up a biomimetic sensing system.

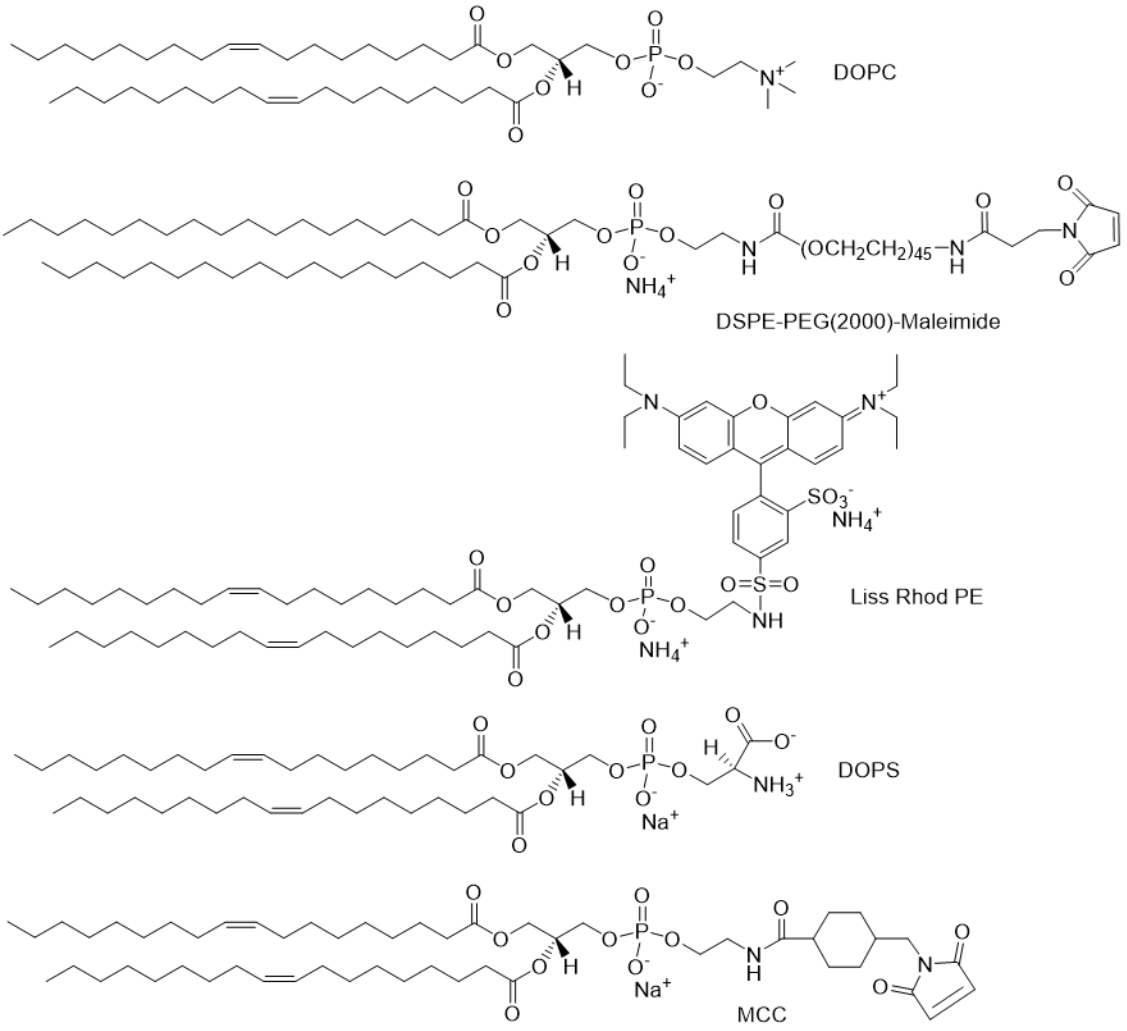

Figure 3- 66 Chemical structures of phospholipids used in this work.

3.4.1. Dip-Pen Nanolithography (DPN)-printed supported lipid bilayers (SLB)

Thanks to the surface tension of the nano-tip, lipid molecules can flow from the tip onto the surface through the water film around by increasing the humidity and then writing inks of structured lipid membranes. The substantial differences in the topologies depend on the nature of the surface, where the membrane assembles in water and air (Figure 3-67).[93] As a pre-test, 5 mol% of DSPE-PEG-Maleimide in DOPC was patterned on a clean glass in the humidity of 40% and 50% (Figure 3- 68). With less spreading of (a), the SLB in 40% seems better, thus this diameter was kept for all following SLB printed by DPN.

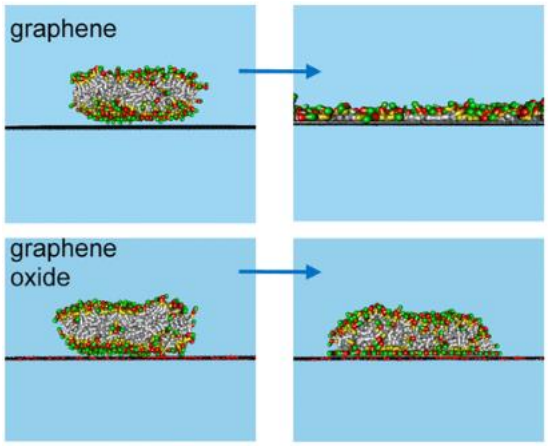

Figure 3- 67 Assembly of DPN-printed SLB on graphene and graphene oxide.

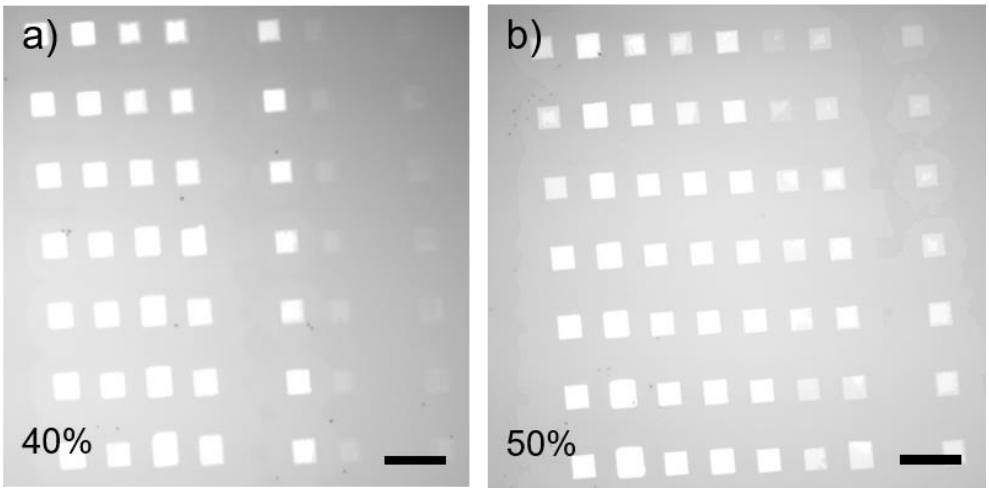

Figure 3- 68 DSPE-PEG-Maleimide (5 mol% in DOPC) microarray micropatterned in different humidity of a) 40% and b) 50%. Scale bars equal to 100 µm. BF 4 ms.

3.4.1.1. Lipid microarray for the establishment of CB7/indicator chemosensor

A second DSPE-PEG-Maleimide microarray was printed having Liss Rhod PE as a reference beside for positioning (Figure 3- 69). DSPE-PEG-Maleimide is visible in the

bright field but not fluorescent. To further establish a CBn based chemosensor, the generated microarray was incubated with HS-DAP-SH for 10 min able to link with the maleimide group. As shown in Figure 3- 70, the blue lipid pattern shows the immobilization of DAP indicator. However, the lipid structures spread a lot during incubation and are not stable enough for subsequent CBn and analyte incubation.

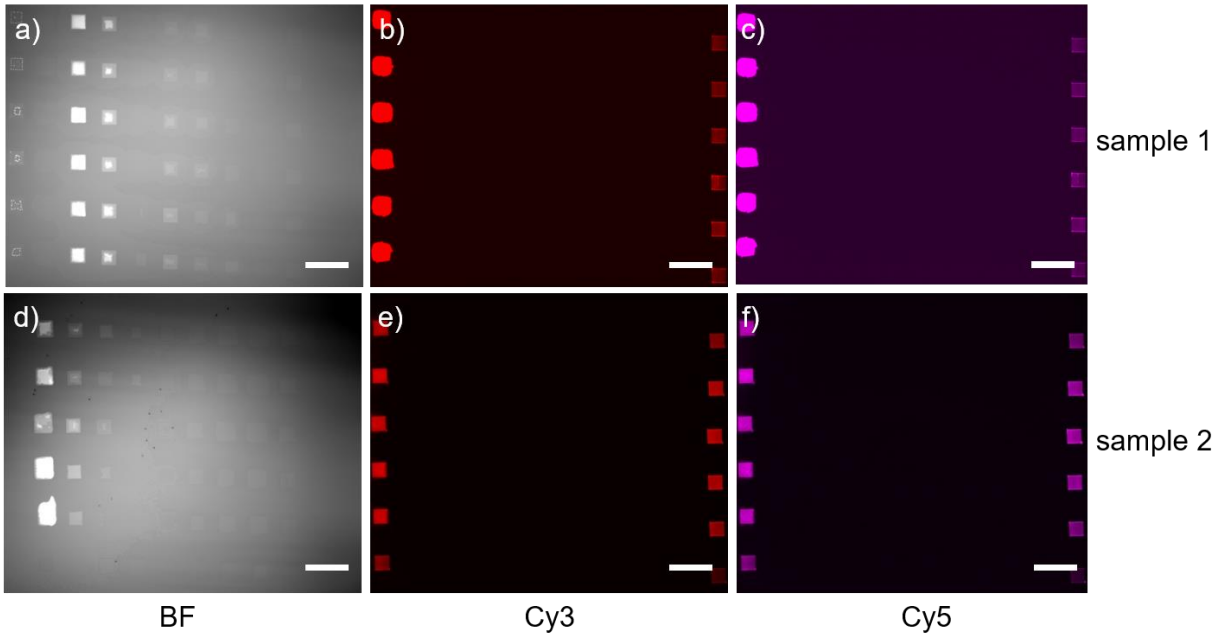

Figure 3- 69 DSPE-PEG-Maleimide (5 mol% in DOPC) microarray, Liss Rhod PE as a reference (0.5 mol% in DOPC). Sample 1 a) in BF, b) Cy3 and c) Cy5. Sample 2 d) in BF, e) Cy3 and f) Cy5. Scale bars equal to 100 µm. BF 4 ms, Cy3 30 ms, Cy5 1 s.

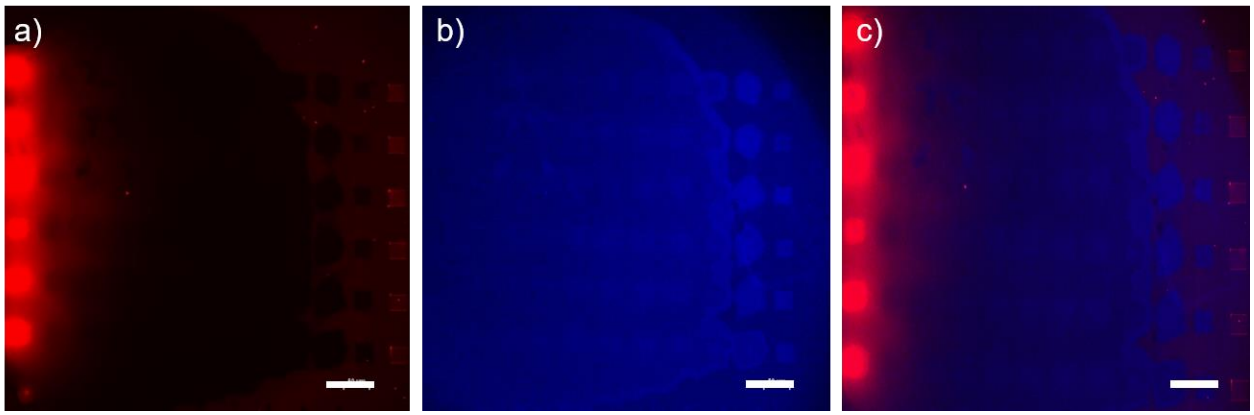

Figure 3- 70 DSPE-PEG-Maleimide (5 mol% in DOPC) microarray after 100µm HS-DAP-SH incubation for 10 min a) in Cy3, b) DAPI and c) overlay, Liss Rhod PE as a reference (0.5 mol% in DOPC). Scale bars equal to 100 µm. Cy3 1 s, DAPI 5 s.

3.4.1.2. CBn/indicator microarray covered with supported lipid bilayers (SLB)

CB immobilized CB7/BE microarray has been half-covered with a DOPS bilayer (Figure 3- 71). DPN can print lipid layers thin enough to be invisible in the bright field but still detective in fluorescence, and precisely printed on the desired position. The fluorescence of the covered part of the microarray is weaker. In order to evaluate the sensing property, a half DOPS-covered CB7/BE microarray was incubated with Ama for 1 min. There seem to be a sensing delay on the covered microarray with a slight resting fluorescence (Figure 3- 72). This delay is more obvious when CB7/MDAP microarray is half-covered with DOPS and incubated with Ama for 5 min (Figure 3- 73). However, the difference with/without lipid bilayers seems not stable, which may be because of the indicator leakage between the printed lipid lines.

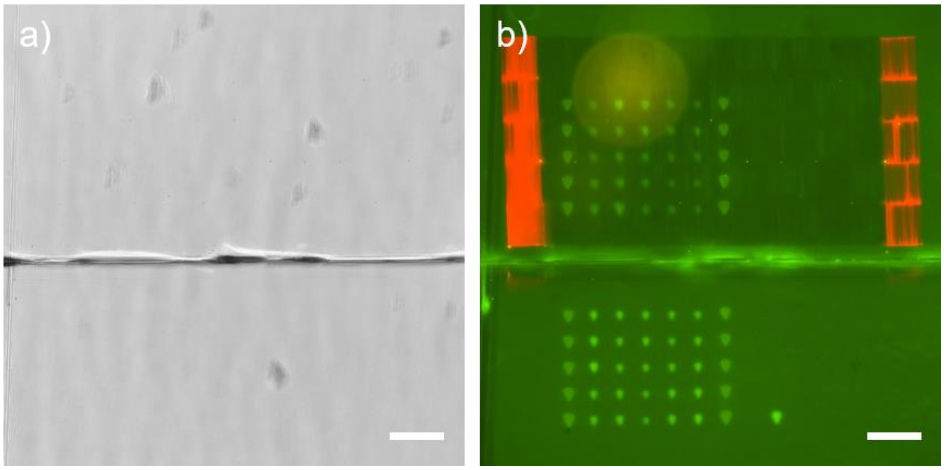

Figure 3- 71 CB7/BE microarrays, half covered with a DOPS layer (10 mol% in DOPC, 0.5 mol% Liss Rhod PE as reference) printed by DPN. Images in a) BF 500 ms, b) overlayed in GFP 10 s and Cy3 50 ms. Scale bars equal to 100 µm.

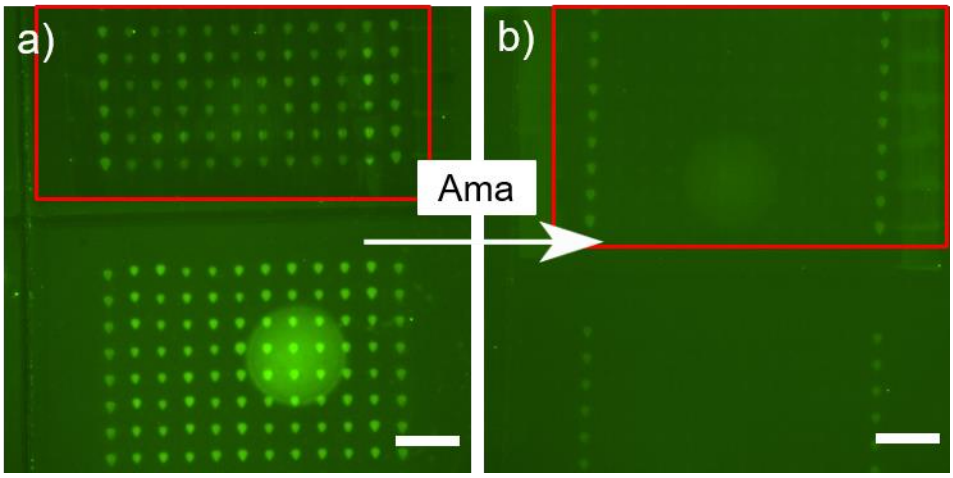

Figure 3- 72 CB7/BE microarray, half covered with a DOPS (10 mol% in DOPC) layer marked in the red box. a) Before and b) incubation of 10 µM Ama for 1 min, GFP 10 s. Scale bars equal to 100 µm.

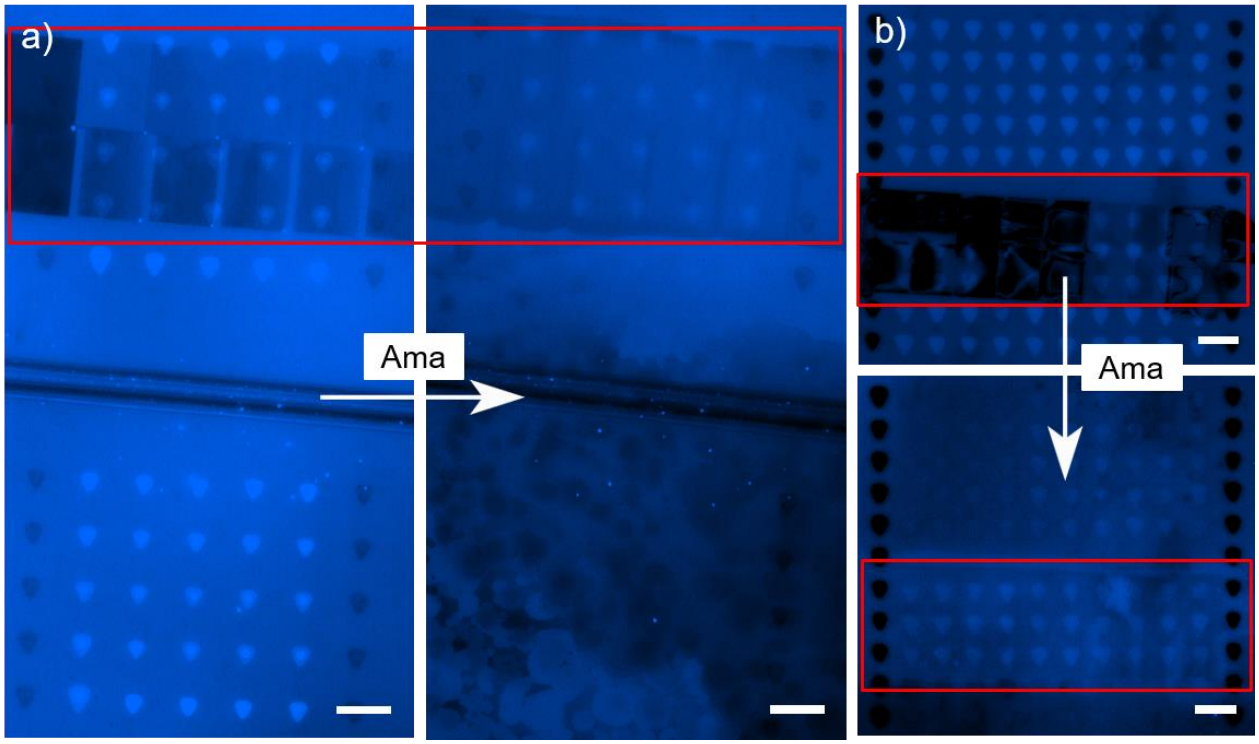

Figure 3- 73 CB7/MDAP microarray, half-covered with a DOPS (10 mol% in DOPC) layer marked in the red box. a) Before and incubation of 1 mM Ama for 5 min, DAPI 6 s. A repetition in b). Scale bars equal to 100 µm.

3.4.2. Polymer Pen Lithography (PPL)-printed supported lipid bilayers

DPN can micropattern lipid in a precise position but is time-consuming for patterning in large areas. Polymer Pen Lithography (PPL) with a side of polymer pens printing at the same time just solves this problem and the stamping mode might generate suitable lipid bilayers (Figure 3- 74). Therefore, PPL was used to print lipid bilayers on the top of CBn/indicator microarrays to explore the sensing delay due to the covering by lipid bilayers.

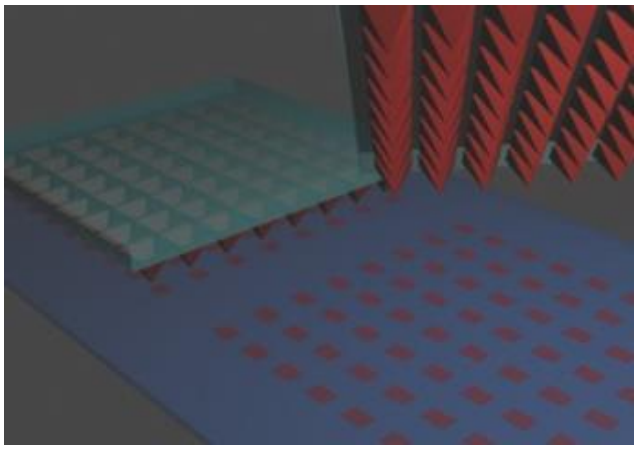

Figure 3- 74 Polymer Pen Lithography.

3.4.2.1. Non-linked chemosensor microarray covered with PPL-printed SLB

In order to confirm the stability of lipid bilayers printed by PPL, CB8/MDAP complex was firstly printed on a glass surface and then partially covered with a mixture of DOPS and Biotin PE (Figure 3- 75a). After Ama incubation, the substrate was immersed in a streptavidin-Cy3 (Strep-Cy3) solution for 30 min. The bright red squares in Figure 3- 75c demonstrate the still staying lipid bilayers. A half-covered substrate in Figure 3- 75d shows PPL can homogenously cover a specified area.

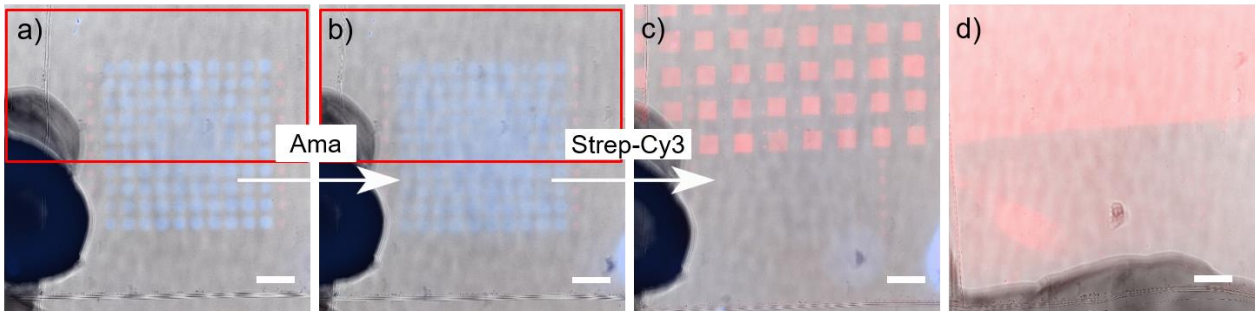

Figure 3- 75 Non-linked CB8/MDAP microarray printed on a plasma-activated glass, partially covered with a mixed layer of 10 mol% DOPS and 5 mol% Biotin PE in DOPC. Overlay of a) before 10 µM Ama incubation, b) after Ama incubation, c) after streptavidin-Cy3 incubation for 30 min

and d) a substrate half-covered with same lipid layer after incubation of streptavidin-Cy3. BF 500 ms, Cy3 500 ms, DAPI 6 s. Scale bars equal to 100 µm.

In order to further confirm if PPL-printed lipid layers store sensor on the surface, reported CB7-TEG-BE [94] was printed on a clean glass surface by µCS and then partially covered with DOTAP bilayers by PPL (Figure 3- 76). After HEPES incubation for 5 min, the covered sub-pattern in the red frame keeps bright fluorescence and no spreading observed compared to the bottom part spreaded and less fluorescent. After the incubation of Cad, the fluorescence decreases in both areas, which means the sensing of Cad.

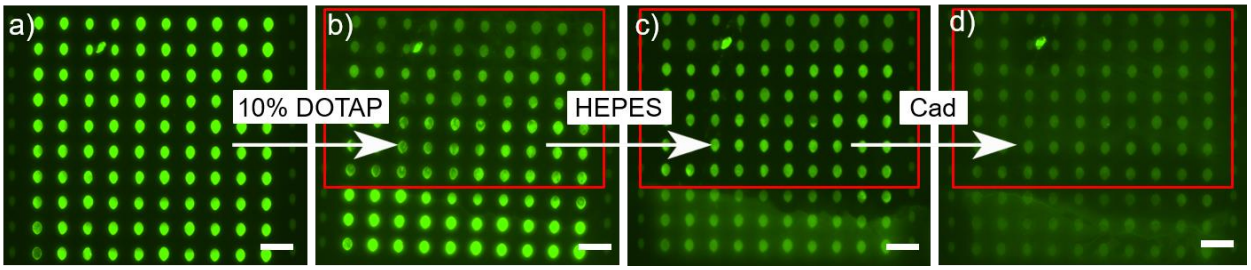

Figure 3- 76 a) CB7-TEG-BE microarray, b) half-covered with 10 mol% DOTAP in DOPC, c) after HEPES incubation for 5 min and d) after 10 µM Cad incubation for 1 min, GFP 6 s. Scale bars equal to 50 µm.

3.4.2.2. CB-linked chemosensor microarray covered with PPL-printed SLB

In order to check if PPL printed lipid layers can impact the sensing, a CB7/MDAP microarray was half-covered with DOPC by PPL and used for Ama sensing (Figure 3- 77). However, the remaining fluorescence in the covered or uncovered sensor seems not much different. The same phenomenon appears on DOPS-covered CB7/MDAP microarrays with incubation of 1-Adamantanol (Ad-OH) and Ama (Figure 3- 78). Therefore, the PPL-printed SLB might not be suitable for CBn/indicator microarrays.

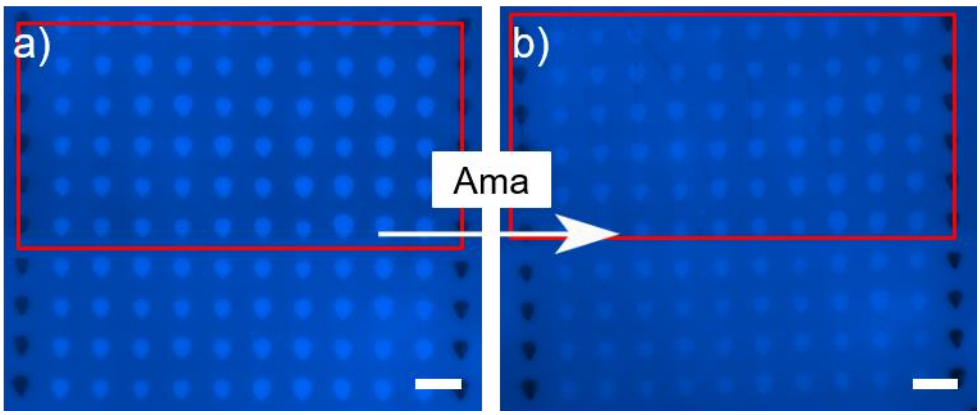

Figure 3- 77 CB7/MDAP microarray half-covered with DOPC layer, shown in the red frame, for Ama incubation, DAPI 8 s. Scale bars equal to 50 µm.

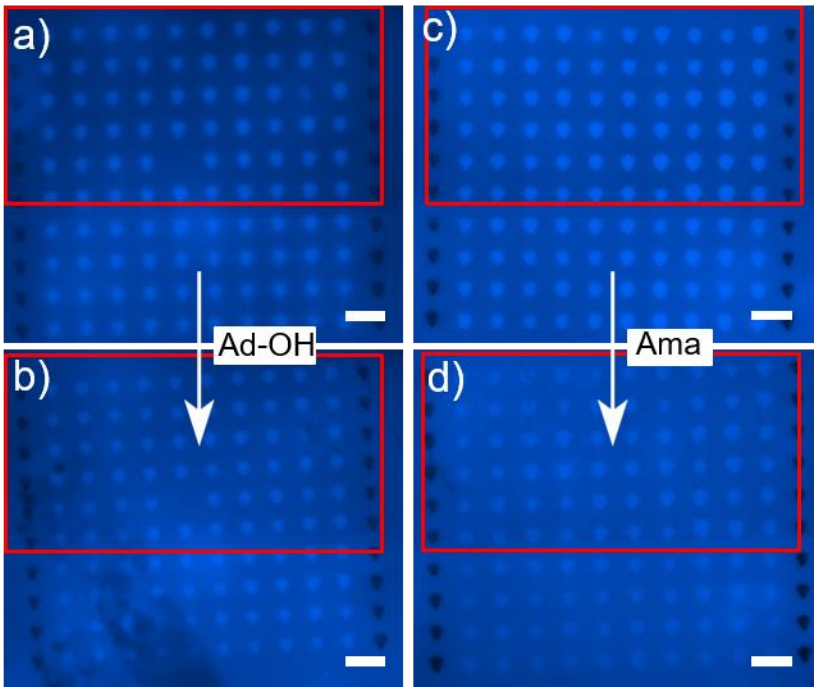

Figure 3- 78 CB7/MDAP microarrays, half-covered with 10 mol% DOPS in DOPC, for a) Ad-OH and b) Ama incubation, 10 s. Scale bars equal to 50 µm.

3.4.3. Microchannel cantilever spotting (µCS) printed SLB

After dissolving in ethanol, lipids can be printed on the exact desired spots by µCS and form supported lipid bilayers after getting dried (Figure 3- 79). So the generated SLB might be suitable for permeability imaging through the different quenching fluorescence compared with the covered chemosensors.

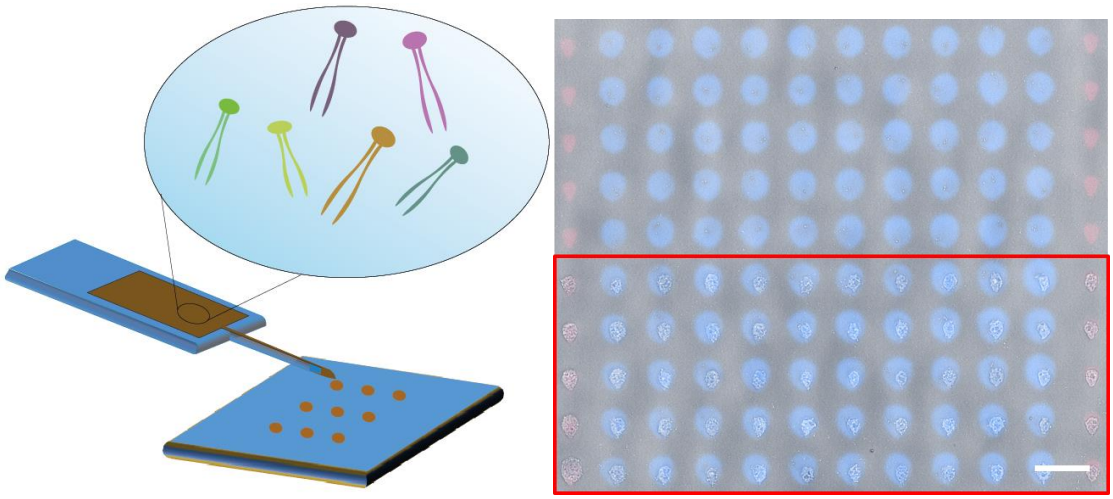

Figure 3- 79 Scheme of lipid spotting by μCS and a half DOPC-covered CB7/MDAP microarray. BF 10 ms, DAPI 10 s and Cy3 500 ms. Scale bars equal to 50 μm.

To firstly check if the SLB keeps molecules well on the surface, a TMR-Cad microarray printed on SiO_2-MCC surface by μCS was partially covered with DOPC by μCS, too (the white frame in Figure 3- 80a). Then the microarray was incubated with HEPES and monitored in a microfluidic channel. From Figure 3- 80, the uncovered spots lose their fluorescence and spread around but the covered sub-microarray is much more stable and keeps fluorescence within 20 min (Figure 3- 81 and Table 3- 21). Therefore, μCS printed lipid layers might be suitable for chemosensor microarrays.

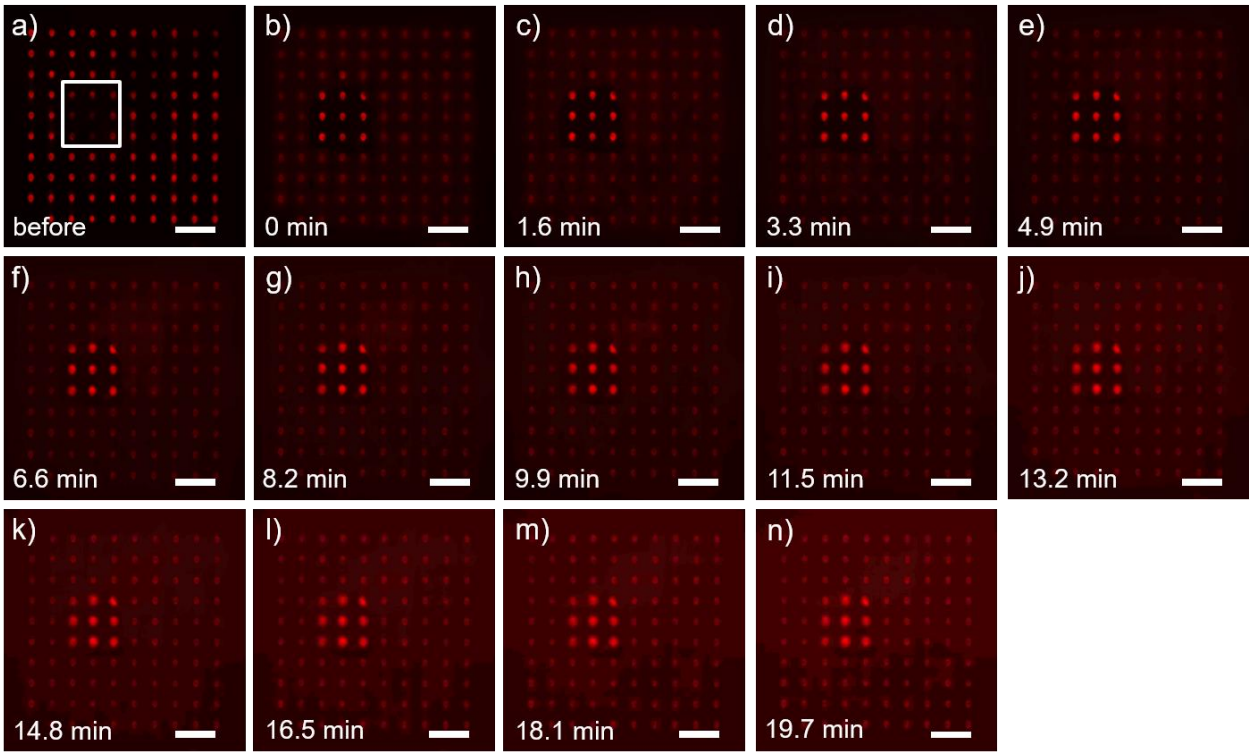

Figure 3- 80 a) TMR-Cad microarray on SiO_2-MCC surface partially covered with DOPC in the white frame. b)-n) HEPES incubation in microfluidic channel. Cy3 300 ms. Scale bars equal to 100 µm.

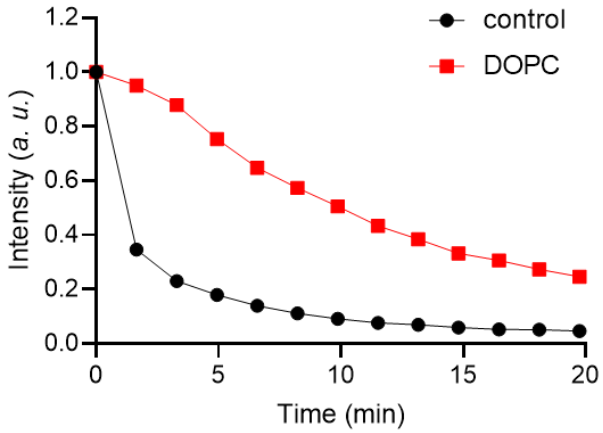

Figure 3- 81 Graph of fluorescence intensity in TMR-Cad microarray with (red) or without (black) DOPC layer during HEPES incubation.

Table 3- 21 Fluorescence intensities of TMR-Cad microarray with or without DOPC layer during HEPES incubation.

time (min)	0	1.6	3.3	4.9	6.6	8.2	9.9	11.5	13.2	14.8	16.5	18.1	19.7
control	1.00	0.35	0.23	0.18	0.14	0.11	0.09	0.08	0.07	0.06	0.05	0.05	0.05
DOPC	1.00	0.95	0.88	0.75	0.65	0.57	0.51	0.43	0.38	0.33	0.31	0.27	0.25

CB8/MDAP sensor complex was printed on a SiO_2-NEM surface and this non-immobilized chemosensor microarray was then half-covered with DOPS (Figure 3- 82). After incubation of tryptamine for 5 min. The remaining fluorescence on the covered microarray is brighter than the uncovered one, which demonstrates that the SLB delays the sensing process, reflecting the slower diffusion through the SLB.

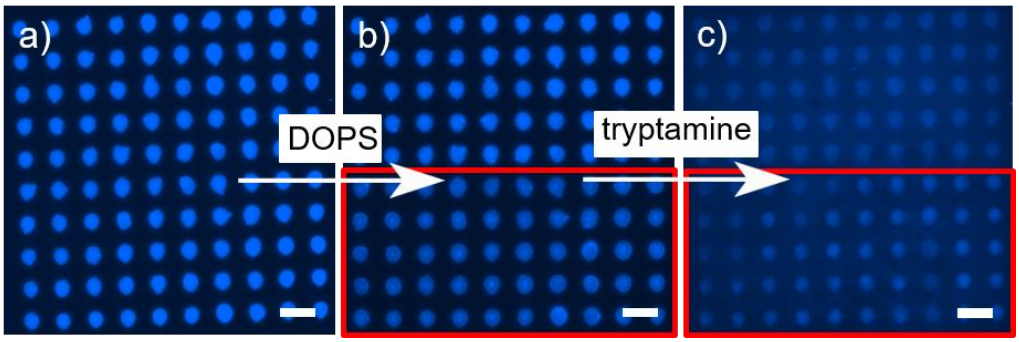

Figure 3- 82 a) Non-linked CB8/MDAP microarray on SiO_2-NEM surface, b) after half array being printed 10 mol% DOPS in DOPC and c) after 10 µM tryptamine incubation for 5 min. DAPI 10 s. Scale bars equal to 50 µm.

3.4.4. Solvent-assisted lipid bilayers (SALB)

When only composition of lipids is needed, homogenously coated lipid bilayers are also an option to cover sensor microarray, which will be useful for permeability assessment. Solvent-assisted lipid bilayers (SALB), one of the best homogenous SLB as reported,[63] form by the transition of lipid phase from inverted micelles and monomers to conventional micelles and vesicles through the solvents exchange from isopropanol to water buffer and subsequant spread on the surface (Figure 3- 83). This SALB can be easily achieved in the mentioned microfluidic channels. By combining with the solvent-resisted rotaxane microarray, it will enable to monitor the permeability of the lipid bilayers.

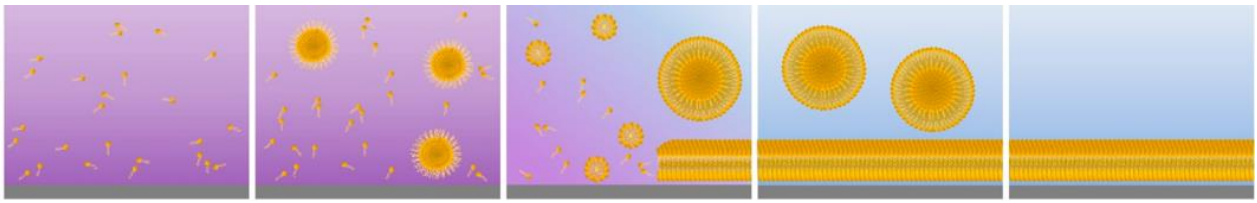

Figure 3- 83 Scheme of SALB formation from literature.[63]

3.4.4.1. SALB formation

In order to monitor the formation of SALB, 0.5 mol% Liss Rhod PE in DOPC dissolved in isopropanol was injected in the microfluidic channel combined with SiO_2-NCO surface and then, HEPES buffer was injected to mix with the lipid solution. The fluorescence intensity on the surface is getting stronger according to the mixing within 9 s (Figure 3- 84). The homogenous fluorescence stays constant even after washing of the sample with HEPES. To further prove SALB is homogeneously coated on the surface, an AlexaFluor488 linked Albumin from Bovine Serum (AlexaFluor-BSA) solution was injected in the microchannel. From Figure 3- 85, the SALB-covered surface is less green compared with the control, SiO_2-NCO surface incubated with AlexaFluor-BSA, which demonstrates the unspecific adsorption of AlexaFluor-BSA is significantly reduced by the lipid bilayers. In addition, there is no inhomogeneous adsorption on the SALB, which shows the SALB is homogeneously coated on the surface and defect free.

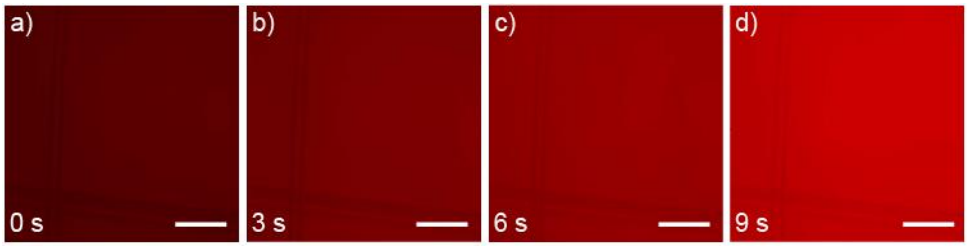

Figure 3- 84 Images of SALB formation in a) 0 s, b) 3 s, c) 6 s and d) 9 s on SiO_2-NCO surface in a microfluidic channel, Cy3 100 ms. Scale bars equal to 50 µm. Q = 2.22 µL/s.

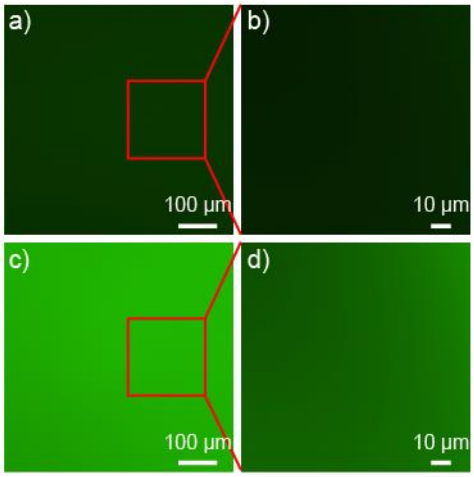

Figure 3- 85 a) and b) SALB covered SiO_2-NCO surface after incubation of AlexaFluor-BSA. c) and d) SiO_2-NCO surface after incubation of AlexaFluor-BSA.

3.4.4.2. SALB on TMR-Cad microarray

To pre-evaluate the covering property of SALBs for microarrays, a microchannel with a TMR-Cad microarray on SiO_2-MCC surface was firstly injected with DOPC solution in isopropanol and then HEPES buffer to form SALB. Ignoring the speaded spots before HEPES, the SALB-covered spots in the white frame in Figure 3- 86 remain more than 20 min with less fluorescence loss (Figure 3- 87 and Table 3- 22) compared with µCS-printed SLB (Figure 3- 81).

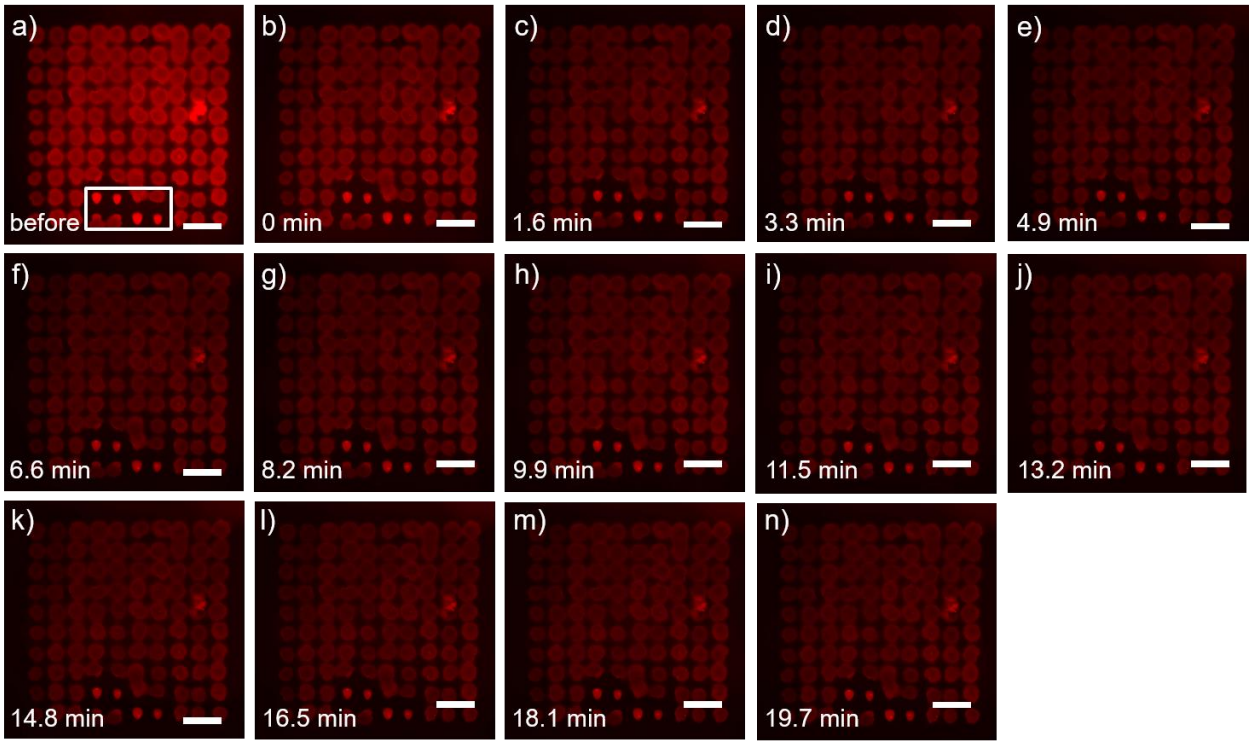

Figure 3- 86 TMR-Cad microarray on SiO_2-MCC surface partially covered with DOPC through SALB in the white frame. b)-n) HEPES incubation in a microfluidic channel. Cy3 300 ms. Scale bars equal to 100 µm.

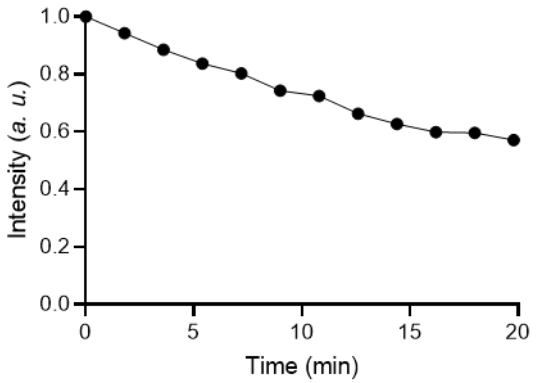

Figure 3- 87 Graph of fluorescence intensity in TMR-Cad microarray with DOPC layer during HEPES incubation.

Table 3- 22 Fluorescence intensities of TMR-Cad microarray with or without DOPC layer during HEPES incubation.

time (min)	0	1.8	3.6	5.4	7.2	9.0	10.8	12.6	14.4	16.2	18.0	19.8
control	1.00	0.94	0.89	0.84	0.80	0.74	0.72	0.66	0.63	0.60	0.6	0.57

3.4.4.3. SALB on rotaxane microarray

As both CB8 and the DAP indicator are immobilized on the surface, the rotaxane microarray is solvent-resisted and suitable to be covered by a SALB to monitor diffenence in analyte detection, thus evaluating the permeability of the SALB. Firstly, two controls, rotaxane microarray with and without DOPC SALB were incubated with HEPES for 5 min. The stable fluorescence shown in Figure 3- 88 and Figure 3- 89 demonstrate the stability of rotaxane microarrays in HEPES buffer. Afterward, the rotaxane microarrays were covered with DOPC, 1%, 5% and 10% DOPS in DOPC membranes respectively (mol%, same as bellow) for tryptamine detection (Figure 3- 90 and Figure 3- 91). On visible inspection the fluorescence of both uncovered and DOPC covered microarrays, is quenched after 2 min, which shows the similar time scales of detecting defection (Figure 3- 90a and b). However, quantifying the fluorescence reveals that DOPS-covered rotaxane microarrays detect tryptamine slower and the fluorescence of 10% DOPS-covered microarray exists until after 5 min, which demonstrates the detection speed of DOPS-covered microarray gets slower. The slower fluorescence quenching means less permeability, which demonstrate that more DOPS in the membrane slows down the diffusion of tryptamine through the membrane. The reason may be the negative charge of the DOPS membrane slow down the transport of positive tryptamine going through the membrane.[95]

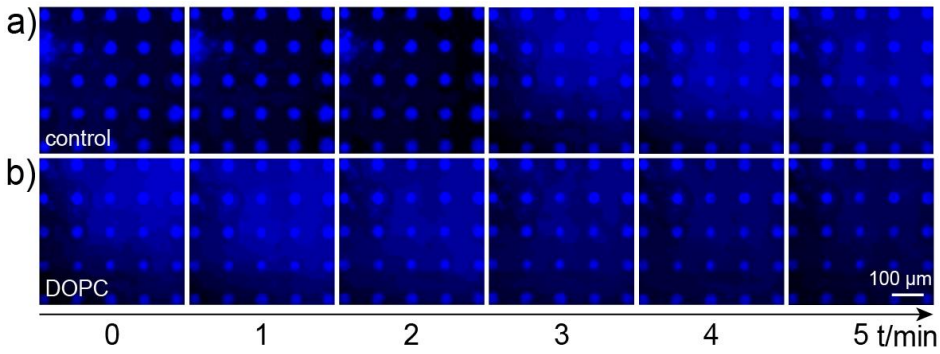

Figure 3- 88 Images of a) rotaxane microarray and b) rotaxane microarray covered with DOPC in the incubation of HEPES whthin 5 min. Scale bars equal to 100 µm. DAPI 10 s.

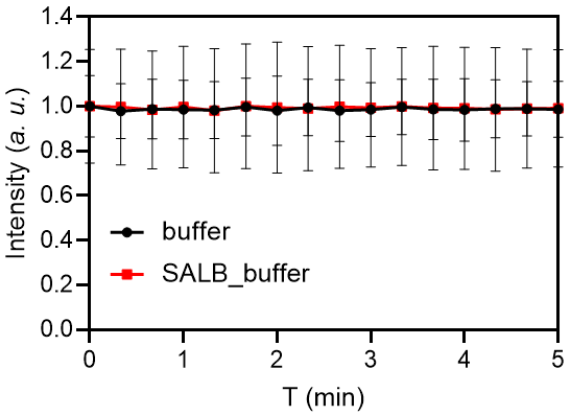

Figure 3- 89 Intensity graph of rotaxane microarray (black) and rotaxane microarray covered with DOPC (red) in the incubation of HEPES whthin 5 min.

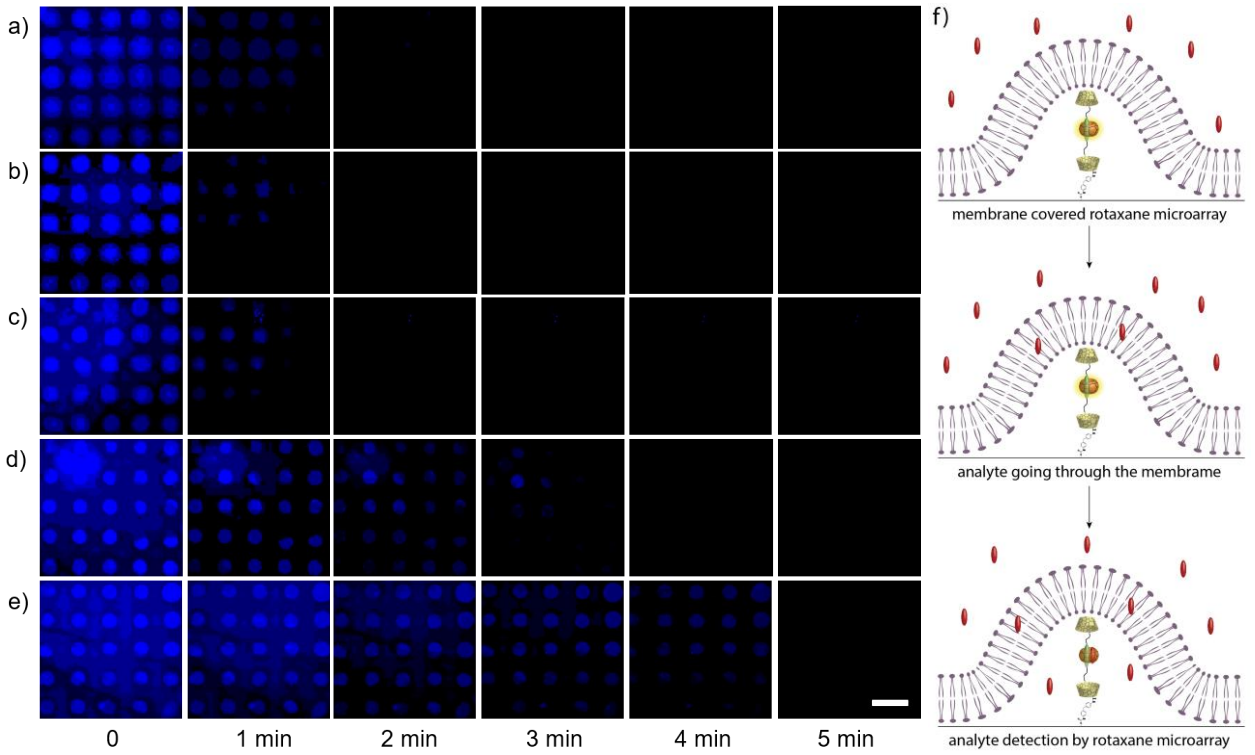

Figure 3- 90 Images of a) rotaxane microarray, rotaxane microarray covered with b) DOPC c) 1 mol% DOPS, d) 5 mol% DOPS, e) 10 mol% DOPS in DOPC for in the incubation of tryptamine for 5 min. Scale bar equals to 100 µm. DAPI 10 s. f) Scheme of analyte detection on SALB covered roraxane microarray.

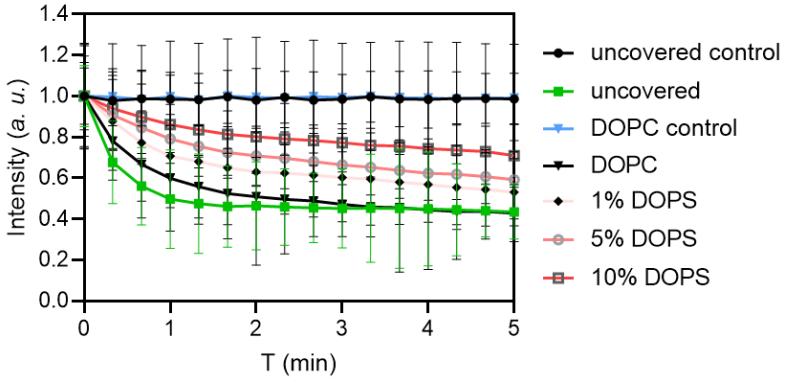

Figure 3- 91 Intensity graph of rotaxane microarray and rotaxane microarray covered with DOPC, 1 mol% DOPS, 5 mol% DOPS and 10 mol% DOPS in DOPC for in the incubation of tryptamine for 5 min.

3.4.5. Summary of biomimetic lipid membrane systems

Combined with the CBn/indicator chemosensor microarrays, biomimetic lipid membranes, SLB micropatterned by DPN, PPL and µCS, or homogenous SALB, provides an approach to evaluate its permeability. Compared with DPN-printing, PPL and µCS-printed SLB cover sensor arrays keep them on the surface for a longer time. However, the permeability of the lipid membrane to the analyte is not obviously to be seen due to either the leakage on the edge of the membrane or the loss of non-immobilized chemosensor in the SPL generated lipid.

In contrast, SALB is a homogenous coating lipid membrane that covers the wall of the microchannel including the microarray substrate, thus the leakage was avoided. After combination with rotaxane microarrays, where both CB8 and DAP are immobilized, the analyte detection together with the membrane permeability could be observed in a biomimetic cell-like environment. Increase of DOPS slows down the diffusion of tryptamine through the membrane thus slows down the transport onto the surface from 2 min to 5 min, due to the charge effect.

3.5. CB8 stabilized methyl viologen (MV) dimer for molecular junctions

This chapter focuses on the immobilization of CB8 by surface-bonded MV in order to increase the stability of $[MV^{\bullet+}]_2$ SAM and was done during the exchange in the group of Prof. Dr. Ir. Pascal Jonkheijm and group of Prof. Dr. Christian A. Nijhuis in the University of Twente (UT), Enschede, the Netherlands.

Firstly, diluted MV SAMs on Au/Ag were prepared by incubation of mixtures of MV-SH and alkyl-SH (Alk-SH) in varying ratios from 5% (mol) to 100%. Then the SAM modified electrodes were characterized through cyclic voltammetry (CV) to prove the CB8 immobilization and then $[MV^{\bullet+}]_2$ formation with CB8/MV complex in the electrolyte. Afterward, voltammetric measurements with a Eutectic Gallium-Indium (EGaIn) contact electrode were conductive to show the stabilized hysteresis and enhanced conductance.

3.5.1. Surface modification

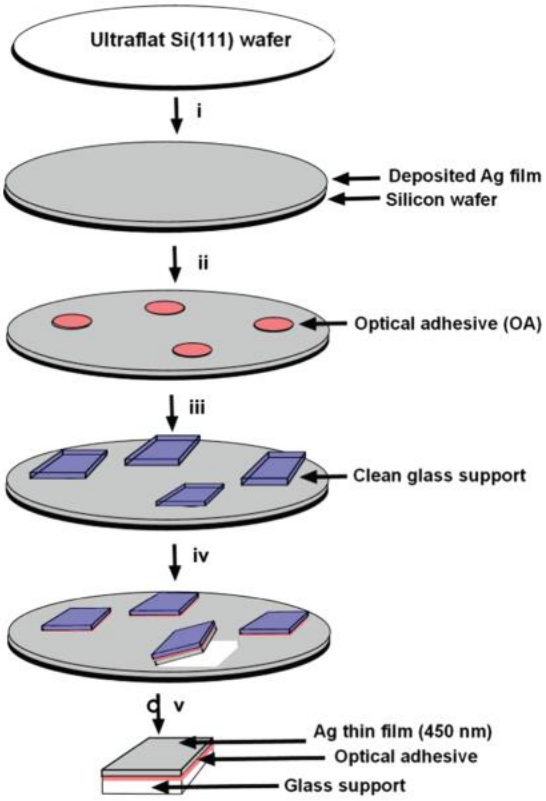

Figure 3- 92 Fabrication of template-stripped bottom electrode (Au and Ag).[96]

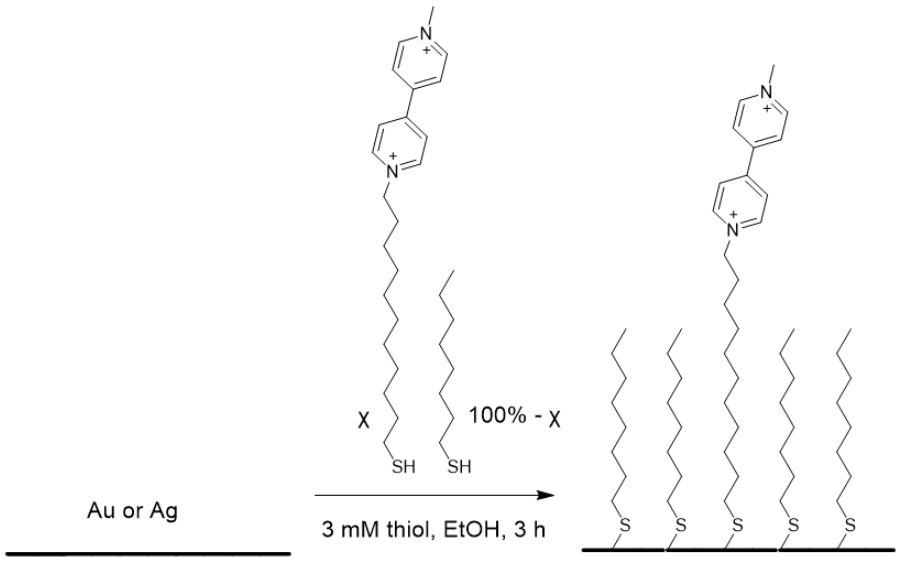

Figure 3- 93 Surface modification with mixed SAM.

All substrates used for this chapter were template-stripped bottom electrodes (Au and Ag) and fabricated according to the scheme in Figure 3- 92.[96] The electrode was freshly modified with mixed SAMs of MV-thiol (MV-SH) and alkyl-thiol (Alk-SH) in varying composition *X* (0%, 5%, 10%, 20%, 50% and 100%), shown in Figure 3- 93.

3.5.2. CB8 immobilization and $[MV^{\bullet+}]_2$ of stabilization

The immobilization of CB8 and stabilization of $[MV^{\bullet+}]_2$ were firstly characterized through CV measurement before and after incubation of 50 μM CB8, 50 μM MV and 50 μM CB8/MV 1:1 complex in 0.1 M NaCl electrolyte. The bottom electrode is the gold surface (Au).

3.5.2.1. *X* = 0% MV SAM

When *X* = 0%, the surface is without any MV unit, namely pure alkyl surface (Figure 3- 94Figure 3- 94, left). This alkyl surface was measured as the first control of CB8 immobilization. From Figure 3- 94 (right), no peak signal was generated after incubation of 0.1 M NaCl, 50 μM CB8 and CB8/MV in 0.1 M NaCl, which demonstrates no CB8 was immobilized and no $[MV^{\bullet+}]_2$ formed.

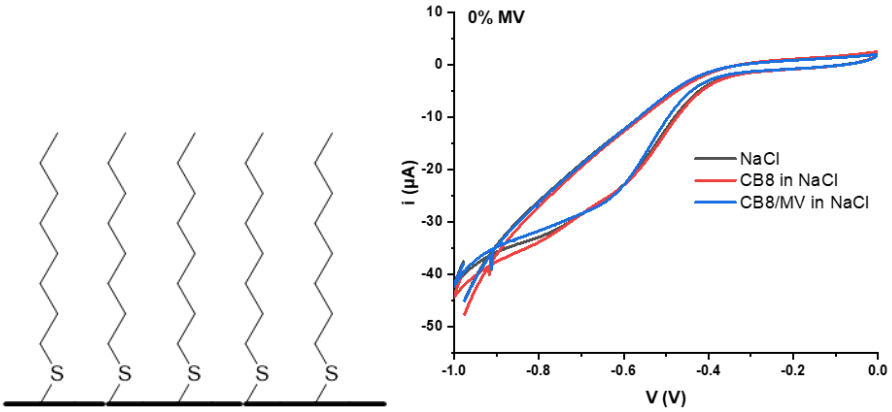

Figure 3- 94 Structure of 0% MV SAM (left) and cyclic voltammograms (right) of 0% MV SAM (black), after 50 μM CB8 (red) and 50 μM CB8/MV (blue), 0.1 M NaCl as electrolyte at a scan rate of 0.2 V/s.

3.5.2.2. 5% MV SAM

When *X* = 5%, only few MV in dispersed positions on the surface exist (Figure 3- 95, left) so there is enough space for CB8 and the second MV assembly. CV measurement of 5% MV SAM in shown in Figure 3- 95 (right). In the incubation of NaCl (black) and CB8 in NaCl (red) for 30 min, no peak signal including assembly appears. If the electrolyte only contains MV^{2+} shown in the blue line, MV^{2+} can be first reduced to $MV^{\bullet+}$ radical after taking one electron, which generates a peak at -0.52 V. $MV^{\bullet+}$ radical can be further reduced to neutral MV^{0} and generates another higher signal at -0.63 V. These two peaks disappear if the electrolyte contains 1:1 CB/MV complex (green) and a new peak at -0.5 V appear. According to former reports,[34, 97] the new peak is from the formation of $[MV^{\bullet+}]_2$ stabilized with CB8 and it tentatively infers the assembly shown in Figure 3- 96.

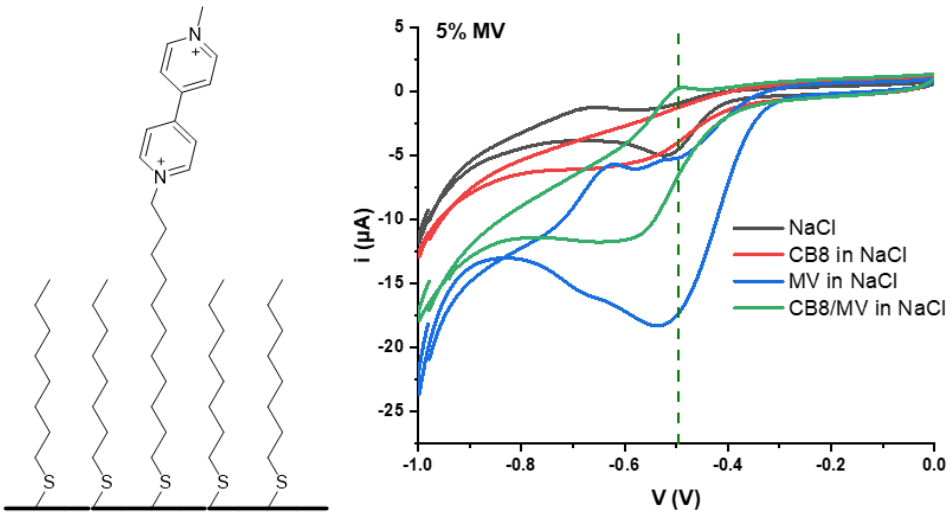

Figure 3- 95 Sturcture of *X* MV SAM (left) and cyclic voltammograms (right) of 5% MV SAM on Au (black) after 30 min incubation of 50 μM CB8 (red), 50 μM MV (green) and 50 μM CB8/MV (blue), 0.1 M NaCl as electrolyte at a scan rate of 0.2 V/s.

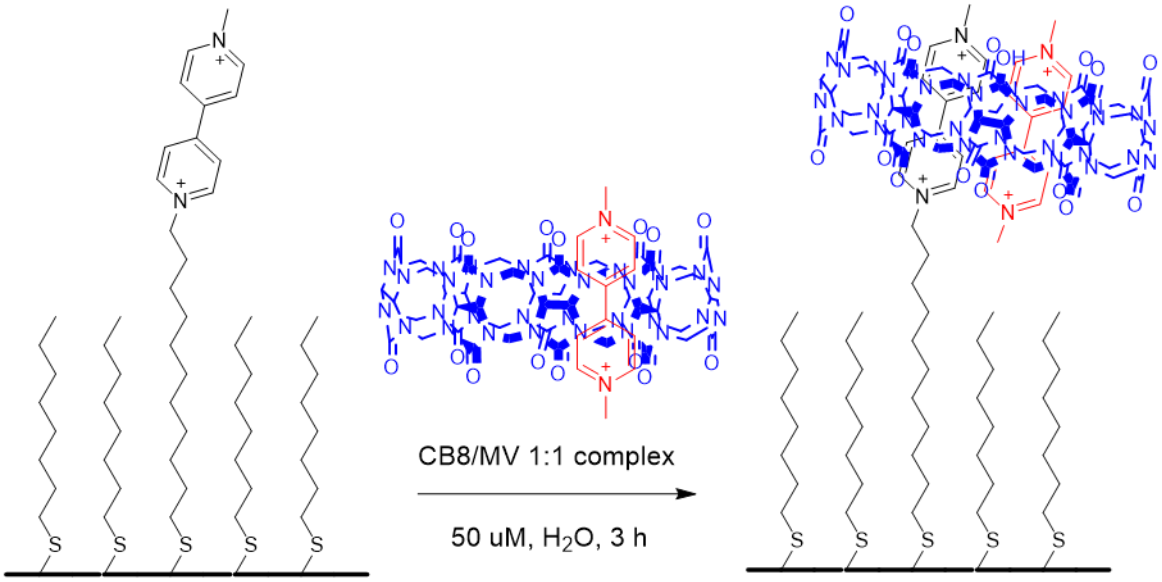

Figure 3- 96 CB8 immobilization and formation of MV_2 dimer.

In order to know the exact amount of $[MV^{\bullet+}]_2$ in CB8 and single $MV^{\bullet+}$, $[MV^{\bullet+}]_2$ peaks in Figure 3- 95 was further deconvoluted (Figure 3- 97c) and the absolute value of surface coverage was calculated by equation

$$\Gamma = Q/(nFA)$$

Where *Q* is the total charge calculated from integration of the redox curve (Figure 3- 97); *n* is the number of electrons for per mole of reaction, here *n* = 1; *A* is the surface area of the working electrode, where *A* is 0.28 cm^2; *F* is Faraday constant 96485.33 C / mol. The scan rate is 0.2 V/s. The calculated surface density of the viologen unit after CB8/MV incubation is 5.02 x 10^{-11} mol / cm^2, which corresponds to 10% of pure MV SAM. [71] After the deconvolution it possible to derive the surface density of $[MV^{\bullet+}]_2$ (4.63 x 10^{-11} mol / cm^2) and $MV^{\bullet+}$ (0.39 x 10^{-11} mol / cm^2) on the SAM (Table 3- 23 Surface densities of 5% MV SAM.Table 3- 23). The ratio of $[MV^{\bullet+}]_2$ to $MV^{\bullet+}$ is 12:1, demonstrating that more than 90% of bonded MV immobilizes CB8 and then forms MV_2 together with a second MV from the solution.

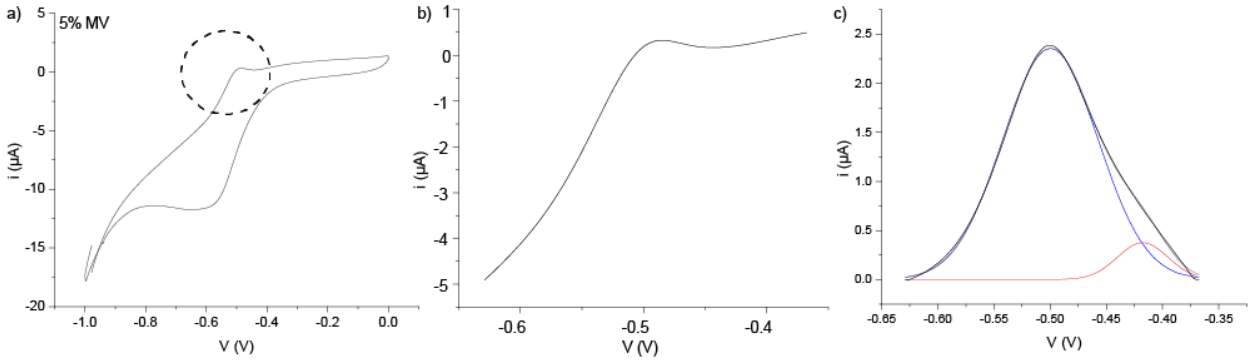

Figure 3- 97 Cyclic voltammograms of a) 5%MV SAM on Au after 30 min incubation of CB8/MV, b) zoom in and c) the corresponding deconvolution of anodic peak of the first redox wave. The blue line indicates the $[MV^{\bullet+}]_2$ in CB8 and the red line indicates the one-electron reduction of MV^{2+}.

Table 3- 23 Surface densities of 5% MV SAM.

	MV in total	MV from $[MV^{\bullet+}]_2$	MV from $MV^{\bullet+}$	CB8
E_{FWHM} (mV)		100	53	
Q / 10^{-7} C	2.71	2.50	0.21	
Γ / (10^{-11} mol cm^{-2})	5.02	4.63	0.39	2.32
ratio		**12**	**1**	

3.5.2.3. 10% MV SAM

On 10% MV SAM, the surface density of viologen unit after CB8/MV incubation is 4.98 x 10^{-11} mol / cm^2 (Table 3- 24). It seems there was no difference compared with 5% MV

SAM. However, the peak of $[MV^{\bullet+}]_2$ (blue line) decreases and that of $MV^{\bullet+}$ increases (Figure 3- 98). Therefore, the surface density of $[MV^{\bullet+}]_2$ decreases to 2.91 x 10^{-11} mol / cm^2 and that of $MV^{\bullet+}$ increase up to 2.08 x 10^{-11} mol / cm^2. The ratio of $[MV^{\bullet+}]_2$ to $MV^{\bullet+}$ decreases to 1.4:1. In summary, there are more viologen units on the surface but less space for CB8 assembly when *X* increases to 10%, which results in less second viologens from the solution to form dimers.

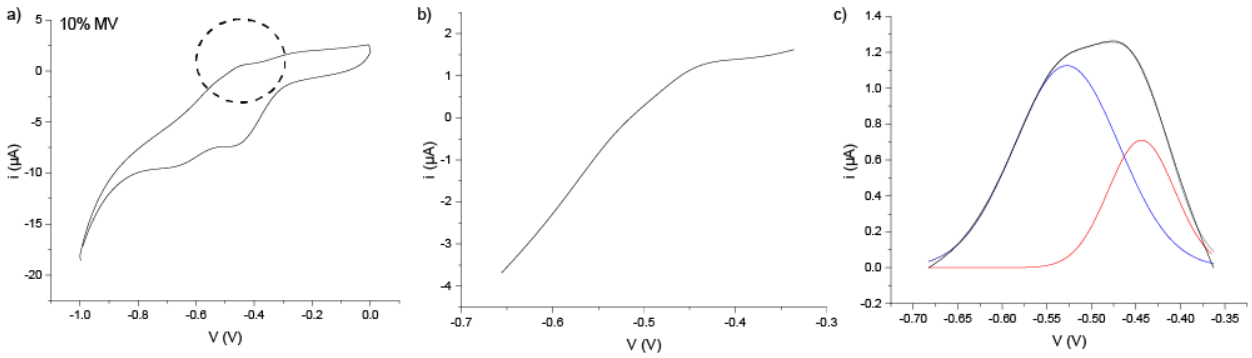

Figure 3- 98 Cyclic voltammograms of a) 10% MV SAM on Au after 30 min incubation of CB8/MV, b) zoom in and c) the corresponding deconvolution of the anodic peak of the first redox wave. The red lines indicate the $[MV^{\bullet+}]_2$ in CB8 peak and the blue lines indicate the one-electron reduction of MV^{2+}.

Table 3- 24 Surface densities of 10% MV SAM.

	MV in total	MV from $[MV^{\bullet+}]_2$	MV from $MV^{\bullet+}$	CB8
E_{FWHM} (mV)		128	107	
Q / 10^{-7} C	2.69	1.57	1.12	
Γ / (10^{-11} mol cm^{-2})	4.98	2.91	2.08	1.46
ratio		**1.4**	**1**	

As the interaction between CB8 and MV is not covalent, it is necessary to evaluate how stable the $CB8/MV_2$ complex is. Additional CV measurement scans every 10 min and 30 scans at a time, are shown in Figure 3- 99. In the first 30 min, the signal increases and moves to the positive direction, which represents the assembly between CB8 and MV. The assembly finishes after 30 min demonstrated by the stabilization of the signal. In the right figure, continuous scanning keeps a stable curve.

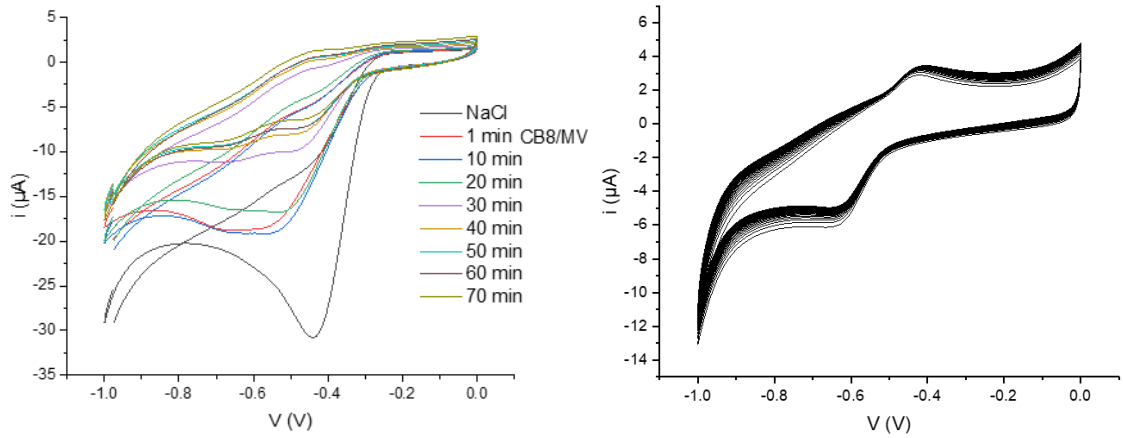

Figure 3- 99 Cyclic voltammograms of 10% MV SAM on Au after each 10 min of CB8/MV incubation (left) and 30 scans at a certain time (right). 0.1 M NaCl as electrolyte at a scan rate of 0.2 V/s.

3.5.2.4. 20% MV SAM

The cyclic voltammograms and surface densities of 20% MV SAM are shown in Figure 3-100 and Table 3- 25. The surface density of total viologen unit after CB8/MV incubation is 5.37 x 10^{-11} mol / cm^2, of which only 0.9 x 10^{-11} mol / cm^2 belongs to $[MV^{\bullet+}]_2$ and the rest 4.48 x 10^{-11} mol / cm^2 belongs to $MV^{\bullet+}$. The ratio of $[MV^{\bullet+}]_2$ to $MV^{\bullet+}$ sharply decreases to 0.2:1. Keep in mind the above results, the immobilized viologen units are too crowded to assembly CB8 and bring another viologen from the solution. Therefore, even fewer viologen forms $[MV^{\bullet+}]_2$.

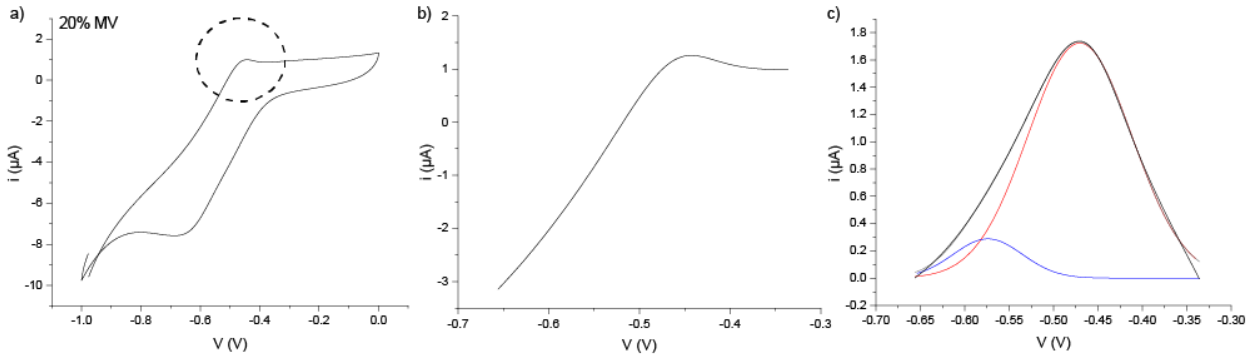

Figure 3- 100 Cyclic voltammograms of a) 20%MV SAM on Au after CB8/MV incubation, b) zoom in and c) the corresponding deconvolution of the anodic peak of the first redox wave. The red lines indicate the $[MV^{\bullet+}]_2$ in CB8 peak and the blue lines indicate the one-electron reduction of MV^{2+}.

Table 3- 25 Surface densities of 20% MV SAM.

	MV in total	MV from $[MV^{\bullet+}]_2$	MV from $MV^{\bullet+}$	CB8
E_{FWHM} (mV)		101	133	
Q / 10^{-7} C	2.90	0.48	2.42	
Γ / (10^{-11} mol cm^{-2})	5.37	0.90	4.48	0.45
ratio		**0.2**	**1**	

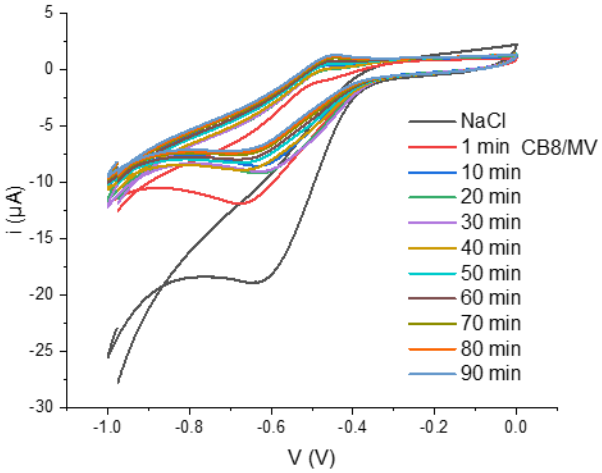

Figure 3- 101 Cyclic voltammograms of 20%MV SAM on Au after varying time of CB8/MV incubation. 0.1 M NaCl as electrolyte at a scan rate of 0.2 V/s.

The cyclic voltammograms of varying time (Figure 3- 101) show the signal increases and moves to the positive direction, which represents the assembly between CB8 and MV in the first 20 min. The assembly finishes after 20 min demonstrated by no more obvious change in curve shape.

3.5.2.5. 50% MV SAM

The cyclic voltammograms and surface densities of 50% MV SAM are shown in Figure 3-102 and Table 3- 26. The surface density of total viologen unit after CB8/MV incubation is 8.60 x 10^{-11} mol / cm^2, of which only 0.25 x 10^{-11} mol / cm^2 belongs to $[MV^{\bullet+}]_2$ and the rest 8.35 x 10^{-11} mol / cm^2 belongs to $MV^{\bullet+}$. The ratio of $[MV^{\bullet+}]_2$ to $MV^{\bullet+}$ decreases to 0.03:1. Compared to the above results, the immobilized viologen unit is not even more crowded, assembly of further the CB8 and receiving of additional viologen from the solution to form $[MV^{\bullet+}]_2$.

The cyclic voltammograms of varying time (Figure 3- 103) show no more obvious change after 20 min of CB8/MV incubation. In the right figure, continuous scanning keeps a stable signal.

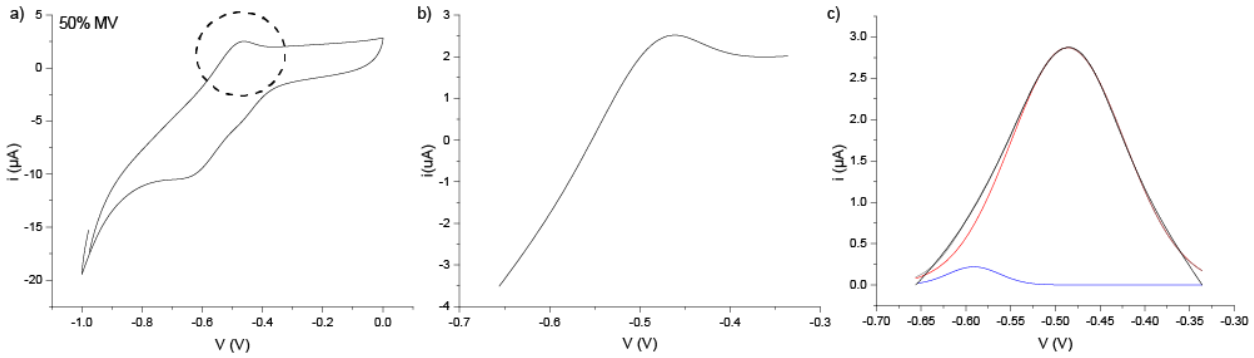

Figure 3- 102 Cyclic voltammograms of a) 50%MV SAM on Au after CB8/MV incubation, b) zoom in and c) the corresponding deconvolution of the anodic peak of the first redox wave. The red lines indicate the $[MV^{\bullet+}]_2$ in CB8 peak and the blue lines indicate the one-electron reduction of MV^{2+}.

Table 3- 26 Surface densities of 50% MV SAM.

	MV in total	MV from $[MV^{\bullet+}]_2$	MV from $MV^{\bullet+}$	CB8
E_{FWHM} (mV)		68	149	
Q / 10^{-7} C	2.65	0.08	2.57	
Γ / (10^{-11} mol cm^{-2})	8.6	0.25	8.35	0.13
ratio		**0.03**	**1**	

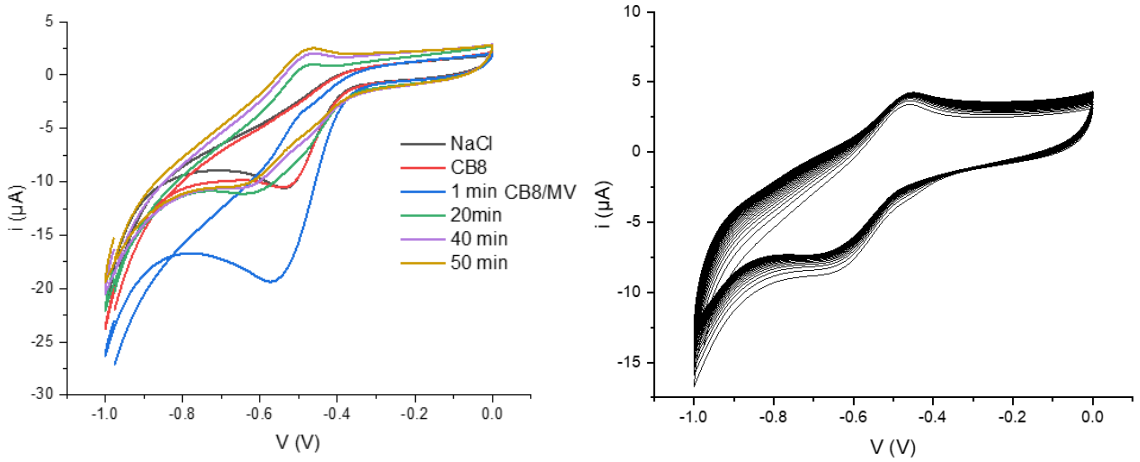

Figure 3- 103 Cyclic voltammograms of 50% MV SAM on Au varying time of CB8/MV incubation (left) and in 30 scans (right). 0.1 M NaCl as electrolyte at a scan rate of 0.2 V/s.

3.5.2.6. 100% MV SAM

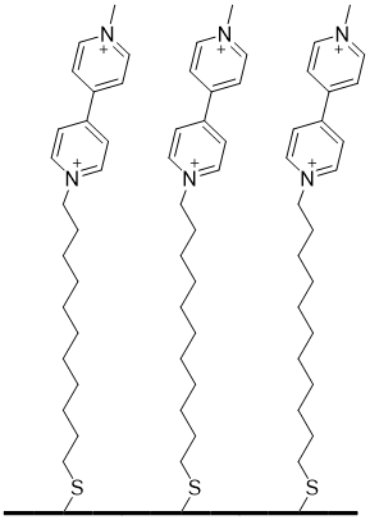

Figure 3- 104 Structure of χ = 100% MV SAM.

To compare the stability of $[MV^{\bullet+}]_2$ immobilized by CB8 and from the 100% MV SAM (Figure 3- 104), the same CV measurement was repeated and the results are shown in Figure 3- 105 and Table 3- 26. The surface density of total viologen unit is 2.05 x 10^{-10} mol / cm^2, of which 1.79 x 10^{-10} mol / cm^2 belongs to $[MV^{\bullet+}]_2$ and the rest 0.26 x 10^{-10} mol / cm^2 belongs to $MV^{\bullet+}$. The ratio of $[MV^{\bullet+}]_2$ to $MV^{\bullet+}$ is 7:1, which is higher than in previous work (2.3:1),[71] higher than with 10%, but still lower than that with 5% MV SAM even with high surface density. The reason is through a high amount of MV forms $[MV^{\bullet+}]_2$ as well but might be affected by the other MV structures around, so the overall density of dimer as well as the stability are lower.

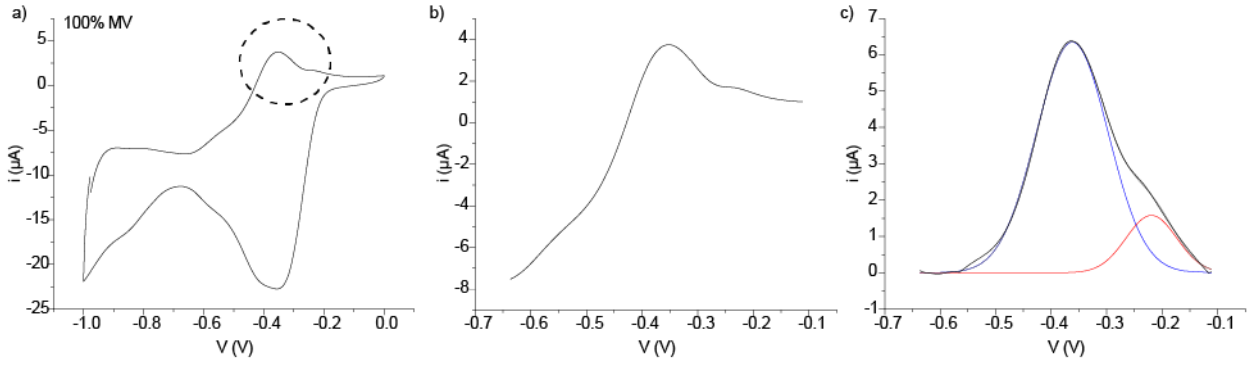

Figure 3- 105 Cyclic voltammograms of a) 100% MV SAM on Au, b) zoom in and c) the corresponding deconvolution of anodic peak of the first redox wave. The red lines indicate the

$[MV^{\bullet+}]_2$ in CB8 peak and the blue lines indicate the one-electron reduction of MV^{2+}. 0.1 M NaCl as electrolyte at a scan rate of 0.2 V/s

Table 3- 27 Surface densities of 100% MV SAM.

	MV in total	MV from $[MV^{\bullet+}]_2$	MV from $MV^{\bullet+}$
E_{FWHM} (mV)		148	95
Q / 10^{-7} C	11.1	9.71	1.39
Γ / (10^{-11} mol cm^{-2})	20.5	17.94	2.56
ratio		**7**	**1**

3.5.3. Comparison of immobilized CB8

The surface densities of CB8 were calculated from $[MV^{\bullet+}]_2$ and listed in Table 3- 28. From the table, it's clear to compare the surface densities of $[MV^{\bullet+}]_2$, $MV^{\bullet+}$ and CB8. When the composition of viologen on SAMs increases from 5% to 50%, the *r* decreases from 12:1 to 0.03:1. The amount of $[MV^{\bullet+}]_2$ as well as CB8 decreases from 2.32 x 10^{-11} mol / cm^2 to 0.13 x 10^{-11} mol / cm^2.

Table 3- 28 Summary of surface densities.

χ	Γ_{sum} (mol/cm^{-2})	Γ ($[MV^{\bullet+}]_2$) (mol/cm^2)	Γ ($MV^{\bullet+}$) (mol/cm^2)	*r*	Γ_{CB8}
5%	5.02 x 10^{-11}	2.32 x 10^{-11}	0.39 x 10^{-11}	12:1	**2.32 x 10^{-11}**
10%	4.98 x 10^{-11}	1.45 x 10^{-11}	2.08 x 10^{-11}	1.4:1	**1.45 x 10^{-11}**
20%	5.37 x 10^{-11}	0.45 x 10^{-11}	4.48 x 10^{-11}	0.2:1	**0.45 x 10^{-11}**
50%	8.60 x 10^{-11}	0.13 x 10^{-11}	8.34 x 10^{-11}	0.03:1	**0.13 x 10^{-11}**
100%	2.05 x 10^{-10}	0.90 x 10^{-10}	0.26 x 10^{-10}	7:1	

3.5.4. Hysteresis and enhanced conductance of molecular junctions

Numbers of *J*(V) curves measured of mixed SAMs were measured by the EGaIn system shown in Figure 3- 106. The bottom electrode was Ag unless specified. A microscaled EGaIn tip was brought onto the SAM surface and then applied a voltage sweep. The voltage range of a completed curve starts from 0 and goes to positive applied bias. When

reaching +1 V, it shifts towards the negative applied bias until -1 V. Finally the curve goes back to 0. The hysteresis and conductance are reported in the following.

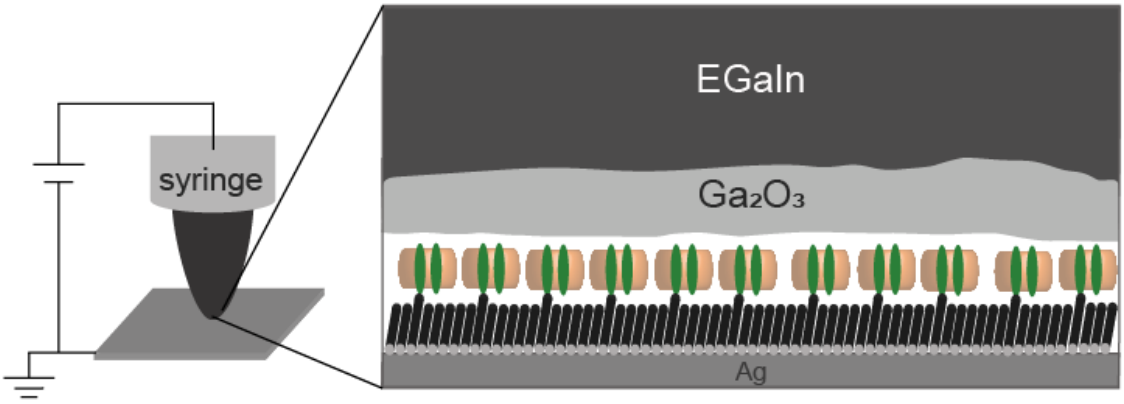

Figure 3- 106 Scheme of Eutectic Gallium-Indium (EGaIn) measurement.

3.5.4.1. 5% MV SAM

The representative *J*(V) curve of 5% MV SAM is shown in Figure 3- 107, Cl^- as the counterion. The current density *J* increases when voltage increases and decreases when the voltage decreases. *J* at the positive applied bias is higher than at the negative one and the forward and reverse curves overlay well. The current rectification ratio was calculated by equation

$$I_{RR} = I_{higher}/I_{lower}$$

where I_{higher} and I_{lower} are the currents at the same voltage in two biases. At ±1.0 V, I_{RR} is 7.08 on the positive side. In order to know how stable the SAM is, more *J*(V) curves are shown in Figure 3- 108 and they keep the same features. Similar properties appear to I^- a counterion and the I_{RR} is 7.94 (Figure 3- 109 and Figure 3- 110).

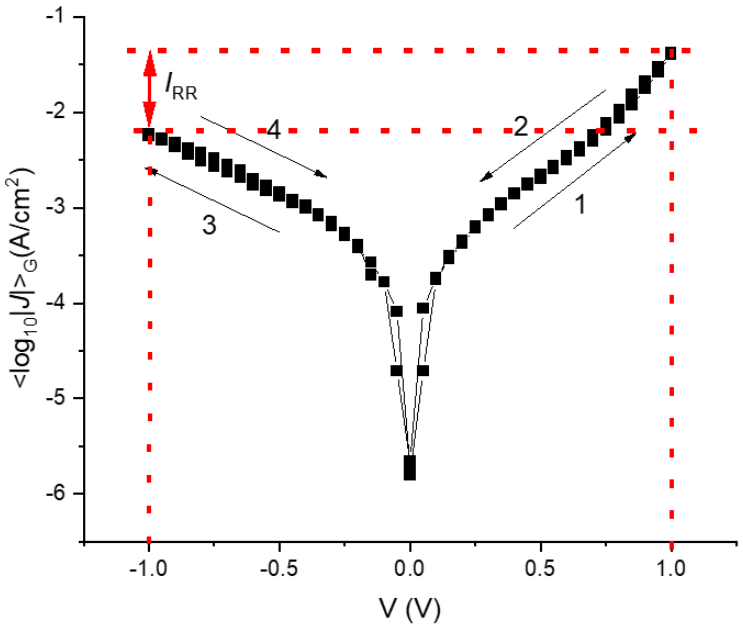

Figure 3- 107 Representative *J*(V) curve of 5% MV SAM with Cl^- as a counterion, voltage from -1.0 V to 1.0 V. I_{RR} is the current rectification ratio (positive).

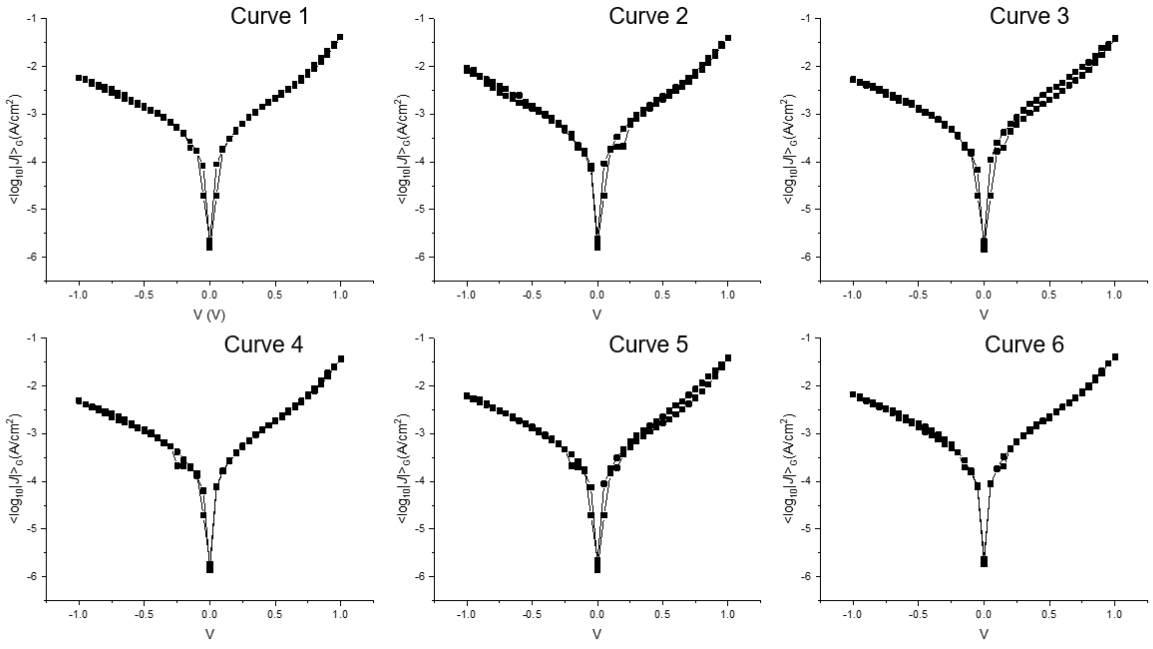

Figure 3- 108 Stability of *J*(V) curves of 5% MV SAM with Cl^- as a counterion.

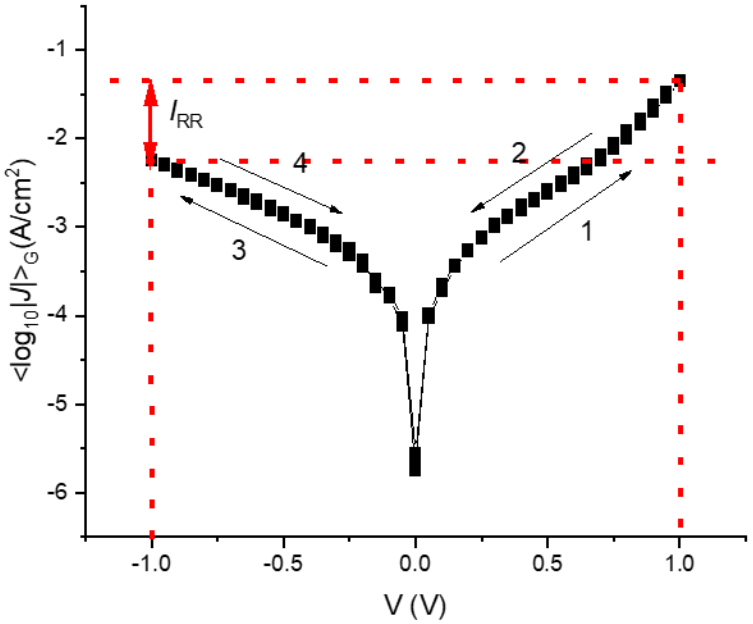

Figure 3- 109 Representative *J*(V) curve of 5% MV SAM, I^- as a counterion, voltage from -1.0 V to 1.0 V. I_{RR} is the current rectification ratio (positive).

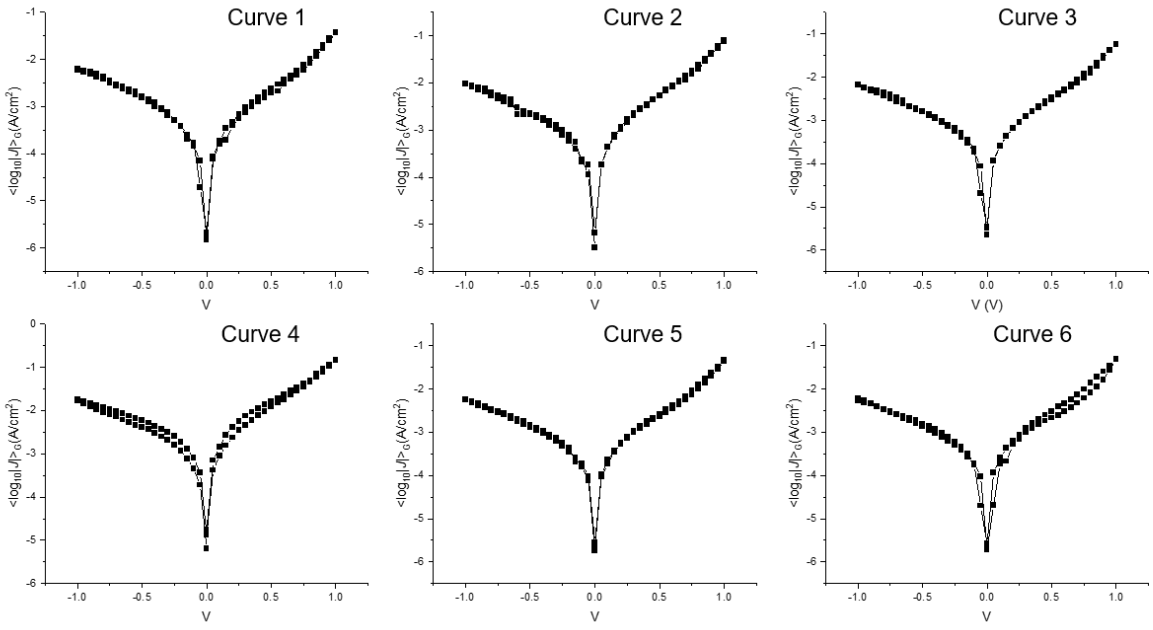

Figure 3- 110 Stability of *J*(V) curves of 5% MV SAM with I^- as a counterion.

Table 3- 29 List of I_{RR} and $R_{2/1}$ of 5% MV SAM.

	V	I_{RR}
Cl^-	±1.0	7.08
I^-	±1.0	7.94

3.5.4.2. 5% MV SAM after CB8/MV incubation

The representative *J*(V) curve of 5% MV SAM after CB8/MV incubation is shown in Figure 3- 111, Cl^- as a counterion. Same as 5% MV SAM in the positive bias, *J* increases when voltage increases, and decreases when the voltage decreases. The forward and reverse curves overlay. On the negative side, *J* jumps three magnitudes higher at -1.25 V and stays in the on-state steadily, generating a hysteresis while going back to 0 V. I_{RR} at ±1.0 V is 8.91 x 10^2 that is two orders of magnitude higher than MV SAM before CB8/MV incubation. The stable on-state exist in all more *J*(V) curve in Figure 3- 112. The highest on/off state ratio $R_{2/1}$ extracted from *J*(V) curve is 2.34 x 10^4. After being exchanged to counterion I^-, the curve keeps the hysteresis in the negative bias and the stability in on-state (Figure 3- 113 and Figure 3- 114), where I_{RR} is 1.10 x 10^3 and $R_{2/1}$ is 3.16 x 10^4. These results are consistent with to the published work[71].

It is worth noting that the surface density of viologen in this system is much lower, only 10% including noncovalent bonded MV hosted by CB8. The crucial factor is CB8 which not only highly stabilized $[MV^{\bullet+}]_2$ but also provided a microenvironment for the redox reaction[30]. The cavity of CB8 enables the $[MV^{\bullet+}]_2$ to have more stable and stronger intermolecular LUMO−LUMO couplings because the MV is unable to rearrange inside CB8. This leads to enhanced intermolecular charge transport, thus the conductance of the EGaIn junction has been increased even with the lower density of dimer.[18]

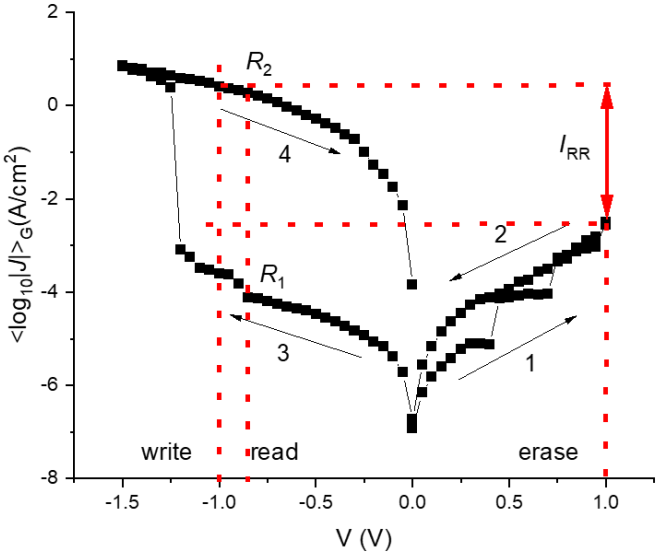

Figure 3- 111 Representative *J*(V) curve of 5% MV SAM after 50 μM CB8/MV incubation, with low conductance (R_1) and high conductance (R_2) states labeled, together with write, read and erase voltages. The black arrows indicate the scanning direction and are numbered accordingly. Cl^- as a counterion, the voltage from -1.5 V to 1.0 V. I_{RR} is the current rectification ratio (negative).

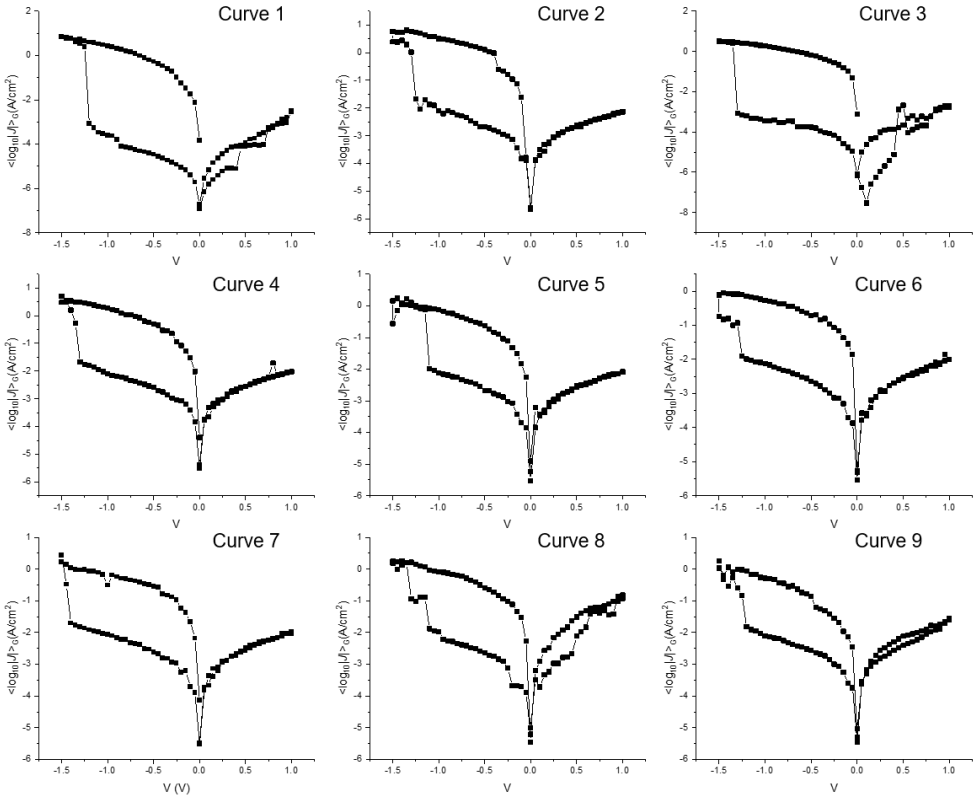

Figure 3- 112 Stability of *J*(V) curves of 5% MV SAM after 50 μM CB8/MV incubation, Cl^- as a counterion.

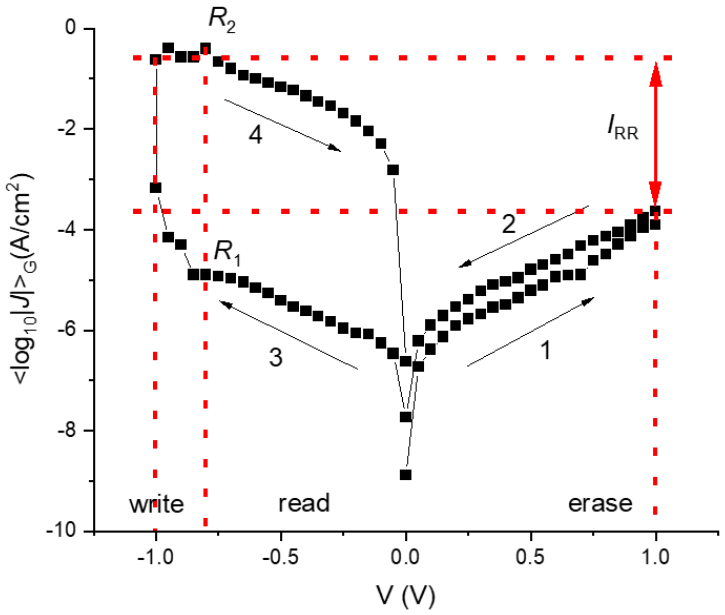

Figure 3- 113 Representative *J*(V) curve of 5% MV SAM after 50 μM CB8/MV incubation, with low conductance (R_1) and high conductance (R_2) states labeled, together with write, read and erase voltages. The black arrows indicate the scanning direction and are numbered accordingly. I^- as a counterion, voltage from -1.0 V to 1.0 V. I_{RR} is the current rectification ratio (negative).

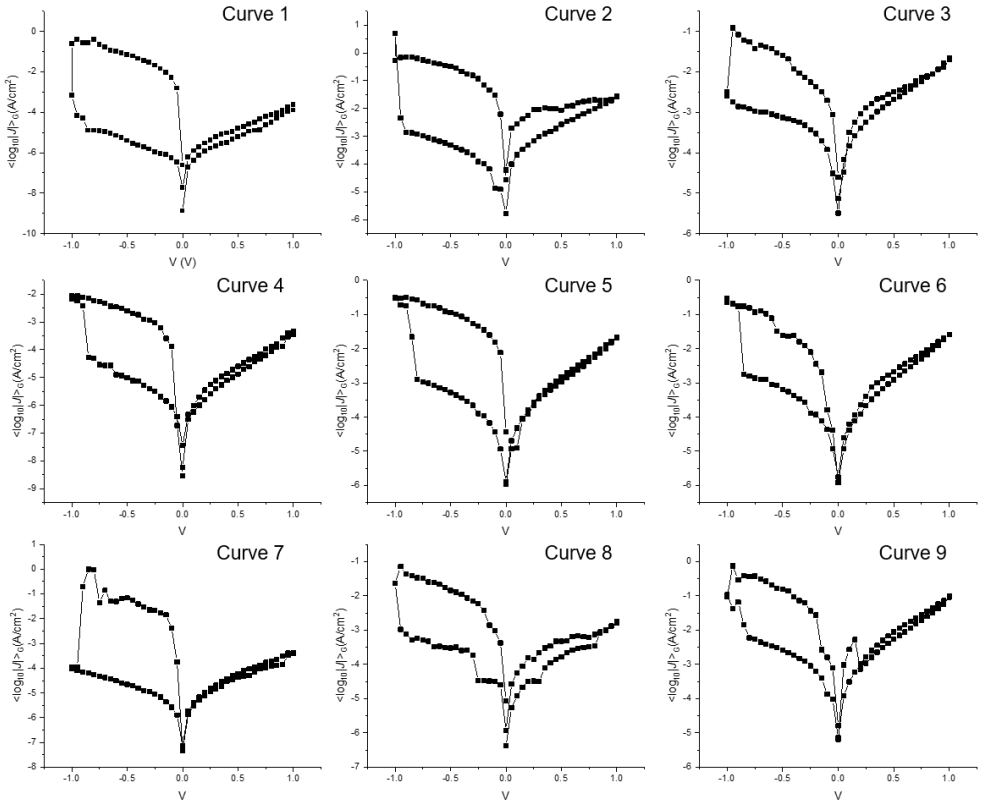

Figure 3- 114 Stability of *J*(V) curves of 5% MV SAM after 50 μM CB8/MV incubation, I^- as a counterion.

Table 3- 30 List of I_{RR} and $R_{2/1}$ of 5% MV SAM after 50 μM CB8/MV incubation.

	V	I_{RR}	V	$R_{2/1}$
Cl^-	±1.0	8.91×10^2	-0.85	2.34×10^4
I^-	±1.0	1.10×10^3	-0.8	3.16×10^4

3.5.4.3. 20% MV SAM after CB8/MV incubation

The representative *J*(V) curve of 20% MV SAM after CB8/MV incubation is shown in Figure 3- 115, Cl^- as a counterion. Same as above in the positive bias, *J* increases when voltage increases, and decreases when the voltage decreases. The forward and reverse curves overlay mostly. However, on the negative side, the hysteresis is much smaller than in the 5% MV SAM, which is caused by less $[MV^{\bullet+}]_2$ being inside CB8 between the crowded viologen on the surface. I_{RR} at ±1.0 V is 82.28 and $R_{2/1}$ is 2.99×10^2, both of which are significantly lower. The stable on-state exists until at -0.3 V, from where the $R_{2/1}$ is. The stability is getting lost shown in more *J*(V) curves shown in Figure 3- 116.

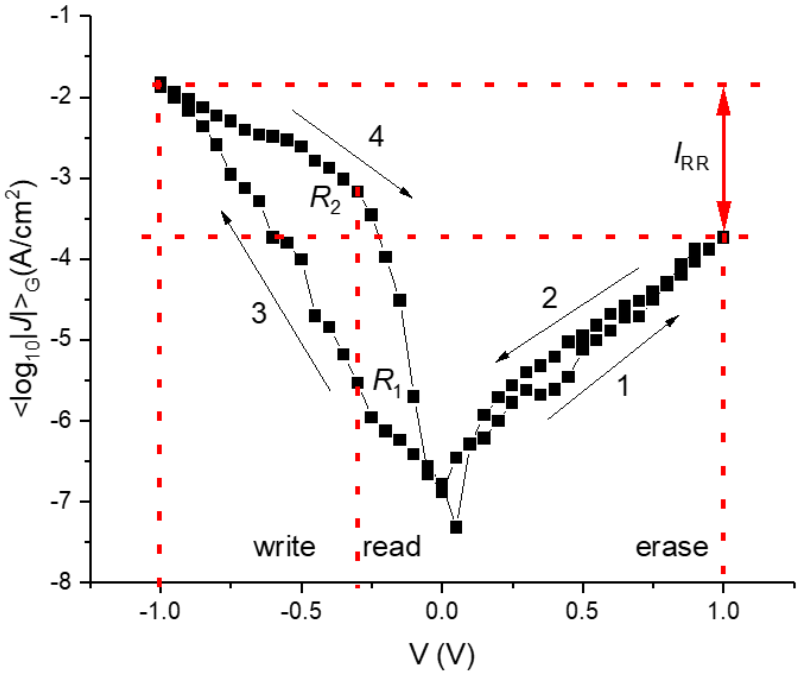

Figure 3- 115 Representative *J*(V) curve of 20% MV SAM after 50 μM CB8/MV incubation, with low conductance (R_1) and high conductance (R_2) states labeled, together with write, read and erase voltages. The black arrows indicate the scanning direction and are numbered accordingly. I^- as a counterion, voltage from -1.0 V to 1.0 V. I_{RR} is the current rectification ratio (negative).

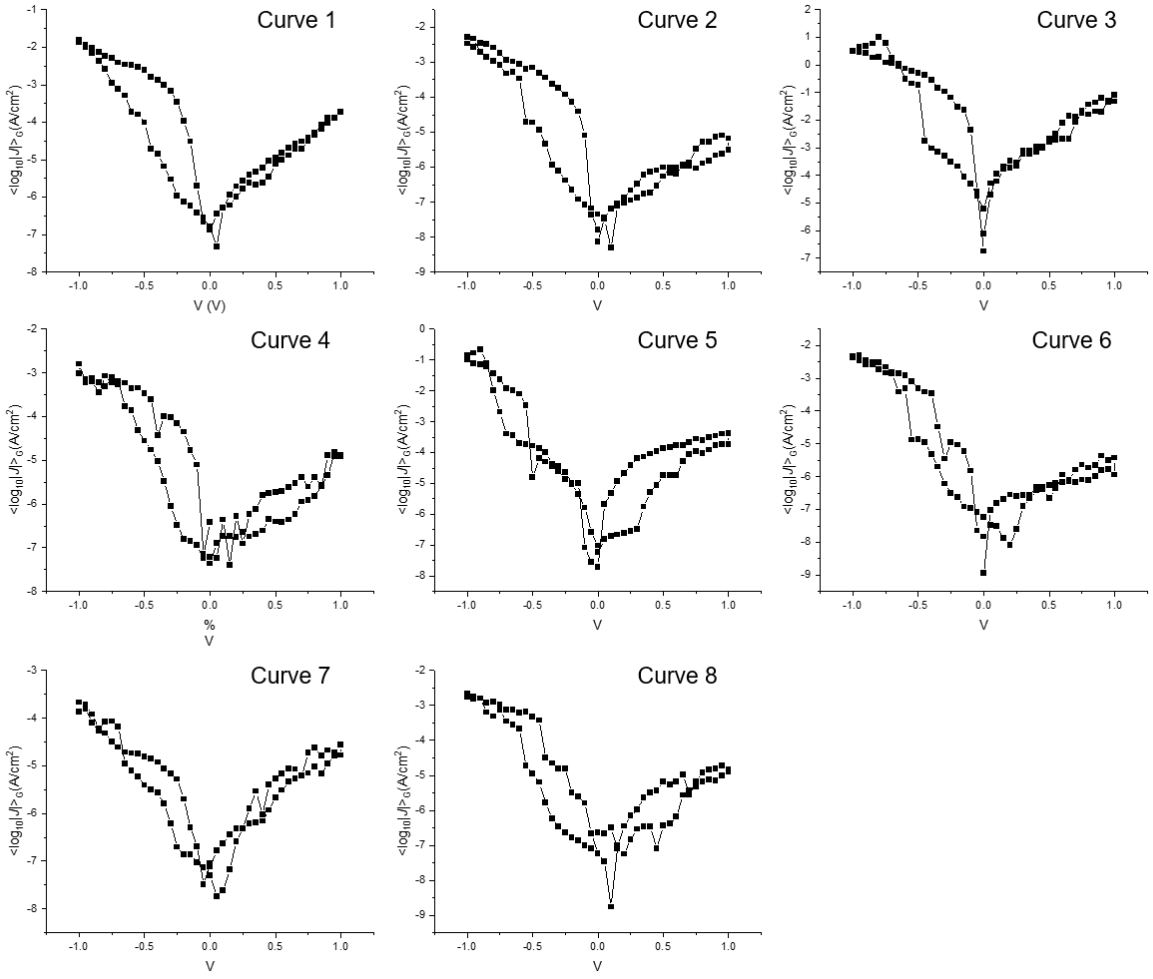

Figure 3- 116 Stability of *J*(V) curves of 20% MV SAM after 50 µM CB8/MV incubation, with I^- as a counterion.

Table 3- 31 List of I_{RR} and $R_{2/1}$ of 20% MV SAM after 50 µM CB8/MV incubation.

	V	I_{RR}	V	$R_{2/1}$
I^-	±1.0	82.28	-0.3	2.99×10^2

3.5.4.4. 100% MV SAM

The representative *J*(V) curve of 100% MV SAM is shown in Figure 3- 117, Cl^- as the counterion. Similar to the 5% MV SAM after CB8/MV incubation, the forward and reverse curves overlay well in the positive bias. There is a unipolar hysteresis at the negative side, where the $R_{2/1}$ is 1.42×10^4 in agreement to previous work in the group of Prof. Dr.

Christian A. Nijhuis.[71] I_{RR} from the curve is 1.42 x 10^4. After being exchanged to counterion I^-, the curve keeps the hysteresis in the negative bias and (Figure 3- 118), where I_{RR} is 4.90 x 10^3 and $R_{2/1}$ is 1.38 x 10^5. In further comparison, the stability of on-state is lower than for 5% MV SAM after CB8/MV incubation, more *J*(V) curve shown in Figure 3- 119 with Cl^- and Figure 3- 120 with I^-.

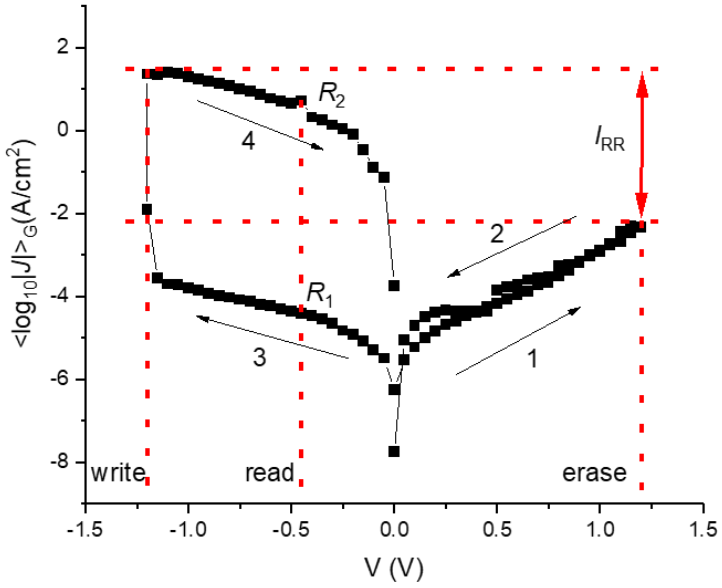

Figure 3- 117 Representative *J*(V) curve of 100% MV SAM with low and high conductance (R_1 and R_2) states labelled, together with write, read and erase voltages. The black arrows indicate the scan direction and are numbered accordingly. Cl^- as a counterion, voltage from -1.2 V to 1.2 V. I_{RR} is the current recification ratio (negative).

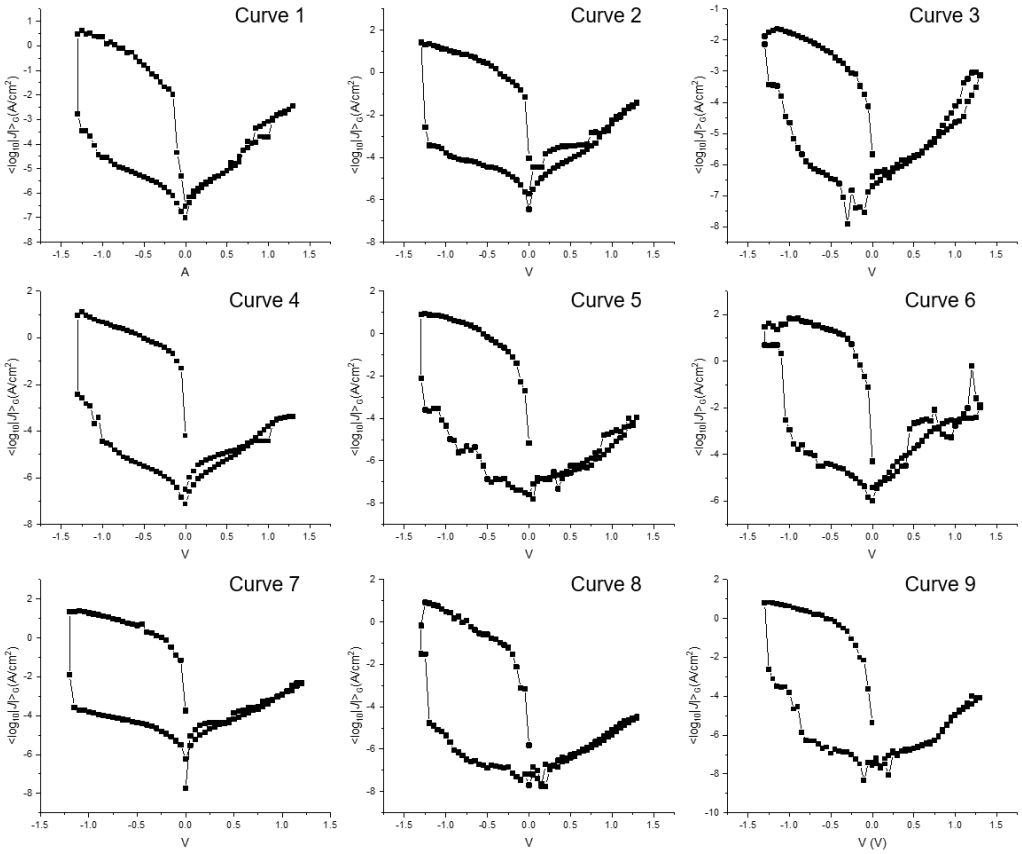

Figure 3- 118 Stability of *J*(V) curves of 100% MV SAM, counterion Cl^-.

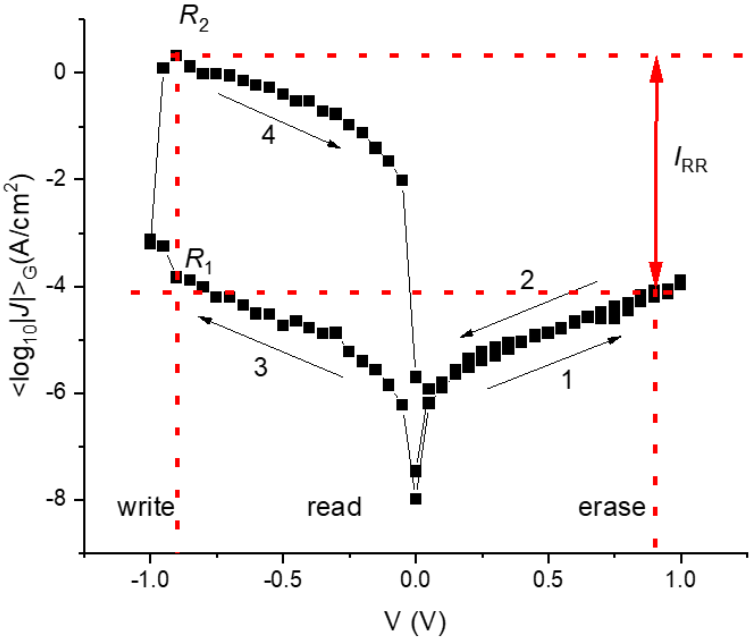

Figure 3- 119 Representative *J*(V) curve of 100% MV SAM with low conductance (R_1) and high conductance (R_2) states labeled, together with write, read and erase voltages. The black arrows

indicate the scanning direction and are numbered accordingly. I^- as a counterion, voltage from -1.0 V to 1.0 V. I_{RR} is the current rectification ratio (negative).

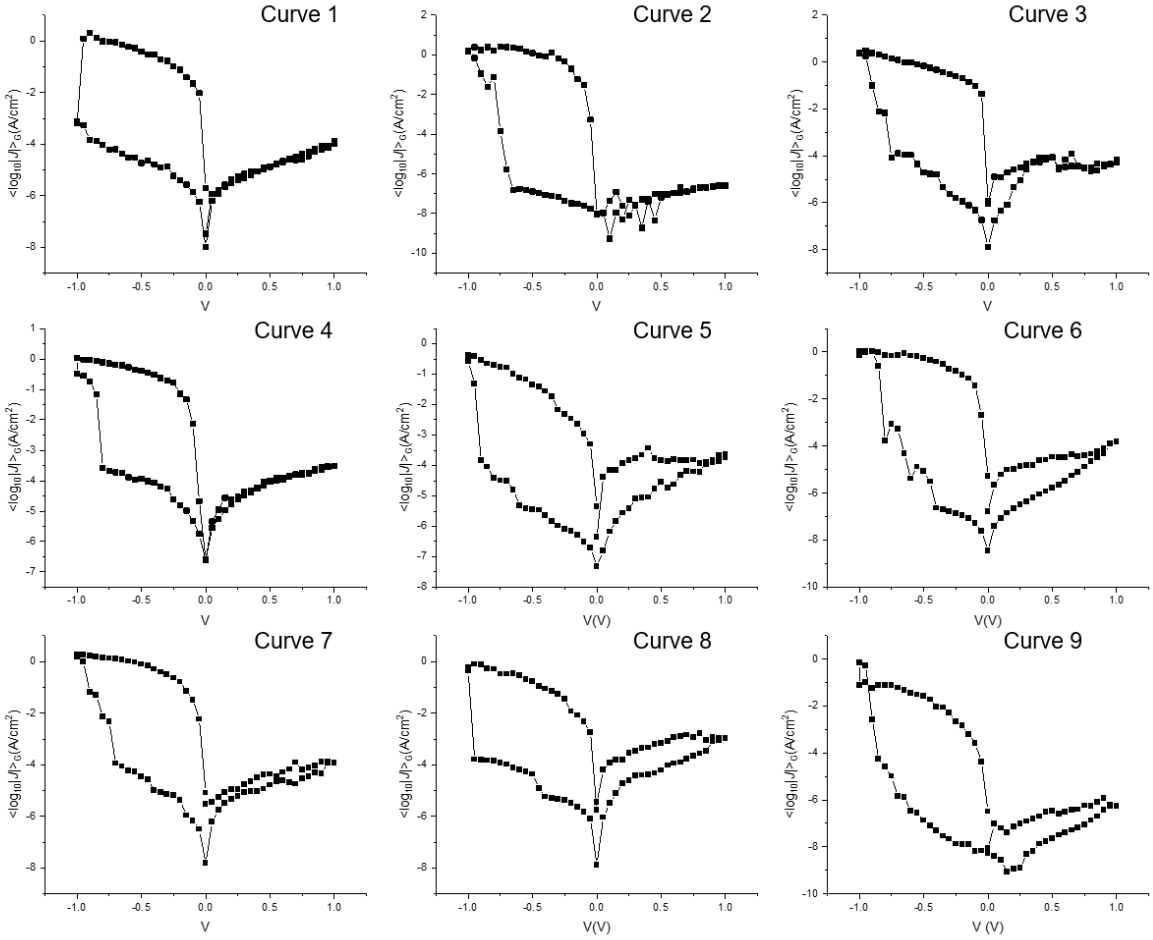

Figure 3- 120 Stability of *J*(V) curves of 100% MV SAM, counterion I^-.

Table 3- 32 List of I_{RR} and $R_{2/1}$ of 100% MV SAM.

	V	I_{RR}	V	$R_{2/1}$
Cl^-	±0.9	2.51×10^4	-0.85	1.42×10^4
I^-	±1.2	4.90×10^3	-0.45	1.38×10^5

When the SAM is transferred onto the Au electrode (Figure 3- 121, Table 3- 33 and Figure 3- 122), the stability during the whole process decreases with smaller $R_{2/1}$ and I_{RR}, 32.44 and 1.88×10^2 respectively.

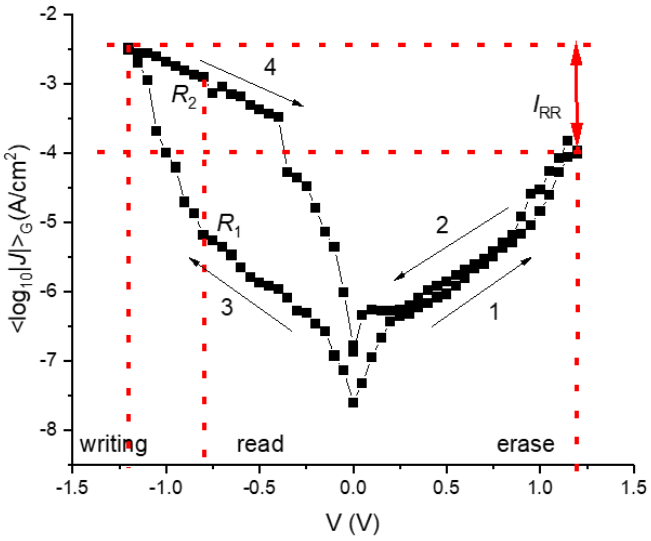

Figure 3- 121 Representative *J*(V) curve of 100% MV SAM on Au, with low conductance (R_1) and high conductance (R_2) states labeled, together with write, read and erase voltages. The black arrows indicate the scanning direction and are numbered accordingly. Br^- as a counterion, the voltage from -1.2 V to 1.2 V. I_{RR} is the current rectification ratio (negative).

Table 3- 33 List of I_{RR} and $R_{2/1}$ of 100% MV SAM on Au.

	V	I_{RR}	V	$R_{2/1}$
Br^-	±0.9	32.44	-0.85	1.88×10^2

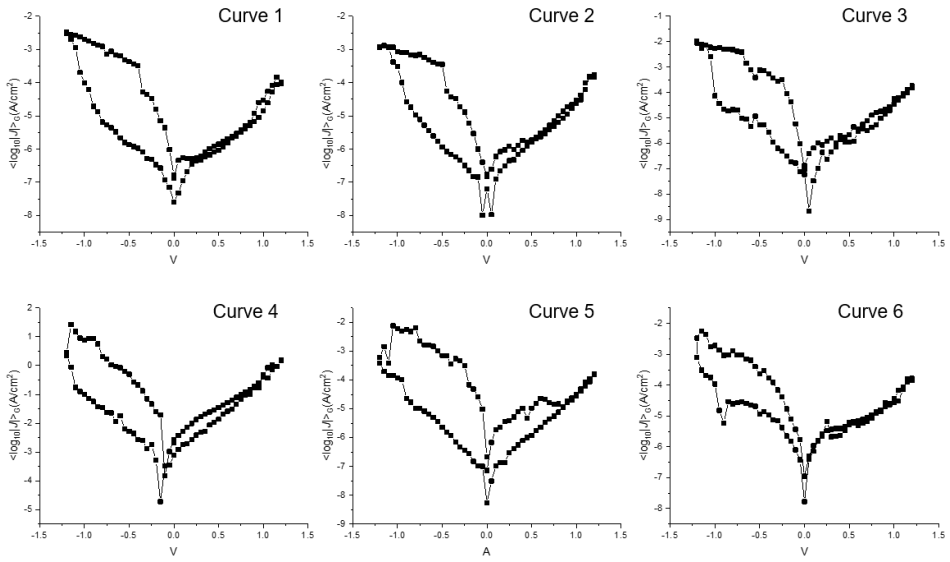

Figure 3- 122 Stability of *J*(V) curves of 100% MV SAM on Au, counterion Br^-.

3.5.4.5. Comparison of EGaIn measurement of mixed SAMs

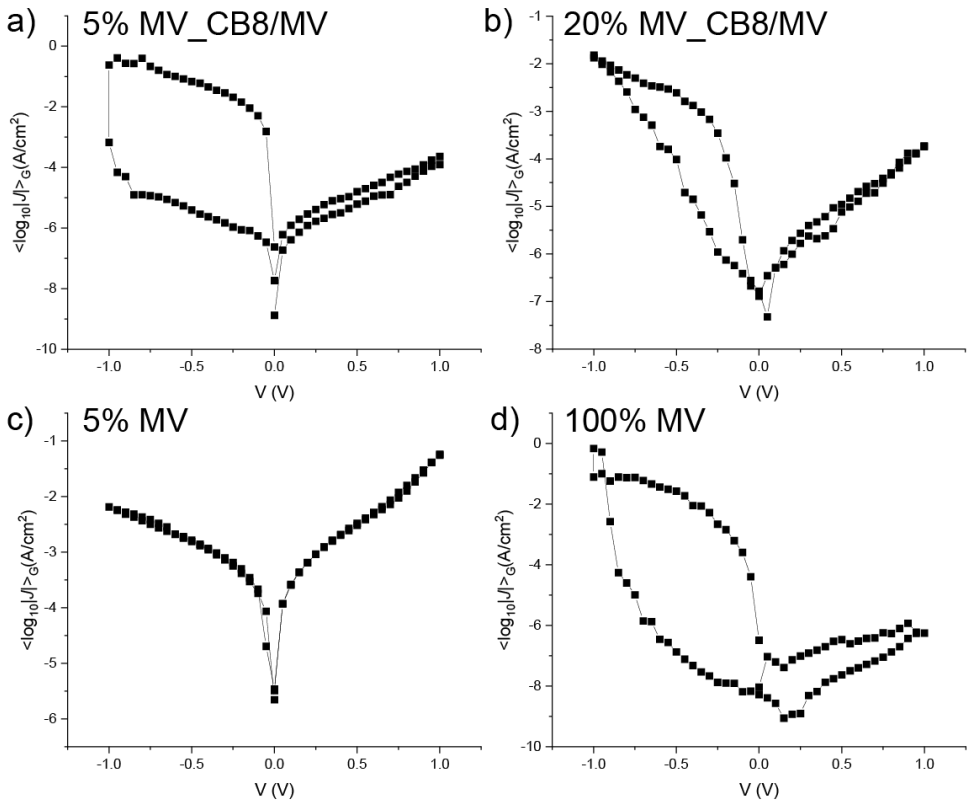

Figure 3- 123 Comparison of representative *J*(V) curves of MV SAMs on Ag. a), χ = 5% after 50 μM CB8/MV incubation. b), χ = 20% after 50 μM CB8/MV incubation. c), χ = 5%. d), χ = 100%.

The representative *J*(V) curves in different viologen compositions from EGaIn measurement are in Figure 3- 123. When χ = 5%, there is a stable and big unipolar hysteresis at negative bias after CB8/MV incubation a) compared with the absence of CB8/MV in c). It becomes smaller if χ increases to 20%, after CB8/MV incubation. If the SAM is of 100% MV, the hysteresis appears again in the negative bias. These representative curves present CB8 stabilizes $[MV^{\bullet+}]_2$ on the surface and increases the conductance of the junction.

3.5.5. Summary of CB8/MV_2 system

In this subchapter, the viologen unit was immobilized on Au/Ag electrode in varying composition from 5% to 100% for the immobilization of CB8 through host-guest interaction. The bonded CB8 was able to assembly the second viologen from the solution. The

absolute surface coverages of CB8, $MV^{\bullet+}$ and $[MV^{\bullet+}]_2$ were obtained by CV measurement, in which the amount of CB8 equaled to $[MV^{\bullet+}]_2$. The surface density of CB8 ($[MV^{\bullet+}]_2$) decreased from 2.32 x 10^{-11} mole / cm^2 at 5% MV SAM to 0.13 x 10^{-11} mole / cm^2 at 50% MV SAM, on which almost no $[MV^{\bullet+}]_2$ formed due to space effect. The EGaIn junctions of 5% MV SAM kept the unipolar hysteresis in the negative applied bias with a high current rectification ratio of 1.10 x 10^3 and an on/off state ratio of 3.16 x 10^4. The stability of the on-state has been increased compared with 100% MV SAM. CB8 creates an ideal microenvironment to stabilize $[MV^{\bullet+}]_2$ by avoiding molecular rearrangement and interference from other molecules around, which enhance the charge transport resulting from large intermolecular LUMO-LUMO coupling. This highly increases the conductance of the junctions even with lower $[MV^{\bullet+}]_2$ densities. CB8/MV_2 molecular junctions have a high potential as a constituent of resistive random access memories (RRAMs) in the future. The concept of building-up microenvironment to increase the stability and conductance (less leakage currents) through host-guest chemistry can be applied in other transistors such as developments in CMOS (complementary metal-oxide semiconductor) technology.

4. Overall summary and conclusion

In my thesis I showed various ways of the use of CBn in surface for analyte detection, biomimetic sensing and electronics. Now I will briefly summarize the main findings and conclusions for the different systems.

4.1. CBn-immobilized of CBn/indicator chemosensor for analyte detection

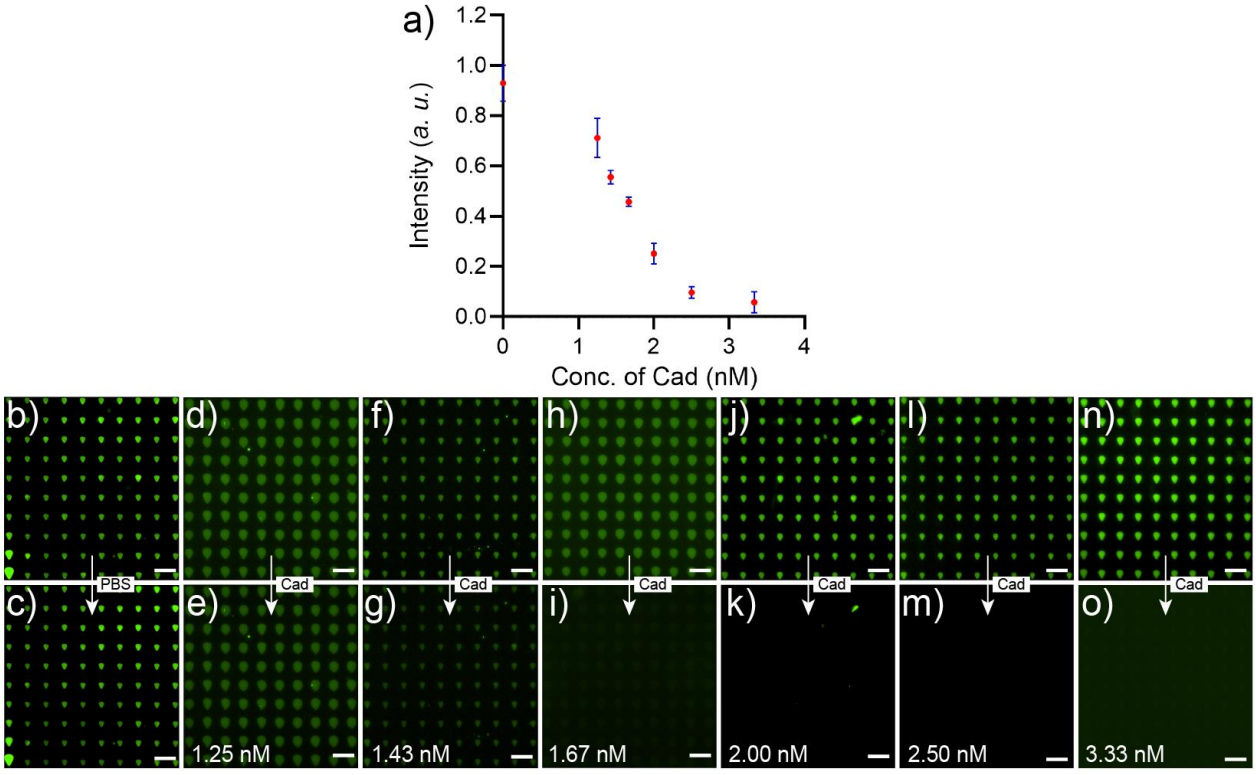

Figure 4- 1 CB7/BE chemosensor microarray for Cad detection in nanomolar concentration. a) The intensity changes in different concentrations. Images of microarray for PBS control b) and c). Images of microarrays for Cad detection from 1.25 – 3.33 nM d) – o). At 1 to 2 nM, no full replacement is achieved.

CBn-Pro were micropatterned on SiO_2-SH surface automatically controlled by μCS and CBn microarrays were established after 10 min of thiol-yne photoreaction under UV light. The generated CBn microarrays were assembled with corresponding indicators and obtained a series of CBn/indicator chemosensor microarrays. They have high sensitivity for detection of non-chromophoric analytes through emissive IDA and the limit of detection (LOD) is down to nanomole (Figure 4- 1). The CBn/indicator microarrays solve the problem of signal interference by the displaced dye to interfere because the remaining

indicator can be simply washed away. Moreover, the integration of these CBn/indicator chemosensor microarrays into microfluidic chips builds up microfluidic systems that provides, an efficient way to real-time monitor the whole process of analyte detection at the liquid-solid interface, simplify handling, and reduce the amount of analyte needed (Figure 4- 2). Finally, the multiplexed microarrays show the general advantage of surface-immobilized IDA for detection of multi-component through multi-CBn and/or multi-indicators responding differentially to different analytes. The demonstrated approaches provide significant value for the development of the IDA detecting strategies in the future for multiplexed detection of analytes in complex fluids. In addition, it can build up host-guest sensing libraries by the multiplexing of CBn and indicators (Figure 4- 3), which opens up routes for industrialization in biological or environmental applications.

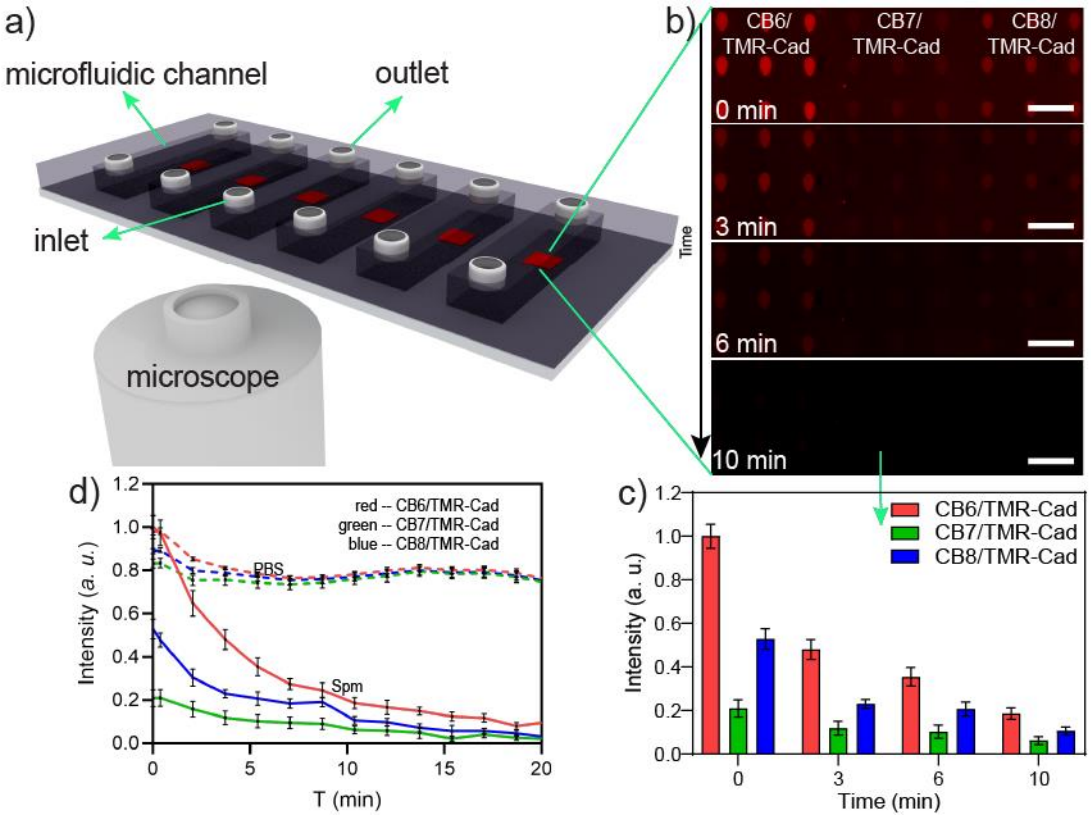

Figure 4- 2 CB6-CB7-CB8/TMR-Cad microarray for Spm detection in microfluidic channels. (a) Scheme of the microfluidic channel chip. (b) Images of chemosensor microarray containing 9 × 10 spot subpatterns of CB6, CB7 and CB8, all loaded with TMR-Cad in fluorescence, at time points of 0, 3, 6 and 10 min on incubation with 10 μM Spm. Scale bars equal to 50 μm. (c) Intensities of CB6-CB7-CB8/TMR-Cad microarray at 0, 3, 6 and 10 min incubated with 10 μM Spm in PBS screenshotted from live videos. (d) Graph of the fluorescence intensity time evolution of an array in PBS (negative control) and 10 μM Spm.

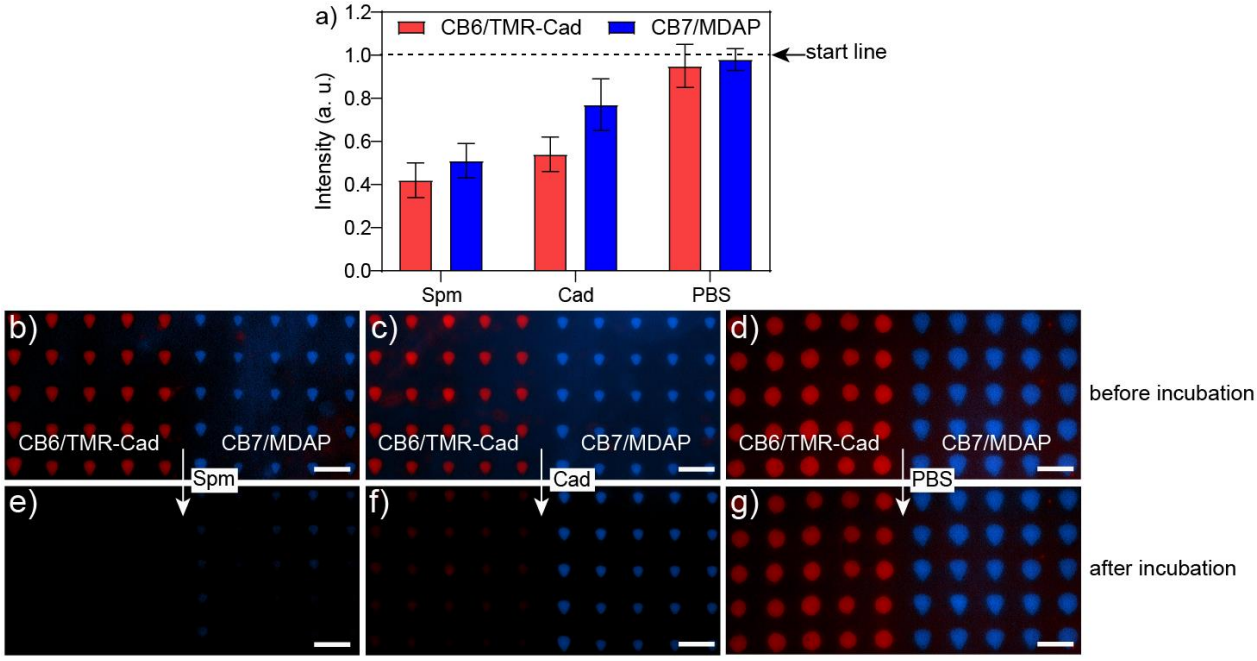

Figure 4- 3 CB6/TMR-Cad and CB7/MDAP multiplexed microarray for Cad and Spm detection. a) Fluorescence intensity graph of Spm, Cad, and PBS control after 5 min incubation. Overlay images of three CB6/TMR-Cad and CB7/MDAP multiplex microarrays b), c), and d) of Cy3 (red) and DAPI channel (blue). Overlay images of these microarrays after e) 1 μM Spm, f) Cad, or g) PBS incubation. Scale bars equal 50 μm.

4.2. Guest-mediated CBn/indicator chemosensor for analyte detection

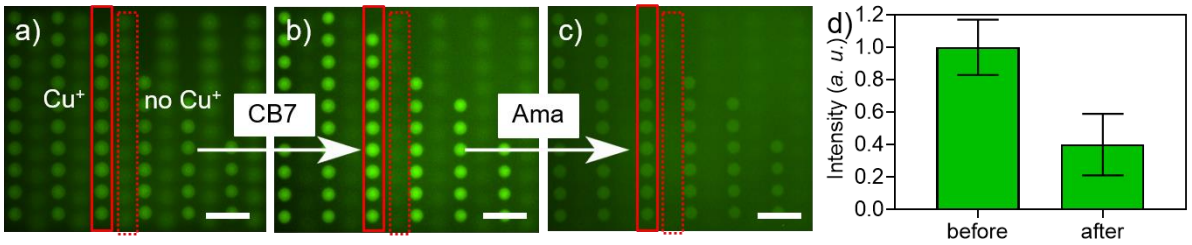

Figure 4- 4 Micropatterning of PEP-N_3 (Cu^+) and PEP-N_3 on SiO_2-Alk surface. a) Before CB7 incubation, b) after 10 mM CB7 incubation for 2 h and c) after 10 mM Ama incubation for 2 h. Scale bars equal to 100 μm. FITC 2 s.

SiO_2-Alk and SiO_2-DBCO were prepared for guest immobilization through alkyne-azide or thiol-DBCO reaction. The micropatterning of functionalized guest azides, BE-N_3, PEP-N_3 and PCP-N_3 on SiO_2-Alk was implanted by μCS. Then CBn were assembled with the bound guest to form chemosensor microarrays that are visible and were used for analyte

detection (Figure 4- 4). However, the unspecific adsorption proved by negative controls is too strong thus this strategy is not ideal for CBn immobilization.

4.3. Solvent-resisted rotaxane microarray for analyte detection

An isocyanate-functionalized (SiO_2-NCO) glass substrate was prepared for rotaxane micropatterning by µCS on SiO_2-NCO through the reaction between the HO-groups of the β-CD stopper and isocyanate. The fabricated rotaxane microarray allows for L-Trp detection down to submicromolar concentrations which shows the remarkable sensitivity enhancement. Importantly, the rotaxane-functionalized microarrays are more selective than printed microarrays with the binary CB8/MDAP chemosensor complex, proved by the detection of hydrophobic and strongly CB8-binding guest Mem (Figure 4- 6). Mem is not an electron-rich aromatic compound and thus cannot bind next to the rotaxane-protected reporter dye DAP. Furthermore, the µCS immobilization also allows for printing reference dyes next to the chemosensor array to normalize the emission signal. The immobilization of CB8/indicator complex through the form of rotaxane on surfaces opens up its potential for future integration into lab-on-a-chip designs with plasmonic biosensors.

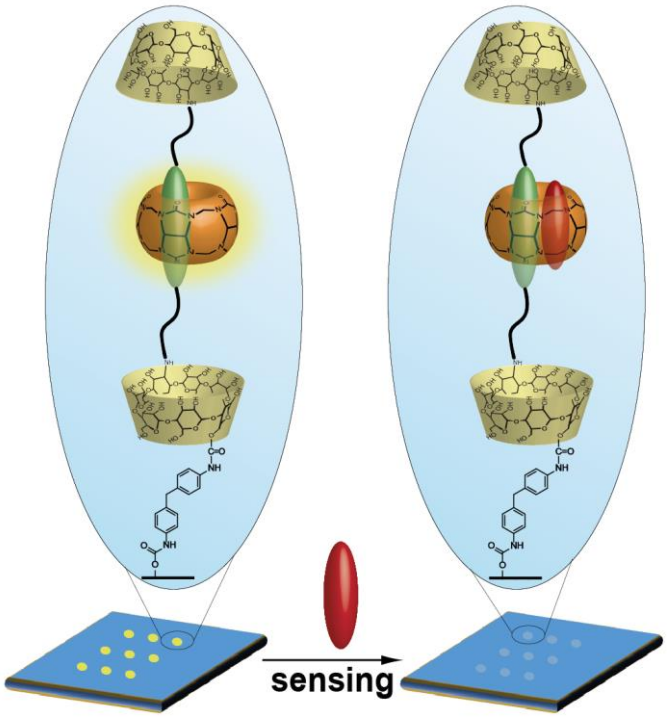

Figure 4- 5 Scheme of rotaxane microarray for analyte detection.

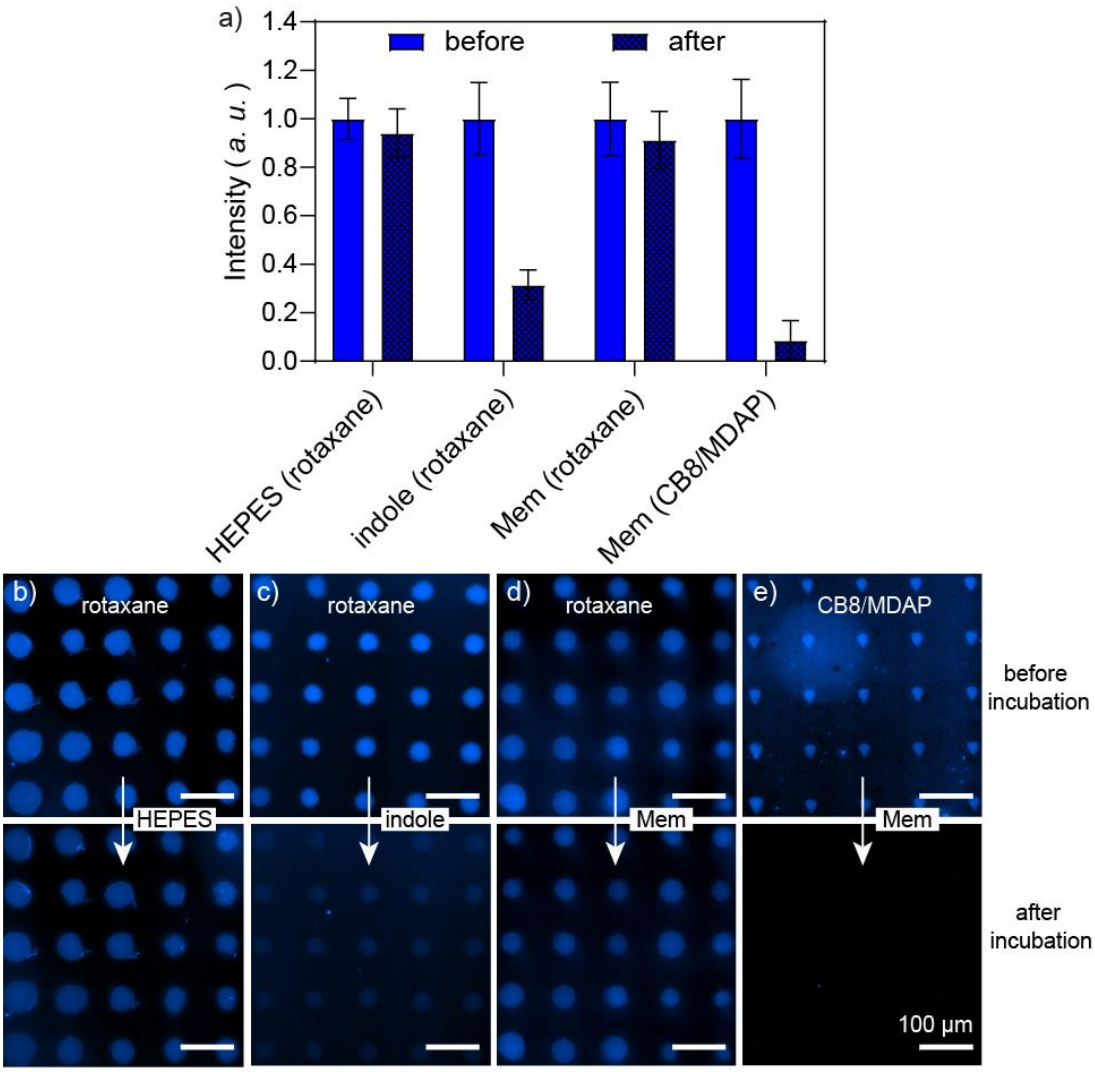

Figure 4- 6 Detection of indole and Mem with rotaxane and CB8/MDAP microarrays. a) Quantification of the fluorescence intensities of the microarray spots before and after the indole and Mem incubation. b)-e) Fluorescence images of the microarrays before and after incubation with an analyte (10 µM) or pure HEPES as control. Images were taken with 10 s exposure time and DAPI filter. Scale bars equal 100 µm.

4.4. Analyte sensing in a biomimetic cell environment

Combined with the CBn/indicator chemosensor microarrays, biomimetic lipid membranes, SLB micropatterned by DPN, PPL and µCS, or homogenous SALB, provides an approach to evaluate membrane permeability. Compared with DPN-printing, PPL and µCS-printed SLB cover sensor arrays keep them on the surface for a longer time. SALB is a homogenous coating lipid membrane that covers the wall of the microchannel including the microarray substrate, thus possible leakage on the edges of the membranes can be

avoided. After combination with rotaxane microarray, where both CB8 and DAP are immobilized, analyte detection together with membrane permeability can be evaluated in a biomimetic cell-like environment. DOPS slows down the transport onto the surface from 2 min to 5 min, which caused by the slower diffusion rate of tryptamine through the membrane due to charge effects.

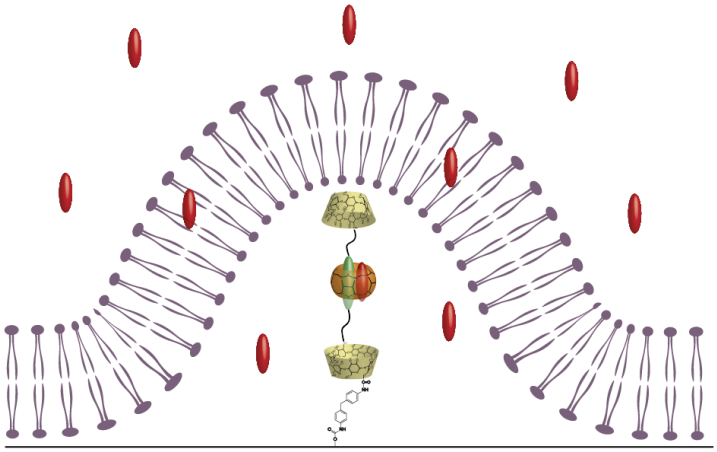

Figure 4- 7 Scheme of lipid membrane-covered rotaxane chemosensor.

4.5. Application of CBn in molecular electronics

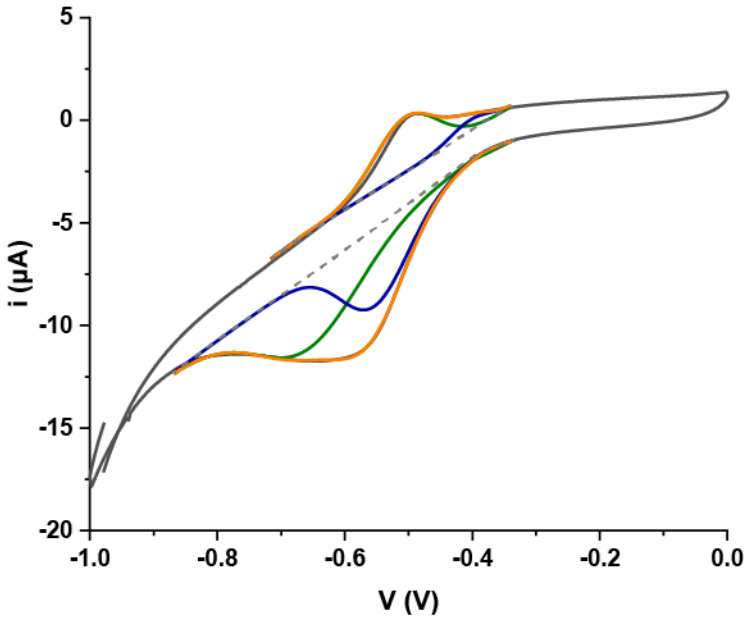

Figure 4- 8 Cyclic voltammogram of 5%MV SAM on Au after CB8/MV incubation, with Ag/AgCl as the reference electrode. The first redox wave is split into two components associated with the

reduction of MV^{2+} to $MV^{\bullet+}$ radical (blue line) and $[MV^{\bullet+}]_2$ formation (green line). The orange line is the sum of the blue and green lines.

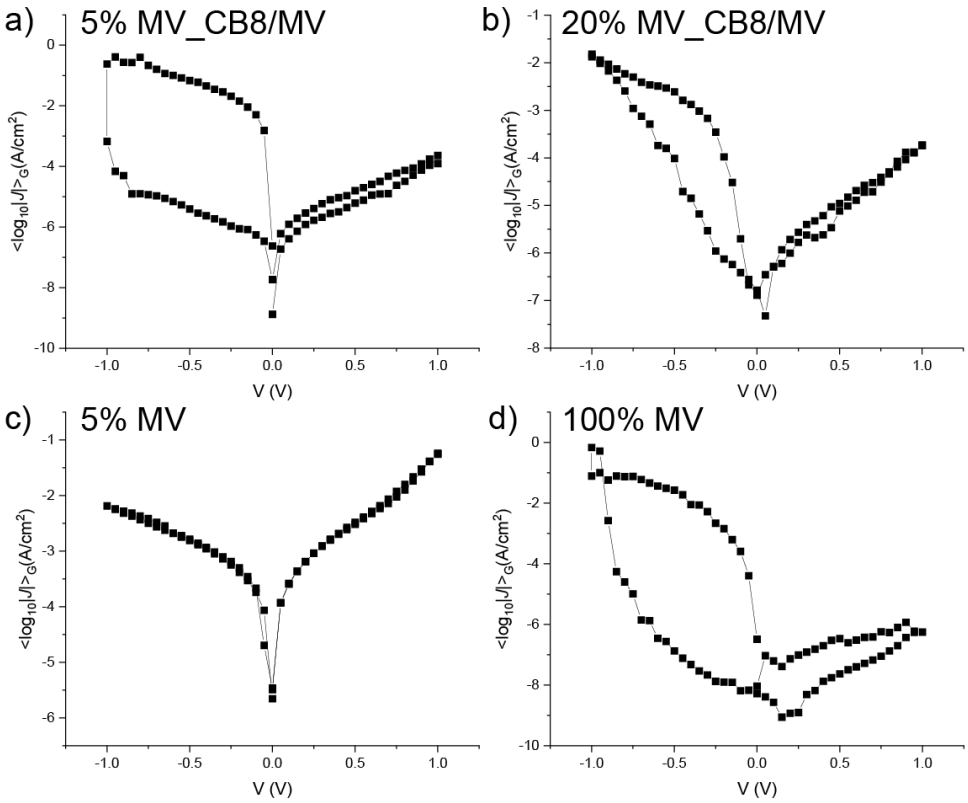

Figure 4- 9 Comparison of representative *J*(V) curves of MV SAMs on Ag. a), χ = 5% after 50 μM CB8/MV incubation. b), χ = 20% after 50 μM CB8/MV incubation. c), χ = 5%. d), χ = 100%.

Viologen units are immobilized on Au/Ag electrodes in varying compositions from 5% to 100% of a alkanethiol SAM for the immobilization of CB8 through host-guest interaction. The MV mediated CB8 was able to assembly a second viologen from the solution. The absolut surface coverages of CB8, $MV^{\bullet+}$ and $[MV^{\bullet+}]_2$ were obtained by CV measurement (Figure 4- 8), in which the amount of CB8 equaled to $[MV^{\bullet+}]_2$. The surface density of CB8 ($[MV^{\bullet+}]_2$) decreased from 2.32 x 10^{-11} mole / cm^2 at 5% MV SAM to 0.13 x 10^{-11} mole / cm^2 at 50% MV SAM, on which almost no $[MV^{\bullet+}]_2$ formed due to steric effects. The EGaIn junctions of 5% MV SAM kept the unipolar hysteresis in the negative applied bias with a high current rectification ratio of 1.10 x 10^3 and an on/off state ratio of 3.16 x 10^4. The stability of the on-state has been increased compared with 100% MV SAM. CB8 highly increases the conductance of the junctions even with lower $[MV^{\bullet+}]_2$ through the enhancement of charge transport by avoiding molecular rearrangement and interference

from other molecules around resulting from large intermolecular LUMO-LUMO coupling. The built-up CB8/MV_2 molecular junction has high potential as a member of resistive random access memories (RRAMs) in the future. The concept of microenvironment to increase the stability and conductance (less leakage currents) through host-guest chemistry can be applied in other transistors such as developments in CMOS (complementary metal-oxide semiconductor) technology.

The results overall give new impulses to CBn immobilization, which will influence future applications e.g. in, but surely not limited to, chemical engineering, bioengineering and electronic engineering.

5. Experimental section

5.1. Surface modification

Except a few compounds including modified CBn, modified indicator and rotaxane provided from the group of Dr. Frank Biedermann, INT, KIT, all materials are commercially available.

5.1.1. Plasma activation

Standard glass coverslip SiO_2 (VWR, Germany) was sonicated with chloroform, ethanol and water for 5 min, respectively. Then, SiO_2 was activated with oxygen plasma (10 sccm O_2, 0.2 mbar, 100 W, 2 min, ATTO system, Diener electronics, Germany) to get hydroxylated surface SiO_2-OH.

5.1.2. Thiol surface

SiO_2-OH was immersed in 2 vol% MPTMS ((3-mercaptopropyl) trimethoxysilane) in toluene for 5 h. Finally, this SiO_2-SH substrate was ready to use for lithography after rinsing with acetone for 2 min and water and then dried with N_2.

5.1.3. Homogeneous SiO_2-CBn surfaces

SiO_2-SH was covered with 1 mg/mL CBn-Pro (CB6-Pro, CB7-Pro and CB8-Pro) in DMSO, irradiated under 254 nm UV light for 10 min and washed away the rest of the solution with water and ethanol, to get homogeneous SiO_2-CB6, SiO_2-CB7 and SiO_2-CB8 surfaces.

5.1.4. Alkyne surface

SiO_2-SH were silanized in a 1 vol% (3-Glycidyloxypropyl)-trimethoxysilane (GPTMS) solution in toluene for 8–12 h.[98] To clean off excess silane, glass slides were sonicated in acetone for 1 min and then finally submerged into a solution of 2 vol% propargylamine in acetonitrile for 8 h at 50 °C. After the alkynization, the cover slips were sonicated in ethanol for 30 s, dried with N_2 and stored in a glass petri dish until use.

5.1.5. Isocyanate surface

SiO_2-OH surface was immersed in 1 mg/mL 4,4′-diisocyanato methylendibenzol (MDI) containing 1 µL/mL dibutyltin dilaurate (TDL) as catalyst in anhydrous DMSO at 80°C for

24 h. Finally, the substrate (SiO_2-NCO) was rinsed with acetone for 2 min and dried with N_2.

5.1.6. Template-stripped bottom electrode fabrication

The bottom electrodes were prepared according to previously reported literature.[71] Shortly, 400-nm-thick Ag and 200 nm Au layers were deposited on clean silicon (Si, 100) wafers using a thermal evaporator (Shen Yang Ke Yi). The cleaned glass slides were glued by thermal adhesive (EPOTEK 353ND) on the metal surface, then heated at 80 °C for 3 h. The metal surface in contact with the wafer was then peeled off from the template and immediately immersed in the corresponding thiol solution in ethanol.

5.1.7. MV surface

Solutions (1 mM) with different mole factions of MV-C11-SH (χ) in C8-SH were prepared in ethanol under an atmosphere of N_2. The freshly template-stripped substrates (Ag, Au) were immediately immersed in the solution kept under a N_2 atmosphere at room temperature for 3 h. Finally, the substrates were sligtly washed with ethanol to remove unspecific adsorbed thiols followed by drying gently in a stream of N_2.

5.1.8. Contact angle characterization

The static contact angles of water droplets on SiO_2 and homogeneously functionalized surfaces were recorded at room temperature through an OCA-20 contact angle analyzer (Data Physics Instruments GmbH). For each measurement, more than five water droplets with 2 µL were dropped on the surface at the rate of 2 µL s^{-1} and the average contact angle value was reported.

5.1.9. X-ray photoelectron spectroscopy (XPS) characterization

XPS characterization was carried out by a K-Alpha+ XPS spectrometer (ThermoFisher Scientific, East Grinstead, UK). Data acquisition and processing were obtained by the Thermo Avantage software. Sample analysis was conducted by a micro-focused, monochromated Al Kα X-ray source (400 µm spot size). The electrons kinetic energy was measured through a 180° hemispherical energy analyzer for elemental spectra in the constant analyzer energy mode at 50 eV pass energy. The K-Alpha+ charge compensation system was applied to avoid any localized charge build-up at the use of 8

eV energy electrons and low-energy argon ions. The spectra were fitted with Voigt profiles (BE uncertainty: ±0.2 eV) and Scofield sensitivity factors were employed for quantification.[99] All spectra were referenced on the C 1s peak (C-C, C-H) at 285.0 eV binding energy controlled through the well-known photoelectron peaks of metallic Cu, Ag and Au, respectively.

5.2. Ink preparation

5.2.1. CBn inks

CB6 ink contained 1 mg/mL of crude CB6-Pro in DMSO, 40 vol% 3 mg/mL tris(2-carboxyethyl)phosphine hydrochloride (TCEP) in water and 20 vol% glycerol. CB7 ink contained 1 mg/mL of CB7-Pro in DMSO, 40 vol% 3 mg/mL of TCEP in water and 20 vol% glycerol. CB8 ink contained 1 mg/mL of crude CB8-Pro in DMSO, 40 vol% 3 mg/mL of TCEP in water and 20 vol% glycerol. Reference ink included 100 μg/mL of RD in DMSO, 40 vol% 3 mg/mL of TCEP in water and 20 vol% glycerol. The inks for the printing controls contained 1 mg/mL pure CB7, CB7-OH or CB7-Pro in DSMO, 40 vol% 3 mg/mL tris(2-carboxyethyl)phosphine hydrochloride (TCEP) in water and 20 vol% glycerol for each. The solubility of CB7-Pro is lower than its crude product used above.

5.2.2. CBn/indicator and indicator-azide inks

CBn/indicator ink or indicator-azide ink contained 70% CBn/indicator complex or indicator-azide ink solution in water and 30% glycerol for each.

5.2.3. Rotaxane and DAP-thiol inks

Rotaxane ink contained 80% (v/v) 3 mg/mL rotaxane in anhydrous DMSO, 10% (v/v) TDL and 10% (v/v) PEG 600. DAP-thiol ink contained 80% (v/v) 3 mg/mL DAP-thiol in anhydrous DMSO, 10% (v/v) TDL and 10% (v/v) PEG 600.

5.2.4. Lipid inks

2 μL of the desired phospholipid mixture (20 mg/mL in chloroform) were transferred into resevoirs of inkwell (ACST, U.S.A.) seperacterally and the solvent was evaporated under a low pressure through storing in a vacuum desiccator for 30 min.

5.3. Printing techniques

5.3.1. Microchannel cantilever spotting (µCS)

0.5 µL of the prepared ink was applied to the microchannel cantilever[100] (SPT-S-C10S, Bioforce Nanosciences), the chip was then mounted to the lithography setup (NLP2000, Nanoink) and spotting took place by contacting the tip with surface for defined durations (~0.5 to 1 s) at a controlled humidity of 40% to prevent premature drying.

After printing with CBn-Pro microarrays together with RD, SiO_2-SH substrates were irradiated under 254 nm UV light for 10 min, then washed with water and ethanol, and finally dried with a nitrogen stream.[101] The rest of the thiols were reacted with N-ethylmaleimide (NEM) acting as a blocking agent through incubation in 10 mg/mL NEM water solution, pH 7.0, for 2 h and then washed with water, dried with N_2 stream.

After printing with rotaxane or DAP-SH, SiO_2-NCO substrates were heated to 80°C for 24 h, then washed with ethanol, dried with a stream of N_2.

5.3.2. Dip-Pen Nanolithography (DPN)

The lipid patches were micropatterned by DPN 5000 (Nanoink Inc., U.S.A.) with the B-side of M-type cantilever array where there are 12 tips with a 66 µm pitch (Advanced Creative Solutions Technology (ACST, U.S.A.). These tips were homogenously coated with lipid by dipping into the matched inkwells for 5 minutes in a 60 % humidity (RH). Afterwards, the coated tips were moved to the desired location on the substrate and lipid patch arrays were written by moving tips at 30% - 40% RH with hatch lines of 0.5 µm pitch and a writing speed of 0.2 to 2 µm/s.

5.3.3. Polymer-Pen Lithography (PPL)

PPL Stamps were prepared as according to reported procedure in the literature.[98] The polymer pen array was inked with 4 µL of the respective ink solutions through spin coating (3500 rpm, 3 min). Micropatterning was controlled on the NLP 2000 instrument with a custom made pen array holder. The pen array was firstly glued with a mixture of two component epoxy resin adhesive (Uhu, Germany) on a microscopic glass slide, then this glass slide was glued on the bar of a custom made holder that would be mounted onto the instrument. Leveling of the stamp parallel onto the substrate was controlled by an optical alignment procedure, which allowed the elastic tip deformation of the stamp upon tip array-surface to contact a clean sacrificial cover slip. Patterning was carried out under

humidity-controlled conditions (60% to 80% RH). Writing schemes were arrays of 10 × 10 dot features with a pitch of 10 µm or 100 × 100 dot features to cover whole surface, dwell times of 1–5 s. After lithography, all samples were kept at ambient conditions until use.

5.4. Analyte detection

5.4.1. Indicator assembly

Indicator solutions solutions were prepared in PBS. For indicator assembly, the CBn-patterned substrates were covered with 20 µL of indicator solution for 1 min and then washed with water, dried with a stream of N_2.

5.4.2. Analyte detection

Analyte solutions were prepared in 1X PBS or 10 mM HEPES buffer, pH 7.0. 20 µL of analyte solution was dropped on the substrate with ready chemosensor microarray. After corresponding time, the substrate was washed with water and dried with a stream of N_2.

5.4.3. Fluorescence microscopy

The fluorescence imaging was performed on a Nikon Eclipse Ti2 inverted fluorescence microscope (Nikon, Germany) equipped with an Intensilight illumination, a Nikon DS Qi2 camera, and DIA, Cy3, GFP and DAPI filters sets (Nikon Y-2E/C), and connected with the professional software Nikon-Elements.

5.4.4. Statictical analysis

All data is expressed as mean ± standard deviation of at least three independent measurements.

5.4.5. Microfluidic systems

Dynamic analyte detection or lipid bilayer stability were performed in a microfluidic channel. Matching substrates printed with CBn microarrays, lipid bilayers or rotaxane microarray were mounted with microfluidic channels (sticky-Slide VI 0.4 Luer, ibidi Germany) and set on the inverted microscope. Buffer, or solutions with indicators or analytes, were added in each channel from one on-chip reservoir (the Luer connector) and then removed from the other side through manually pipetting 100 µL each time (the chips can accommodate 30

µl in the micro-channel, plus 120 µl in the reservoirs, 60 µl in each). Except CBn microchannels, only buffer or analyte soltions were injected into the microchannls.

In CBn microchannels, indicator solutions were firstly injected and then washed with PBS buffer until excess indicator was removed and arrays were clearly visible under the inverted microscope. Afterwards, analyte solution of desired concentration was introduced by pipetting on 100 µl again (3x for Spm within a minute, 1x for Cad detection, as here the detection process is happening on a much shorter timescale).

The whole process was monitored and recorded to videos by microscope.

5.5. Solvent-assisted lipid bilayers (SALB)

SALB were prepared according to the previously reported literature.[63] Corresponding lipid dissolved in isopropanol at a concentration of 0.5 mg mL^{-1} was firstly injected into the microchannel followed by an aqueous buffer solution of 150 mM NaCl and 10 mM Tris (pH 7.5) for the solvent-exchange. Afterwards, the channel was recycled with the buffer for three time.

5.6. Molecular electronics

5.6.1. MV_2@CB8 formation

The χMV SAMs (except χ = 100%) were immersed in aqueous solutions of 50 µM CB8/MV 1:1 complex for 3 h and washed with water, dried with a stream of N_2.[38, 71]

5.6.2. Ion excnange for SAMs on Au

The χMV SAMs (except χ = 100%) were immersed in aqueous solutions of 50 µM CB8/MV 1:1 complex in 0.1 M NaX (X=I^-, Cl^-, Br^-) for 10-30 min under an atmosphere of N_2, then rinsed first with deionized (DI) water and briefly with ethanol, followed by drying in a stream of N_2.[71] As controls, The substrates with χMV SAMs were immersed in aqueous solutions of 0.1 M NaX (X=I^-, Cl^-, Br^-) for 10-30 min under an atmosphere of N_2, then rinsed first with deionized (DI) water and briefly with ethanol, followed by drying in a stream of N_2.

5.6.3. Cyclic voltammetry (CV)

An Autolab PGSTAT 302T system was equipped with NOVA 2.1 software to record the CVs of χMV SAMs on Au in different electrolytes.[71] A custom-made electrochemical cell with three electrodes set (platinum disk counter electrode, Ag/AgCl reference electrode and Au working electrode) was used. 50 μM CB8, MV and CB8/MV 1:1 complex in 0.1 M NaCl were used as the electrolyte. The CVs were recorded at a scan rate of 0.2 V s^{-1}.

5.6.4. Eutectic Gallium-Indium (EGaIn) junctions

The current density J (in A cm^{-2}) as a function of bias V (in V) was measured with cone-shaped tips of GaOx/EGaIn as the top electrode, fabricated according to previously reported procedures.[71] In short, the bottom electrode was grounded and the top electrode of GaOx/EGaIn was biased according to 0 V→+V→0 V→-V→0 V through a costumer made software (NI Labview 2020).

6. Literature

[1] W. A. Freeman, W. L. Mock, N. Y. Shih, Cucurbituril, *Journal of the American Chemical Society* **1981**, *103*, 7367-7368.

[2] S. J. Barrow, S. Kasera, M. J. Rowland, J. del Barrio, O. A. Scherman, Cucurbituril-Based Molecular Recognition, *Chemical Reviews* **2015**, *115*, 12320-12406.

[3] J. Lagona, P. Mukhopadhyay, S. Chakrabarti, L. Isaacs, The Cucurbit[n]uril Family, *Angewandte Chemie International Edition* **2005**, *44*, 4844-4870.

[4] R. Behrend, E. Meyer, F. Rusche, I. Ueber Condensationsproducte aus Glycoluril und Formaldehyd, *Justus Liebigs Annalen der Chemie* **1905**, *339*, 1-37.

[5] L. A. Wingard, E. C. Johnson, J. J. Sabatini, Efficient method for the cycloaminomethylation of glycoluril, *Tetrahedron Letters* **2016**, *57*, 1681-1682.

[6] C. Marquez, H. Fang, W. M. Nau, Cucurbiturils: molecular nanocapsules for time-resolved fluorescence-based assays, *IEEE Transactions on NanoBioscience* **2004**, *3*, 39-45.

[7] J. Kim, I.-S. Jung, S.-Y. Kim, E. Lee, J.-K. Kang, S. Sakamoto, K. Yamaguchi, K. Kim, New Cucurbituril Homologues: Syntheses, Isolation, Characterization, and X-ray Crystal Structures of Cucurbit[n]uril (n = 5, 7, and 8), *Journal of the American Chemical Society* **2000**, *122*, 540-541.

[8] J. W. Lee, S. Samal, N. Selvapalam, H.-J. Kim, K. Kim, Cucurbituril Homologues and Derivatives: New Opportunities in Supramolecular Chemistry, *Accounts of Chemical Research* **2003**, *36*, 621-630.

[9] K. Kim, N. Selvapalam, Y. H. Ko, K. M. Park, D. Kim, J. Kim, Functionalized cucurbiturils and their applications, *Chemical Society Reviews* **2007**, *36*, 267-279.

[10] B. Vinciguerra, L. Cao, J. R. Cannon, P. Y. Zavalij, C. Fenselau, L. Isaacs, Synthesis and Self-Assembly Processes of Monofunctionalized Cucurbit[7]uril, *Journal of the American Chemical Society* **2012**, *134*, 13133-13140.

[11] M. M. Ayhan, H. Karoui, M. Hardy, A. Rockenbauer, L. Charles, R. Rosas, K. Udachin, P. Tordo, D. Bardelang, O. Ouari, Comprehensive synthesis of monohydroxy-cucurbit[n]urils (n = 5, 6, 7, 8): High purity and high conversions, *Journal of the American Chemical Society* **2015**, *137*, 10238-10245.

[12] S. Y. Jon, N. Selvapalam, D. H. Oh, J.-K. Kang, S.-Y. Kim, Y. J. Jeon, J. W. Lee, K. Kim, Facile Synthesis of Cucurbit[n]uril Derivatives via Direct Functionalization: Expanding Utilization of Cucurbit[n]uril, *J. Am. Chem. Soc.* **2003**, *125*, 10186–10187.

[13] S. Zhang, Z. Domínguez, K. I. Assaf, M. Nilam, T. Thiele, U. Pischel, U. Schedler, W. M. Nau, A. Hennig, Precise supramolecular control of surface coverage densities on polymer micro- and nanoparticles, *Chemical Science* **2018**, *9*, 8575-8581.

[14] S. Walker, R. Oun, F. J. McInnes, N. J. Wheate, The Potential of Cucurbit[n]urils in Drug Delivery, *Israel Journal of Chemistry* **2011**, *51*, 616-624.

[15] L. Zheng, S. Sonzini, M. Ambarwati, E. Rosta, O. A. Scherman, A. Herrmann, Turning Cucurbit[8]uril into a Supramolecular Nanoreactor for Asymmetric Catalysis, *Angewandte Chemie International Edition* **2015**, *54*, 13007-13011.

[16] Dönüs Tuncel, Özlem Ünal, M. Artar, Supramolecular Assemblies Constructed by CucurbiturilCatalyzed Click Reaction, *Israel Journal of Chemistry* **2011**.

[17] C. Zhong, C. Hu, R. Kumar, V. Trouillet, F. Biedermann, M. Hirtz, Cucurbit[n]uril-Immobilized Sensor Arrays for Indicator-Displacement Assays of Small Bioactive Metabolites, *ACS Applied Nano Materials* **2021**, *4*, 4676-4687.
[18] H. Yu, J. Li, S. Li, Y. Liu, N. E. Jackson, J. S. Moore, C. M. Schroeder, Efficient Intermolecular Charge Transport in pi-Stacked Pyridinium Dimers Using Cucurbit[8]uril Supramolecular Complexes, *J Am Chem Soc* **2022**.
[19] H. Chen, S. Hou, H. Ma, X. Li, Y. Tan, Controlled gelation kinetics of cucurbit[7]uril-adamantane cross-linked supramolecular hydrogels with competing guest molecules, *Scientific Reports* **2016**, *6*, 20722.
[20] X. J. Loh, J. del Barrio, T.-C. Lee, O. A. Scherman, Supramolecular polymeric peptide amphiphile vesicles for the encapsulation of basic fibroblast growth factor, *Chemical Communications* **2014**, *50*, 3033-3035.
[21] S. Sinn, F. Biedermann, Chemical Sensors Based on Cucurbit[n]uril Macrocycles, *Israel Journal of Chemistry* **2018**, *58*, 357-412.
[22] R. Wang, D. H. Macartney, Cucurbit[7]uril host–guest complexes of the histamine H2-receptor antagonist ranitidine, *Organic & Biomolecular Chemistry* **2008**, *6*, 1955-1960.
[23] A. T. Bockus, L. C. Smith, A. G. Grice, O. A. Ali, C. C. Young, W. Mobley, A. Leek, J. L. Roberts, B. Vinciguerra, L. Isaacs, A. R. Urbach, Cucurbit[7]uril–Tetramethylrhodamine Conjugate for Direct Sensing and Cellular Imaging, *Journal of the American Chemical Society* **2016**, *138*, 16549-16552.
[24] S. K. Ghosh, A. Dhamija, Y. H. Ko, J. An, M. Y. Hur, D. R. Boraste, J. Seo, E. Lee, K. M. Park, K. Kim, Superacid-Mediated Functionalization of Hydroxylated Cucurbit[n]urils, *Journal of the American Chemical Society* **2019**, *141*, 17503-17506.
[25] C. Hu, L. Grimm, A. Prabodh, A. Baksi, A. Siennicka, P. A. Levkin, M. M. Kappes, F. Biedermann, Covalent cucurbit[7]uril–dye conjugates for sensing in aqueous saline media and biofluids, *Chemical Science* **2020**, *11*, 11142-11153.
[26] S. Sinn, E. Spuling, S. Bräse, F. Biedermann, Rational design and implementation of a cucurbit[8]uril-based indicator-displacement assay for application in blood serum, *Chemical Science* **2019**.
[27] J. Bai, X. Li, Z. Zhu, Y. Zheng, W. Hong, Single-Molecule Electrochemical Transistors, *Adv Mater* **2021**, *33*, e2005883.
[28] H. Chen, J. Fraser Stoddart, From molecular to supramolecular electronics, *Nature Reviews Materials* **2021**, *6*, 804-828.
[29] Y. H. Wang, Y. F. Zhou, L. Tong, H. Huang, J. F. Zheng, W. Xie, J. Z. Chen, Y. Shao, X. S. Zhou, Revealing Supramolecular Interactions and Electron Transport in Single Molecular Junctions of Cucurbit[n]uril, *Advanced Electronic Materials* **2021**, *7*, 2100399.
[30] W. Zhang, S. Gan, A. Vezzoli, R. J. Davidson, D. C. Milan, K. V. Luzyanin, S. J. Higgins, R. J. Nichols, A. Beeby, P. J. Low, B. Li, L. Niu, Single-Molecule Conductance of Viologen-Cucurbit[8]uril Host-Guest Complexes, *ACS Nano* **2016**, *10*, 5212-5220.
[31] S. V. Aradhya, M. Frei, M. S. Hybertsen, L. Venkataraman, Van der Waals interactions at metal/organic interfaces at the single-molecule level, *Nat Mater* **2012**, *11*, 872-876.

[32] Z. Liu, S. Y. Ding, Z. B. Chen, X. Wang, J. H. Tian, J. R. Anema, X. S. Zhou, D. Y. Wu, B. W. Mao, X. Xu, B. Ren, Z. Q. Tian, Revealing the molecular structure of single-molecule junctions in different conductance states by fishing-mode tip-enhanced Raman spectroscopy, *Nat Commun* **2011**, *2*, 305.

[33] L. Zhang, T.-Y. Zhou, J. Tian, H. Wang, D.-W. Zhang, X. Zhao, Y. Liu, Z.-T. Li, A two-dimensional single-layer supramolecular organic framework that is driven by viologen radical cation dimerization and further promoted by cucurbit[8]uril, *Polymer Chemistry* **2014**, *5*, 4715-4721.

[34] W. S. Jeon, H. J. Kim, C. Lee, K. Kim, Control of the stoichiometry in host-guest complexation by redox chemistry of guests: inclusion of methylviologen in cucurbit[8]uril, *Chem Commun (Camb)* **2002**, 1828-1829.

[35] K. M. Park, M. Y. Hur, S. K. Ghosh, D. R. Boraste, S. Kim, K. Kim, Cucurbit[n]uril-based amphiphiles that self-assemble into functional nanomaterials for therapeutics, *Chemical Communications* **2019**, *55*, 10654-10664.

[36] M. Wiemann, P. Jonkheijm, Stimuli-Responsive Cucurbit[n]uril-Mediated Host-Guest Complexes on Surfaces, *Israel Journal of Chemistry* **2018**, *58*, 314-325.

[37] A. Gonzalez-Campo, M. Brasch, D. A. Uhlenheuer, A. Gomez-Casado, L. Yang, L. Brunsveld, J. Huskens, P. Jonkheijm, Supramolecularly oriented immobilization of proteins using cucurbit[8]uril, *Langmuir* **2012**, *28*, 16364-16371.

[38] L. Qi, H. Tian, H. Shao, H.-Z. Yu, Host–Guest Interaction at Molecular Interfaces: Binding of Cucurbit[7]uril on Ferrocenyl Self-Assembled Monolayers on Gold, *The Journal of Physical Chemistry C* **2017**, *121*, 7985-7992.

[39] Z. Walsh-Korb, Y. Yu, E. R. Janecek, Y. Lan, J. Del Barrio, P. E. Williams, X. Zhang, O. A. Scherman, Single-Molecule Force Spectroscopy Quantification of Adhesive Forces in Cucurbit[8]Uril Host-Guest Ternary Complexes, *Langmuir* **2017**, *33*, 1343-1350.

[40] K. Kim, W. S. Jeon, J.-K. Kang, J. W. Lee, S. Y. Jon, T. Kim, K. Kim, A Pseudorotaxane on Gold: Formation of SelfAssembled Monolayers, Reversible Dethreading and Rethreading of the Ring, and Ion-Gating Behavior, *Angewandte Chemie* **2003**, *115*, 2395-2398.

[41] C. Hu, Y. Lan, F. Tian, K. R. West, O. A. Scherman, Facile method for preparing surface-mounted cucurbit[8]uril-based rotaxanes, *Langmuir* **2014**, *30*, 10926-10932.

[42] J. Kim, Y. Kim, K. Baek, Y. H. Ko, D. Kim, K. Kim, Direct force measurement between cucurbit[6]uril and spermine using atomic force microscopy, *Tetrahedron* **2008**, *64*, 8389-8393.

[43] F. Tian, D. Jiao, F. Biedermann, O. A. Scherman, Orthogonal switching of a single supramolecular complex, *Nat Commun* **2012**, *3*, 1207.

[44] A. B. Braunschweig, F. Huo, C. A. Mirkin, Molecular printing, *Nature Chemistry* **2009**, *1*, 353-358.

[45] M. Hirtz, J. Brglez, H. Fuchs, C. M. Niemeyer, Selective Binding of DNA Origami on Biomimetic Lipid Patches, *Small* **2015**, *11*, 5752-5758.

[46] F. Huo, Z. Zheng, G. Zheng, R. Giam Louise, H. Zhang, A. Mirkin Chad, Polymer Pen Lithography, *Science* **2008**, *321*, 1658-1660.

[47] J. Atwater, D. S. Mattes, B. Streit, C. von Bojnicic-Kninski, F. F. Loeffler, F. Breitling, H. Fuchs, M. Hirtz, Combinatorial Synthesis of Macromolecular Arrays by Microchannel Cantilever Spotting (microCS), *Adv Mater* **2018**, *30*, e1801632.

[48] A. Kumar, G. M. Whitesides, Features of gold having micrometer to centimeter dimensions can be formed through a combination of stamping with an elastomeric stamp and an alkanethiol ‘‘ink’’ followed by chemical etching, *Applied Physics Letters* **1993**, *63*, 2002-2004.
[49] B. D. Gates, Q. Xu, M. Stewart, D. Ryan, C. G. Willson, G. M. Whitesides, New Approaches to Nanofabrication: Molding, Printing, and Other Techniques, *Chemical Reviews* **2005**, *105*, 1171-1196.
[50] Z. Zheng, J. W. Jang, G. Zheng, C. A. Mirkin, Topographically flat, chemically patterned PDMS stamps made by dip-pen nanolithography, *Angew Chem Int Ed Engl* **2008**, *47*, 9951-9954.
[51] M. Hirtz, A. M. Greiner, T. Landmann, M. Bastmeyer, H. Fuchs, Click-Chemistry Based Multi-Component Microarrays by Quill-Like Pens, *Advanced Materials Interfaces* **2014**, *1*, 1-7.
[52] D. S. Ginger, H. Zhang, C. A. Mirkin, The evolution of dip-pen nanolithography, *Angew Chem Int Ed Engl* **2004**, *43*, 30-45.
[53] D. Piner Richard, J. Zhu, F. Xu, S. Hong, A. Mirkin Chad, "Dip-Pen" Nanolithography, *Science* **1999**, *283*, 661-663.
[54] L. M. Demers, D. S. Ginger, S. J. Park, Z. Li, S. W. Chung, C. A. Mirkin, Direct Patterning of Modified Oligonucleotides on Metals and Insulators by Dip-Pen Nanolithography, *Science* **2002**, *296*, 1836-1838.
[55] N. A. Amro, S. Xu, G.-y. Liu, Patterning Surfaces Using Tip-Directed Displacement and Self-Assembly, *Langmuir* **2000**, *16*, 3006-3009.
[56] P. T. Hurley, A. E. Ribbe, J. M. Buriak, Nanopatterning of Alkynes on Hydrogen-Terminated Silicon Surfaces by Scanning Probe-Induced Cathodic Electrografting, *Journal of the American Chemical Society* **2003**, *125*, 11334-11339.
[57] D. A. Weinberger, S. Hong, C. A. Mirkin, B. W. Wessels, T. B. Higgins, Combinatorial Generation and Analysis of Nanometer- and Micrometer-Scale Silicon Features via “Dip-Pen” Nanolithography and Wet Chemical Etching, *Advanced Materials* **2000**, *12*, 1600-1603.
[58] D. J. Eichelsdoerfer, X. Liao, M. D. Cabezas, W. Morris, B. Radha, K. A. Brown, L. R. Giam, A. B. Braunschweig, C. A. Mirkin, Large-area molecular patterning with polymer pen lithography, *Nature Protocols* **2013**, *8*, 2548-2560.
[59] U. Bog, A. De los Santos Pereira, S. L. Mueller, S. Havenridge, V. Parrillo, M. Bruns, A. E. Holmes, C. Rodriguez-Emmenegger, H. Fuchs, M. Hirtz, Clickable Antifouling Polymer Brushes for Polymer Pen Lithography, *ACS Applied Materials and Interfaces* **2017**, *9*, 12109-12117.
[60] H.-Y. Liu, R. Kumar, C. Zhong, S. Gorji, L. Paniushkina, R. Masood, U. A. Wittel, H. Fuchs, I. Nazarenko, M. Hirtz, Rapid Capture of Cancer Extracellular Vesicles by Lipid Patch Microarrays, *Advanced Materials* **2021**, *33*, 2008493.
[61] M. Hirtz, S. Varey, H. Fuchs, A. Vijayaraghavan, Attoliter Chemistry for Nanoscale Functionalization of Graphene, *ACS Applied Materials and Interfaces* **2016**, *8*, 33371-33376.
[62] A. Angelin, U. Bog, R. Kumar, C. M. Niemeyer, M. Hirtz, Writing Behavior of Phospholipids in Polymer Pen Lithography (PPL) for Bioactive Micropatterns, *Polymers (Basel)* **2019**, *11*.

[63] M. C. Kim, J. J. Gillissen, S. R. Tabaei, V. P. Zhdanov, N. J. Cho, Spatiotemporal dynamics of solvent-assisted lipid bilayer formation, *Phys Chem Chem Phys* **2015**, *17*, 31145-31151.
[64] A. R. Ferhan, B. K. Yoon, S. Park, T. N. Sut, H. Chin, J. H. Park, J. A. Jackman, N. J. Cho, Solvent-assisted preparation of supported lipid bilayers, *Nat Protoc* **2019**, *14*, 2091-2118.
[65] H. Su, H.-Y. Liu, A.-M. Pappa, T. C. Hidalgo, P. Cavassin, S. Inal, R. M. Owens, S. Daniel, Facile Generation of Biomimetic-Supported Lipid Bilayers on Conducting Polymer Surfaces for Membrane Biosensing, *ACS Applied Materials & Interfaces* **2019**, *11*, 43799-43810.
[66] K. Kolahdouzan, J. A. Jackman, B. K. Yoon, M. C. Kim, M. S. Johal, N. J. Cho, Optimizing the Formation of Supported Lipid Bilayers from Bicellar Mixtures, *Langmuir* **2017**, *33*, 5052-5064.
[67] R. R. Nair, S. Debnath, S. Das, P. Wakchaure, B. Ganguly, P. B. Chatterjee, A Highly Selective Turn-On Biosensor for Measuring Spermine/Spermidine in Human Urine and Blood, *ACS Applied Bio Materials* **2019**, *2*, 2374-2387.
[68] J. T. Fletcher, B. S. Bruck, Spermine detection via metal-mediated ethynylarene 'turn-on' fluorescence signaling, *Sens Actuators B Chem* **2015**, *207*, 843-848.
[69] N. Kaur, S. Chopra, G. Singh, P. Raj, A. Bhasin, S. K. Sahoo, A. Kuwar, N. Singh, Chemosensors for biogenic amines and biothiols, *Journal of Materials Chemistry B* **2018**, *6*, 4872-4902.
[70] A. Thomas, D. Iacono, A. L. Luciano, K. Armellino, A. Di Iorio, M. Onofrj, Duration of amantadine benefit on dyskinesia of severe Parkinson's disease, *Journal of Neurology, Neurosurgery & Psychiatry* **2004**, *75*, 141.
[71] Y. Han, C. Nickle, Z. Zhang, H. Astier, T. J. Duffin, D. Qi, Z. Wang, E. Del Barco, D. Thompson, C. A. Nijhuis, Electric-field-driven dual-functional molecular switches in tunnel junctions, *Nat Mater* **2020**, *19*, 843-848.
[72] S. M. M. Dadfar, S. Sekula-Neuner, V. Trouillet, M. Hirtz, A Comparative Study of Thiol-Terminated Surface Modification by Click Reactions: Thiol-yne Coupling versus Thiol-ene Michael Addition, *Advanced Materials Interfaces* **2018**, *5*, 1801343.
[73] M. V. Rekharsky, Y. H. Ko, N. Selvapalam, K. Kim, Y. Inoue, Complexation Thermodynamics of Cucurbit[6]uril with Aliphatic Alcohols, Amines, and Diamines, *Supramolecular Chemistry* **2007**, *19*, 39-46.
[74] V. Sindelar, M. A. Cejas, F. M. Raymo, A. E. Kaifer, Tight inclusion complexation of 2,7-dimethyldiazapyrenium in cucurbit 7 uril, *New Journal of Chemistry* **2005**, *29*, 280-282.
[75] Z. Miskolczy, M. Megyesi, L. Biczok, A. Prabodh, F. Biedermann, Kinetics and Mechanism of Cation-Induced Guest Release from Cucurbit 7 uril, *Chemistry-a European Journal* **2020**, *26*, 7433-7441.
[76] D. M. Bailey, A. Hennig, V. D. Uzunova, W. M. Nau, Supramolecular tandem enzyme assays for multiparameter sensor arrays and enantiomeric excess determination of amino acids, *Chemistry-a European Journal* **2008**, *14*, 6069-6077.
[77] S. Sinn, J. Kramer, F. Biedermann, Teaching old indicators even more tricks: binding affinity measurements with the guest-displacement assay (GDA), *Chemical Communications* **2020**, *56*, 6620-6623.

[78] D. Das, K. I. Assaf, W. M. Nau, Applications of Cucurbiturils in Medicinal Chemistry and Chemical Biology, *Frontiers in Chemistry* **2019**, *7*.
[79] G. Wenz, M. Weickenmeier, J. Huff, in *Associative Polymers in Aqueous Media, Vol. 765*, American Chemical Society, **2000**, pp. 271-283.
[80] M. Onda, K. Yoshihara, H. Koyano, K. Ariga, T. Kunitake, Molecular Recognition of Nucleotides by the Guanidinium Unit at the Surface of Aqueous Micelles and Bilayers. A Comparison of Microscopic and Macroscopic Interfaces, *Journal of the American Chemical Society* **1996**, *118*, 8524-8530.
[81] X. A. Cha, K. Ariga, M. Onda, T. Kunitake, MOLECULAR RECOGNITION OF AQUEOUS DIPEPTIDES BY NONCOVALENTLY ALIGNED OLIGOGLYCINE UNITS AT THE AIR/WATER INTERFACE, *Journal of the American Chemical Society* **1995**, *117*, 11833-11838.
[82] H. T. Minoru Sakurai, Yoshio Inoue, Katsuhiko Ariga,, T. Kunitake, Theoretical Study of Intermolecular Interaction at the Lipid - Water Interface. 1. Quantum Chemical Analysis Using a Reaction Field Theory, *J. Phys. Chem. B* **1997**.
[83] H. Tamagawa, M. Sakurai, Y. Inoue, K. Ariga, T. Kunitake, Theoretical Study of Intermolecular Interaction at the Lipid−Water Interface. 2. Analysis Based on the Poisson−Boltzmann Equation, *The Journal of Physical Chemistry B* **1997**, *101*, 4817-4825.
[84] K. Ariga, T. Makita, M. Ito, T. Mori, S. Watanabe, J. Takeya, Review of advanced sensor devices employing nanoarchitectonics concepts, *Beilstein J Nanotechnol* **2019**, *10*, 2014-2030.
[85] G. F. Versteeg, J. A. M. Kuipers, F. P. H. Van Beckum, W. P. M. Van Swaaij, Mass transfer with complex reversible chemical reactions—I. Single reversible chemical reaction, *Chemical Engineering Science* **1989**, *44*, 2295-2310.
[86] H. Jangara, K. Shayesteh, M. Shahedi Asl, Mathematical modeling of absorption accompanied by a non-elementary reversible chemical reaction, *Chemical Engineering Research and Design* **2020**, *157*, 58-64.
[87] F. Zhang, C. Lu, M. Wang, X. Yu, W. Wei, Z. Xia, A Chiral Sensor Array for Peptidoglycan Biosynthesis Monitoring Based on MoS2 Nanosheet-Supported Host-Guest Recognitions, *ACS Sensors* **2018**, *3*, 304-312.
[88] X. Zhu, X. Fan, G. Ju, M. Cheng, Q. An, J. Nie, F. Shi, A facile method to immobilize cucurbituril on surfaces through photocrosslinking with azido groups, *Chem Commun (Camb)* **2013**, *49*, 8093-8095.
[89] T. M. Squires, R. J. Messinger, S. R. Manalis, Making it stick: convection, reaction and diffusion in surface-based biosensors, *Nat Biotechnol* **2008**, *26*, 417-426.
[90] L. P. Sanford, S. M. Crawford, Mass transfer versus kinetic control of uptake across solid-water boundaries, *Limnology and Oceanography* **2000**, *45*, 1180-1186.
[91] S. Oberhansl, M. Hirtz, A. Lagunas, R. Eritja, E. Martinez, H. Fuchs, J. Samitier, Facile modification of silica substrates provides a platform for direct-writing surface click chemistry, *Small* **2012**, *8*, 541-545.
[92] S. M. M. Dadfar, S. Sekula-Neuner, U. Bog, V. Trouillet, M. Hirtz, Site-specific surface functionalization via microchannel cantilever spotting (µCS): Comparison between Azide–alkyne and thiol–alkyne click chemistry reactions, *Small* **2018**, *14*, 1-10.
[93] N. Willems, A. Urtizberea, A. F. Verre, M. Iliut, M. Lelimousin, M. Hirtz, A. Vijayaraghavan, M. S. P. Sansom, Biomimetic Phospholipid Membrane

Organization on Graphene and Graphene Oxide Surfaces: A Molecular Dynamics Simulation Study, *ACS Nano* **2017**, *11*, 1613-1625.
[94] C. Hu, L. Grimm, A. Prabodh, A. Baksi, A. Siennicka, P. A. Levkin, M. M. Kappes, F. Biedermann, Covalent cucurbit[7]uril-dye conjugates for sensing in aqueous saline media and biofluids, *Chem Sci* **2020**, *11*, 11142-11153.
[95] W. M. Nau, A. Hennig, G. G. Ghale, F. Biedermann, Fluorescent Artificial Receptor-Based Membrane Assay (FARMA) for Spatiotemporally Resolved Monitoring of Biomembrane Permeability, *ChemRxiv* **2019**.
[96] M. M. Thuo, W. F. Reus, C. A. Nijhuis, J. R. Barber, C. Kim, M. D. Schulz, G. M. Whitesides, Odd-even effects in charge transport across self-assembled monolayers, *J Am Chem Soc* **2011**, *133*, 2962-2975.
[97] E. Blanco, L. Rocha, M. D. Pozo, L. Vazquez, M. D. Petit-Dominguez, E. Casero, C. Quintana, A supramolecular hybrid sensor based on cucurbit[8]uril, 2D-molibdenum disulphide and diamond nanoparticles towards methyl viologen analysis, *Anal Chim Acta* **2021**, *1182*, 338940.
[98] R. Kumar, A. Bonicelli, S. Sekula-Neuner, A. C. B. Cato, M. Hirtz, H. Fuchs, Click-Chemistry Based Allergen Arrays Generated by Polymer Pen Lithography for Mast Cell Activation Studies, *Small (Weinheim an der Bergstrasse, Germany)* **2016**, *12*, 5330-5338.
[99] J. H. Scofield, Hartree-Slater subshell photoionization cross-sections at 1254 and 1487 eV, *Journal of Electron Spectroscopy and Related Phenomena* **1976**, *8*, 129-137.
[100] J. T. Xu, M. Lynch, J. L. Huff, C. Mosher, S. Vengasandra, G. F. Ding, E. Henderson, Microfabricated quill-type surface patterning tools for the creation of biological micro/nano arrays, *Biomedical Microdevices* **2004**, *6*, 117-123.
[101] E. R. Nagarajan, D. H. Oh, N. Selvapalam, Y. H. Ko, K. M. Park, K. Kim, Cucurbituril anchored silica gel, *Tetrahedron Letters* **2006**, *47*, 2073-2075.

7. Acknowledgments

Chemistry is an interdisciplinary field that covers host-guest chemistry, electrochemistry, nanotechnology and so on. I am very grateful for the opportunity to be a part of this advanced field at the Institute of Nanotechnology (INT), Karlsruhe Institute of Technology (KIT), Karlsruhe, Germany. I learn and enhance my research experience from some of the best professionals in the fields of chemistry.

I owe my profound gratitude to my official supervisor Prof. Dr. Annie K. Powell, who gave me an opportunity to work in the field of Nanotechnology. She provides me an environment to explore my ideas and projects in her group at INT, KIT. Regardless of her busy schedule, she was always available for discussions and advice. Thank you very much Prof. Dr. Annie K. Powell!

I would like to express my sincere gratitude to my first supervisor PD Dr. Dr. Michael Hirtz at INT, who was directly involved in all my thesis projects. He always provides me with a good working environment in Scanning Probe Lithography (SPL). I appreciate his guidance and all the invaluable advice throughout this thesis work. I deeply appreciate your work attitude and your work efficiency. It was a great pleasure and honor to work with you. This thesis would not have been possible without your extraordinary support.

My sincere appreciation is extended to my co-supervisor Dr. Frank Biedermann at INT, KIT, for giving me the opportunity to do my PhD under his guidance and in his working group. Due to the varied topics, I had the opportunity to learn a lot of new things and to discover topics that were completely new to me. Your expertise in the various field helped me a lot in many aspects from planning the experiments till the final revision of the papers.

I would like to thank Prof. Dr. Pascal Jonkeijm and Prof. Dr. Christian A. Nijhuis at MESA+ Institute for Nanotechnology, University of Twente (UT), the Netherlands, for giving me

the opportunity to do my exchange study in their groups. I appreciate their guidance, work efficiency and all advice throughout electronics projects.

I thank the financial support from the China Scholarship Council (CSC) fellowship for PhD study and Karlsruhe House of Young Scientists (KHYS) in KIT for exchange stays.

I would like to thank my colleagues Changming Hu, Joana Krämer, Dr. Laura Grimm and Yichuan Wang who shared compounds to proceed with chemosensor projects. In addition, very special thanks to Dr. Hui-yu Liu, Dr. Ravi Kumar and Dr. Seyed Mohammad Mahdi Dadfar, who taught me lithography skills and helped to find solutions when there were tricky steps, Fuad A. Alami and in UT, who taught me electronics modification and measurements. Furthermore, I would like to acknowledge my labmates and colleagues in KIT: Dr. Eider Berganza Eguiarte, Dr. Sylwia Sekula-Neuner, Srivatsan Vasantham, Dr. Uwe Bog, Dr. Picchetti, Pierre, Dr. Stephan Sinn, Navid Hussain, Bingquan Yang, Rui Kang, Amrutha Prabodh and Nazami Mohammad, and in UT: Lijie Li, Nataliya Debera and Mireia Vilar.

I am especially grateful to my family for giving me the freedom to follow my dreams. Thank my father Cuihui Deng taking care of my mother Jianmei Zhong, and they have always been encouraging me to do well throughout my studies, and my source of motivation. I would like to thank my sister Qilian Zhong, she gave me chance for long-term education; and brother Xuexian Zhong for sharing the stress of life. They have been always taking care of our parents. 特别感谢我的家人给我追梦的自由！感谢我的父亲邓翠辉一直照顾我的母亲钟枧妹，让我没有后顾之忧；感谢我的姐姐钟启连给了我继续上学的机会；感谢我的弟弟钟学贤一直照顾父母，和我分担生活的压力。最深的爱献给我的家人！

Last but not least, I would like to thank all my friends, including my football team and hiking mates. We played football, went climbing, did other sports and explored different cities

and mountains in Germany and Europe. It was great fun with all of you. This thesis would not have been possible without your direct or indirect contribution.

8. Appendix

8.1. List of abbreviations

CBn	cucurbit[*n*]urils
SLB	supported lipid bilayer
CD	β-cyclodextrin
SiO_2	glass
Au	gold
Ag	silver
SiO_2-OH	hydroxylated surface
SiO_2-SH	thiol surface
SiO_2-CBn	cucurbit[*n*]uril surface
SiO_2-CB6	cucurbit[6]uril surface
SiO_2-CB7	cucurbit[7]uril surface
SiO_2-CB8	cucurbit[8]uril surface
SiO_2-NCO	isocyanate surface
SiO_2-Alk	Alkyne surface
SiO_2-DBCO	Dibenzocyclooctyne surface
DPN	dip-pen nanolithography
PPL	polymer-pen lithography
µCS	microchannel cantilever spotting
IDA	indicator displacement assays
LOD	limit of detection
DBA	direct-binding assay
ABA	associative-binding assay
TMR	tetramethylrhodamine
Kd	equilibrium dissociation constant
HRP	horseradish peroxidase
BE	berberine
STM-BJ	scanning tunneling microscopy break junction
TERS	tip-enhanced Raman spectroscopy
AFM	atomic force microscope

DFT	density functional theory
LUMO	highest occupied molecular orbital
SOF	supramolecular organic framework
AD	adamantine
MA	molecular amphiphile
FcC11SH	ferrocenylundecanethiol
CnSH	n-alkanethiolate
SMFS	single-molecule force spectroscopy
χ	mole percentage
μCP	microcontact printing
SPL	scanning probe lithography
PDMS	polydimethylsiloxane
CuAAC	copper(I)-catalyzed azide-alkyne cycloaddition
TAMRA	tetramethylrhodamine
EV	extracellular vesicle
SLM	supported lipid membrane
SALB	solvent-assisted lipid bilayer
Spm	spermine
Cad	cadaverine
Ama	amantadine
L-Trp	L-tryptophan
Mem	memantine
Pen	penicillin
IAA	indole acetic acid
H-IAA	hydroxyl indole acetic acid
MPTMS	3-mercaptopropyl) trimethoxysilane
CBn-Pro	propargyl curcubit[*n*]urils
CA	contact angle
XPS	X-ray Photoelectron Spectroscopy
RD	reference-dye (BDP-630/650-alkyne)
BF	bright field

NEM	N-ethylmaleinimid
TMR-Cad	tetramethylrhodamine cadaverine
MDAP	N,N’-dimethyl-2,7,diazapyrenium
PBS	phosphate buffered saline
log K_a	binding affinity
DSMI	trans-4-[4-(dimethylamino)styryl]-1-methylpyridinium iodide
BE-N_3	berberine azide
$CuSO_4$	copper sulfate
TAMRA-N_3	tetramethylrhodamine azide
PEP-N_3	N,N-dimethyl-4^3-(pyridin-4-yl)-1,4(1,4)-dibenzenacyclohexaphan-1^2-amine azide
PCP-N_3	(E)-N,N-dimethyl-4-(2-(pyridin-4-yl)vinyl)aniline azide
HS-DAP-SH	azapyrenium dithiol
DAP	azapyrenium
MDI	4,4′-diisocyanato-methylenedibenzene
TDL	dibutyltin dilaurate
HEPES	2-[4-(2-Hydroxyethyl)piperazin-1-yl]ethane-1-sulfonic acid
DSPE-PEG-Maleimide	1,2-distearoyl-sn-glycero-3-phosphoethanolamine-N-[maleimide-(polyethylene glycol)-2000]
Liss Rhod PE	1,2-dioleoyl-sn-glycero-3-phosphoethanolamine-N-(lissamine rhodamine B sulfonyl)
DOPS	1,2-dioleoyl-sn-glycero-3-phospho-L-serine
Strep-Cy3	streptavidin-Cy3
Ad-OH	1-adamantanol
MCC	1,2-dioleoyl-sn-glycero-3-phosphoethanolamine-N-[4-(p-maleimidomethyl)cyclohexane-carboxamide]
AlexaFluor-BSA	AlexaFluor488 linked Albumin from Bovine Serum
Alk-SH	Alkyl thiol
MV	methyl viologen
MV^{2+}	methyl viologen with positive charges
MV-SH	methyl viologen thiol

$MV^{\bullet+}$	methyl viologen radical
$[MV^{\bullet+}]_2$	methyl viologen radical dimer
CV	cyclic voltammetry
EGaIn	Eutectic Gallium-Indium
SAM	self-assembled monolayer
RRAM	resistive random access memories
Q	charge
n	number of electrons involved per mole of reaction
A	surface area of the working electrode
F	Faraday constant, 96485.33 C mol^{-1}
J	current density
V	voltage
I_{higher}, I_{lower}	currents at the same voltage in two biases
I_{RR}	current rectification ratio
$R_{2/1}$	highest on/off state ratio
R_1	low conductance
R_2	high conductance
RH	humidity
DI	deionized
CMOS	complementary metal-oxide semiconductor

8.2. List of tables

8.3. List of figures

8.4. Publications and conference contributions

8.4.1. Publications

C. Zhong, S. Soni, F. A. Alami, F. Biedermann, M. Hirtz, P. Jonkheijm, C. A. Nijhuis. "Conductance enhancement of dual-functional molecular switches in tunneling junctions via host-guest chemistry", *Nature Communication*. preparing

J. Krämer, L. M. Grimm, **C. Zhong**, M. Hirtz, F. Biedermann. "A cucurbit[8]uril-rotaxane enables optical sensing of tryptophan in biofluids", *Nature Communication*. Under review

C. Zhong, C. Hu, R. Kumar, V. Trouillet, F. Biedermann, M. Hirtz. "Microchannel cantilever spotted sensor arrays for highly affinitive indicator-displacement assays", *ACS Applied Nano Materials*. **2021**, 4, 4676-4687

H. Y. Liu, R. Kumar, **C. Zhong**, S. Gorji, L. Paniushkina, R. Masood, U. A. Wittel, H. Fuchs, I. Nazarenko, M. Hirtz. "Rapid capture of cancer extracellular vesicles by lipid patch microarrays". *Advanced Materials*. **2021**, 33, 2008493

E. Berganza; M.P. Ebrahimkutty, S.K. Vasantham, **C. Zhong**, A. Wunsch, A. Navarrete, M. Galic, M. Hirtz. "Multiplexed phospholipid membrane platform for curvature sensitive protein screening", *Nanoscale*. **2021**,13, 12642-12650.

8.4.2. Conference contributions

MNE 2022 EUROSENSORS, 19th -23rd September 2022, Leuven, Belgium. Application of Cucurbit[n]urils Immobilization in Chemosensor Microarrays and Molecular Electronics, **talk**

SupraChem**,** 3rd -5th July 2022, Mainz, Germany. Cucurbit[n]uril/indicator Chemosensor Microarrays for Indicator-Displacement Assays of Small Bioactive Metabolites, **poster**

1st International Supramolecular Chemistry Summer School, 29th May - 2nd June 2022, Santa Margherita di Pula (CA), Italy, **poster**

Modelling in Molecular Spintronics, 6th – 8th April 2022, Ecole Normale Paris-Saclay, Paris, France.

1st International Electronic Conference on Chemical Sensors and Analytical Chemistry (CSAC2021), 1st -15th July 2021, online. “Cucurbit[*n*]uril-Immobilized Sensor Arrays for Indicator-Displacement Assays of Small Bioactive Metabolites”.

Nanobiotechnology for Cell Interfaces, 17th -18th March 2021, online. “Cucurbit[n]uril-Immobilized Sensor Arrays for Indicator-Displacement Assays of Small Bioactive Metabolites”, **poster**

KNMF user Meeting, 10th -11th March 2020, Karlsruhe, Baden-Württemberg, Germany. “Cucurbit[n]uril-microarrays for highly sensitive Indicator-Displacement Assays”, **poster**